UNIVERSITY OF BERGAMO

Department of Management, Information and Production Engineering

Doctoral Degree in Technology Innovation and Management

XXXIV Cycle

Friction Stir Welding: from the Corrosion, Mechanical, Microstructural and Thermal Behavior of Aluminum Joints to the Development of a Comprehensive Simulation Model

Thesis Supervisor

Prof. Gianluca Danilo D'Urso

Author

Sara Bocchi

PhD Candidate ID: 1014841

Academic year 2020/2021

Acknowledgements

I would like to express my gratitude to my tutor Prof. Gianluca D'Urso, whose guidance stimulated me during all the activities carried out in these three years. His help and support have been crucial in my academic experience and his trust in my competences has been a great incentive to achieve these results.

Besides my tutor, I am deeply grateful to Prof. Giancarlo Maccarini and Prof. Claudio Giardini for supervising my work, kindly sharing their wide-ranging knowledge and skill and guiding me towards all the academic and doctoral activities. They have been always extremely available to any question I had, also helping me to deepen my own understanding of all the involved scientific aspects.

My sincere gratefulness to all my co-authors, from whom I had the opportunity to learn and become a better researcher, and to Prof. Chiara Ravasio, for all the activities in which she has involved me.

I would like to thank Prof. Renato Redondi and Prof. Caterina Rizzi, the actual and previous coordinator of the Doctoral School, and all Faculty Members of the Doctoral Program in Technology, Innovation and Management of the University of Bergamo and University of Napoli Federico II.

Many thanks to Prof. Mariangela Quarto and to Doc. Mattia Carminati, with whom I shared victories and defeats and for whom I have deep esteem.

I thank also all the UniBg laboratories staff I worked with and especially the laboratory technicians Daniele, Luca and Massimiliano, always available for any request.

Thanks to all the PhD mates and PhD students of the PhD room and the UniBg laboratories, especially to Alice, who immediately welcomed me into the PhD students room, and to Chiara, not only a valuable colleague, but a close friend as well.

Last but not least, a very special thank goes to my family, above all to my parents and my sister, for the possibilities they offered me, the moral support and trust granted to me and for always being there to share even my smallest success.

Abstract

In the last decades, aluminum has been proving to be a material of considerable importance in the engineering field, especially in the aeronautic and automotive sectors, because of its advantageous ratio between mechanical properties and weight. Significant importance in these fields is assumed by the aluminum precipitation-hardening alloys, which can achieve mechanical properties comparable to those of structural steel.

However, these alloys, called high-strength alloys, are difficult to be welded with traditional methods and, to overcome this problem, alternative joining methods have been studied.

In 1991, a new solid-state welding process called Friction Stir Welding (FSW) was developed at The Welding Institute, which allows the joining of a wide range of parts and geometries.

In addition to the possibility of using this technology to weld materials that are difficult to weld, friction stir welding is demonstrating to be a promising green technology as it is characterized by high energy efficiency, due to the involved lower temperatures with respect to the traditional fusion welding techniques, and respect for the environment, because of the limited waste material and the avoided radiation and hazardous fumes.

This characteristic is not negligible as it is well-known that, within the production field, manufacturing is one of the most polluting sectors and, nowadays, one of the most important challenges that the world is called to face is a sustainable development to reduce global pollution.

This challenge especially regards CO_2 direct and indirect emissions, an issue strictly related to the industry field which causes about 40% of the world emissions. Indeed, CO_2 emissions due to the industry have increased in recent years, except for the recent COVID effect.

The main objective of this thesis is the in-depth study of Friction Stir Welding technology with the final aim of expanding its knowledge and the possibilities of its application, in order to make it more usable in the industrial field.

To do that, this research was divided into two parts. In the first one, the variation of the microstructure and the characterization of the corrosion behavior of high-strength aluminum alloy joints welded with Friction Stir Welding technology were studied. Subsequently, based on the data experimentally collected in the first phase of the study

and on the found importance of the thermal input, the research was implemented by analyzing in detail the influence of the temperature involved in the process on the mechanical behavior and on the microstructure, using different external cooling systems. Downstream of the entire experimental collection, finite element simulation and artificial intelligence techniques were applied, as well as optimization algorithms, to build a predictive model capable of determining the input parameters as a function of the desired output parameters.

Contents

1. Introduction 1
1.1. Aluminum Alloys 1
1.1.1. Chemical composition 2
1.1.2. Heat treatments 7
1.2. Friction Stir Welding 12
1.2.1. Applications 13
1.2.2. Process and tool 14
1.2.3. Main process parameters 16
1.2.4. Weld morphology 18
1.3. Research Issues 22
2. Literature Review 25
2.1. Microstructure 25
2.2. Corrosion behavior 52
2.3. Friction Stir Welding cooling system 66
2.3.1. Underwater Friction Stir Welding 67
2.4. Finite Element Model 79
2.5. Artificial Neural network 80
3. Stress enhanced intergranular corrosion of friction stir welded AA2024-T3 83
3.1. Introduction 83
3.2. Material and methods 84
3.2.1. Base material microstructure 84
3.2.2. Friction Stir Welding (FSW) process setup 85
3.2.3. Intergranular corrosion test 86
3.2.4. Long exposure and SCC corrosion tests 86
3.3. Results and discussion 87

3.3.1. FSWed joints microstructure and intergranular attack 87

3.3.2. Long term exposure tests and SCC 91

3.4. Conclusions 99

4. Stress corrosion cracking of friction stir-welded AA-2024 T3 alloy 101

4.1. Introduction 101

4.2. Materials and Methods 102

4.2.1. Preparation of the Welds 102

4.2.2. Constant Load Tests 103

4.2.3. Slow Strain Rate Tests 105

4.2.4. Electrochemical Characterizations of the Different Zones of the Weld..... 106

4.3. Results and Discussion 107

4.4. Conclusions 119

5. Effect of load on the corrosion behavior of friction stir welded AA7075-T6 aluminum alloy 121

5.1. Introduction 121

5.2. Materials and Methods 121

5.2.1. Welds 121

5.2.2. Metallographic Analysis 122

5.2.3. OCP Monitoring 122

5.2.4. Constant Load Tests 124

5.2.5. Slow Strain-Rate Tests 125

5.3. Results 125

5.3.1. Metallographic Analysis 125

5.3.2. 4PBB Specimens 128

5.3.3. Constant Loading (CL) Tests 130

5.3.4. Slow Strain-Rate (SSR) Tests 133

5.4. Discussion 138

5.5. Conclusions 141

6. Effects of cooling conditions on microstructure and mechanical properties of friction stir welded butt joints of different aluminum alloys 143

6.1. Introduction 143

6.2. Materials and Methods 144

6.3. Results 148

6.3.1. Microstructure analysis 148

6.3.2. Rockwell and Vickers hardness distributions 155

6.3.3. Tensile tests 157

6.4. Discussion 160

6.5. Conclusions 165

7. The effect of heat generated on mechanical properties of friction stir welded aluminum alloys 167

7.1. Introduction 167

7.2. Materials and methods 168

7.2.1. Materials 168

7.2.2. FSW experimental setup 169

7.2.3. Microstructure analysis and Mechanical testing of the joints 173

7.3. Results and discussion 174

7.3.1. Temperature analysis 174

7.3.2. Rockwell hardness distributions 178

7.3.3. Tensile tests 186

7.4. Conclusions 190

8. FSW optimization through Particle Swarm Algorithm and Artificial Neural Network 193

8.1. Introduction 193

8.2. Artificial Neural Network modelling 194
8.2.1. Input and Output Layers structure 195
8.2.2. Hidden Layer structure 196
8.2.3. Training, Validation, and Testing of the ANN 200
8.3. PSO algorithm 205
8.4. Application of PSO algorithm to FSW process optimization 206
8.4.1. Objective function definition and PSO application 206
8.4.2. Validation of optimization methodology 207
8.5. Conclusions 210
9. Hybrid FEM-ANN approach for hardness prediction of AA6082 Friction Stir Welded joints 213
9.1. Introduction 213
9.2. Proposed Hybrid FEM-ANN approach 214
9.3. FSW simulation model setup 215
9.3.1. FEM model validation 217
9.4. Implementation and validation of ANN 224
9.5. Results and discussion 227
9.6. Conclusions 229
10. General conclusions 231
11. References 235

List of Figures

Figure 1.1: World primary aluminum production (data from The International Aluminium Institute [1]). 1

Figure 1.2: Aluminum-copper phase diagram [2]. 2

Figure 1.3: Aluminum-magnesium phase diagram [2]. 4

Figure 1.4: Aluminum-magnesium-silicon phase diagram [2]. 5

Figure 1.5: Aluminum-copper phase diagram [2]. 6

Figure 1.6: Trend of tensile strength as a function of ageing time for different aluminum alloys [5]. 8

Figure 1.7: Artificial ageing of AA6082 [8]. 10

Figure 1.8: Artificial ageing of AA7075. 11

Figure 1.9: FSW process. 12

Figure 1.10: Schematic representation of the FSW process [29]. 14

Figure 1.11: FSW tool types [32]. 15

Figure 1.12: Schematic illustration of the areas that have undergone variations during the process [42]. 18

Figure 1.13: AA7055 nugget microstructure [44]. 20

Figure 1.14: Nugget (NZ)-TMAZ transition zone [48]. 21

Figure 2.1: Dimensions of the grains with relative deformations at the nugget [55]. 25

Figure 2.2: Dimensions of the grains with relative deformations in the advancing side [55]. 26

Figure 2.3: Dimensions of the grains with relative deformations undergone in the retreating side [55]. 27

Figure 2.4: Microstructure of: a) Base metal. b) HAZ. c) Advancing Side. d) Retreating Side. e) Nugget [56]. 28

Figure 2.5: SEM images of the precipitates distribution in the base metal (a), in the nugget (b) and (c), and in the thermally affected zone (d) and (e) [56]. 29

Figure 2.6: Microstructure of the nugget of the AA2024 joints welded using different parameters: a) optical images, b) SEM close up of the precipitates [57]. 31

Figure 2.7: Microstructure of the HAZ of the AA2024 joint: a) optical images, b) SEM close up of the precipitates phases [57]. 32

Figure 2.8: Hardness profile of the FSWed AA2024 joints as a function of different welding parameters [57]. 33

Figure 2.9: Tensile strength of the joints (UTS) as a function of feed rate [mm/min] and rotational speed [rpm] [57]. 33

Figure 2.10: AA2024 hardness distribution as a function of different rotational speed [58]. 35

Figure 2.11: Optical micrographs of AA5754 base material at different magnifications [59]. 36

Figure 2.12: The microstructure of the stir zone for FSWed samples at 1070 rpm and three feed rates: (a) 36 mm/min; (b) 70 mm/min; (c) 140 mm/min [59]. 36

Figure 2.13: High magnification EDS elemental analysis of the second phase particles present in (a) base metal and (b) stir zone [59]. 37

Figure 2.14: Particle morphology and population measured at (a) base material and welding zone for samples welded with different feed rates: (b) 36 mm/min, (c) 70 mm/min, and (d) 140 mm/min [59]. 38

Figure 2.15: Metallurgical EBSD analysis. b HAZ and TMAZ at advancing side. c Weld nugget. d HAZ and TMAZ at advancing side [60]. 39

Figure 2.16: Grain size over the joint [60]. 39

Figure 2.17: Vickers micro-hardness map (in the transversal section) [60]. 40

Figure 2.18: Hardness distribution across weldments welded at different feed rates [59]. 40

Figure 2.19: Engineering stress-strain curves of the base material and friction stir welded joints of AA5754 [59]. 41

Figure 2.20: Microstructure of the as received material in (a) and across the weld nugget from the base metal (BM) through the TMAZ [22]. 42

Figure 2.21: Micro-hardness profile on the transverse section showing the effect of varying rotational speeds in (a) and of varying feed rates in (b) [22]. 43

Figure 2.22: Engineering stress–strain response for the FSWed welded samples showing the effect of feed rate in (a) and the effect of rpm in (b) [22]. 44

Figure 2.23: Variation of ultimate tensile strength for various welding conditions of feed rates (mm/min) and rotational speeds (rpm) in (a). Variation of Vickers hardness for various welding conditions of feed rates (mm/min) and rotational speeds (rpm) in (b) [22]. 44

Figure 2.24: Maps of base metal (SR) and FSW (SA) weld metal microstructures [64]. 45

Figure 2.25: Microstructure of the base material (a) and of the nugget (b) for a FSWed AA7075 [65]. 46

Figure 2.26: Microstructure of the AA7075 base metal [66]. 47

Figure 2.27: Microstructure of the nugget of an AA7075 alloy as the rotational speed varies [66]. 47

Figure 2.28: Microstructure of the boundary between nugget and TMAZ in the advancing side (AS) and in the retreating side (RS) of a FSWed AA7075 [66]. 48

Figure 2.29: Distribution of the second phases within the welding zones characteristic of an AA7075 alloy. a) Nugget. b) Thermo-mechanically affected area. c) Thermally affected zone [66]. 49

Figure 2.30: Microstructure of the nugget of the AA7075 joints welded using different parameters: a) optical images, b) SEM close up of the precipitates [57]. 50

Figure 2.31: Microstructure of the HAZ of the AA7075 joint: a) optical images, b) SEM close up of the precipitates phases [57]. 50

Figure 2.32: Hardness profile of the FSW AA7075 joints as a function of different welding parameters [57]. 51

Figure 2.33: Tensile strength of the joints (UTS) as a function of feed rate [mm/min] and rotational speed [rpm] [57]. 52

Figure 2.34: Pitting and intergranular attack of a) Base metal. b) HAZ. c) TMAZ. d) Nugget [70]. 54

Figure 2.35: Local corrosion potential measurements [70]. 54

Figure 2.36: Visualization test using gel on the cross section (A) advancing side and (R) retreating side [56]. 55

Figure 2.37: Etching on the cross section of specimens immersed in 0.1M NaCl for 24h. (A) advancing side and (R) retreating side [56]. 56

Figure 2.38: SEM images of the corrosion morphology on sections immersed in 0.1M NaCl for 24 hours and subsequent treatment with HNO3 for 30 seconds [56]. 57

Figure 2.39: Profile of local corrosion potential for the AA2024 unloaded specimen welded with S=1500 rpm and f=10 mm/min [57]. 59

Figure 2.40: Profile of local corrosion potential for the AA2024 unloaded specimen welded with S=1500 rpm and f=35 mm/min [57]. 59

Figure 2.41: Metallographic section of unloaded (a) and loaded (b–c) AA2024 joint after 1400 h of immersion in aerated 0.6M NaCl solution (a and b specimen welded with S=1000 rpm and f=10 mm/min, c specimen welded with S=1500 rpm and f=10 mm/min) [57]. 60

Figure 2.42: Chemical analysis and SEM image of the precipitates in the AA2024 nugget welded with S=1000 rpm and f=10 mm/min (red dots underline the presence of copper) [57]. 60

Figure 2.43: Etching on an AA7075-T651 immersed in a solution formed by 4M NaCl, 0.5M KNO_3, 0.1M HNO3 diluted to 10% [73]. 61

Figure 2.44: Potentiodynamic polarization curves for FSW AA7075-T651 in 0.5M NaCl: in (a) base metal behavior, corrosion zone, nugget. In (b) base metal in the region of the pitting potential [73]. 62

Figure 2.45: Intergranular attack at different rotational speeds: a) 630 rpm. b) 1000 rpm. c) 1600 rpm [66]. 62

Figure 2.46: Polarization curve at different rotational speed [66]. 63

Figure 2.47: Profile of local corrosion potential for the AA7075 unloaded specimen welded with S=1500 rpm and f=10 mm/min [57]. 64

Figure 2.48: Profile of local corrosion potential for the AA7075 unloaded specimen welded with S=1500 rpm and f=35 mm/min [57]. 64

Figure 2.49: Corrosion morphology of an AA7075 joint welded with S=1000 rpm and f=10 mm/min [57]. 65

Figure 2.50: Percentage of magnesium in the FSWed AA7075-T6: L indicates the traditional FSW process, the LW the UFSW process [90]. 68

Figure 2.51: Thermal cycle curves measured for FSW advancing side (a) ,FSW retreating side (b), UFSW advancing side (c), UFSW retreating side (d) [91]. 69

Figure 2.52: Macromorphologies of the welded joint with FSW (a) and UFSW (b) [87]. 70

Figure 2.53: Microstructure of the section of UFSWed joint (left) and FSWed joint (right) [88]. 71

Figure 2.54: Groove defect in an UFSWed AA7055 [94]. 71

Figure 2.55: Tunnel defect in an UFSWed AA7055 [94]. 72

Figure 2.56: S-line on the section of an AA2024 alloy joint welded with FSW. 72

Figure 2.57: Stress-strain curves of AA5083 joints welded with FSW (S5) and with UFSW (S1) [93]. 74

Figure 2.58: Schematic position of the low hardness zones relating to the tool [95]..... 75

Figure 2.59: .Distribution of residual stress of the plate welded in different media [91]. 76

Figure 2.60: Distribution of micro-hardness for FSWed and UFSWed AA7055 [91]. . 77

Figure 2.61: Distribution of micro-hardnesses of a FSWed and UFSWed AA2219 joints [93]. 77

Figure 2.62: Distribution of micro-hardness of a FSWed (S5) and UFSW (S1) AA5083 joint [88]. 78

Figure 3.1: α-Al grains oriented along the rolling direction (a). EDS analysis of Al-Cu-Mg intermetallic precipitates (b). EDS analysis of Al-Cu-Fe-Mn intermetallic precipitates (c). 85

Figure 3.2: The microstructure of the nugget of the specimens - optical images after Keller attack (a) and SEM close up of the precipitates distribution without the metallographic attack (b). 88

Figure 3.3: The microstructure of the HAZ of the specimens - optical images (c) and SEM close up of the precipitates phases (d). 88

Figure 3.4: Attack morphology of the specimens after six hours of immersion (C and D indicates the center of the welds). 90

Figure 3.5: The intergranular attack on the top of the specimen welded at S1000 and F35 (a) and of the specimen welded at S=1500 and F=10 (b); nugget images of the specimen welded at S1000 and F35 (c) and welded at S=1500 and F=10 (d). 91

Figure 3.6: Open circuit potential for the loaded and unloaded specimens as a function of the immersion time. 92

Figure 3.7: Nyquist representations of the EIS spectra for the loaded and unloaded specimens as a function of the immersion time. 94

Figure 3.8: Bode representations of the EIS spectra for the loaded and unloaded specimens as a function of the immersion time. Empty markers represent the modulus of impedance and filled ones indicate the phase angle. 95

Figure 3.9: Metallographic section of un-loaded (a), loaded (b) 4PBB after 1000 hours of immersion in aerated 0.6 M NaCl solution (a welded at S 1000 rpm and F 10 mm/min, b specimen welded at S 1500 rpm and F 10 mm/min). 96

Figure 3.10: Attack morphology for each loaded sample after 1000 h of immersion. In particular, on the upper left, the macro photos of the samples just after dipping are reported. 98

Figure 4.1: Schematic representation of the friction stir welding (FSW) and the machining of the specimens. 102

Figure 4.2: FWSed specimen used in constant load (CL) e SSR test; the specimens of the slow strain rate (SSR) test on base materials have the same dimension without weld. 103

Figure 4.3: (a) Image of the cell used for the CL tests. (b) Schematic illustration of the test apparatus and (c) image of one specimen under the CL testing machine. 105

Figure 4.4: Scheme of the sampling of the different areas of the welding and of the base metal for the monitoring of open circuit potential (OCP) and electrochemical impedance spectroscopy (EIS). 107

Figure 4.5: OCP in function of exposure time of the different zones of AA-2024 T3 FSWed joint in aerated NaCl 0.6 M at 23 °C. 108

Figure 4.6: EIS spectra (a), (c), and (e) Nyquist and (b), (d), and (e) Bode representation, of the separate different zones of the weld; (a) and (b) just dipped; (c) and (d) after 24 h; (e) and (f) after 72 h of immersion in aerated NaCl 0.6 M solution. 110

Figure 4.7: OCP measurements during 720 h exposure of CL specimen of the FSWed AA-2024 T3 alloy in aerated NaCl 0.6 M at 23 °C. 111

Figure 4.8: Corrosion morphology of FSWed AA-2024 T3 alloy after CL test in aerated 35 g/L NaCl. 111

Figure 4.9: Metallographic section of Figure 4.6: (a) Macro image of the nugget with several localized attacks; (b) close-up of the red zone in (a). 112

Figure 4.10: EIS spectra (a), (c), and (e) Nyquist representation, (b), (d), and (e) Bode representation of the constant load specimen without load just dipped and after 24 h (a,b), after 48 h without load, and after 175 MPa, and after 480 h loaded at 175 MPa (a,d) and after 480 h at 175 MPa and 650 h at 268 MPa (e,f) in aerated NaCl 0.6 M solution. 113

Figure 4.11: Effect of the time of immersion on the OCP of un-loaded and loaded 4PBB specimens of the FWSed alloy AA2024-T3 in aerated NaCl 0.6 M at 23 °C (data obtained by [135]). 114

Figure 4.12: Stress vs. strain and OCP FSWed AA2024-T3 alloy during the SSR test in aerated NaCl 0.6 M solution at 23 °C. 115

Figure 4.13: (a) Image of a FSWed specimen after the SSR test in NaCl 35 g/L; (b) close-up of the lateral surface in the correspondence of the fracture surface; (c) close-up of the dimples in the fully ductile fracture surface; (d) and (e) SCC microcracks in the nugget of the specimen of the FWSed AA2024-T3. 115

Figure 4.14: Stress vs. strain and OCP of the base and FSWed AA-2024 T3 alloy during the SSR test in aerated NaCl 0.6 M solution at 23 °C. 116

Figure 4.15: Microstructure of the AA2024-T3 alloy (Keller attack). 117

Figure 4.16: SEM image of the nugget without metallographic attack: the bright zones are the macro and micrometric precipitates of S-phase. 118

Figure 5.1: Schematic representation of specimens obtained by means of friction stir welding (FSW). 123

Figure 5.2: CL and SSR specimen: the weld is in the center of the gouge length, the thermomechanical. 125

Figure 5.3: CL test device (a) and SSR test device (b). 125

Figure 5.4: Optical image (Keller attack) of the alloy AA7075-T6 (base material). Elongated grains along the rolling direction and the macro-precipitates are visible. .. 126

Figure 5.5: SEM image of the nugget of the FWS 7075 alloy (no metallographic attack) the rounded recrystallized grains are visible owing to the precipitates of MgZn2 on their grain borders and EDX spectra in which is visible an enrichment of zinc and copper in the correspondence of the precipitates. In the image the grain border is demonstrated; (b) optical image of the nugget with metallographic attack (Keller's reagent) that better demonstrated the rounded recrystallized grains. 127

Figure 5.6: Optical image (Keller attack) of the HAZ of the FWS AA7075 alloy. The grains appear elongated along the rolling direction; presence of macro-precipitates is evident. 127

Figure 5.7: Open circuit potential (OCP) vs time for loaded and unloaded 4PBB specimens. The decreasing of the OCP of the specimens in the correspondence of the partial refresh of the test solution that breaks the aluminum oxide scale and exposes fresh metal surface to the aggressive solution. 128

Figure 5.8: OCP vs time of the different zones (base materials, TMAZ and nugget) of the alloy AA7075-T6. 129

Figure 5.9: (a) Image of a 4PBB specimens after the test: an intense localized attack in the attack in the correspondence of the TMAZ and (b) SEM image of the metallographic

longitudinal section of the loaded specimen in which is visible the deviation of the attack along the rolling direction, (c) particular of the attack and EDX analysis. 130

Figure 5.10: Open circuit potential measurements of the specimen loaded at different values during CL test. The decrease in the OCP mainly occurs as loading increase due to aluminum corrosion products cracking. 131

Figure 5.11: Aspect of the specimen at the end of the constant load test. (a) Macro image: the dark zone in the central part exposed to the NaCl 0.6 M solution; (b) close-up of the red circle with the selective attack of the TMAZ; (c) metallographic section of localized attack..... 132

Figure 5.12: (a) Metallographic section of the enlarged localized attack in the TMAZ zone of the CL specimen. Close-up of the arrow in (b) in which is evident the change the morphology of attack that allows the rolling direction..... 132

Figure 5.13: Stress vs. time and OCP of the specimens during the slow strain-rate tests. 133

Figure 5.14: SEM image of the fracture surface of the AA7075-T6 specimen after the SSR test (a) macro at air, (b) macro in 0.6 M NaCl solution. 134

Figure 5.15: SEM image of the fracture surface of the AA7075-T6 specimen after the SSR test (a) specimen surface with corrosion products of aluminum and several microcracks at macro-precipitates (black arrows); (b) particular of fracture initiation zone after SSR test in 0.6 M NaCl solution. 135

Figure 5.16: SEM image of the fracture surface of the AA7075-T6 specimen after the SSR test: (a) particular of the fracture surface at air and (b) in 0.6 M NaCl solution (the arrows indicate small areas with typical SCC morphology). 135

Figure 5.17: Backscatter electron detector (BSD) image of the external surface of a base material 136

Figure 5.18: (a) Hardness profile along the FSW butt joint; (b) SEM image of the fracture surface, a flat..... 137

Figure 5.19: (a) Particular of the mixed ductile/brittle fracture zone and (b) of the ductile shearing..... 137

Figure 5.20: EDS spectrum of the precipitates present on the mixed ductile/brittle zone of the fracture..... 138

Figure 6.1: FSW tool geometry (dimensions unit: mm)..... 145

Figure 6.2: Support plate for the FSW process. 145

Figure 6.3: Water-cooling system (a) and the used bulkhead (b)..... 146

Figure 6.4: Appearance and morphology of a FSWed joint..... 147

Figure 6.5: Microstructure of the base alloys: a) AA2024, b) AA6082 and c) AA7075. 149

Figure 6.6: Microstructure of the nugget (a-b) and the TMAZ (c-d) of AA2024 air-cooled (on the left) and water-cooled (on the right) welded joints. 150

Figure 6.7: Microstructure of the nugget (a-b) and the TMAZ (c-d) of AA6082 air-cooled (on the left) and water-cooled (on the right) welded joints. 151

Figure 6.8: Microstructure of the nugget (a-b) and the TMAZ (c-d) of AA7075 air-cooled (on the left) and water-cooled (on the right) welded joints. 152

Figure 6.9: Part of the welded sheet on which the hardness tests were carried out. 155

Figure 6.10: Specimen surface on which Rockwell hardness tests were performed.... 155

Figure 6.11: Rockwell hardness maps. 156

Figure 6.12: Specimen surface on which Vickers hardness tests were performed..... 156

Figure 6.13: Vickers hardness maps. 157

Figure 6.14: Ultimate tensile strength vs. elongation [%] data obtained from tensile tests for all the alloys and for all the tested conditions. The continuous line indicates the UTS value of the base alloy. 159

Figure 6.15: Fracture location for each alloy and for each cooling condition..... 160

Figure 7.1: Microstructure of the base alloys. 169

Figure 7.2: FSW tool geometry. 170

Figure 7.3: Water-cooling system (a) and Bulkhead particular (b) [138]. 171

Figure 7.4: Type-K thermocouple. 172

Figure 7.5: Thermocouples housings inside the plates to be welded. 172

Figure 7.6: Flir System ThermoVision A40 infrared camera..... 173

Figure 7.7: Temperature cycles showing thermal gradients in all the welded alloys with and without water-cooling system. In the legend "nugget proximity" indicates the measurements executed at 10 mm from the center of the weld..... 175

Figure 7.8: Example of thermo-vision of the infrared camera (AA2024 S1500-F35). 176

Figure 7.9: Logarithmic regression function of air-cooled and water-cooled AA2024-AA2024 (a), AA5754-AA5754 (b), AA6082-AA6082 (c) and AA7075-AA7075 (d).178

Figure 7.10: Rockwell harness diagrams for each alloy and for each cooling conditions. In each diagram the advancing side is on the right and the retreating side on the left. 179

Figure 7.11: Schematic diagram showing the microstructure evaluation of the AA6082-T6 (a) and AA7108-T6 (b) during the welding [19]. 181

Figure 7.12: Correlation between logarithmic regression of air-cooled and water-cooled AA2024-AA2024 and Rockwell harness map in function of the temperature of reversion of θ' phase. 182

Figure 7.13: Correlation between logarithmic regression of air-cooled and water-cooled AA6082-AA6082 and Rockwell harness map in function of the temperature of reversion of β" phase. 182

Figure 7.14: Correlation between logarithmic regression of air-cooled and water-cooled AA7075-AA7075 and Rockwell harness map in function of the temperature of reversion of η' phase. 183

Figure 7.15: Microstructure of the welding zones of each cooling condition and for each alloy. 184

Figure 7.16: Fracture location for each cooling condition and for each alloy..... 188

Figure 8.1: Artificial Neural Network. 195

Figure 8.2: The structure of the ANN..... 199

Figure 8.3: Prediction test data and actual values of UTS..... 201

Figure 8.4: Prediction test data and actual values of HRB in the nugget. 202

Figure 8.5: Prediction test data and actual values of HRB in the TMAZ, advancing side. 203

Figure 8.6: Prediction test data and actual values of HRB in the TMAZ, retreating side. 204

Figure 8.7: Flowchart of the PSO algorithm. 206

Figure 8.8: Percentage error between predicted and experimental process performances. 210

Figure 9.1: Hybrid FEM-ANN approach flowchart. 215

Figure 9.2: Mesh of the aluminum workpiece. 216

Figure 9.3: Thermocouples housings inside the plates to be welded [187]. 218

Figure 9.4: Simulated and measured values of temperature reached in air-cooled joint. 221

Figure 9.5: Simulated and measured values of temperature reached in water-cooled joints. 222

Figure 9.6: FEM model. 223

Figure 9.7: ANN structure definition flowchart. 225

Figure 9.8: Reference system for identifying ordered pairs of points. 226

Figure 9.9: ANN validation. 226

Figure 9.10: Application of hybrid FEM-ANN model to air-cooled FSW. 227

Figure 9.11: Application of hybrid FEM-ANN model to water-cooled FSW. 228

List of Tables

Table 1.1: AA2024 chemical composition. 2

Table 1.2: AA5754 chemical composition. 4

Table 1.3: AA6082 chemical composition. 6

Table 1.4: AA7075 chemical composition. 7

Table 2.1: ANOVA results [57]. 34

Table 2.2: Distribution of intermetallic precipitates before (SR) and after FSW (SA) [64]. 46

Table 2.3: ANOVA results [57]. 52

Table 3.1: Chemical composition (%wt) and mechanical properties of the AA2024-T3. 84

Table 4.1: Mechanical properties (yield strength, YS and ultimate tensile strength, UTS) of the base materials and the welded joint. 103

Table 5.1: Chemical composition (% weight) of the alloy 7075-T6. 122

Table 5.2: Mechanical properties of the base materials and the welded joint. 122

Table 6.1: Chemical composition (% weight) of the base materials. 144

Table 6.2: Mechanical properties of the base materials. 144

Table 6.3: Parameters used for the experimental setup. 146

Table 6.4: Counts of the grain boundary intersections with the drawn line for each alloy. 153

Table 6.5: Average grain size in the base alloy, in the nugget and in the TMAZ of air-cooled and water-cooled AA2024 welds. 154

Table 6.6: Average grain size in the base alloy, in the nugget and in the TMAZ of air-cooled and water-cooled AA6082 welds. 154

Table 6.7: Average grain size in the base alloy, in the nugget and in the TMAZ of air-cooled and water-cooled AA7075 welds. 154

Table 6.8: Average UTS data, real elongation A and standard deviations of all the tested conditions. 158

Table 7.1: Chemical composition (wt. %) of the base materials. 168

Table 7.2: Mechanical properties of the base materials. 168

Table 7.3: Complete information about CNC machine employed. 170

Table 7.4: Parameters set-up for each alloy. 171

Table 7.5: Time in which the welding zones have remained above the phase transition temperature characteristic of the A2024 (230 °C). 185

Table 7.6: Time in which the welding zones have remained above the phase transition temperature characteristic of the AA6082 (220 °C). 186

Table 7.7: Time in which the welding zones have remained above the phase transition temperature characteristic of the AA7075 (200 °C). 186

Table 7.8: Average UTS data, real elongation A and ratio between the average ultimate tensile strength of joints and base material (UTSb) for all the tested conditions. 187

Table 7.9: Interval plots, the F-values and the P-values about the effects of the cooling condition on UTS and A%. 190

Table 8.1: Summary of Input and Output. 196

Table 8.2: Main characteristics of applied Heuristics approach. 197

Table 8.3: CV comparison using different hidden neurons. 199

Table 8.4: Forced input and predicted optimal process parameters. 208

Table 8.5: Predicted and experimental output. 209

Table 9.1: Parameters and their range considered for the sensitivity analysis. 217

Table 9.2: Considered combination of inputs and relating outputs for the air-cooled joints. 219

Table 9.3: Considered combination of inputs and relating outputs for the water-cooled joints. 220

1. Introduction

1.1. Aluminum Alloys

Since its discovery in the nineteenth century, aluminum has established itself as a valid substitute for ferrous metals in various engineering applications. In fact, over the years both the production and the industrial consumption of this metal and its alloys have seen a rapid and constant development (Figure 1.1).

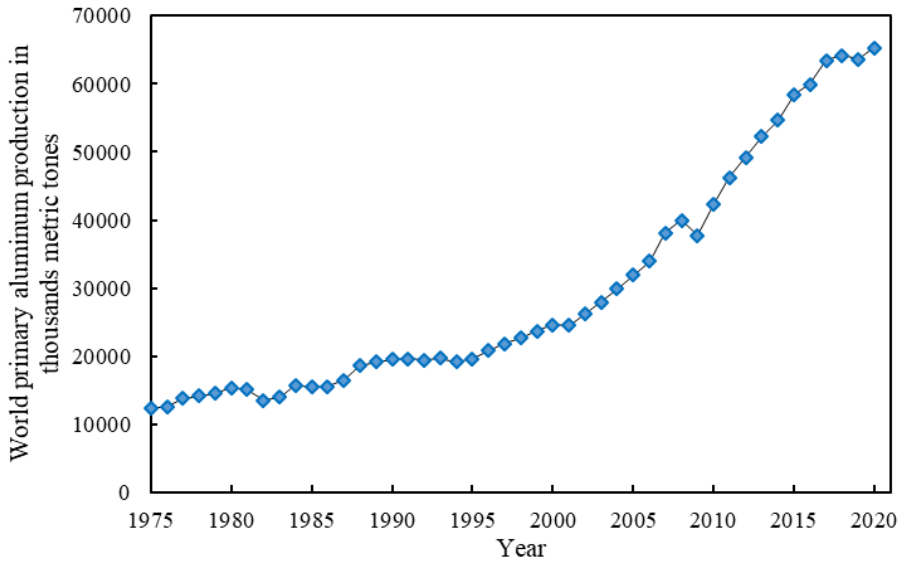

Figure 1.1: World primary aluminum production (data from The International Aluminium Institute [1]).

The success of aluminum is to be found in its specific properties. In fact, with a density equal to one third of steel, aluminum excels where the lightness of the components is a critical factor, such as in the automotive and aeronautical sectors. Aluminum also has excellent resistance to atmospheric corrosion, which makes it particularly used in the architectural field and for interior furnishings. Aluminum is also often used for its electrical conductivity, which, for the same weight, is about double of copper. This makes it functional in electric motors as well as in high voltage lines.

However, perhaps the most interesting feature of this metal is its predisposition to form alloys. By adding different alloying elements within the pure metal, it is possible to obtain a wide range of mechanical and physical properties, making aluminum extremely versatile and interesting from an engineering point of view.

1.1.1. Chemical composition

2xxx Series

The aluminum alloys belonging to the 2xxx series are aluminum/copper alloys (copper additions ranging 0.7-6.8 wt%). The main characteristic of this alloy family is the high mechanical strength, which allows the use of these aluminum alloys for aerospace and aircraft applications. Although they have excellent strength over a wide range of temperature, they are considered non-weldable by the traditional arc welding processes because of their susceptibility to hot cracking and stress corrosion cracking.

As the main alloying element, the copper solubility within the aluminum matrix is shown in the phase diagram in Figure 1.2.

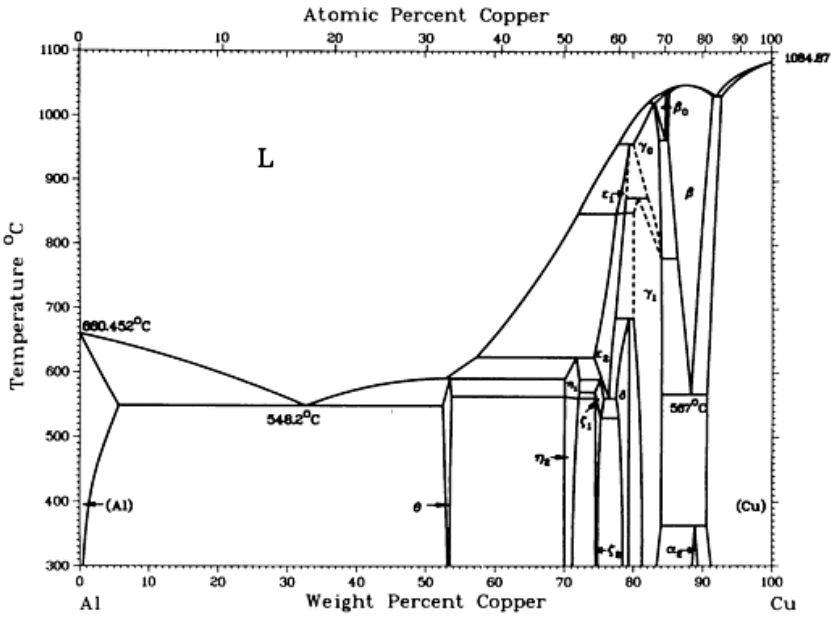

Figure 1.2: Aluminum-copper phase diagram [2].

Within the 2xxx series, the most industrially used alloy is the AA2024, whose chemical composition is shown in Table 1.1, where it can be noted that the second most present alloying element is magnesium.

Table 1.1: AA2024 chemical composition.

	Composition (wt%)							
	Si	Fe	Cu	Mn	Mg	Cr	Zn	Ti
AA2024	0.50	0.50	3.80-4.90	0.30-0.90	1.20-1.80	0.10	0.25	0.15

The main benefit of the addition of copper and magnesium within the aluminum matrix consists in the increase of the mechanical resistance, mainly obtainable through alloy heat treatments.

Moreover, small percentages of iron allow to stabilize the size of the precipitates and improve the mechanical characteristics at high temperatures. However, with iron contents equal to -or greater than- 0.5% of the atomic weight, a decrease in the tensile strength is traceable; in fact, iron binds to copper to form Cu_2FeAl_7, decreasing the amount of copper available to harden the alloy by precipitation. To avoid this, silicon is added to the alloy in small quantities. This additional element binds both to iron, preventing the formation of Cu_2FeAl_7, and to magnesium, forming Mg_2Si, which contributes to hardening by precipitation.

5xxx Series

The aluminum alloys belonging to the 5xxx series are aluminum/magnesium alloys (magnesium additions ranging 0.2-6.2 wt.%). This series are characterized by the highest strength among the non-heat treatable aluminum alloys, and for these reasons they are used for a wide variety of applications such as transportation, shipbuilding, pressure vessels, buildings and bridges. In addition, being non-heat treatable alloys, these series are weldable also with traditional welding techniques. In particular, the aluminum/magnesium alloys are often welded with filler alloys, which are selected after consideration of the magnesium content within the aluminum matrix and the application and working conditions of the welded component.

As the main alloying element, the magnesium solubility within the aluminum matrix is shown in the phase diagram in Figure 1.3.

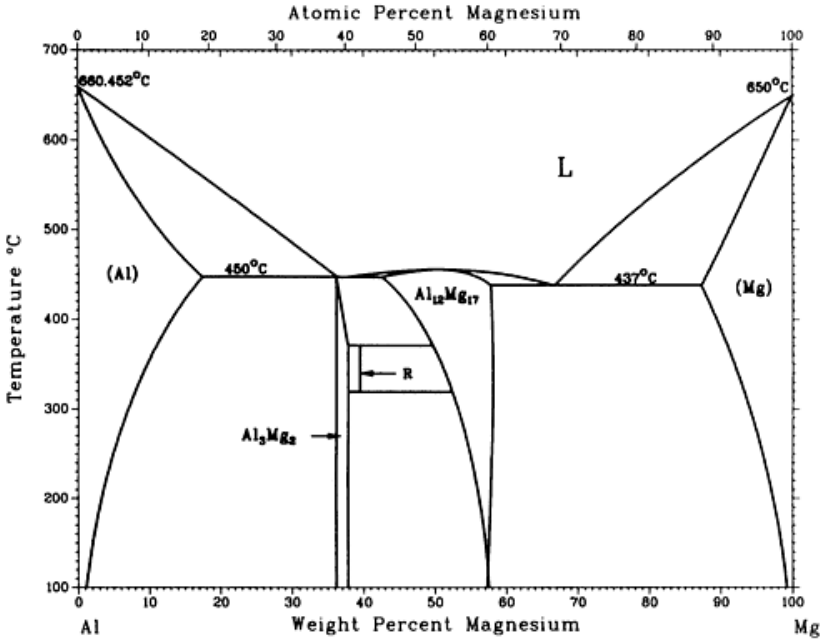

Figure 1.3: Aluminum-magnesium phase diagram [2].

Within the 5xxx series, the most industrially used alloy is the AA5754, whose chemical composition is shown in Table 1.2.

Table 1.2: AA5754 chemical composition.

	Composition (wt%)							
	Si	Fe	Cu	Mn	Mg	Cr	Zn	Ti
AA5754	0.40	0.40	0.10	0.50	2.60-3.60	0.30	0.20	0.15

Magnesium forms intermetallic compounds with aluminum (Al_3Mg_2 and Al_2Mg_3): despite this, the 5xxx series alloys do not come subjected to heat treatments, because the treatment does not lead to a sensitive improvement of mechanical properties. In fact, the 5xxx series is a work-hardening alloy series.

As the content of magnesium rises, the mechanical characteristics increase, but the ductility is progressively reduced.

Moreover, it is important to underline that 5xxx series alloys with more than 3.0% magnesium are not recommended for elevated temperatures because of their potential susceptibility to stress corrosion cracking, or problems associated with eutectic melting and with poor mechanical properties.

6xxx Series

The aluminum alloys belonging to the 6xxx series are the aluminum/magnesium-silicon alloys (magnesium and silicon additions ~1%) and are widely used primarily in the form of extrusions and incorporated in many structural components. Their main characteristics are the high deformability, machinability and good corrosion resistance and mechanical properties (even if lower with respect to 2xxx and 7xxx alloys). The addition of magnesium and silicon to aluminum matrix produces a compound which provides to this material its ability to become solution heat treated for improved its mechanical strength. These alloys are naturally solidification-crack-sensitive and, for this reason, they should not be welded without filler material, thus generating possible corrosion problems due to galvanic coupling.

The ternary aluminum-magnesium-silicon alloy phase diagram is shown in Figure 1.4.

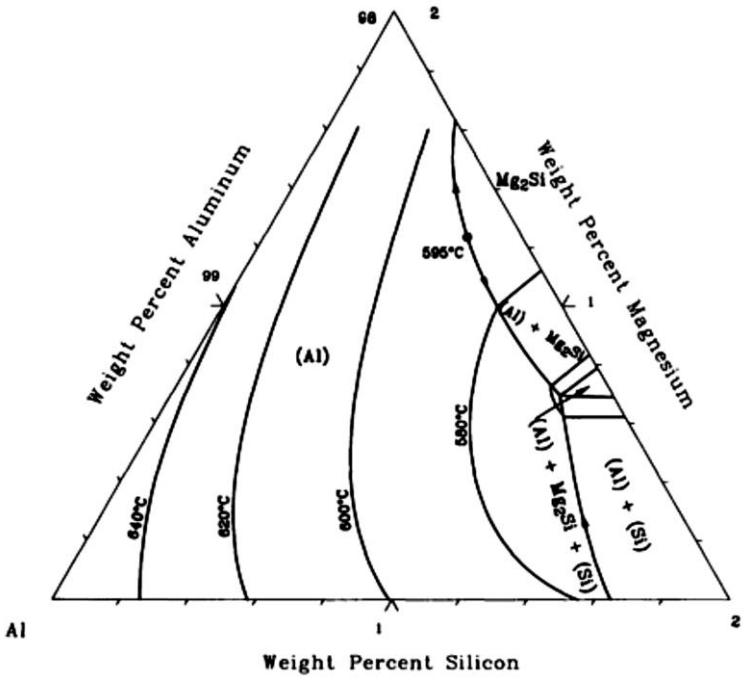

Figure 1.4: Aluminum-magnesium-silicon phase diagram [2].

Within the 6xxx series, the most industrially used alloy is the AA6082, whose chemical composition is shown in Table 1.3.

Table 1.3: AA6082 chemical composition.

	Composition (wt%)							
	Si	Fe	Cu	Mn	Mg	Cr	Zn	Ti
AA6082	0.70-1.30	0.50	0.10	0.40-1.00	0.60-1.20	0.25	0.20	0.10

The presence of silicon is due to the possibility to guarantee during the heat treatments the formation of the intermetallic Mg_2Si, characterized by a strong hardening effect. In particular, the hardening treatment followed by an artificial ageing allows to ensure the precipitation of Mg_2Si intermetallic particles finely dispersed in the matrix.

7xxx Series

The aluminum alloys belonging to the 7xxx series are aluminum/zinc alloys (zinc additions ranging 0.8-12.0 wt%). They include some of the highest strength aluminum alloys and, for this reason, these alloys are used in high performance applications such as aerospace, aircraft and competitive sporting equipment. Similarly to the 2xxx series, this series is considered non-weldable by the traditional arc welding processes.

As the main alloying element, the zinc solubility within the aluminum matrix is shown in the phase diagram in Figure 1.5.

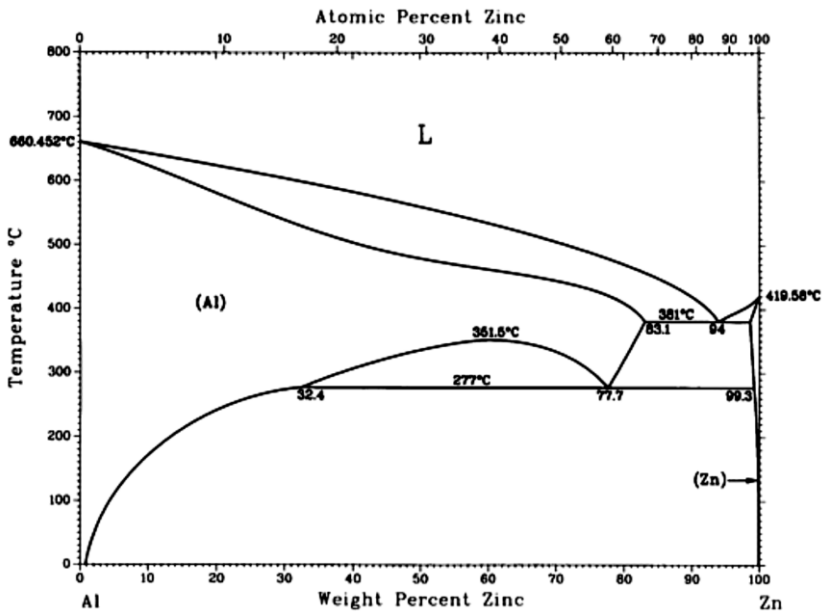

Figure 1.5: Aluminum-copper phase diagram [2].

Zinc has the greater solubility within the aluminum matrix. The rapid decrease in solubility with decreasing temperature causes zinc to precipitate abundantly as a second phase. However, the zinc particles do not have significant effects on the mechanical properties but, on the contrary, generate defects in case of hot working.
Within the 7xxx series, the most industrially used alloy is the AA7075, whose chemical composition is shown in Table 1.4.

Table 1.4: AA7075 chemical composition.

	Composition (wt%)							
	Si	Fe	Cu	Mn	Mg	Cr	Zn	Ti
AA7075	0.40	0.50	1.20-2.00	0.30	2.10-2.90	0.18-0.28	5.10-6.10	0.20

The addition of magnesium permits the formation of $MgZn_2$ precipitates which, unlike pure zinc precipitates, allow a better response to heat treatments. The alloy may have chromium in small quantities, which reduces the susceptibility to stress corrosion phenomena. The further addition of copper and small quantities of manganese allow to obtain the best mechanical properties for commercial aluminum alloys, creating $CuMgAl_2$. However, both copper and zinc significantly worsen the corrosion behavior of aluminum, making this alloy particularly susceptible to corrosive phenomena.

1.1.2. Heat treatments

Aluminum has proven to be a material of considerable interest in engineering, especially in the aeronautic and automotive sectors, because of its advantageous ratio between mechanical properties and weight. Significant importance in these fields is assumed by the aluminum precipitation-hardening alloys, which can achieve mechanical properties comparable to those of structural steel (Figure 1.6) [3, 4].

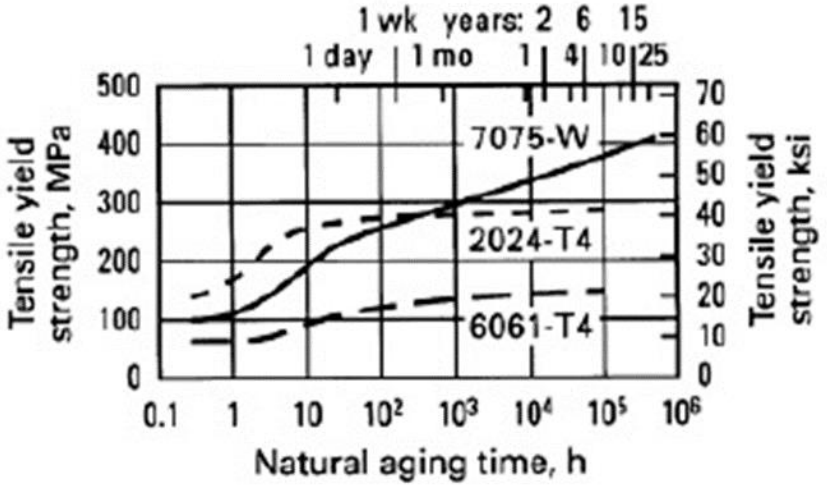

Figure 1.6: Trend of tensile strength as a function of ageing time for different aluminum alloys [5].

The precipitation hardening mechanism is based on the reduction of the solubility of the alloying elements (i.e. copper for the AA2024 and zinc for the AA7075), which occurs moving from high temperatures to room temperature at controlled cooling rate [6].

To obtain the desired result through the heat treatment, it is necessary to have elements whose solubility decreases with temperature inside the matrix.

All the heat treatments that allow to increase the aluminum alloys mechanical characteristics are based on two different and subsequent processes: solubilization and ageing.

By carrying out a solubilization quench, that is moving in the solubility field with sudden cooling, the dispersion of the alloy elements is obtained in the form of clusters. Successively, these clusters split up to give nano-metric precipitates dispersed in the matrix that permit these alloys to reach the mechanical characteristics that distinguish them, by preventing the movement of the dislocations [7].

Solubilization involves maintaining the alloy at high temperatures for a long time. This consents to maximize the solubility of the elements that then will be involved in the subsequent treatment. The most effective temperatures are close to the solidus or eutectic temperature, where the greatest solubility and diffusivity occur, avoiding an incipient melting that could cause cracks or ductility loss.

After the maintenance phase at high temperatures, a water or air quenching is conducted, depending on the desired cooling rate. In this way it is possible to obtain an oversaturated solid solution containing both the solute elements and the vacancies.

If at room temperature the percentage of the alloy element is greater than its solubility threshold, this tends to segregate within the matrix. Therefore, there is the formation of agglomerates of solute atoms (called clusters) which, maintaining the same crystalline structure of the matrix, lead to a severe deformation of the crystal lattice. The clusters allow the stabilization of the dislocations, allowing to reach higher mechanical properties in terms of hardness and tensile strength. On the other hand, the precipitation of the second phases solute should be avoided, since they would lower the resistance of the alloy.

The solubilized alloy is not stable, since the supersaturated solute tends to segregate over time with a process known as ageing. The increase in mechanical characteristics is maximum when a fine dispersion of the precipitates is obtained. The ageing of the alloy can be accelerated through a second heating at a temperature lower than the solubilization temperature, obtaining an artificial ageing.

The temperature and the ways in which artificial ageing is achieved vary both according to the treated alloy and to the characteristics to be obtained.

The alloys belonging to the 2xxx series are normally supplied in the T3 or T4 state, abbreviations that indicate a heat treatment of solubilization and a subsequent natural ageing. The T3 heat treatment involves a cold processing phase between solubilization and ageing. Cold plastic deformation allows to obtain even higher mechanical properties than ageing alone.

Natural ageing consists of maintaining the alloy at room temperature (or slightly higher) for a prolonged period. During this time, a structure is spontaneously formed characterized by the presence of Guinner-Preston (G.P.) zones, where the clusters of precipitates and solutes aggregate in the crystal lattice. The zones thus formed oppose greater resistance to the path of the dislocations with respect to the crystal lattice of the base metal, generating the desired increase in mechanical strength.

Natural ageing is an extremely slow process and, for some alloys such as those belonging to the 7xxx series, it does not ensure the achievement of stable conditions. On the

contrary, the 2xxx series has a stable structure already for rather limited maintenance periods, as it is possible to observe in Figure 1.6.

The alloys belonging to the 6xxx and 7xxx series are normally supplied in the T6 or T8 state, that indicate a heat treatment of solubilization and artificial ageing. The T8 heat treatment provides, similarly to the T3 treatment, a cold processing phase between solubilization and ageing, which allows to obtain even higher mechanical properties than ageing alone.

Artificial ageing involves exposing the alloy to temperatures higher than the room temperature (Figure 1.7 and Figure 1.8). The goal is to obtain the metastable form, also called transition form, starting from the equilibrium precipitates; this transition form remains consistent with the solid solution matrix and therefore contributes to hardening by precipitation. However, as the ageing temperature increases, the precipitates grow and convert back to the state of equilibrium, which is generally not consistent. These changes result in a loss of mechanical characteristics reaching worse conditions than the untreated base metal. This phenomenon is called over-ageing. To overcome this problem, it is possible to divide the ageing process into two phases, lowering the temperature after a certain period. As shown in Figure 1.8, the AA7075 presents the best mechanical characteristics for a two-step ageing, while the single-step aged alloy shows a decrease in hardness beyond sixty hours.

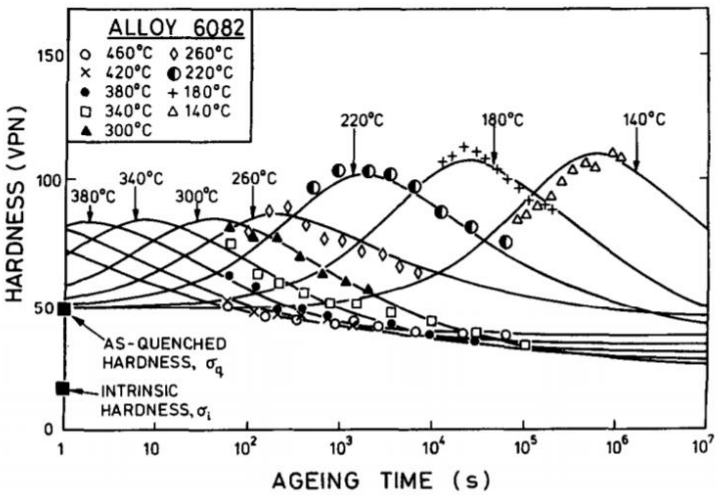

Figure 1.7: Artificial ageing of AA6082 [8].

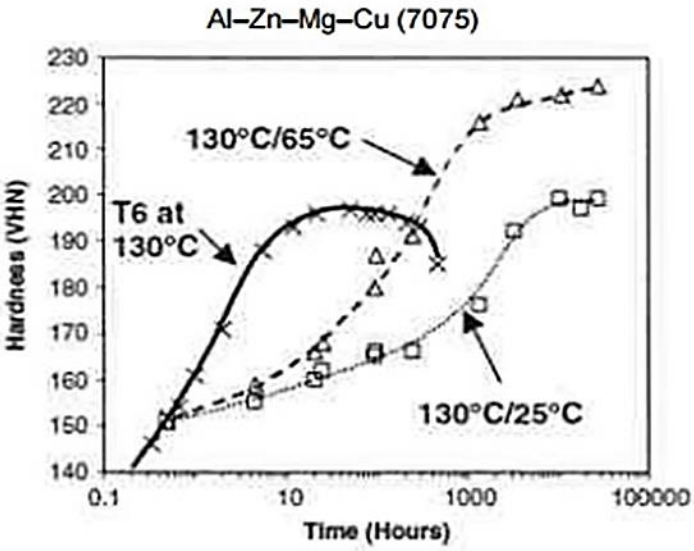

Figure 1.8: Artificial ageing of AA7075.

However, these alloys are characterized by a considerable difficulty in welding, since the achievement of the melting temperature leads to the elimination of this treatment and therefore to the rapid decline of the mechanical properties.

In fact, the high temperature reached in traditional welding techniques leads to the diffusion of the heat coming from the welding joint in the surrounding areas, creating a very wide heat affected zone characterized by an important microstructural alteration. These microstructure changes lead to an enlargement of the grains, responsible for the reduction of mechanical properties. Hall and Petch (H-P) have demonstrated that the strength of metallic materials increases when the grain size is smaller, as shown by the following relationship [9]:

$$\sigma_y = \sigma_0 + k_y/\sqrt{d} \tag{1}$$

where σ_y is the yield strength, σ_0 is a constant for the starting stress for dislocation movement and it depends on the material, k_y is H-P slope and d is the average grain diameter.

For these reasons, over the years, numerous alternative welding technologies have been developed to reduce the amount of heat generated during the process, including Friction Stir Welding.

1.2. Friction Stir Welding

Friction Stir Welding (FSW), patented by The Welding Institute of Cambridge in 1991, is a solid-state welding method that allows permanently joining a wide range of parts and geometries (Figure 1.9) [10, 11].

This process proves to be predominant for the welding of non-operable materials using thermal methods, such as sintered materials, magnesium [12], copper, Inconel and superalloys, titanium [13], metal-matrix composites [14] and thermoplastic materials [15]. In particular, it is used for high resistance aluminum alloys, which are difficult to be joined with traditional techniques because of their typical microstructure alteration during age hardening. Furthermore, this technology permits the solid-state welding in different configurations and the joining of dissimilar alloys [16, 17]. From a structural point of view, FSW introduces joints welded without overlapping flaps and the removal of connecting parts, such as rivets, with a reduction in both weight and cost [18].

Figure 1.9: FSW process.

Since the material is remixed in a solid state, without ever reaching the melting temperature, this type of welding is identified as cold welding. In fact, the maximum reached temperatures do not exceed the 75-80% of the melting temperature (i.e., approximately 660 °C for aluminum) [19].

The main advantages of this technology are, in addition to the ability to weld otherwise problematic metals, the lack of distortion of the joint, the excellent mechanical properties of the latter, as well as the reduction of energy consumption and material waste and the absence of radiation and dangerous emissions for the operator.

As a solid state process, FSW eliminates many of the defects associated with fusion welding techniques such as shrinkage, hot cracks and shrinkage porosity [20], gaseous inclusions and slags in the molten area.

In fact, the heat-affected zone generated by a traditional welding technique is characterized by various types of defects and problems. For example, porosity can be generated due to any gas trapped during solidification, or inclusions of slag, such as oxides, remaining in the joint can make it very brittle. One of the most important welding problems consists of the hot or cold cracks generated during the weld solidification (due to the presence of impurities) or during the weld cooling (due to the residual stress generated by the hydrogen trapped in the joint).

Furthermore, the friction stir welded processed material undergoes intense plastic deformation, generating a microstructure consisting of recrystallized small and equiaxed grains [18, 21] which guarantee a lower decay of mechanical properties compared to fusion welds [16, 22, 23]. The limited thermal flux involved in the FSW process leads to an important reduction of the residual stress state of the welded joints and of the distortions of the final products [24].

1.2.1. Applications

FSW is a relatively simple welding process, quite easy to apply in a high-rate production system since it allows to weld rather thick pieces in a single pass. For these reasons, FSW technology is applied in numerous commercial fields.

The shipbuilding and marine industries are two of the first sectors that have adopted the process for commercial applications [25].

Until now, however, the sector that is most using and investing to implement the application of FSW technology is the aerospace sector. In fact, numerous prototypes have been developed in order to make this technology more usable, especially regarding fuel tanks, airframes, and thin alloy skins [26].

The opportunity to weld skins to spars, ribs and cross members for military and civil aircraft, offers significant advantages over riveting and machining from solid, such as reduced production costs and weight savings. Friction Stir Welding has been also used successfully for performing longitudinal butt welds in Al-alloy fuel tanks for spacecraft.

There are also developments regarding applications in the commercial production of high-speed trains based on aluminum extrusions and the possibility of using this type of joint is being evaluated by various car manufacturers [27].

1.2.2. Process and tool

The flow of the metal and the generation of heat in the plasticized material around the tool are fundamental in the friction process. The deformation of the material redistributes the heat generated by friction, creating a temperature field inside the weld, which also depends on the state of stress to which the sheet is subjected.

In fact, the control of the temperature and the achieved state of stress is the basis of all aspects of the FSW, such as, for example, the optimization of process speeds, the machine loads, the reduction of macroscopic defects, the control of the evolution of the microstructure and, consequently, the resulting properties of the weld [28].

The joining of the parts is achieved by a suitable tool which, during its roto-translation, has the task of mixing the material along the flaps in the plastic field with dynamic recrystallization phenomena (Figure 1.10).

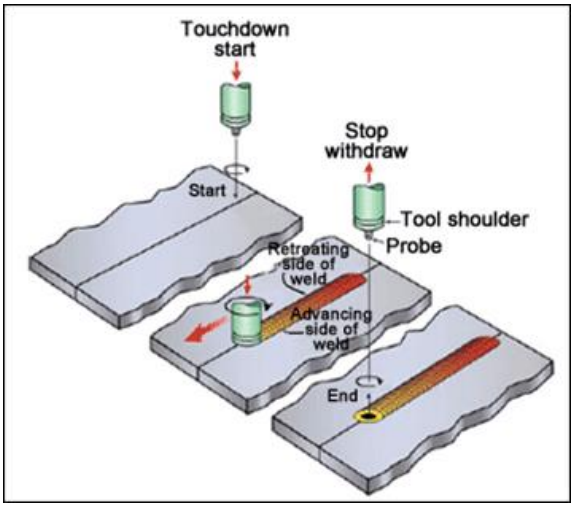

Figure 1.10: Schematic representation of the FSW process [29].

The heat generated by the friction between the pin and the surrounding material and the pressure applied by the tool shoulder cause the plasticization and the mixing of the metal, thus allowing the advancement of the pin and forming a solid solution between the two joint edges [30, 31].

The tool is a critical component for the success of the process. It typically consists of a circular section rotating shoulder and a pin, with many possible configurations (Figure 1.11).

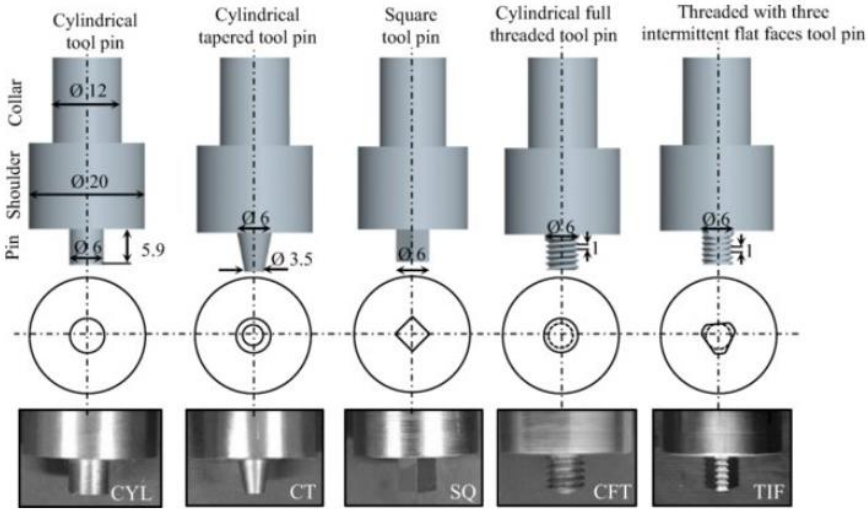

Figure 1.11: FSW tool types [32].

The pin is responsible for heating by friction and remixing the plasticized workpiece. For this reason, the pin diameter should be proportional to -and its length less than- the thickness of the pieces to be weld.

Since its importance for the process quality, several authors studied the influence of different pin geometries on the mechanical properties and on the microstructure of the joints.

Biswas et al. found that straight cylindrical pins were subjected to breakage, as they generate a very high level of stress at the base of the shoulder during processing [33]. The problem of the break may be mitigated by varying the geometry of the pin. For example, using a conical geometry, the amount of cold material still to be welded decreases as the smaller diameter of the pin is approached, involving a lower volume of less ductile material.

A further improvement in the surface quality of the joints was achieved using threaded pins. This kind of pin have a double benefit: firstly, they intensify the mixing of the material around the weld and, secondly, they promote a better fragmentation of the grains.

Regarding the tool shoulder, it performs two important functions: it generates the friction necessary to plasticize the material to be welded and prevents the leak of plasticized material from the joint area.

An analysis conducted on the influence of the tool shoulder geometry demonstrated that the size of the grains increases as the diameter of the shoulder increases, since this leads to a greater generation of heat and a higher plastic deformation.

Furthermore, tools characterized by shoulders having larger diameters allow to obtain joints with improved tensile strength [34].

The lack of molten material along the joint, a feature that makes technology competitive in the modern landscape, is problematic for the duration of the tool's useful life. In fact, the tool is subject to high loads and temperatures resulting from friction, especially for the joining of steel and titanium alloys.

The high cost of the tool and its reduced useful life are the main causes of the still limited commercial applications of FSW applied to steel and titanium alloys.

As regards the machining of light alloys, such as aluminum and magnesium, steel tools are commonly used [35]. Indeed, a material is required whose yield strength must remain high enough to prevent plastic deformation during the process.

In addition, the tool is essential to have excellent resistance to abrasion at high temperature and a high resistance to hot oxidation, to avoid an excessive consumption of the tool and pollution of the welding, with consequent decay of the welding quality.

1.2.3. Main process parameters

The most important parameters for a good FSW process are:

- Tool feed rate [mm/min],
- Tool rotational speed [rpm],
- Tool penetration depth [mm],
- Tool tilt angle [°].

Tool feed rate and rotational speed

The tool feed rate and the rotational speed are the most important parameters for the process.

Indeed, the tool rotation causes the agitation and the mixing of the material around the pin and the translation of the tool along the welding line moves the plasticized material by the front to back of the pin. The higher the tool rotational speed, maintaining constant the feed rate, the higher the temperatures generated by friction, the more intense the agitation and the mixing of the material are obtained [36].

Lee et al. reported higher hardness values recorded on FSWed AA6061 for high tool rotational speed due to the presence of many second phase precipitation hardeners [37]. Similar results were obtained on an AA2024-T3: increasing the tool feed rate, a modest increase in mechanical resistance and in ductility of welded joints was generated [33].

The relationship between the welding speeds (feed rate and rotational speed) and the heat input provided during the process is very complex but, in general, increasing the rotational speed and reducing the feed rate, a welding with a higher temperature is obtained.

However, welded joints with too high temperatures are to be avoided, as welds characterized by too low temperatures are undesirable: if the thermal contribution generated the friction between the tool and the edges to be welded is insufficient, problems of plasticity and deformations of the joint occur [38].

In conclusion, by carefully choosing the combination of the feed rate and rotational speed, it is possible to control the heat input generated by the friction during the process, thus obtaining a quality weld with good mechanical characteristics.

Tool penetration depth

The tool penetration depth is defined as the depth of the plus point shoulder below the surface of the welded plate, and it is considered as a critical parameter to ensure the quality of the weld. The tool penetration depth must be chosen to guarantee both the necessary vertical pressure, responsible for containing the material moved by the tool limiting the generation of excessive burrs, and the complete penetration of the tool into the workpiece.

An excessive penetration depth would risk causing rubbing of the pin against the support plate compromising the use of both tools. On the contrary, a reduced depth, due to possible vibrations of the machine, could lead to a non-filling of the joint and, therefore, to an incomplete welding.

Tool tilt angle

To make the tool mixing function even more efficient, it is appropriate to provide an adequate angle of inclination of the tool (tilt angle). In fact, it has been demonstrated that the FSWed joints made with a tool tilt angle equal to 0° are characterized by a higher incidence of defects, and this consequently leads to the weakening of the joint. This is due to part of the plasticized material accumulated on the shoulder, increasing the force with which the material opposes to the advancement of the tool. On the contrary, exceeding in the dimensioning of the tilt angle would lead to the formation of a concave weld, with a consequent limited resistant section. The best tool tilt angle is strictly related both to the material and to the characteristics of the plates (geometry and thickness) to be weld [39–41].

1.2.4. Weld morphology

The materials welded by Friction Stir Welding have characteristic zones along the section perpendicular to the welding direction with different properties (Figure 1.12).

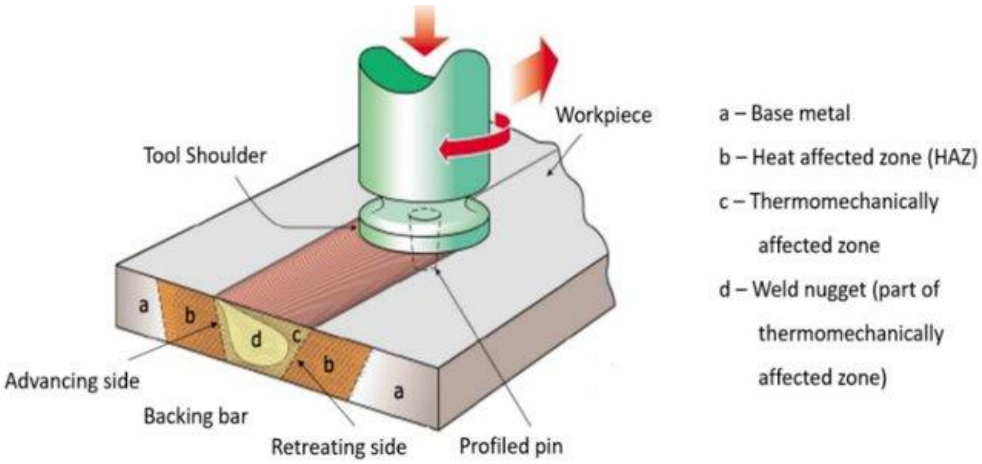

Figure 1.12: Schematic illustration of the areas that have undergone variations during the process [42].

Three different areas of the weld can be identified:

- the advancing side, where the feed rate and the rotational speed have the same direction;
- the retreating side, where the feed rate and the rotational speed have opposite directions;
- the nugget.

G. Sorger et al. demonstrated a difference in heat input between advancing side and retreating side in welded joints [43]. The material in the advancing side undergoes a higher plastic deformation and, consequently, it is always hotter than retreating side.
The intense plastic deformation and the high temperatures involved in the material mixing cause significant changes in the microstructure as well as in the precipitates present in the joints to be welded.
Basing the microstructural characterization of the joints on grains and precipitates size, it is possible to divide the FSWed joint structure in four characteristic zones [30]:

- nugget of fully recrystallized material close to the welding line;
- thermo-mechanically affected zone (TMAZ) that undergoes both heating and plastic deformation;
- heat affected zone (HAZ) in which the welding thermal cycle has caused an important alteration of the microstructure;
- base material that undergoes a weak thermal cycle, linked only to the conduction of heat that comes from the center of the joint, without showing alterations of the microstructure.

Nugget

In this area, a recrystallized microstructure characterized by a fine and equiaxed grains with a preferential distribution of second phases at the grain boundaries is present. The continuous and dynamic recrystallization of the grains is due to the mechanical action performed by the pin. The tool destroys the original microstructure generating new grains, which undergo a dimensional transformation until they become equiaxial.

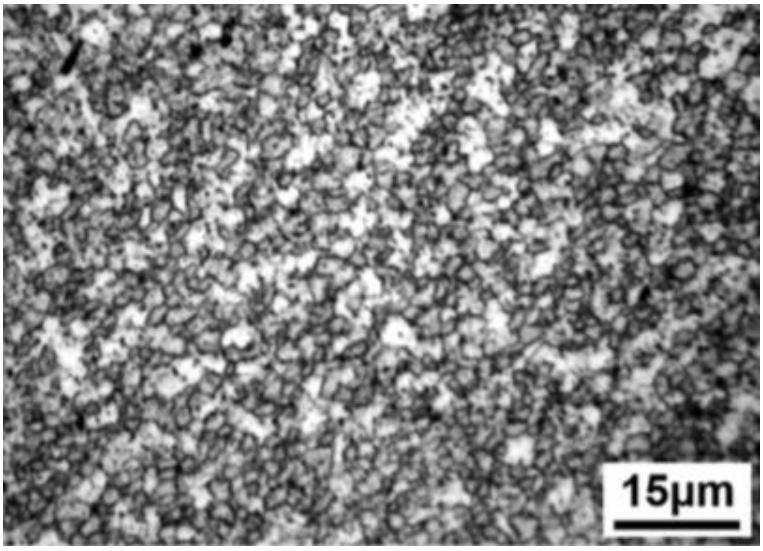

Figure 1.13: AA7055 nugget microstructure [44].

The microstructure of the nugget is strictly dependent on the process parameters, the geometry of the tool and the reached temperatures.

S. Benavides et al. showed that decreasing the reached temperature through external cooling, a recrystallized grains size reduction arises [45]. The same effect is achievable by reducing the ratio between rotational speed and feed rate. The dimensional order of the nugget grains is about one-tenth of the base metal grains. It has been observed that, increasing the tool rotational speed, the nugget zone section enlarges. Furthermore, for high tool rotation speeds, it also increases the average size of the grains in the nugget area [46].

Another characteristic aspect of the nugget is the simultaneous aggregation in clusters and dissolution of precipitates. This phenomenon is due to the high frictional forces that occur along the welding line, which lead to an increase in temperature up to 500 °C.

Thermo-mechanically affected zone

The thermo-mechanically affected zone undergoes both thermal and mechanical action of the process, but it does not manifest the recrystallization phenomenon of the grains as strain stress suffered by the affected material it is not enough [47]. There is a mixed structure in which the original crystalline grains coexist with smaller and rounded grains, and an increase in the dislocation concentration is detachable.

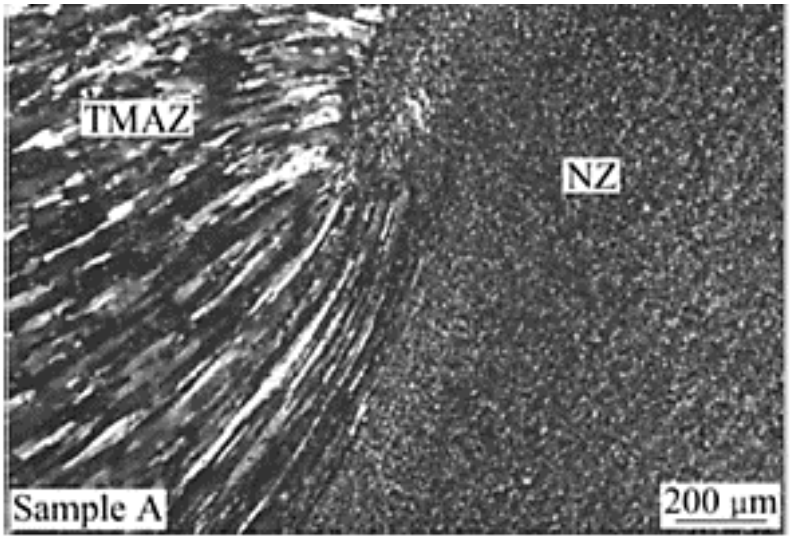

Figure 1.14: Nugget (NZ)-TMAZ transition zone [48].

In the TMAZ, dissolution of some precipitates, due to high temperature exposure during FSW process, was observed [49]. The extent of dissolution depends on the thermal cycle experienced by the single joint.

Heat affected zone

The structural modification of this area depends on the maximum temperature reached and on the starting conditions of the material.

R. S. Mishra et al. defined the HAZ as an area that experiences an increase in temperature above 250°C [30]. This thermal exposure modifies the structure of the precipitates. Indeed, the structure of the grains remains unchanged with respect to the base material ones, but the welding causes in this area the swelling of precipitates with a consequent increase in precipitate free zones (PFZ) [50].

Therefore, the HAZ shows the lowest hardness and strength among the FSW characteristic zones and, generally, the fracture of the joints occurs in this area [51].

1.3. Research Issues

This work aims to study and assess the FSW process from the mechanical and corrosion point of view and study in the deep the applicability of this technology in the production field.

When considering the behavior of Friction Stir Welded joints, it's normal practice to focus the attention on the mechanical characteristics of the welds.

In literature many efforts have been conducted also to investigate the corrosion resistance of the joints, since it can modify the typical behavior of the welded parts, especially if subjected to a load in a potential aggressive environment. Even though studies about the corrosion behavior of friction stir welded joints are already available in literature, a lack of information can be observed in the correlation between corrosion behavior and welding process parameters.

For this reason, the first objective of this work is to analyze if and how the process parameters (namely rotational speed and feed rate) affect both the mechanical properties and the corrosion behavior of butt joints obtained on different aluminum alloys by FSW.

Regarding the corrosion behavior, intergranular corrosion tests, long term exposure tests with and without an external applied load, open-circuit-potential monitoring, electrochemical impedance spectroscopy, constant load tests and slow strain rate tests, varying the process parameters of the Friction Stir Welding process, were conducted.

For the mechanical characterization, Vickers micro-hardness, Rockwell hardness tests and tensile tests were performed.

To validate the results, metallographic and microstructural analyses were done, through the use of both an optical microscope and a SEM EDX equipped.

After that, it was clear how the thermal cycle (linked to the ratio between the feed rate and the rotational speed) of the joints influences the mechanical characteristics. This led to study if and how the mechanical behavior of the joints could be improved by adequately controlling the temperature variation. For this reason, it is very important to increment the knowledge about the thermal history of the joint and how the heat generated by friction and stirring diffuses inside the sheet during the process.

Several researchers have studied in the last years the response of a specific aluminum alloy to a certain cooling treatment during the welding process. However, little has been

done on the comparison of the effects of the same water-cooling approach applied to a different series of aluminum alloys.

To fill this gap, both precipitation-hardening alloys (AA2024-T3, AA6082-T6 and AA7075-T6) and a work-hardening alloy (AA5754-H111) have been considered to evaluate the difference between the properties of the joints welded with traditional air-cooled FSW process and those obtained by combining a traditional FSW setup with a water-cooling system. One of the most important goal of this research is the prediction and the optimization of the process performances and the weld quality as a function of both process conditions and welded materials, but this topic is very difficult to reach, due to the large number of variables involved and the complexity of the process. In fact, the solution of optimizing the process performance by considering each process parameter independently is the simplest approach, but its industrial applications are restricted owing to its very limited validity. To overcome this problem, many techniques such as multi-objective optimization techniques, Artificial Neural Network (ANN) and regression analysis have recently received great attention, above all by combining different optimization algorithms.

In this research, a hybrid methodology involving an Artificial Neural Network together with a Particle Swarm Optimization (PSO) for predicting the main properties and suggesting the optimal process parameters for FSW process was developed in order to set both input and output values leaving to the PSO algorithm the identification of the other values able to minimize or maximize a predefined objective function.

From the literature review, it was possible to notice that, so far, ANN research applied to the FSW process has been focusing only on the analysis of a single material or on a specific combination of materials. Indeed, the approach proposed in this research could efficiently respond to different industry needs, since the technicians are free to set factors from both process parameters (in this case: material, rotational speed, feed rate and cooling condition) and process outputs (i.e., ultimate tensile strength and Rockwell hardness in correspondence to the different characteristic zones of the welding) while the other process variables are automatically optimized.

To conduct a deeper analysis, also a hybrid approach involving a Finite Element Model and an ANN was developed that allowed predicting the mechanical properties of the joint starting from the maximum reached temperature.

Through a comparison with the collected experimental data, a finite element model for the simulation of a friction stir welding process to predict the temperature distribution when using both air and water-cooling systems was set-up.

Then, the temperature data derived from the simulation were used as input for the ANN with the final aim to predict the hardness values, characterizing a specific position on the surface of the samples.

This kind of approach could be useful in the production field as it is able to predict well-determined in space hardness values only as a function of the temperatures locally reached during the welding process.

2. Literature Review

2.1. Microstructure

Since the importance to understand the effects of process parameters and process setup on the weld quality, several authors studied these aspects with particular attention to the quality of FSW joints in terms of mechanical properties (UTS, fatigue resistance etc.) [52–54]. Tool rotational speed has been considered as one of the most important process variables: high rotational speeds may raise the strain rate, so affecting the re-crystallization process. Moreover, some authors showed that high welding speeds are related to low heat inputs, which gives rise to faster cooling rates of the joint. This can reduce the extent of metallurgical transformations taking place during welding (such as solubilization, re-precipitation and coarsening of precipitates) and hence the local strength of individual regions across the weld zone.

AA2024

According to the study conducted by Philippe Heurtier on the AA2024, there is a clear difference in the size and orientation of the grains in the three main areas affected by the welding process [55]. The nugget zone is characterized by a relatively homogeneous structure, with small equiaxed grains with an average size of 4.55 μm. The deformation map reported in Figure 2.1 shows an almost completely recrystallized zone with a lack of intergranular deformations.

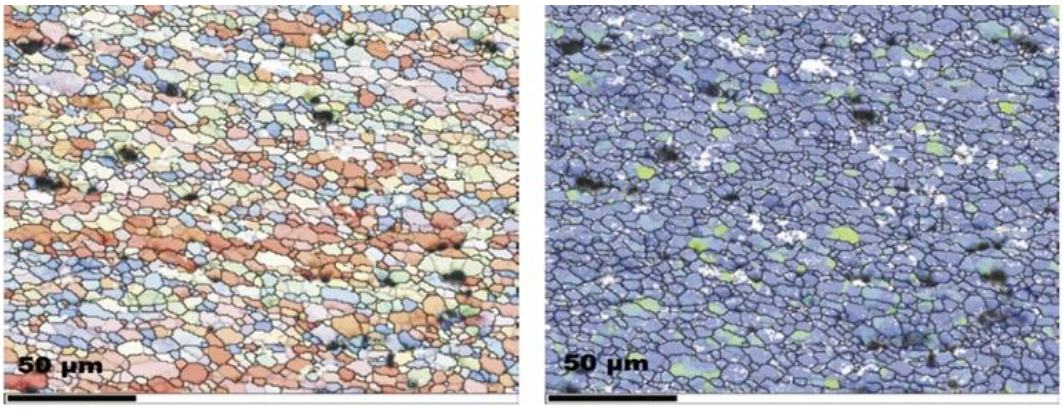

Figure 2.1: Dimensions of the grains with relative deformations at the nugget [55].

The microstructure of the advancing side is characterized by a clear demarcation between the nugget and the TMAZ. The nugget is made up of fine and relatively homogeneous grains, while the TMAZ has larger elongated grains, averaging 13.5 µm (Figure 2.2).

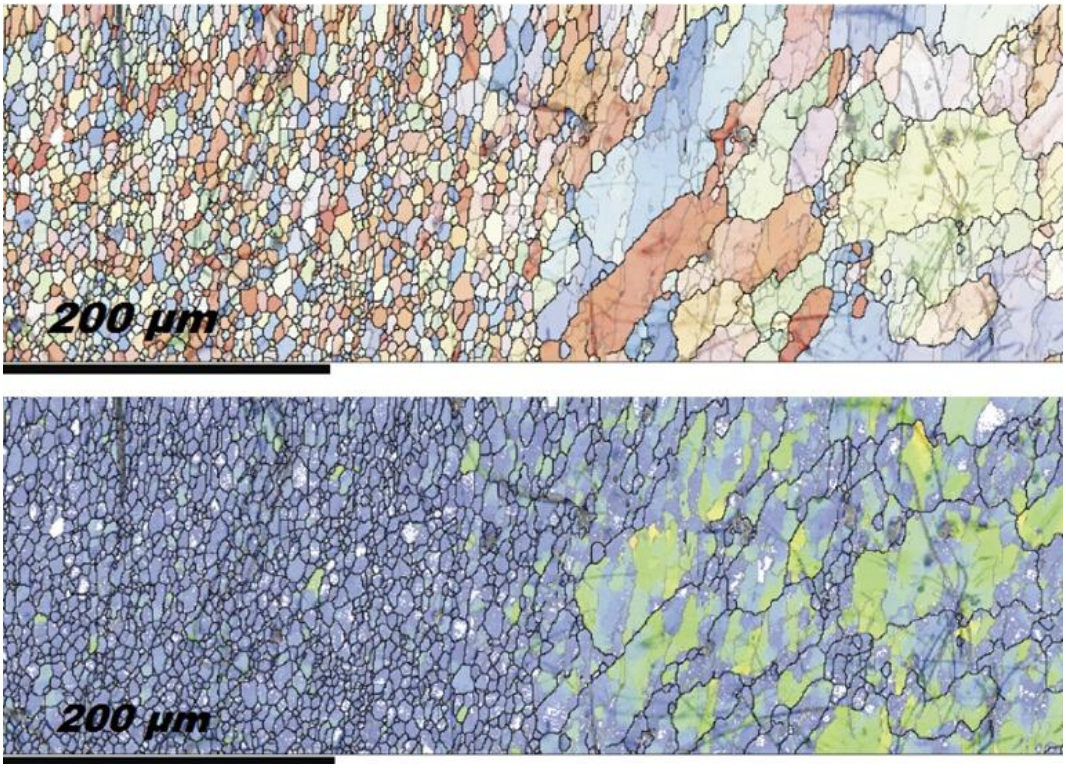

Figure 2.2: Dimensions of the grains with relative deformations in the advancing side [55].

The retreating side of the FSW joint has a more complex microstructure, without a clear demarcation between the nugget and the TMAZ (Figure 2.3).

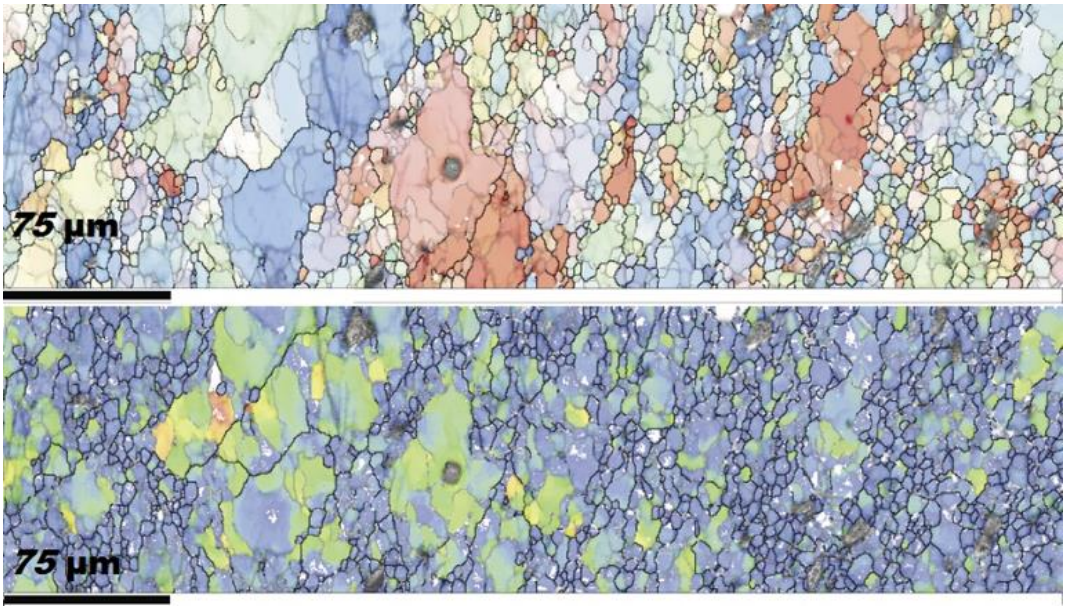

Figure 2.3: Dimensions of the grains with relative deformations undergone in the retreating side [55].

Also M. Jariyaboon et al. claimed that the nugget region consists of fine and equiaxed grains, thanks to dynamic recrystallization [56]. Adjacent to this region, the boundary between the nugget and the TMAZ presents an intense deformation of the grains, which have an orientation perpendicular to the rolling direction. It is also possible to note how the boundary between the TMAZ and the nugget is more marked in the advancing side than in the retreating side (Figure 2.4).

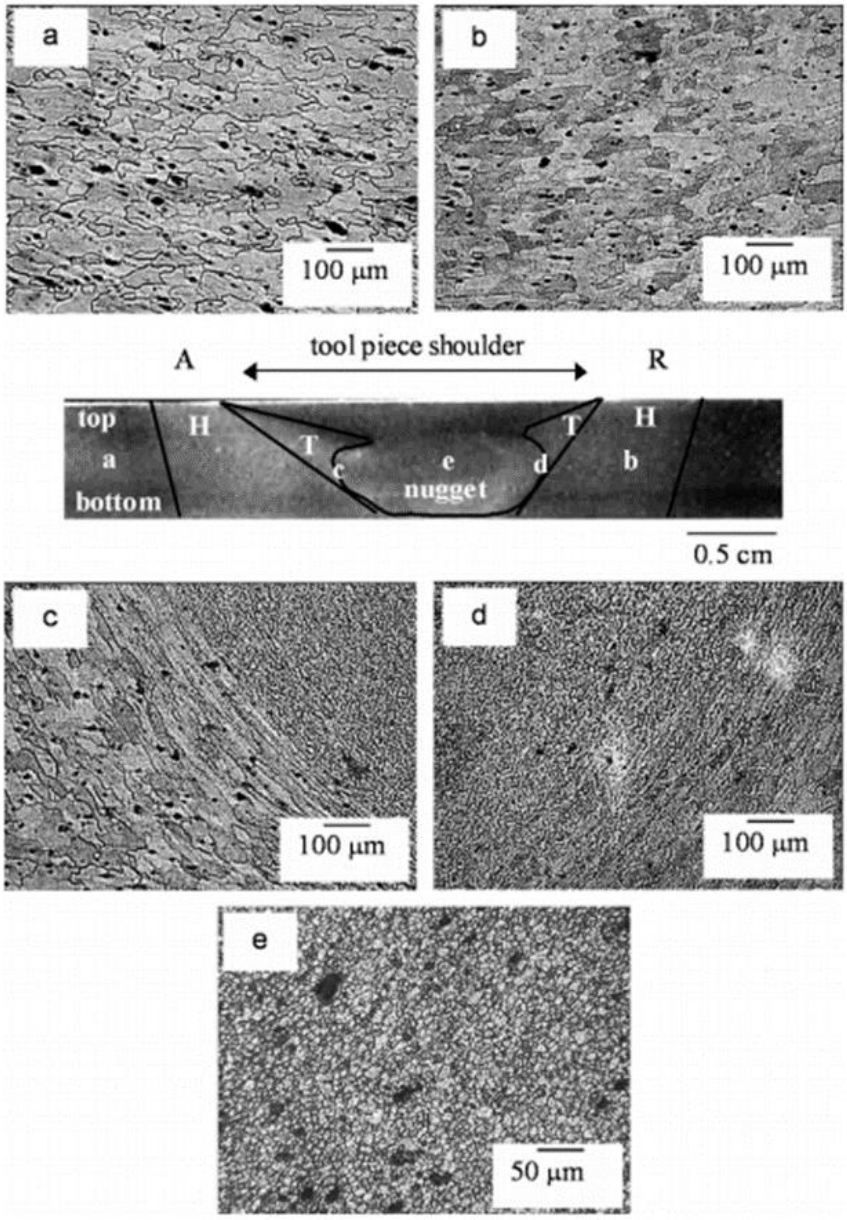

Figure 2.4: Microstructure of: a) Base metal. b) HAZ. c) Advancing Side. d) Retreating Side. e) Nugget [56].

M. Jariyaboon et al. integrated their analysis with the study of the precipitates and of the second phases present in the AA2024-T351. This alloy mainly has two constituent intermetallic particles: Fe-containing particles and S-phase particles (Al_2CuMg). These are typically observable in all regions of the weld. However, the Fe-containing particles are fragmented in the nugget region due to the action of the mixing. On the other hand, the larger S-phase particles remain relatively intact.

A homogeneous distribution of precipitates of approximately 100 nm in size was found. The particles thus identified appear to be $Al_{20}Cu_2Mn_3$ and S-phase precipitates (Figure 2.5).

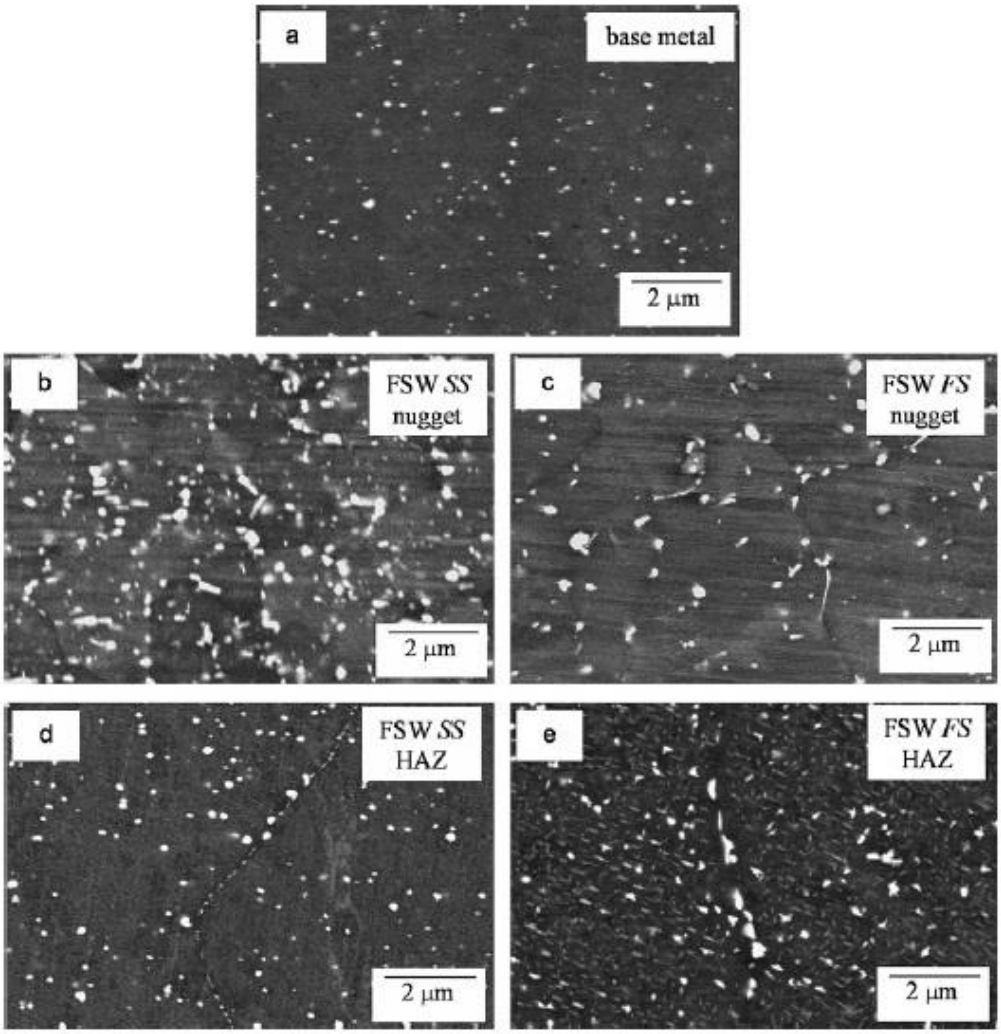

Figure 2.5: SEM images of the precipitates distribution in the base metal (a), in the nugget (b) and (c), and in the thermally affected zone (d) and (e) [56].

Jariyaboon et al. continued by analyzing the influence of welding parameters on microstructure and precipitates. It was demonstrated that the microstructure of the center of the weld was strongly dependent on the process parameters. For low feed rate and rotational speed, a high density of precipitates both at the grain boundary and in the matrix was observed in the central area of the nugget. Approximately 8 mm far from the center of the weld, the HAZ presented a fine precipitation of S-phase particles at the grain boundary, while no precipitates were observed in the matrix.

For higher feed rate and rotational speed, larger grains were observed in the central area of the nugget. The precipitation of S-phase particles mainly affected the grain boundary with a much lower density of particles in the matrix. About 11 mm far from the center of the weld, the HAZ showed S-phase precipitates at the grain boundary [56].

It was noticed that the process parameters have an influence on the fragmentation of the particles; an increase in the rotational speed results in more fragmented particles, while the feed rate does not appear to have an influence on these features.

Bocchi et al. analyzed the effect of different rotational speed (1000, 1500 and 2000 rpm) and feed rate (10 and 35 mm/min) on both the microstructure and on the mechanical properties of AA2024 FSWed joints [57]. Within the considered technological window, no significant differences can be observed as far as the width of the different welding zones.

In this paper, at the nugget, mean grain size of 3-5 μm surrounded by small precipitates of secondary phases was detected, as shown in Figure 2.6. Analyzing the SEM images, a decrease of the number of precipitates at grain boundaries was observed increasing the rotational speed from 1000 to 1500 rpm, whereas the feed rate did not appear to have influence on the precipitates.

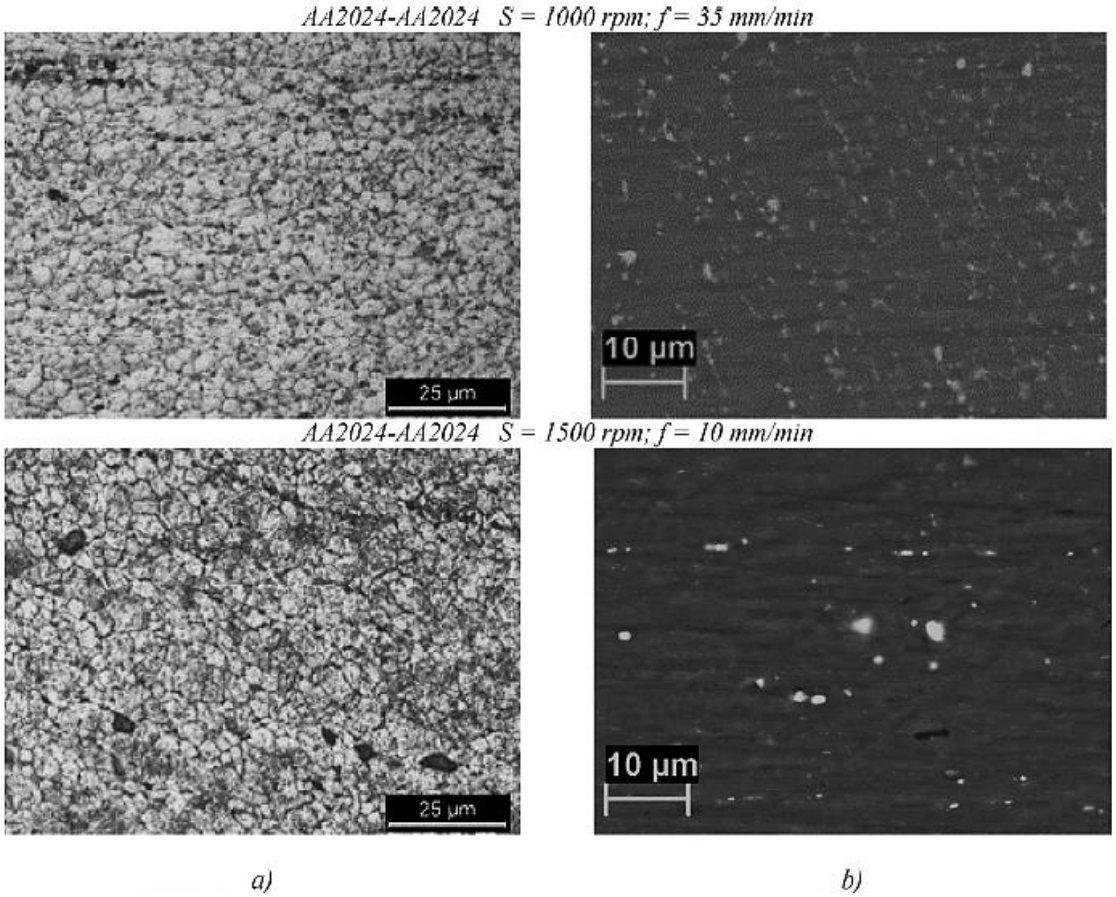

Figure 2.6: Microstructure of the nugget of the AA2024 joints welded using different parameters: a) optical images, b) SEM close up of the precipitates [57].

The HAZ and TMAZ showed elongated grains and micrometric precipitates, with a mean grain size of 100 µm, similar to the base metal (Figure 2.7). The shape and dimension are not altered by the welding parameters.

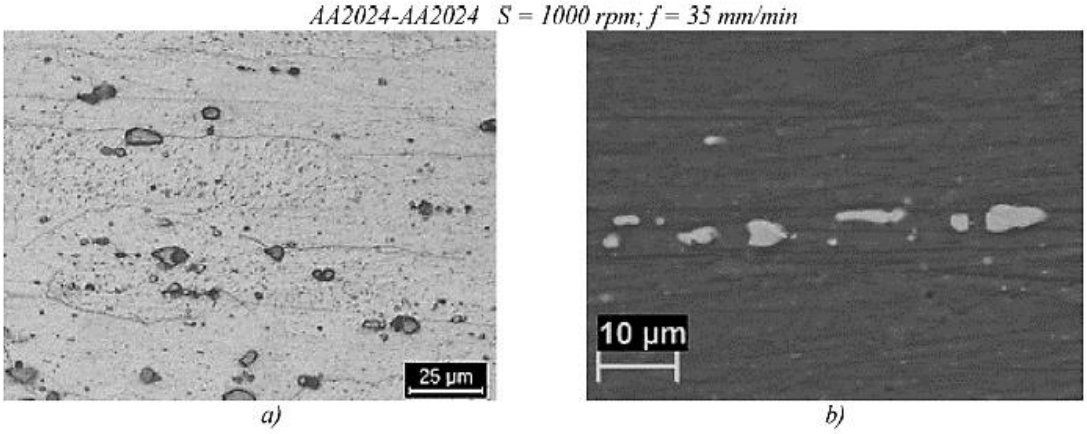

Figure 2.7: Microstructure of the HAZ of the AA2024 joint: a) optical images, b) SEM close up of the precipitates phases [57].

Regarding the hardness distribution, a symmetry was observed with respect to the center of the weld and no significant differences between advancing and retreating zone were noticed (Figure 2.8). The TMAZ showed the lowest hardness, but the major softening occurred in the TMAZ in the conditions that provide higher heat input, that is for low values of feed rate per unit revolution (feed/speed [mm/rev]), which is an index of the thermal power transferred to the joint region during the process.

A peak of hardness was observed in the HAZ of the AA2024 joints, ascribable to high density of fine intragranular precipitates.

The hardness profile was mainly due to the microstructural modifications and to the distribution of precipitates owing to the thermo-mechanical action. In fact, in the HAZ, the decrease of hardness is ascribable to the dissolution of Guinier-Preston (GP) zones. In the center of the HAZ, the hardness is ascribable to high density of fine intragranular precipitates. At the nugget, the hardness map is mainly governed by the presence of both small grain size and high density of G.P.B. zones.

Moreover, in this study, no systemic effect between joint hardness and process parameters were found.

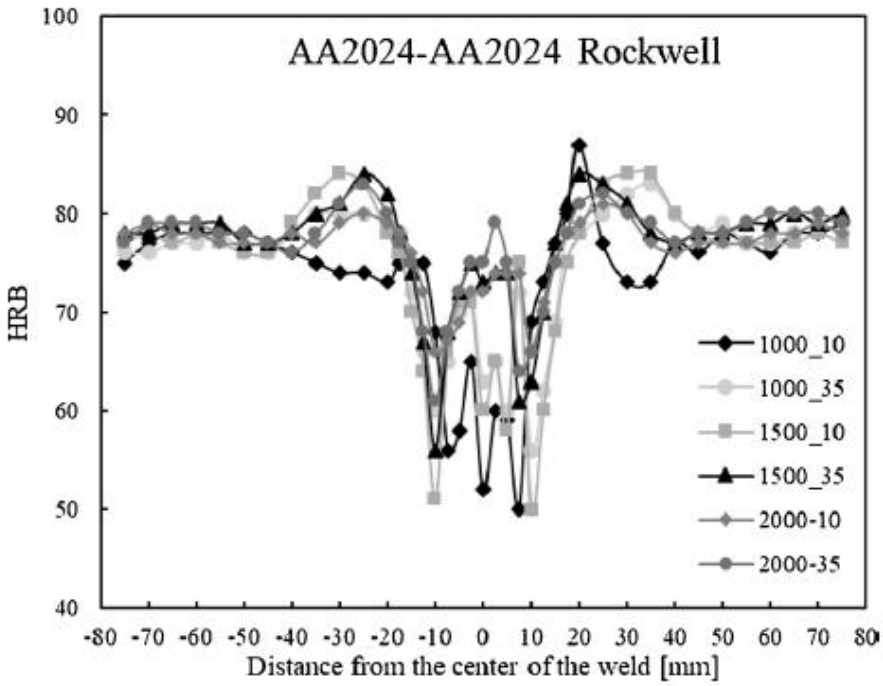

Figure 2.8: Hardness profile of the FSWed AA2024 joints as a function of different welding parameters [57].

Regarding the UTS value, the best conditions were obtained considering the intermediate values of both rotational speed and the feed rate, as reported in Figure 2.9. The failure of the welded joints usually occurs at TMAZ.

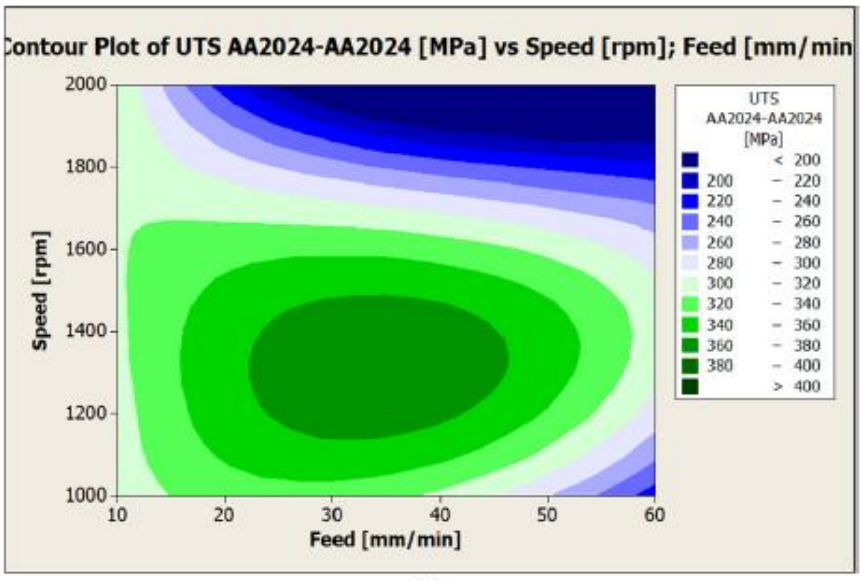

Figure 2.9: Tensile strength of the joints (UTS) as a function of feed rate [mm/min] and rotational speed [rpm] [57].

A general full factorial 3^2 ANOVA analysis was carried out on the already presented UTS data. The F-values and P-values reported in Table 2.1 confirmed a clear dependence of the UTS from the process parameters. In fact, a factor was considered to have a relevant influence if its P value is lower than the cut off limit (in this case set equal to 0.05).

Table 2.1: ANOVA results [57].

	UTS AA2024-AA2024	
	F	P
speed	28.05	0.000
Feed	22.05	0.000
speed * feed	10.76	0.000

I. Radisavljevic et al. focused on the link between the particle size and the heat input generated by the welding process, strictly dependent on the process parameters [48]. They found that the hardness was closely related to the microstructure of the welds and, therefore, to the choice of welding parameters. S. Di et al. [58] demonstrated that the hardness of the nugget and TMAZ increased proportionally to the increase in rotational speed.

On the other hand, this increase in rotational speed, had little relevance with respect to the hardness of the HAZ, where the lowest hardness values are found (Figure 2.10).

As for the feed rate, it was observed that the increase in feed rate, keeping the rotational speed constant, ensured higher hardness at the nugget.

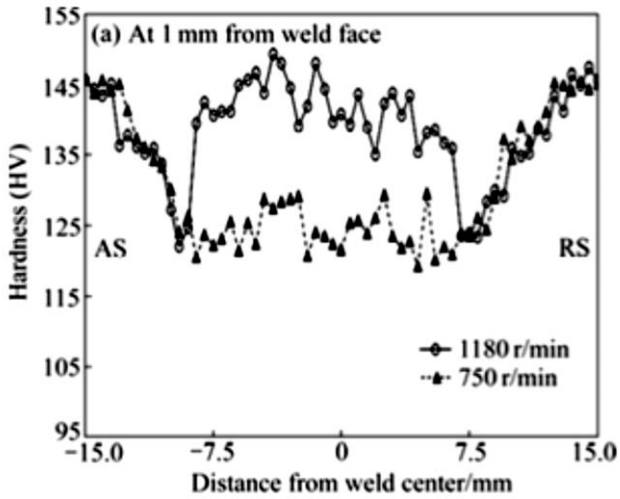

Figure 2.10: AA2024 hardness distribution as a function of different rotational speed [58].

Also the tensile strength of these alloys is dependent on the microstructure and parameters process, in particular on the rotational speed. S. Di et al. showed how the ultimate tensile strength and yield strength increased with the increase in the rotational speed of the tool. Conversely, low rotational speed was linked to low properties of the welded joints and favor the triggering of a brittle fracture [58].

AA5754

The AA5754 is an aluminum alloy of considerable interest as it can be used in several industrial fields. Despite this, the influence of the FSW process parameters on microstructure and mechanical properties of the welded joint has not yet been completely clarified.

M. M. El Rayes et al. considered the microstructural and the mechanical characterization of a FSWed AA5754-H111 varying the welding feed rates at constant rotational speed [59]. The author reported the microstructure of the material before (Figure 2.11) and after the Friction Stir Welding processing (Figure 2.12). The base material was characterized by equiaxed grains averaging of 36 ± 2 μm, while in the recrystallized microstructure, the grain dimensions were strictly linked to the feed rate. In particular, at the slowest feed rate (36 mm/min) the largest grain size was of 12.6 μm, whereas it was 10.8 and 8.9 μm with the feed rates of 70 and 140 mm/min, respectively.

The reason is that the reducing the feed rate at constant rotational speed increases the heat generated by the friction between the tool and the working piece.

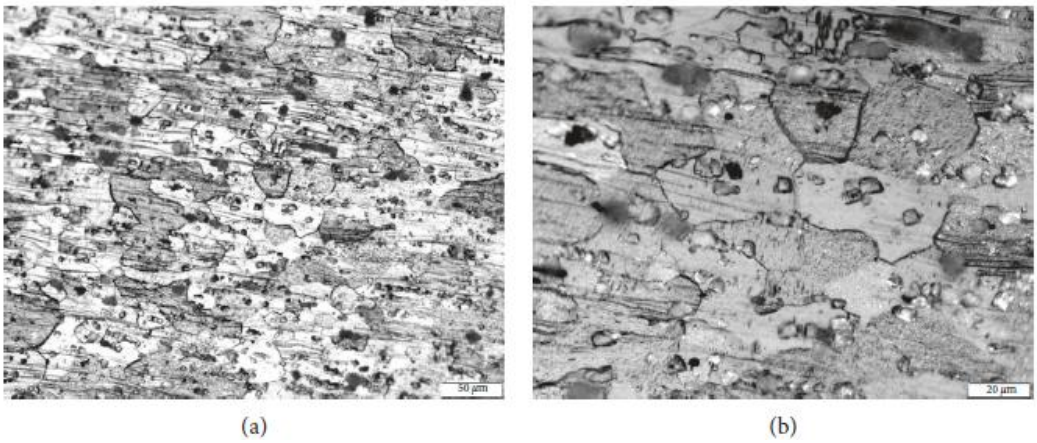

Figure 2.11: Optical micrographs of AA5754 base material at different magnifications [59].

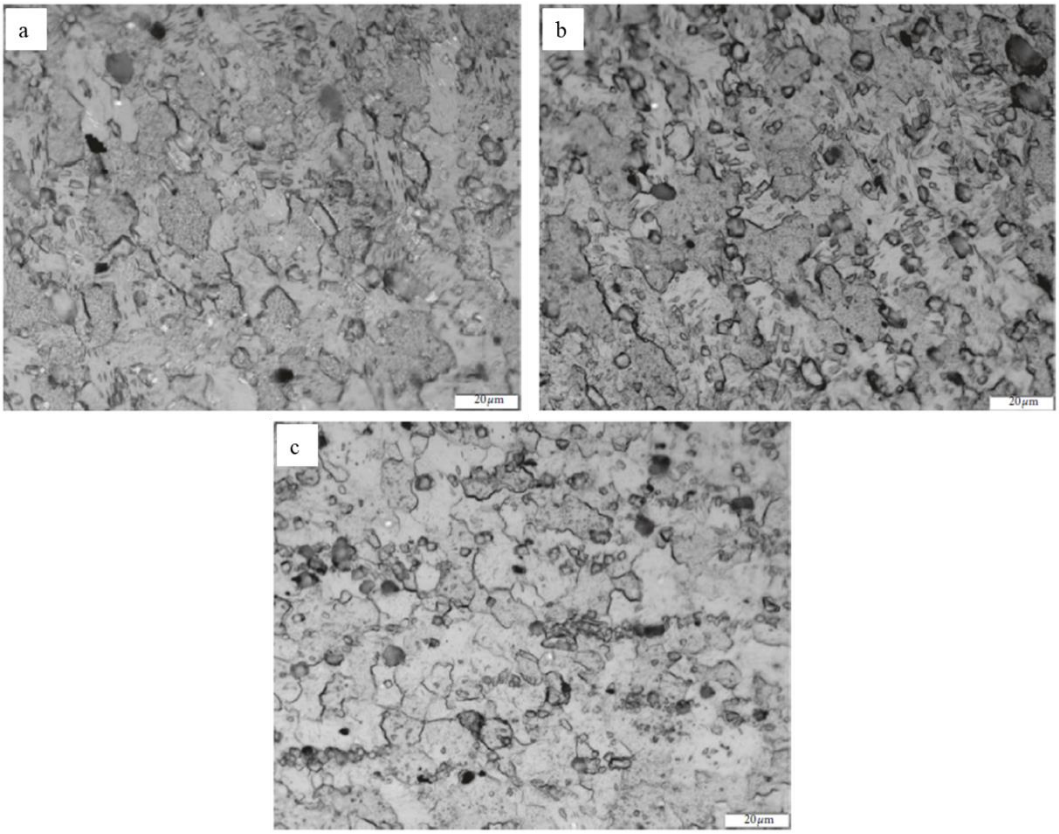

Figure 2.12: The microstructure of the stir zone for FSWed samples at 1070 rpm and three feed rates: (a) 36 mm/min; (b) 70 mm/min; (c) 140 mm/min [59].

Figure 2.13 showed that particles in both base material and welded joint were second phase particles, composed by higher weight percentage of Mg and Si and lower Al.

This difference may be due to the friction heating and fragmentation of these particles, which promote the dissolution and diffusion of such elements into the matrix.

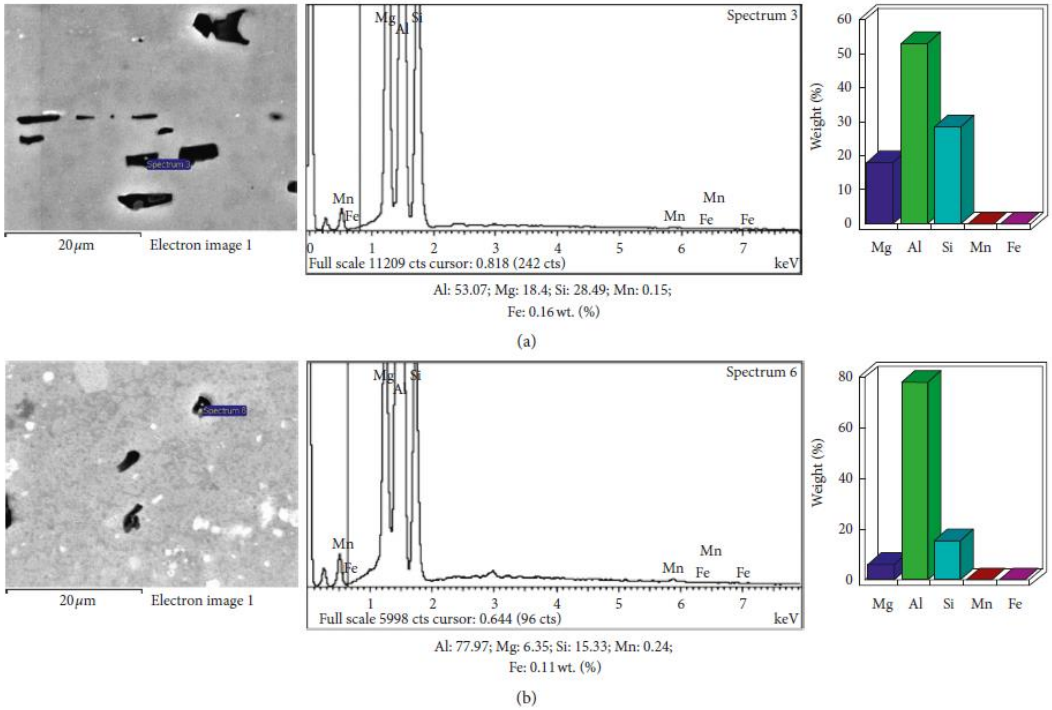

Figure 2.13: High magnification EDS elemental analysis of the second phase particles present in (a) base metal and (b) stir zone [59].

The population of the second phase particles in the base material and in the joints welded with different feed rates was studied, measuring the dark spot areas compared to that of the light matrix (Figure 2.14).

Also this analysis confirmed that the particles had a larger size in the base material when compared to that found in other zones. They were assumed almost round shape and heterogeneously distributed within the aluminum matrix, with an area fraction of 14.4 ± 1.4 %.

Regarding the welding zone, even if fragmented and smaller, the particles were still round-shaped but more homogenously distributed within the matrix.

Figure 2.14 showed that the increasing in the feed rate reduced the particles size and their density leading to a smaller area percentage fraction (12.1 ± 1.4, 9.54 ± 1.1, and 7.73 ± 0.7% corresponding to 36, 70, and 140 mm/min, respectively) because of fragmentation and redistribution within the entire matrix.

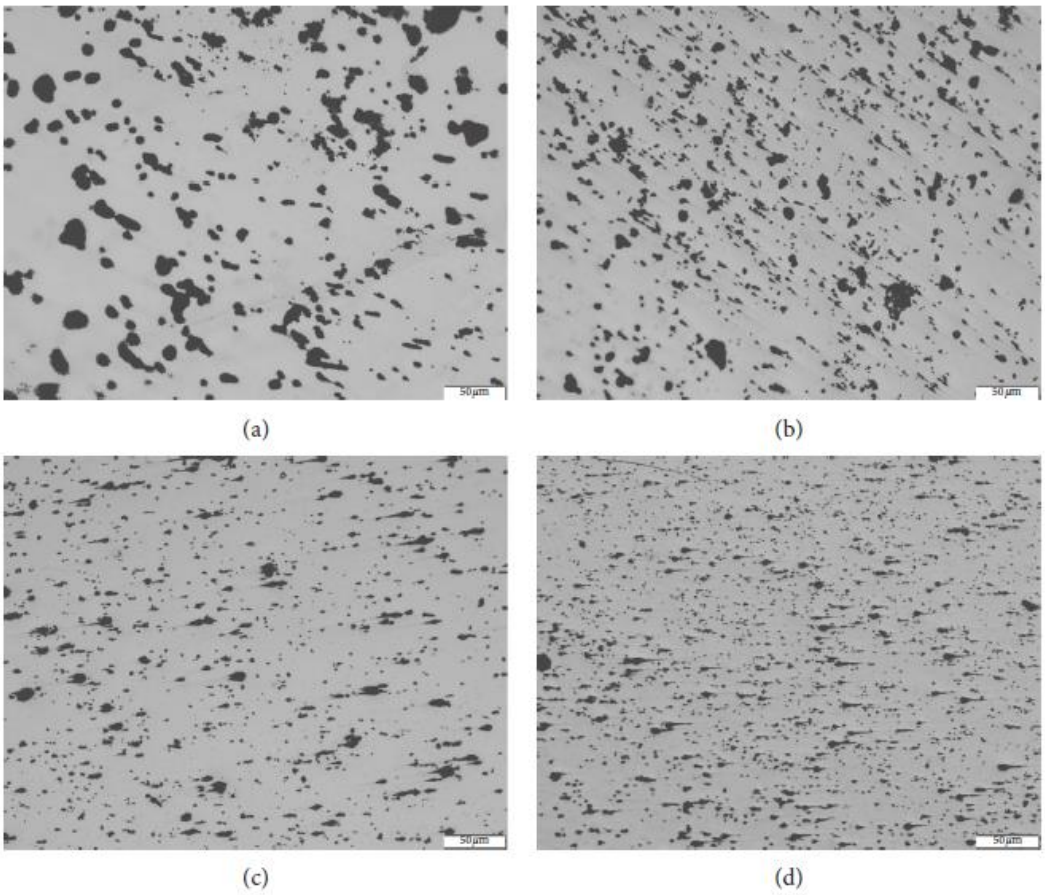

Figure 2.14: Particle morphology and population measured at (a) base material and welding zone for samples welded with different feed rates: (b) 36 mm/min, (c) 70 mm/min, and (d) 140 mm/min [59].

T. Taavitsainen et al. performed EBSD studies over the cross section of FSWed AA5754-H111 joints [60]. From the obtained images, reported in Figure 2.15, it was possible to observe the absence of a texture effect both in the HAZ and in the TMAZ: only the nugget seemed to be affected by the re-mixing action of the tool.

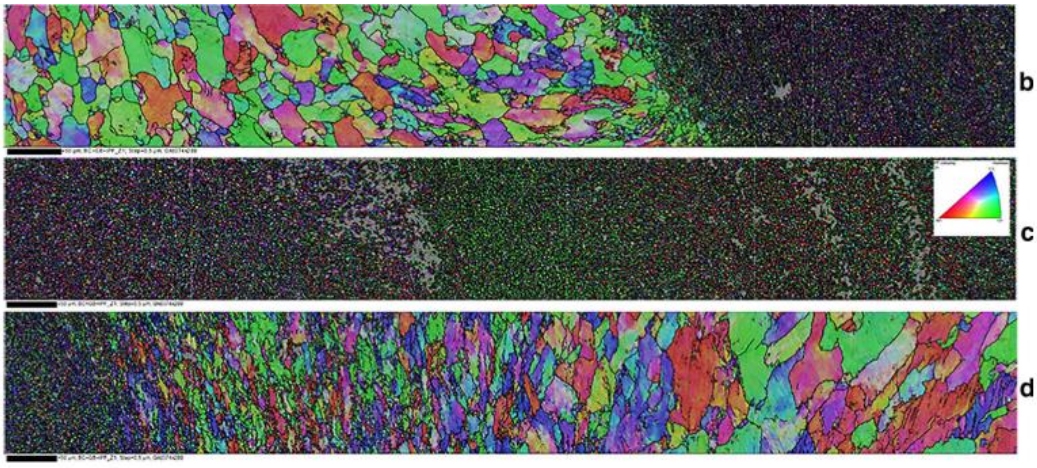

Figure 2.15: Metallurgical EBSD analysis. b HAZ and TMAZ at advancing side. c Weld nugget. d HAZ and TMAZ at advancing side [60].

The grain size over the scanning area is presented in Figure 2.16, where the difference between the small equiaxed grain (≤ 2.1 μm) and the original base material (12.5 μm) was evidenced. On the advancing side, the gradient in the grain size was higher with respect to the retreating side and the width of the zone with refined grain size was slighter than on the retreating side.

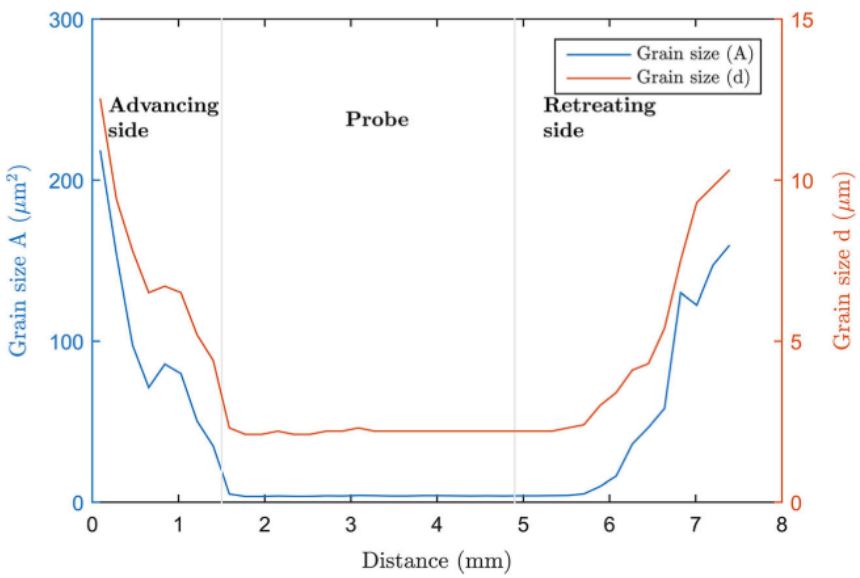

Figure 2.16: Grain size over the joint [60].

Figure 2.17 presents the distribution of the micro-hardness in the proximity of the welded joint measured by T. Taavitsainen. The results showed a significant increase in hardness of the material directly processed by the probe of the tool. In fact, in the nugget zone, the

average hardness was about 110 HV with a maximum hardness of about 130 HV, while the original base material hardness was about 73 HV [60].

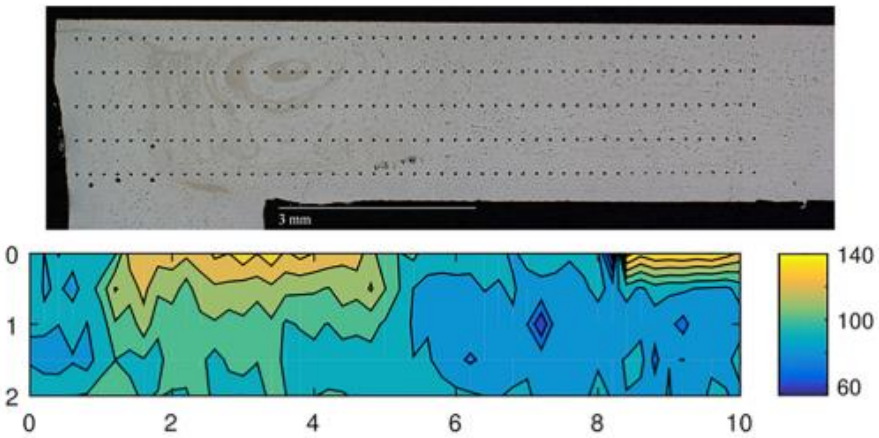

Figure 2.17: Vickers micro-hardness map (in the transversal section) [60].

Generally, the hardness profile across all weldments of a work-hardening alloy give a similar trend: the hardness is maximum at the stirred zone and gradually reduced towards the base material, as in Figure 2.18 [59].

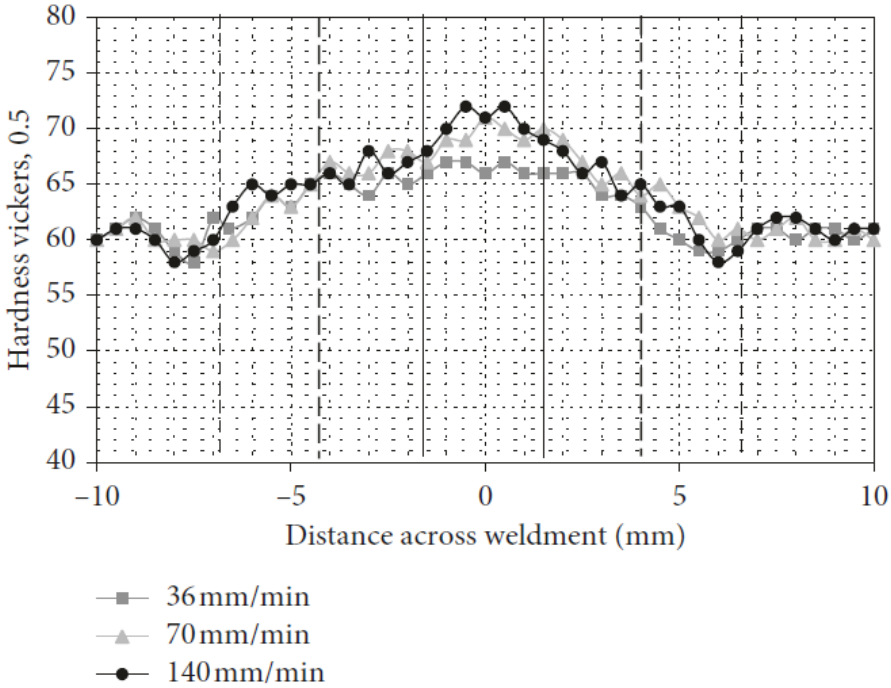

Figure 2.18: Hardness distribution across weldments welded at different feed rates [59].

The reason why the stirred zone is hardest compared to the base material is because of the finer grain size than in the base material, as already mentioned above.
Since the grain boundaries are one of the major obstacles to the dislocations slip, smaller grain size would have a higher resistance to the localized plastic deformation leading to higher hardness values and consequently higher strength resistance [61].
The effect of the feed rate on the mechanical properties was conducted by M. M. El-Rayes, finding that an increase in the feed rate was accompanied by a slight increase in UTS and by a decrease in the ductility of the joint, as reported in Figure 2.19 [59].

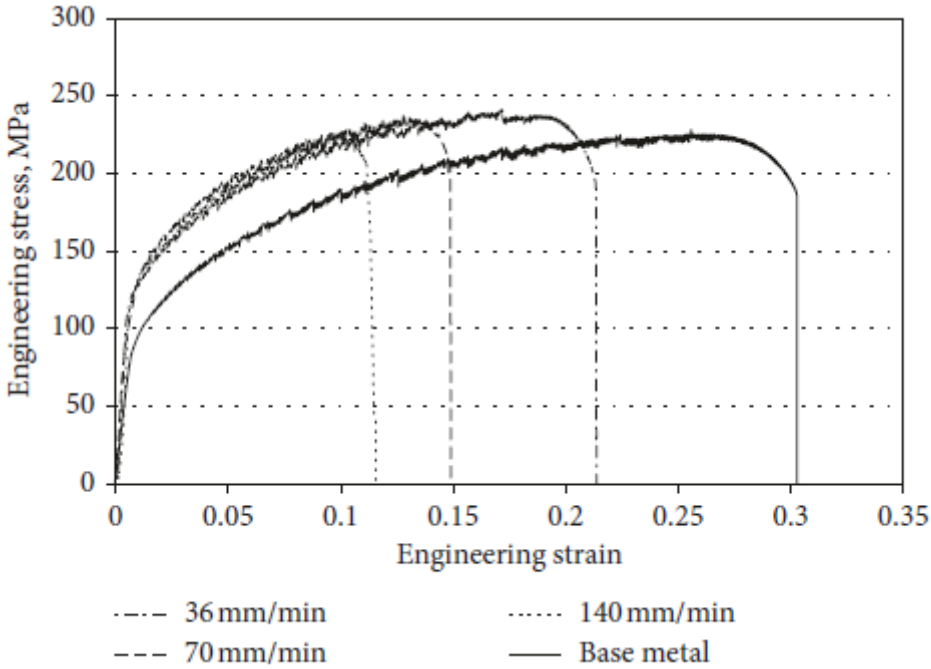

Figure 2.19: Engineering stress-strain curves of the base material and friction stir welded joints of AA5754 [59].

In conclusion, increasing the feed rate leads to an increase of the fragmentation and homogenizes the second phase particles within the welded matrix. For this reason, it enhances the UTS values, reducing the mean ductility of the joints and it also slightly increases the hardness of the welding zone.
As far as the rotational speed, L. M. Serio showed, through an ANOVA analysis, that the mechanical strength of joints (UTS) is influenced also by the tool rotation speed, but it is strictly related to the combination with the other process parameters [61].

AA6082

E. A. El-Danaf and M. M. El-Rayes performed FSWed AA6082-T651 joints using three different combinations of feed rates (90, 140 and 224 mm/min) and tool rotational speeds (850, 1070 and 1350 rpm) [22]. The aim of the authors was to analyze the effect of these process parameters on the microstructure and mechanical properties of the welded parts. It was noticed that, regardless to the welding parameters, the dynamically recrystallized grains in the stir zone were measured to be in the range of 2–3 μm for all the different feeds rates and rotational speeds.

Figure 2.20a shows the elongated rolled structure of the base metal. Figure 2.20b reports the transition in the microstructure from elongated grains in the base metal to ultra-fine equiaxed grains in the nugget (stirred zone – SZ) passing through the elongated grains of the TMAZ.

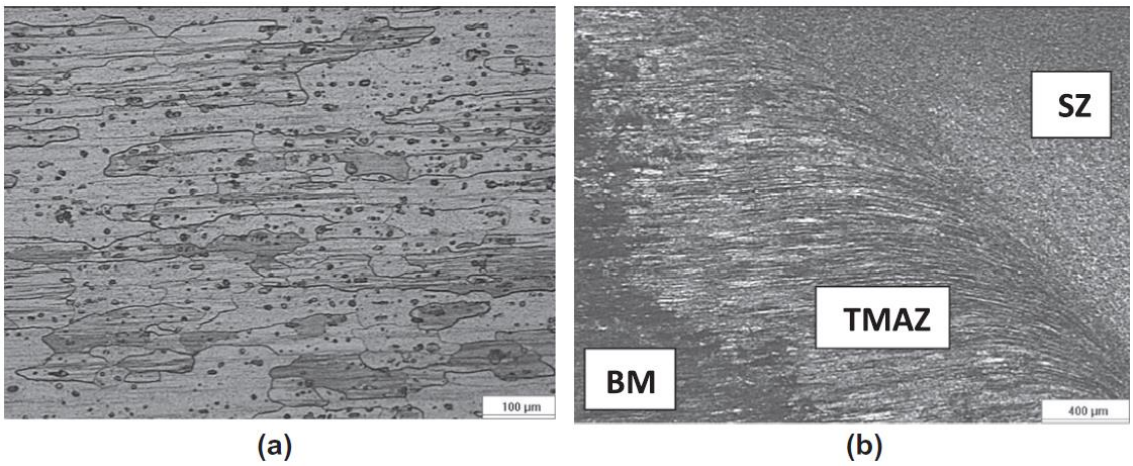

Figure 2.20: Microstructure of the as received material in (a) and across the weld nugget from the base metal (BM) through the TMAZ [22].

The authors also evidenced that all the different combinations of processing parameters resulted in similar hardness profiles, with the TMAZ significantly softened on both the advancing and retreating sides (Figure 2.21).

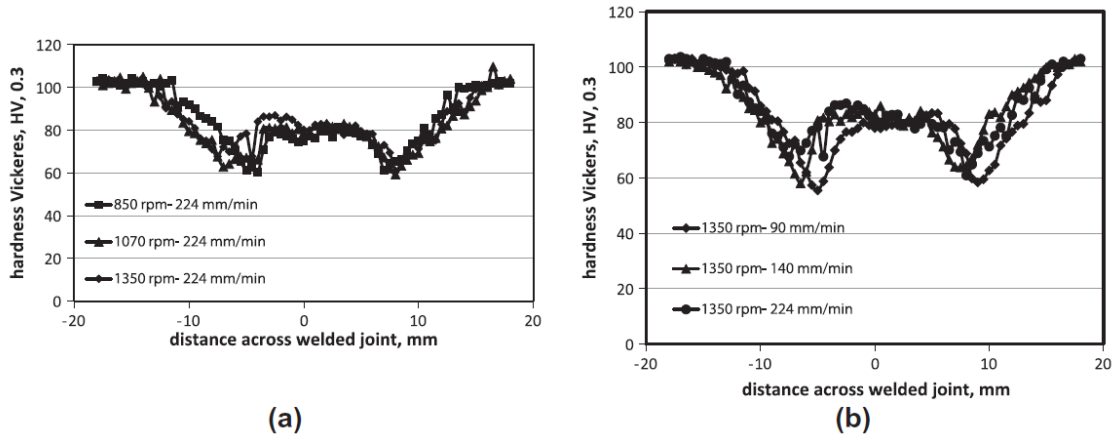

Figure 2.21: Micro-hardness profile on the transverse section showing the effect of varying rotational speeds in (a) and of varying feed rates in (b) [22].

It was evidenced the softening in the nugget and the further considerable softening of the TMAZ compared to the unaffected base metal.

The authors researched the motivation for this behavior in the decomposition of the β" hardening precipitates, the coarsening of the precipitates in an over-aged structure and the low dislocation density due to the structure dynamic recrystallization.

All these microstructural modifies led to a less strain and stress localization contributing to material softening.

Y. S. Sato al., studying the relationship between the hardness profile and the precipitates distribution of a FSwed AA6063, concluded that the precipitates present in the unaffected base metal exhibited a high density of β" hardening precipitates and a low density of β' precipitates, whereas in the TMAZ the density of the β" was strongly reduced and the density of the β' was upraised by the welding process [62, 63].

Moreover, regarding the mechanical properties of the FSWed AA6082 joints, E. A. El-Danaf and M. M. El-Rayes demonstrated that the ultimate tensile strength was mainly influenced by the feed rate, while the effect of rotational speed was found to be marginal within the range of revolutions per minute investigated, as shown in Figure 2.22.

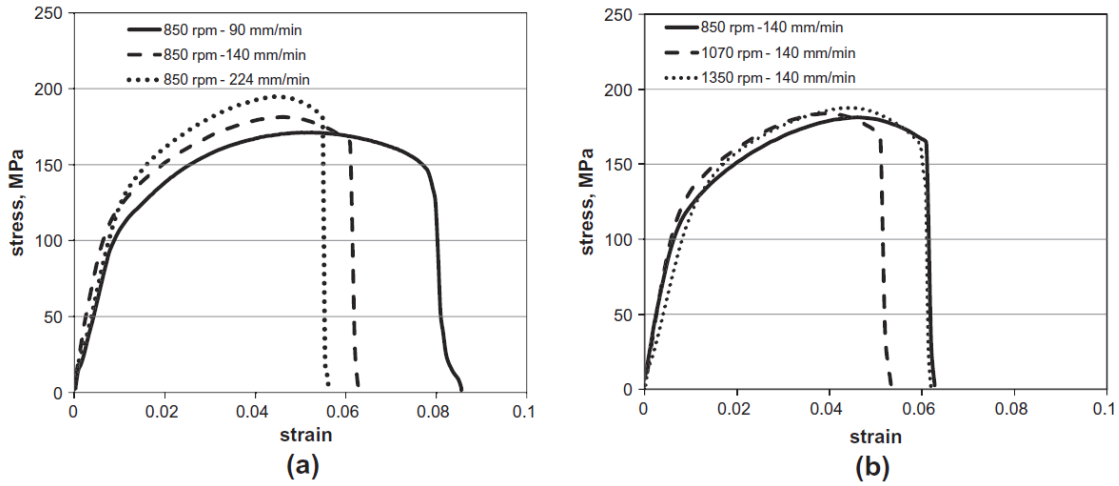

Figure 2.22: Engineering stress–strain response for the FSWed welded samples showing the effect of feed rate in (a) and the effect of rpm in (b) [22].

To conclude their analysis, the aforementioned authors displayed the variation of the average Vickers hardness and of the UTS values, changing the process parameters (Figure 2.23). It was underlined that, maintaining constant the rotational speed, an increase in the feed rate led to an improvement in both the strength and hardness and this is in agreement with the less heat input and, therefore, the less temperature reached in the weld region, corresponding to a less dissolution of the strengthening second phase particles [22].

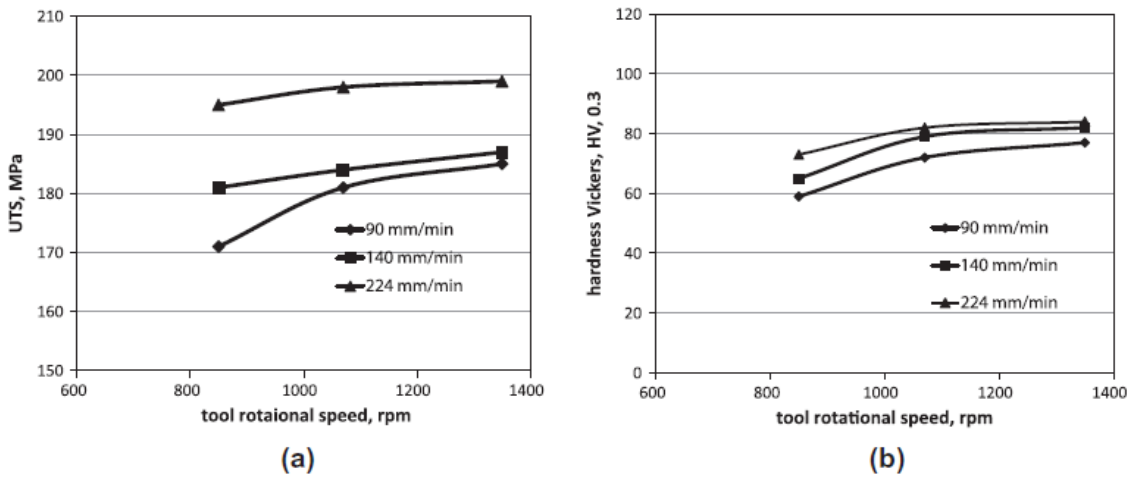

Figure 2.23: Variation of ultimate tensile strength for various welding conditions of feed rates (mm/min) and rotational speeds (rpm) in (a). Variation of Vickers hardness for various welding conditions of feed rates (mm/min) and rotational speeds (rpm) in (b) [22].

AA7075

The AA7075 has a multitude of alloying elements with different solubility and, consequently, during the metallurgical process, it can form a great variety of intermetallic phases within its matrix.

During the welding process the grains are intensely deformed and broken, resulting in the generation of many substructural dislocations. Therefore, heat generated by the friction between the tool and the pieces to be weld can encourage the regeneration and recrystallization of these substructures.

According to the studies conducted by J.J. Pang et al, the joining process appeared to have a significant effect on the AA7075 microstructure [64].

The experiments underlined that the welding process led to a reduction in the size of the grain, as shown in Figure 2.24.

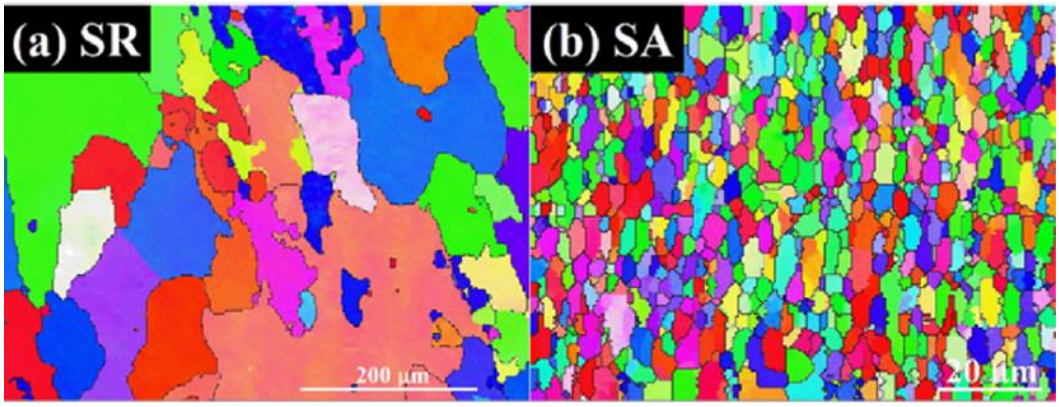

Figure 2.24: Maps of base metal (SR) and FSW (SA) weld metal microstructures [64].

According to J.J. Pang et al., the FSW welding process also generates differences in the concentration of the intermetallic precipitates of magnesium, copper and zinc within the weld. The study focused mainly on the particle size and distribution of Al_7Cu_2Fe and $MgZn_2$ and highlighted a different behavior for the two precipitates. Inside the weld joint, the Al_7Cu_2Fe particles were less present and of a smaller average size than the base metal. On the contrary, the $MgZn_2$ particles were more present and larger in size within the joint than in the base metal, as reported in Table 2.2.

Table 2.2: Distribution of intermetallic precipitates before (SR) and after FSW (SA) [64].

Sample	Average size		Area fraction (%)		Number density	
	Al_7Cu_2Fe (μm)	$MgZn_2$ (nm)	Al_7Cu_2Fe	$MgZn_2$	Al_7Cu_2Fe (counts mm^{-2})	$MgZn_2$ (counts mm^{-2})
SR	1.71	22.8	1.57	1.9	1.1×10^4	3.0×10^7
SA	0.82	28.4	0.87	3.3	2.6×10^3	3.8×10^7

S. Gholami et al. studied the effect of the FSW process on the size of the nugget grains compared to the size of the grains originally present in the AA7075 base metal [65]. The result of their experiments showed that the process reduced the average grain size by about an order of magnitude. In fact, the base metal grains had an average size of about 50-60 μm, while the nugget had grains with an average size of about 500 nm. The authors also highlighted that in the base material the grains were elongated along the rolling direction. On the contrary, in the nugget, due to the dynamic recrystallization undergone by the material, the grains were equiaxed and homogeneous, as shown in Figure 2.25.

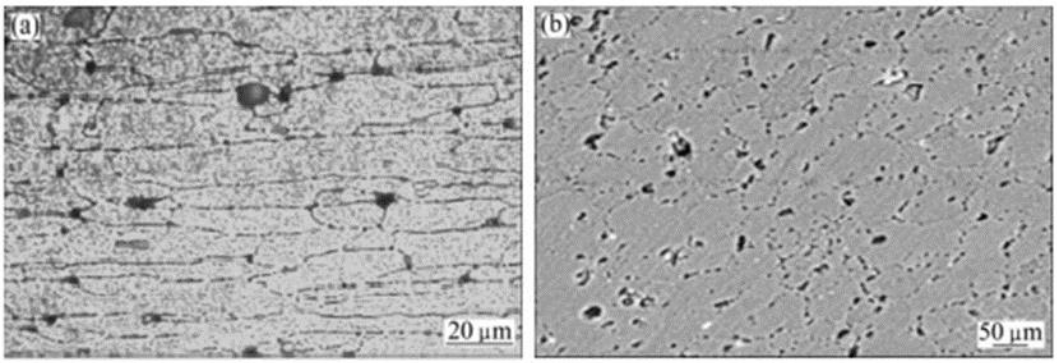

Figure 2.25: Microstructure of the base material (a) and of the nugget (b) for a FSWed AA7075 [65].

M. Navaser at al. studied the variation of the grain size and of the precipitates distribution of an AA7075 welded by FSW, as a function of the pin rotational speed [66]. The base metal, according to their experiments, showed typically elongated grains in the rolling direction with an average size of about 160 μm. The precipitation of the second phases was inhomogeneous, with particles of size between 2-20 μm (Figure 2.26).

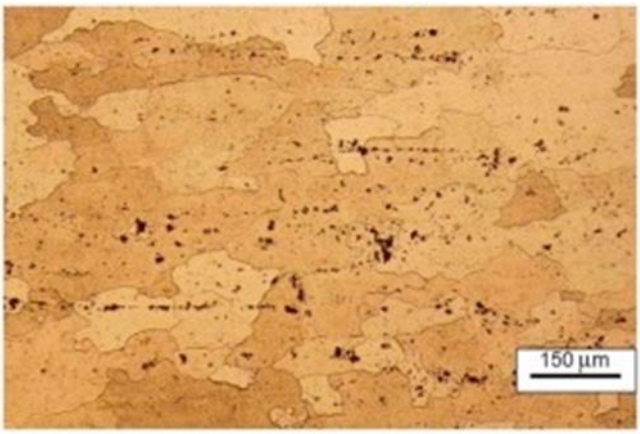

Figure 2.26: Microstructure of the AA7075 base metal [66].

For all the studied welding conditions, M. Navaser et al. recorded a decrease in the grain size for the central area. By studying the average grain size, they identified a linear dependence between this feature and the rotational speed (Figure 2.27).

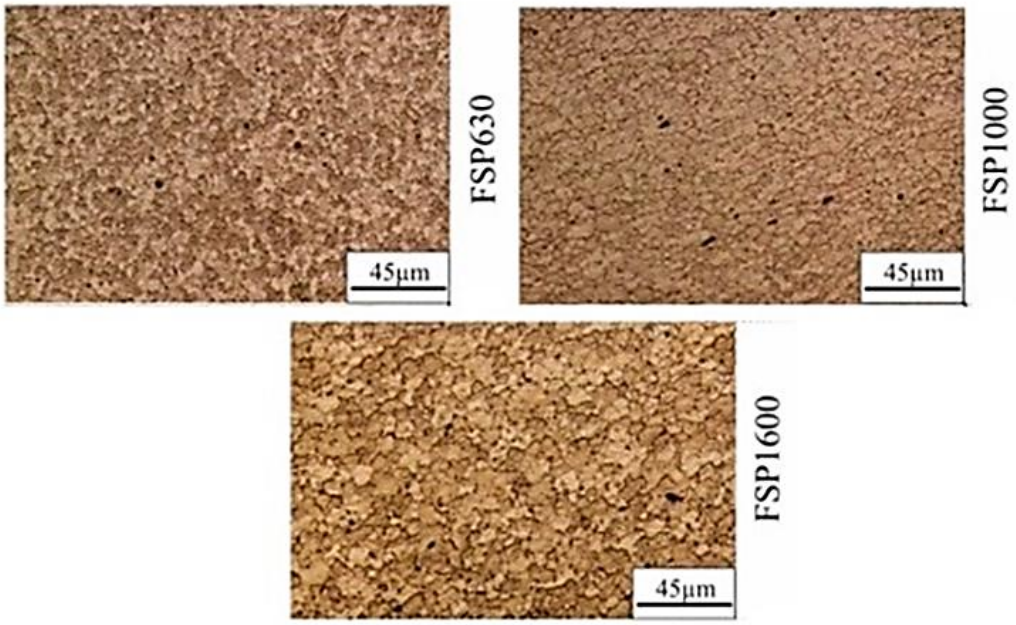

Figure 2.27: Microstructure of the nugget of an AA7075 alloy as the rotational speed varies [66].

The metal in TMAZ undergoes a strong plastic deformation, but the heat input is not high enough to generate a recrystallization. For this reason, the grains, according to M. Navaser et al., appeared to have considerable dimensions and to be elongated according to the stress gradient generated in the plasticized material. The authors highlighted the

difference between advancing side and retreating side. The first presented a clear separation between the microstructure of the nugget and that of the TMAZ. On the contrary, the second did not appear to have a clear separation between the aforementioned areas (Figure 2.28).

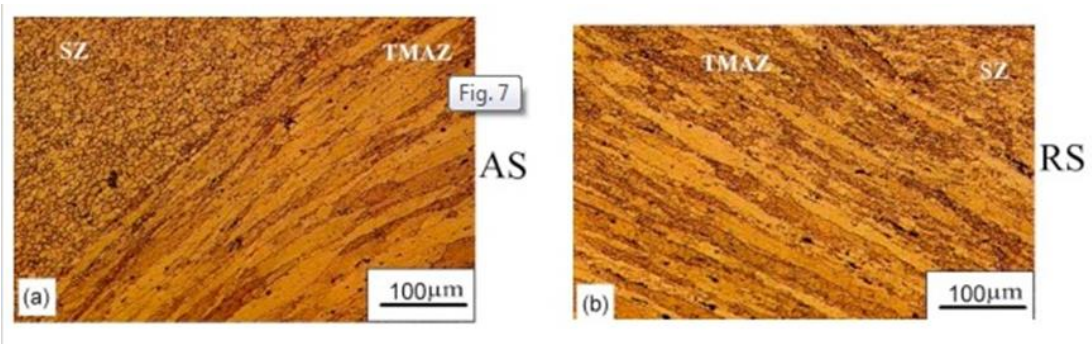

Figure 2.28: Microstructure of the boundary between nugget and TMAZ in the advancing side (AS) and in the retreating side (RS) of a FSWed AA7075 [66].

M. Navaser et al. also identified the difference in the concentration of precipitates in the areas involved in welding: the nugget had a finer and more homogeneous distribution of precipitates than the other areas. The dissolution and re-precipitation of the second phases were facilitated by the intense deformations undergone by the material (Figure 2.29).

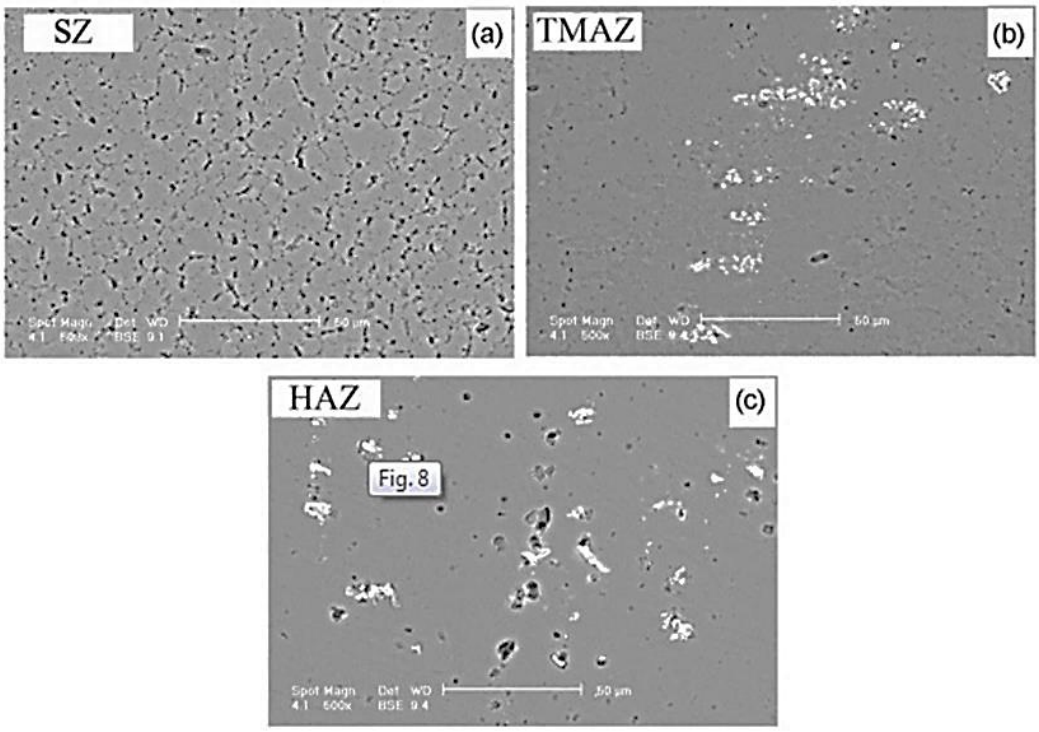

Figure 2.29: Distribution of the second phases within the welding zones characteristic of an AA7075 alloy. a) Nugget. b) Thermo-mechanically affected area. c) Thermally affected zone [66].

Bocchi et al. analyzed the effect of different rotational speed (1000, 1500 and 2000 rpm) and feed rate (10 and 35 mm/min) on both the microstructure and on the mechanical properties of AA7075 FSWed joints [57]. A common FSW structure of the different welding zones was found, regardless the considered process parameters.

In this paper, at the nugget mean grain size of 5-7 μm surrounded by small precipitates of secondary phases was detected, as shown in Figure 2.30. In the HAZ elongated grains and precipitates with a mean grain size of 100 μm were found (Figure 2.31). Increasing the rotational speed from 1000 to 1500 rpm, a decrease of the number of precipitates at grain boundaries was observed whereas the feed rate did not appear to have influence on the precipitates.

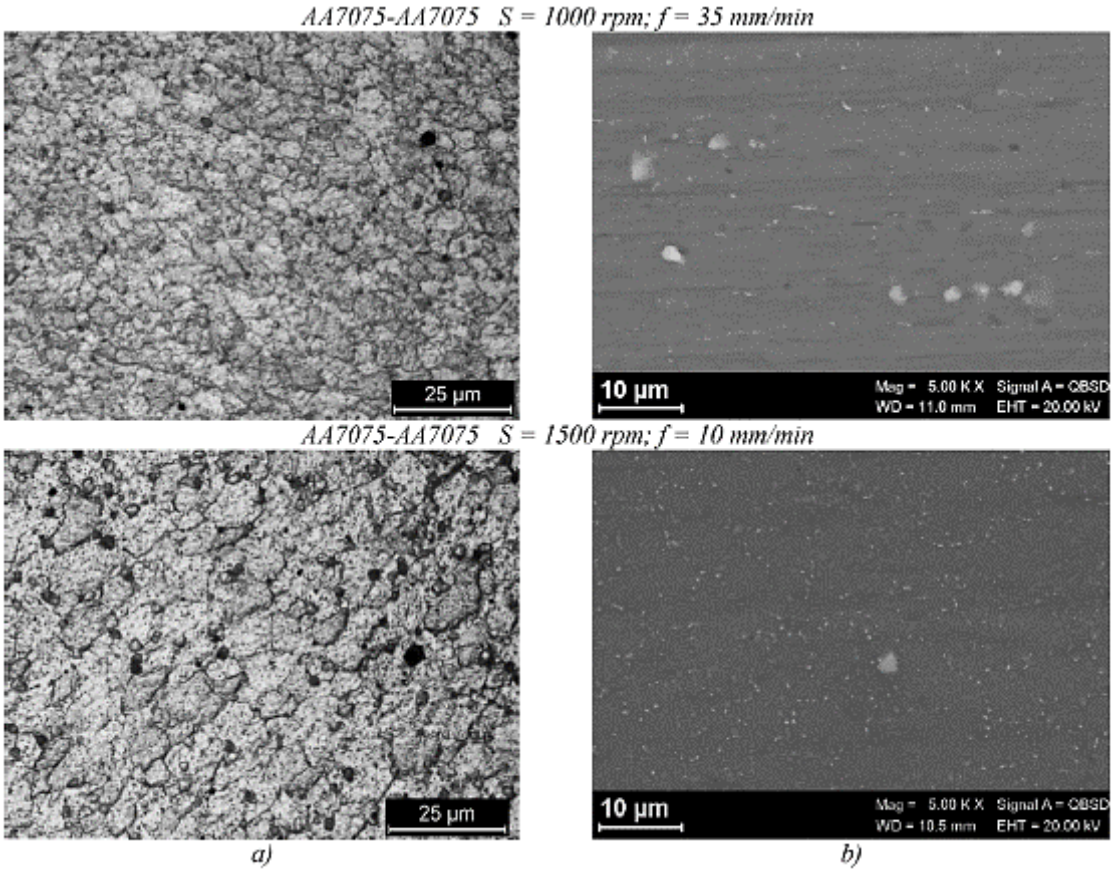

Figure 2.30: Microstructure of the nugget of the AA7075 joints welded using different parameters: a) optical images, b) SEM close up of the precipitates [57].

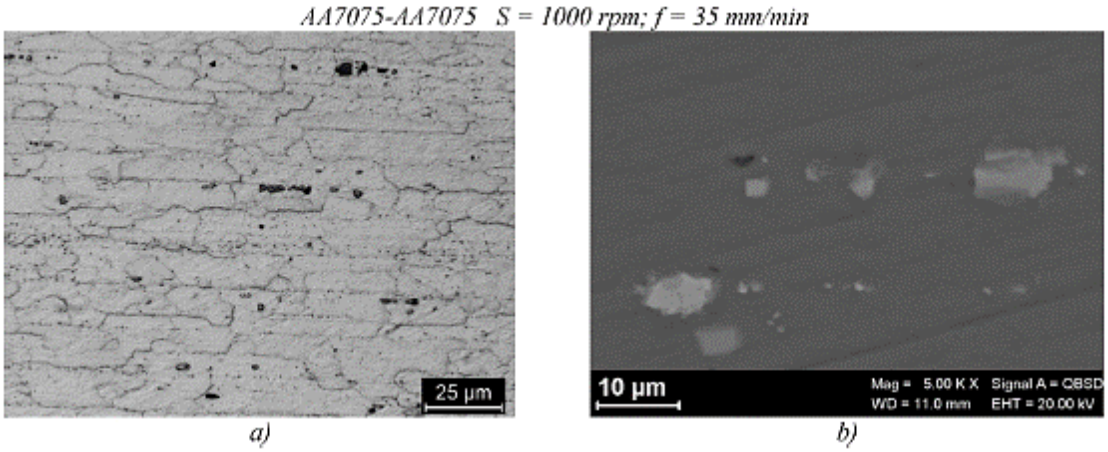

Figure 2.31: Microstructure of the HAZ of the AA7075 joint: a) optical images, b) SEM close up of the precipitates phases [57].

In the AA7075, the dynamic recrystallization in the nugget produces a re-dissolution of the precipitates obtained by the artificially ageing treatment, while these precipitates are

coarsening in the HAZ, reducing the hardness. Like the AA2024 alloys, the reduction of grain size increases the hardness up to intermediate values between base material and HAZ. Also for the AA7075, the process parameters do not influence neither the difference between the advancing and retreating side nor the hardness maps (Figure 2.32).

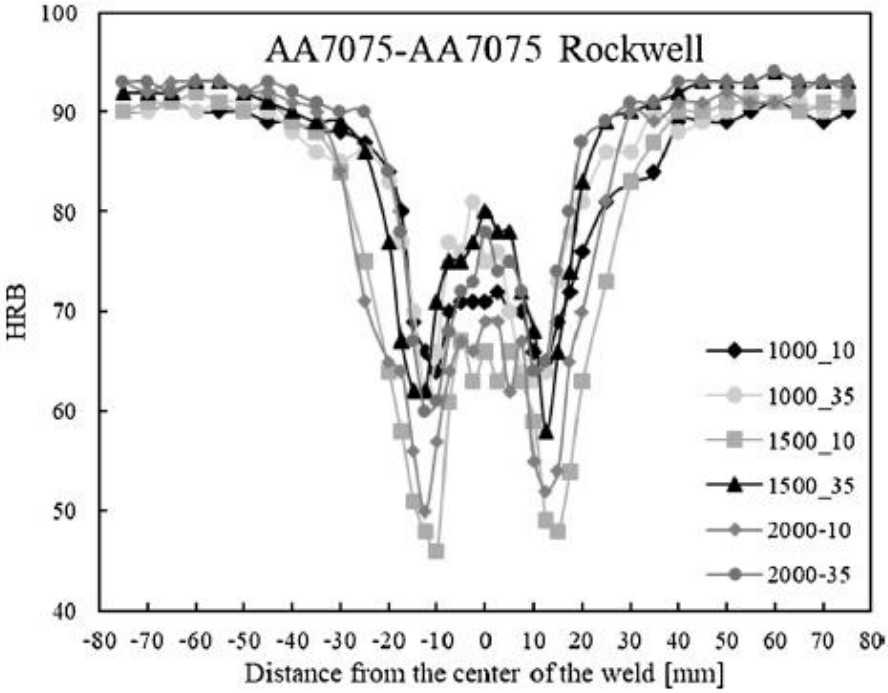

Figure 2.32: Hardness profile of the FSW AA7075 joints as a function of different welding parameters [57].

Regarding the UTS values, the best conditions were obtained considering the low and intermediate values of both rotational speed and the feed rate, as reported in Figure 2.9. The failure of the welded joints usually occurred at TMAZ.

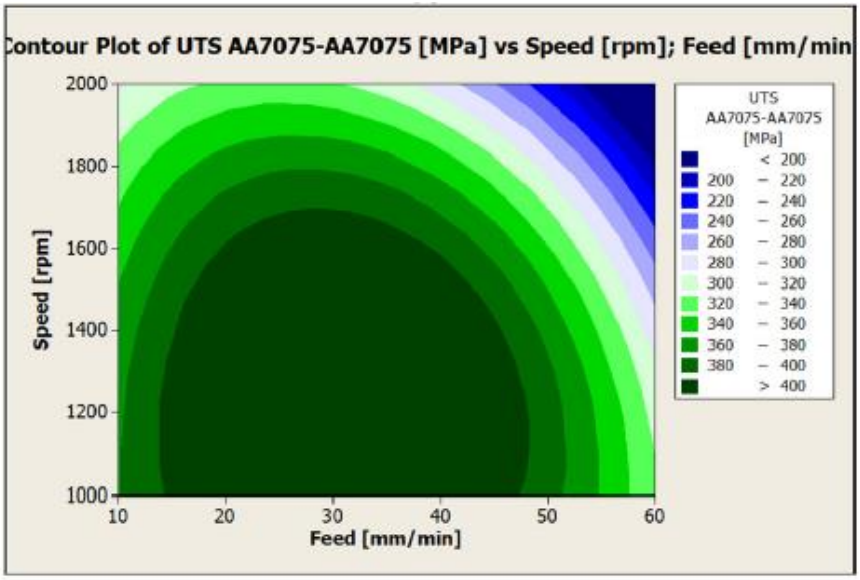

Figure 2.33: Tensile strength of the joints (UTS) as a function of feed rate [mm/min] and rotational speed [rpm] [57].

A general full factorial 3^2 ANOVA analysis was carried out on the already presented UTS data. The F-values and P-values reported in Table 2.3 confirmed a clear dependence of the UTS from the process parameters but not from the combination between the rotational feed and the feed rate. In fact, a factor was considered to have a relevant influence if its P value is lower than the cut off limit (in this case set equal to 0.05).

Table 2.3: ANOVA results [57].

	UTS AA7075-AA7075	
	F	P
speed	5.02	0.019
Feed	6.21	0.009
speed * feed	2.63	0.069

2.2. Corrosion behavior

According to M. Jariyaboon et al., FSW process modifies both the microstructure and, consequently, the corrosion behavior of the joints as the parameters of the welding process vary [56].

In this paragraph only the corrosion behavior of AA2024 and AA7075 FSWed joint will be considered, since they are the most affected alloys by the corrosion behavior, due to the well-known susceptibility of the copper-aluminum and zinc-aluminum alloys to stress corrosion cracking.

In fact, despite the enhanced properties, these alloying elements introduce higher degree of heterogeneity due to the presence of secondary phases or characterized constituent particles [67]. Corrosion behavior can be mainly affected by the presence, the size and the distribution of such phases, modifying the anodic and cathodic behavior of the joints [64, 66, 68].

Several works describing corrosion morphologies that can occur also concomitantly in form of localized corrosion, e.g., galvanic corrosion, pitting, de-alloying or intergranular attack were found, but very few data regarding the correlation between mechanical properties and corrosion behavior can be noticed [69].

AA2024

According to the work of E. Bousquet et al., the joining process significantly changes the corrosion behavior of an AA2024-T3 [70]. Studying the behavior of the various zones, E. Bousquet et al. identified in the interface TMAZ/HAZ the region subjected to the most severe corrosive attack. In fact, in the HAZ the intergranular attack was more homogeneous and significant (Figure 2.34); while in the base metal, in the nugget and in the TMAZ, the attack caused the sporadic formation of pits and a moderate form of intergranular attack.

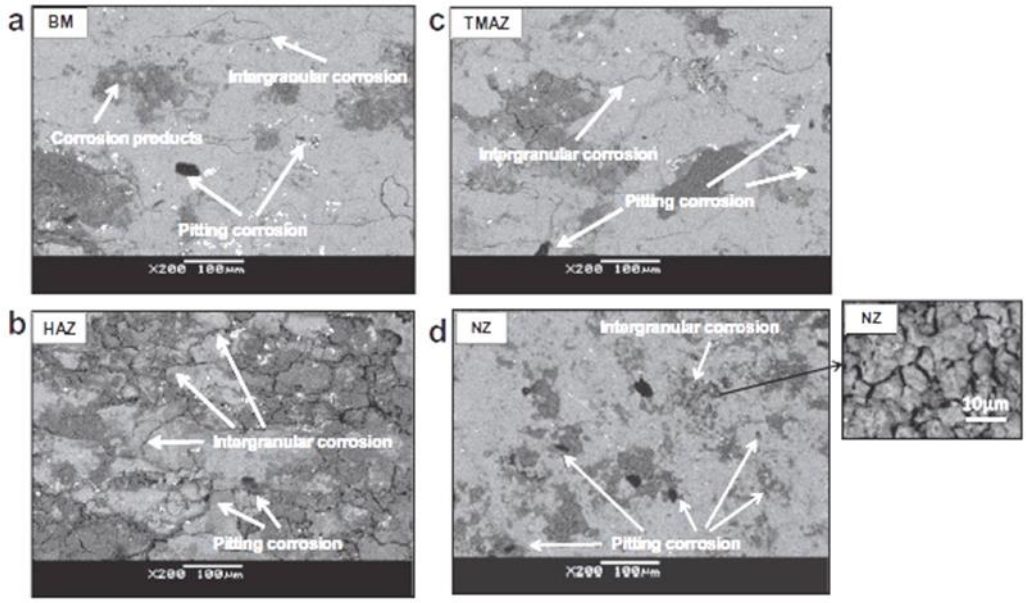

Figure 2.34: Pitting and intergranular attack of a) Base metal. b) HAZ. c) TMAZ. d) Nugget [70].

E. Bousquet et al. continued their analysis by identifying the difference of about 75mV between the base material and the weld bead (Figure 2.35).

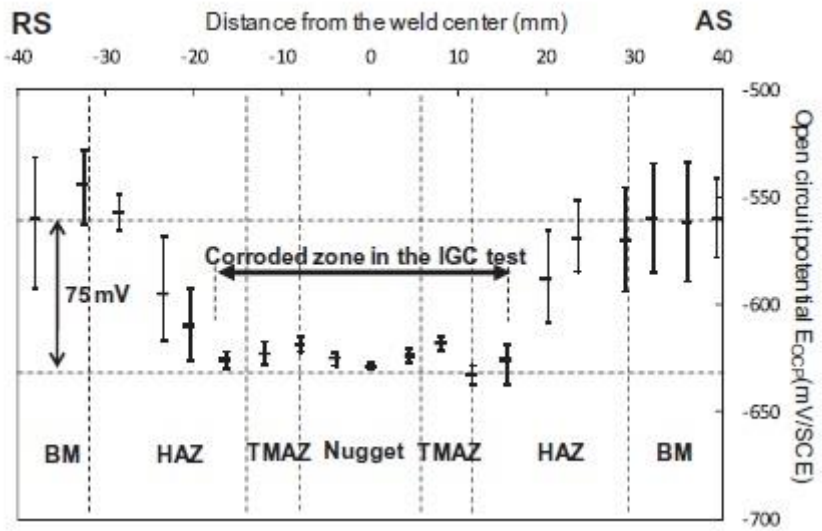

Figure 2.35: Local corrosion potential measurements [70].

M. Jariyaboon et al. studied the corrosion behavior of an AA2024-T351 as the process parameters vary [56]. The authors identified the location of the anodic and cathodic areas within the specimens (Figure 2.36).

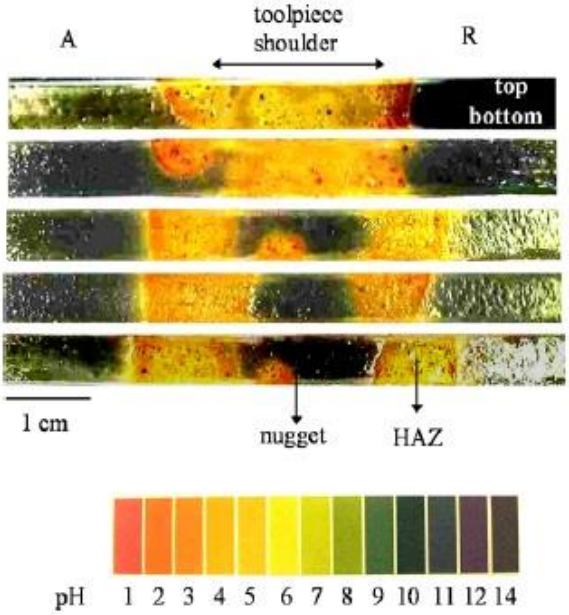

Sample	rpm	mm/min
FSW *SF*	215	154
FSW *SS*	215	75
FSW *MM*	350	95
FSW *FF*	468	154
FSW *FS*	468	75

Figure 2.36: Visualization test using gel on the cross section (A) advancing side and (R) retreating side [56].

They highlighted that the behavior of the weld was strictly dependent on the process parameters. For low rotation speeds, the anodic area was localized at the nugget region, continuously extending into the HAZs. For high rotational speeds, corrosion was mainly localized in the HAZ, while the nugget acts as a cathode.

The width of the anodically active region depends on both the rotational speed and the feed rate. At a fixed rotational speed, an increase in the feed rate leads to a decrease in the width of the anode area. At a given feed rate, a rise in the rotational speed increases the width of the anode area.

Subsequently, the authors performed immersion tests in 0.1 M NaCl solution for 24 hours. The results enriched the information obtained through gel visualization (Figure 2.37).

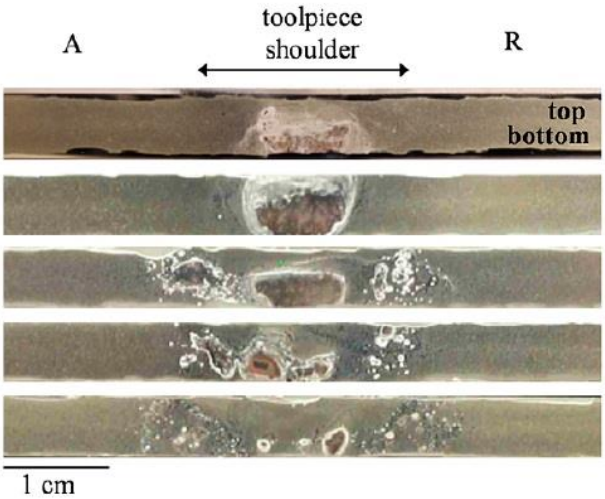

Sample	rpm	mm/min
FSW *SF*	215	154
FSW *SS*	215	75
FSW *MM*	350	95
FSW *FF*	468	154
FSW *FS*	468	75

Figure 2.37: Etching on the cross section of specimens immersed in 0.1M NaCl for 24h. (A) advancing side and (R) retreating side [56].

For low rotational speeds, the attack was manifested as an intergranular attack at the nugget. However, for higher rotational speeds the intergranular attack occurred mainly in the HAZ. In the nugget a cathodic zone was highlighted thanks to the voids around the intermetallic constituents. However, an intergranular attack can also be observed on the bottom of the nugget.

For all the considered process parameters, the base metal showed hollows around the intermetallic particles. This is caused by the cathodic reduction of oxygen which leads to an increase in alkalinity in the solution around the particles, leading to the dissolution of the aluminum matrix (Figure 2.38).

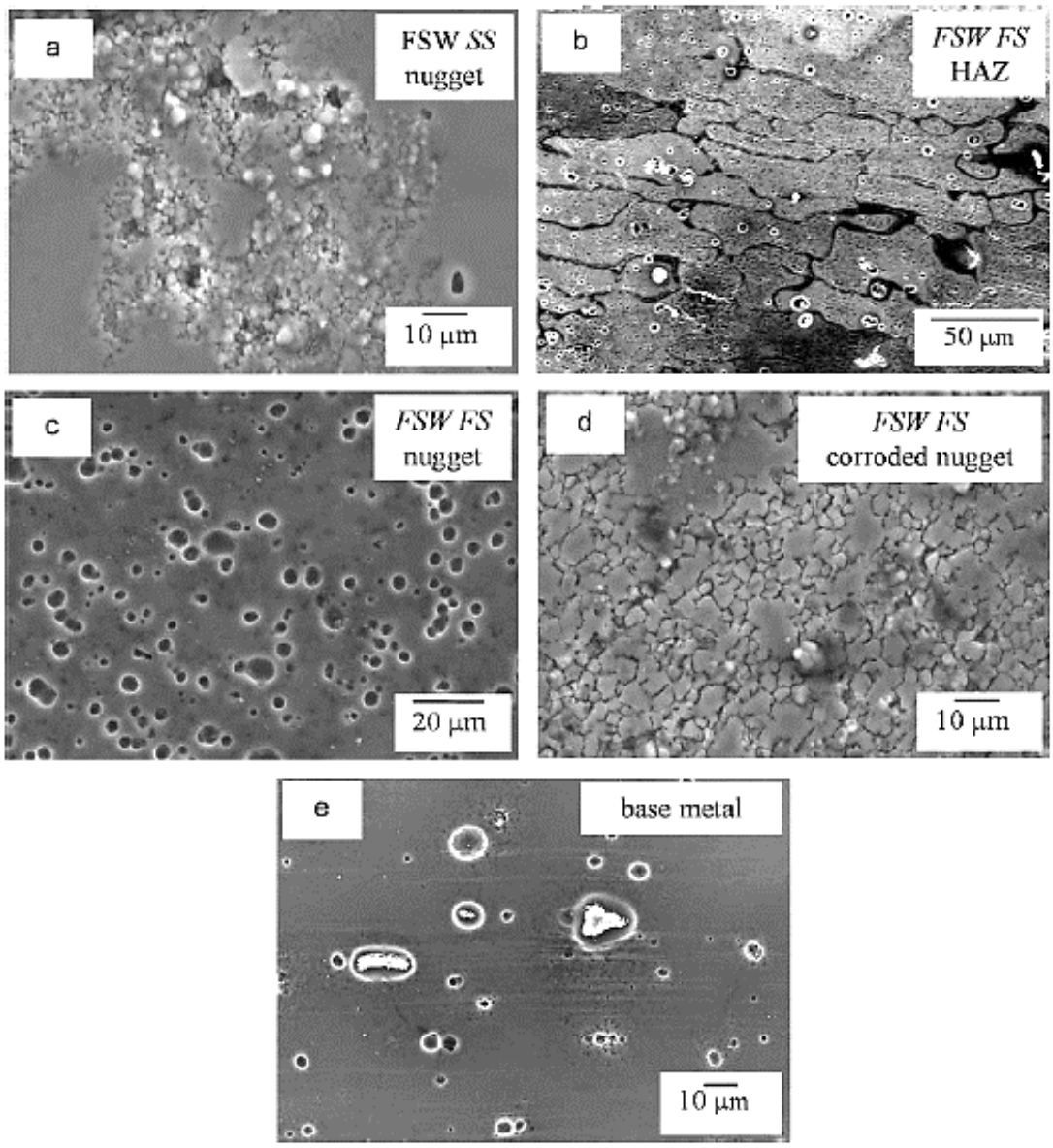

Figure 2.38: SEM images of the corrosion morphology on sections immersed in 0.1M NaCl for 24 hours and subsequent treatment with HNO3 for 30 seconds [56].

Particular attention has also to be paid to stress-corrosion cracking (SCC) due to the well-known susceptibility of the copper-aluminum alloys. As already mentioned, several literature works deal with the corrosion behavior of friction stir welded joints, but the effects on stress corrosion cracking are not yet completely understood. The SCC susceptibility of FSWed AA2024-T4 increased with feed rate due to the increase of the second phase particle size. C. S. Paglia et al. reported a similar SCC behavior for joint and base metal of FSWed AA2219-T87 through slow strain rate tests (SSR) [71].

W. Wang et al. reported SCC insurgence on FSWed AA2024-T3 in the interface nugget/TMAZ in 3.5 wt.% NaCl solution. The stress corrosion cracks nucleated by pitting. The SCC susceptibility of the FSWed joints increased with increasing travel speed, owing to the increase of the size of second phase particles. Also a SCC mechanism controlled by the metal anodic dissolution at the open circuit potential and hydrogen accelerated metal embrittlement in the active zones was suggested [72].

Bocchi et al. studied the corrosion potential and the corrosion morphology of FSWed AA2024 as a function of different rotational speed and feed rate with and without the application of a load equal to the 80% of the base metal UTS. The tests were conducted in 35 g/L sodium chloride solution (Figure 2.39 and Figure 2.40) [57].

In general, the corrosion of AA2024 initiates at micrometric second phases: the corrosion potential distribution is linked to the presence of sub-micrometric precipitate. At the nugget, copper-rich precipitates at grain boundaries and free precipitates zones inside the grain can be noticed. The free precipitate zones are less noble than the base material, unaffected by the welding process. The precipitation of copper-rich second phases produces the depletion of copper in the aluminum matrix and the corrosion potential decreases. In addition, it is well known that copper- and iron-rich phases are more efficient cathodes, which promote a local increase of pH and passive film destabilization occurs [57].

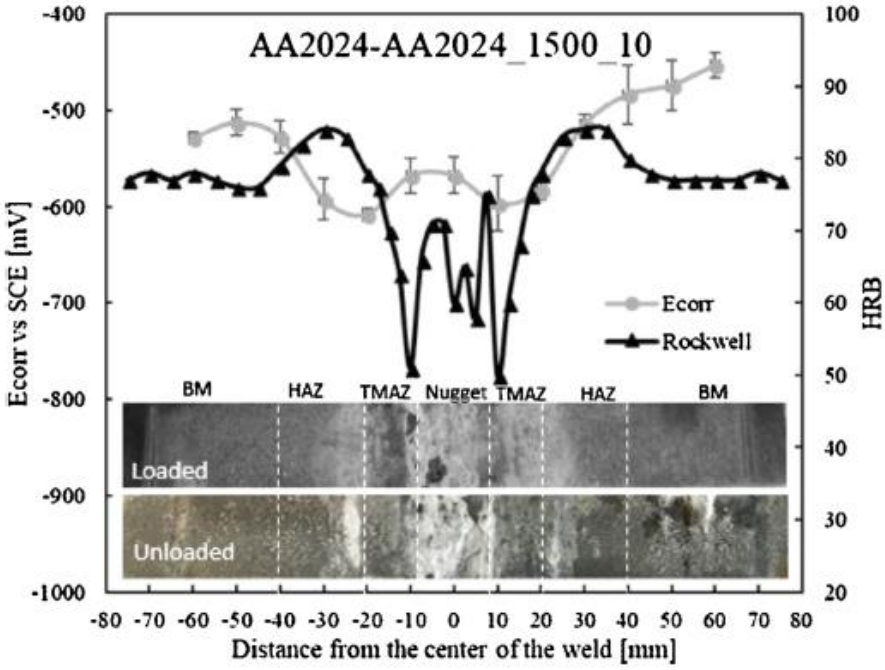

Figure 2.39: Profile of local corrosion potential for the AA2024 unloaded specimen welded with S=1500 rpm and f=10 mm/min [57].

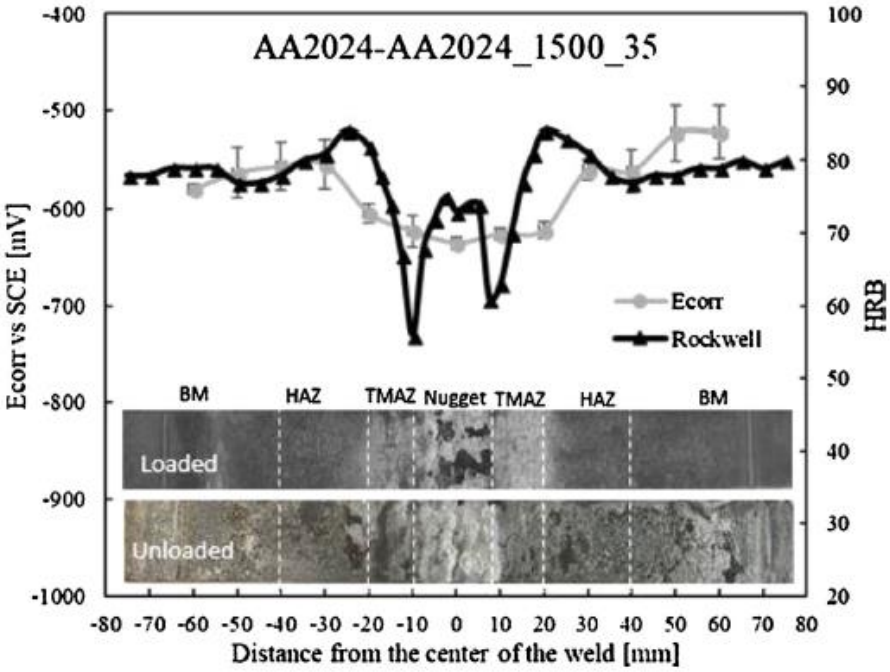

Figure 2.40: Profile of local corrosion potential for the AA2024 unloaded specimen welded with S=1500 rpm and f=35 mm/min [57].

The metallographic section of the FSWed AA2024 showed an intense intergranular attack on the loaded specimens, at the nugget, growing perpendicularly to the direction of load application, both on the tensioned and compressed sides.

This attack was not present on the unloaded joints (Figure 2.41). It is possible to assert that the presence of intergranular attack in FSWed Al-Cu alloy is due to the precipitation of Cu-rich intermetallic particles at grain boundaries in the nugget (Figure 2.42), which results in the formation of anodically-active Cu-depleted regions adjacent to the boundaries [57].

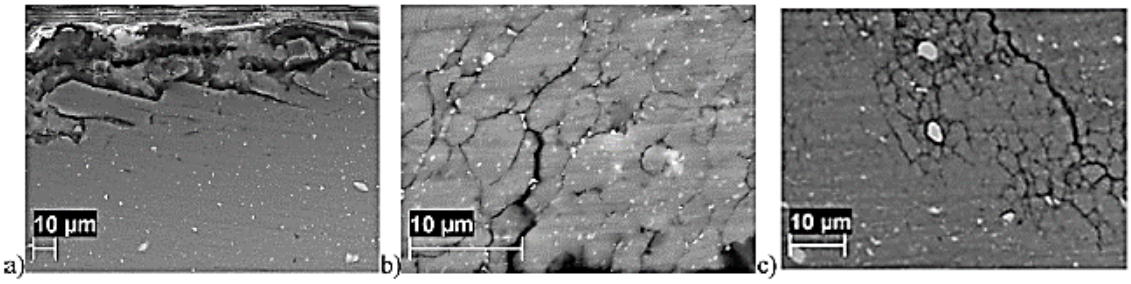

Figure 2.41: Metallographic section of unloaded (a) and loaded (b–c) AA2024 joint after 1400 h of immersion in aerated 0.6M NaCl solution (a and b specimen welded with S=1000 rpm and f=10 mm/min, c specimen welded with S=1500 rpm and f=10 mm/min) [57].

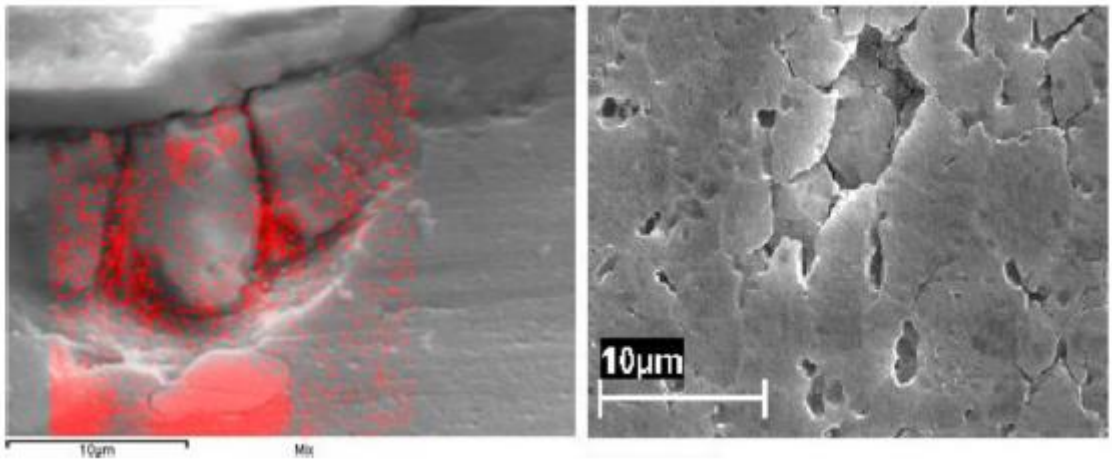

Figure 2.42: Chemical analysis and SEM image of the precipitates in the AA2024 nugget welded with S=1000 rpm and f=10 mm/min (red dots underline the presence of copper) [57].

AA7075

In literature, the behavior of this alloy to intergranular corrosion and pitting have been studied.

- *Intergranular corrosion*

Localized corrosion susceptibility of FSWed AA7075 was investigated by J.B. Lumsden et al. and it was found to be extremely localized in the HAZ and in the outer edges of the TMAZ [73].

J. B. Lumsden et al. also highlighted that, by increasing the exposure period, the intergranular attack became more severe in the region from which it initially developed. However, an asymmetry of distribution remained. While in the HAZ the attack was more evident, in the TMAZ the attack was distributed unevenly, thus revealing a microstructural inhomogeneity and/or an inhomogeneity of the precipitates morphology (Figure 2.43). In fact, despite being lower than the melting point, the reached temperature is in any case high enough to influence the morphology of the hardening precipitates. Local nucleation and the growth of precipitates are functions of the temperature which depends on the distance from the nugget [73].

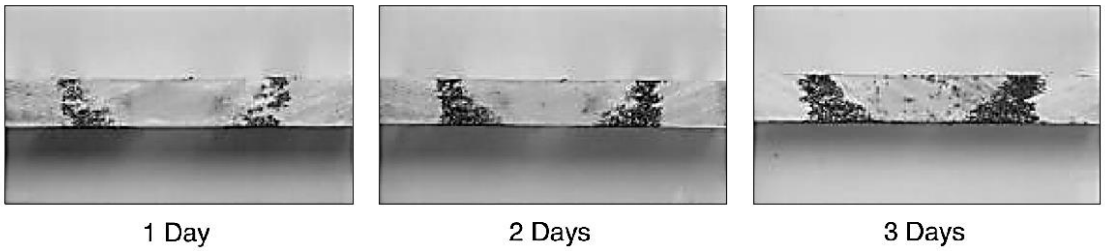

Figure 2.43: Etching on an AA7075-T651 immersed in a solution formed by 4M NaCl, 0.5M KNO_3, 0.1M HNO3 diluted to 10% [73].

- *Pitting*

For the analysis of pitting corrosion, J.J. Pang et al. focused their study on polarization curves for the base material, the corrosion zone and the nugget [64].

For the base material, the curve had two pitting potentials, while for all the other areas there was only one.

The corroded zone had the least pitting potential, followed by the nugget. Both pitting potentials of the base material were greater than those obtained in the other areas (Figure 2.44) [73].

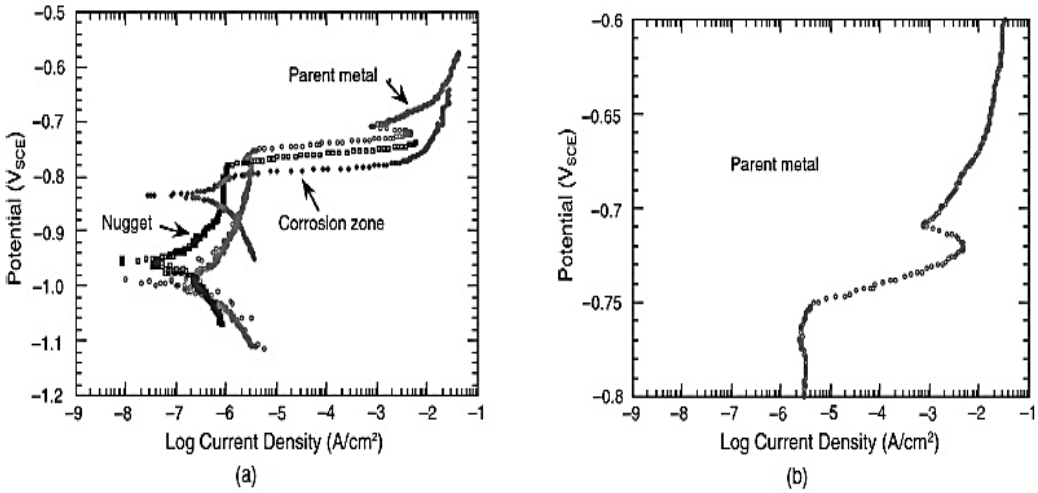

Figure 2.44: Potentiodynamic polarization curves for FSW AA7075-T651 in 0.5M NaCl: in (a) base metal behavior, corrosion zone, nugget. In (b) base metal in the region of the pitting potential [73].

According to J.J Pang et al., the density of the pits was related to the number of Al_7Cu_2Fe precipitates present on the surface. The authors also observed that, near the pits, there were particles rich in copper without the presence of aluminum. These particles were of equal size to the initial ones Al_7Cu_2Fe, thus suggesting that they originated from a re-deposition process.

M. Navaser et al. investigated the effects of rotational speed on the susceptibility to pitting and intergranular corrosion of an AA7075 [66]. By increasing the rotational speed, M. Navaser et al. noted an increase in the susceptibility to pitting of the joint while the extent of intergranular attack decreased (Figure 2.45 and Figure 2.46).

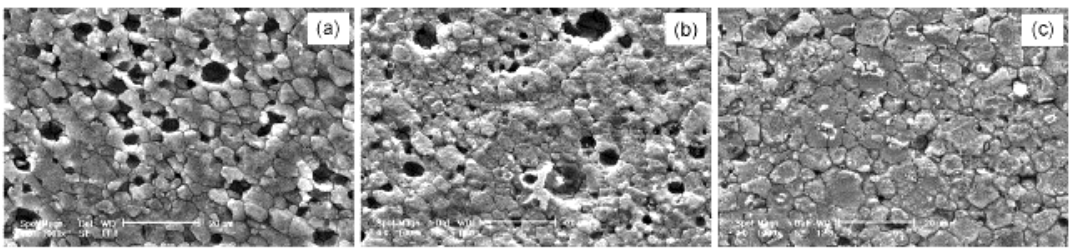

Figure 2.45: Intergranular attack at different rotational speeds: a) 630 rpm. b) 1000 rpm. c) 1600 rpm [66].

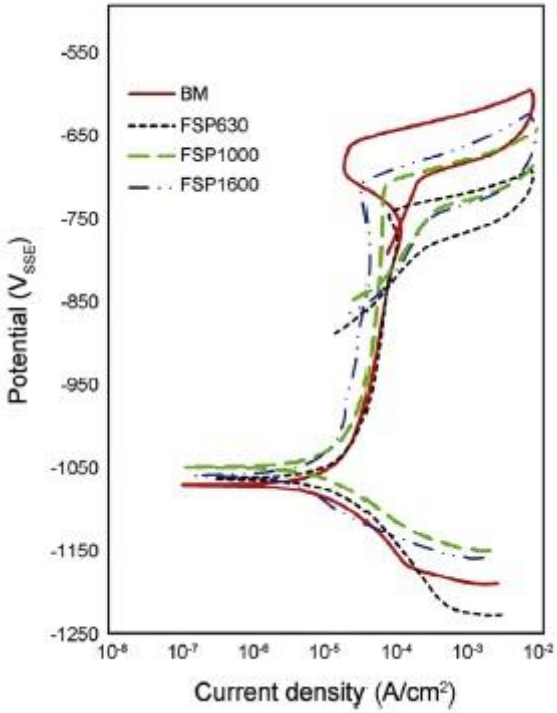

Figure 2.46: Polarization curve at different rotational speed [66].

M. Navaser et al. discovered that, regardless of the process parameters, the HAZs had a greater susceptibility than both the base material and the thermo-mechanically affected zone.

In addition to pitting and intergarnular corrosion, a considerable importance for the understanding of the corrosion behavior of the AA7075 is aimed at the SCC (stress-corrosion cracking) susceptibility, since the resistance of the alloy is significantly affected by the presence of Zn and Mg [74, 75].

The corrosion behavior of such alloys is strictly related to their temper treatment. Several authors confirmed that the 7XXX alloy exhibits SCC susceptibility in peak-aged conditions (T6 temper). However, over-ageing (T7) or retrogression and re-ageing (RRA) treatments are not critical compared to SCC [76, 77].

Bocchi et al. studied the corrosion potential and the corrosion morphology of FSWed AA7075 as a function of different rotational speed and feed rate with and without the application of a load equal to the 80% of the base metal UTS. The tests were conducted in 35 g/L sodium chloride solution (Figure 2.47 and Figure 2.48) [57].

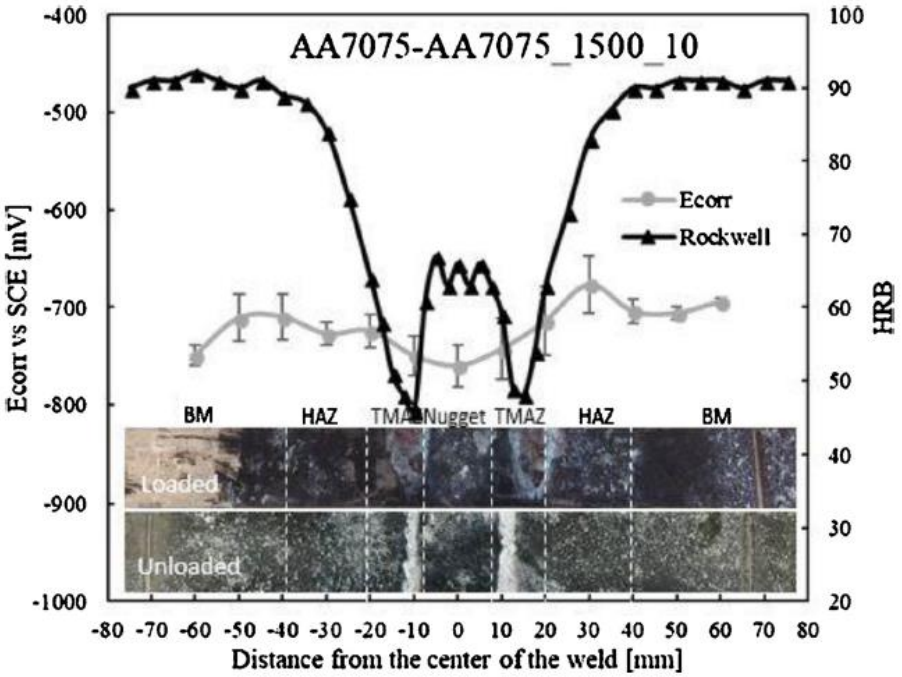

Figure 2.47: Profile of local corrosion potential for the AA7075 unloaded specimen welded with S=1500 rpm and f=10 mm/min [57].

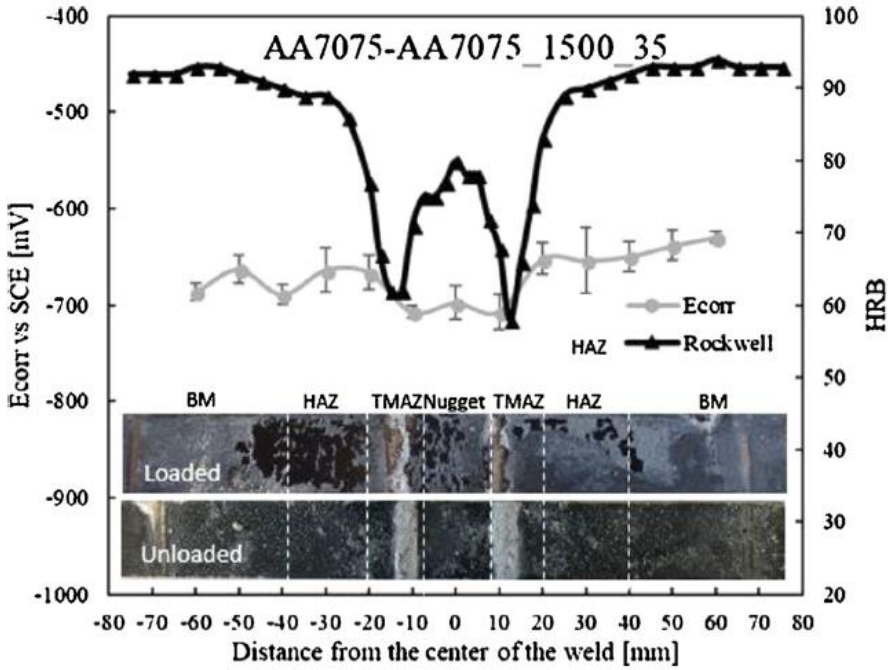

Figure 2.48: Profile of local corrosion potential for the AA7075 unloaded specimen welded with S=1500 rpm and f=35 mm/min [57].

The corrosion potential of the AA7075 did not seem to be influenced neither by the rotational speed nor by the feed rate.

The potential trend varied slightly along the longitudinal direction of the specimen. Moreover, no clear separation between the potentials of base metal, HAZ and nugget was observed.

In the case of AA7075, the precipitates of $MgZn_2$, which are hardening precipitates, are anodic with respect to the matrix. As described by Andreatta et al., these precipitates are particularly reactive and, because of heating, they coalesce to the grain boundary [78]. This situation usually occurs in over-ageing conditions leading to intense intergranular corrosion. These conditions arise mainly in the HAZ, because the grains maintain the original size and orientation; therefore, there is an elongated grain edge in the rolling direction, offering a preferred path to the corrosive attachment. For this reason, the aluminum matrix is fully active in this area.

AA7075 FSWed joints, whatever of the adopted welding parameters, showed a concentrated attack towards the limits of the TMAZ, that propagated becoming exfoliating at the rolling bands of the sheet (Figure 2.49). Contrary to the results observed for the AA2024, the nugget was not corroded. The attack was more affected by the microstructure than by the applied stress and grew in the direction of the precipitates coarsened by the thermal action of the welding [57].

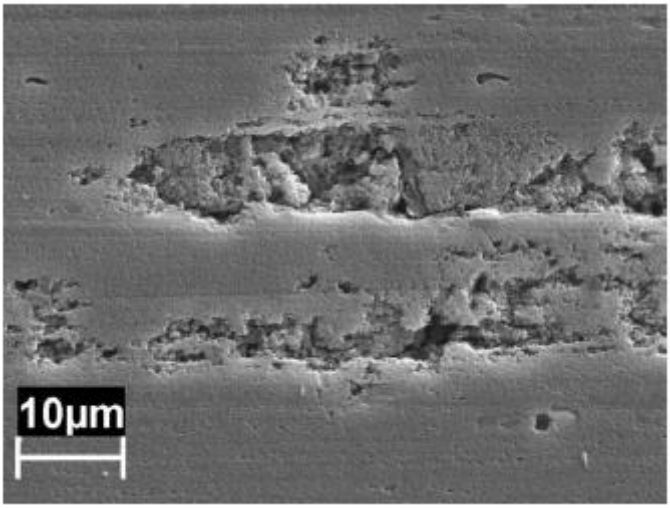

Figure 2.49: Corrosion morphology of an AA7075 joint welded with S=1000 rpm and f=10 mm/min [57].

2.3. Friction Stir Welding cooling system

The heat generated in the FSW process due to the friction between the pieces to be welded and the tool is considerably lower than that developed during a traditional welding technique. Nevertheless, the reached temperatures are sufficiently high to cause the softening problem in the welded joints, even more marked in the precipitation-hardening aluminum alloys.

The softening is due to the dissolution and subsequent enlargement of the hardening precipitates with a consequent reduction of the mechanical properties of the joints. To eliminate or significantly reduce this effect of the process, it is necessary to reduce the heat input, to obtain robust joints with resistance comparable to the base material [79].

To achieve this purpose, post-welding heat treatments were proposed by various authors. R. Priya et al. studied the effect of post weld heat treatment on the mechanical properties of dissimilar FSWed joint of AA2219 and AA6061, finding that a post weld solution treatment at 520 ºC followed by ageing at 165 ºC for 18 h resulted in significant improvement in hardness across the whole weldment [80].

The results obtained by B. Safarbali showed that both AA2024-T6 and AA7075-T6 post-weld heat treatment procedures substantially improved the mechanical strength of the welded joint in comparison with the as-welded joint, with higher strength obtained for the AA7075-T6 [81].

Moreover, a T6 post-weld heat treatment performed on a FSWed AA6061 enhanced the mechanical properties of the joints back to its original state, as demonstrated by A. H. Baghdadi et al. [82].

Despite their proven benefits, post-welding heat treatment cannot always be performed on large products. In addition, the execution of a heat treatment after the welding operations significantly increases energy consumption and lengthens the production time. For these reasons, after having correctly chosen the combination of the process parameters, an alternative to post heat treatments to significantly reduce the softening of the joints, it might be the application of an external cooling system [83, 84].

This kind of system leads to the control of the microstructure of the joints during the welding process, limiting the need for post-process heat treatments.

S. Benavides et al. studied the microstructures in FSWed AA2024 joints at room temperature (30 °C) and low temperature (-30 °C), finding that the grain size is considerably smaller in the low-temperature weld [45].

G. Peng et al. studied the behavior of a dissimilar AA5A06-H112 and AA6061-T651 FSWed joint in presence of a forced air-cooling system and their results demonstrated that the forced air-cooling was able to accelerate the cooling process, improving the ultimate tensile strength by 10% compared with the natural cooled joints [84].

P. Upadhyay et al. analyzed an AA7050-T7451 welded with three different cooling systems applied to the FSW process: in laboratory air, with the plates submerged in water and at a temperature of -25 °C [85]. The best mechanical properties in terms of tensile strength and elongation were reached by the submerged welds.

In all these works, the external cooling during the process led to an improvement of the mechanical behavior accentuated depending on the welded alloy, apart from C. Sharma et al. that, studying the effect of the nitrogen and compressed air, on the friction stir welded joints, found that the highest ultimate tensile strength and elongation were obtained under ambient natural cooling rather than water-cooling [86].

Recent works have introduced the Underwater Friction Stir Welding (UFSW) technology [79, 87, 88].

The UFSW consists in a FSW set-up with a cooling system allowing to limit the effect of the heat flow on the characteristics of the material during the processing. The water is used as a coolant to control the temperature profiles and reduce the heat absorbed by the welded joints.

The high heat absorption capacity of the water allows the removal of heat from the HAZ and TMAZ and prevents the precipitates from reaching the solubilization temperature, avoiding the formation of solute clusters, and the coarsening of the grains, allowing to raise the mechanical strength of the crystalline structure of the welded joints [89].

2.3.1. Underwater Friction Stir Welding

The thermal cycle and the peak temperature are two fundamental parameters for controlling the microstructure and mechanical characteristics of the friction stir welded joints. The use of water as a coolant allows to significantly reduce the thermal coefficient of the joints with a consequent limitation of the dissolution of second hardening phases

in the microstructure during the welding process. Furthermore, it allows the variation of the size of the precipitate free zone, with a consequent improvement of the mechanical properties in the TMAZ [89]. As an example of the benefit of the UFSW, Figure 2.50 shows the weight percentage of magnesium at different distances from the weld line for the FSW and UFSW processes in an AA7075-T6. The heat flow, reduced by the water action, only partially allows the achievement of a local solubilization temperature. Consequently, a water-cooled joint consists of a higher density of hardening precipitates $MgZn_2$ [90].

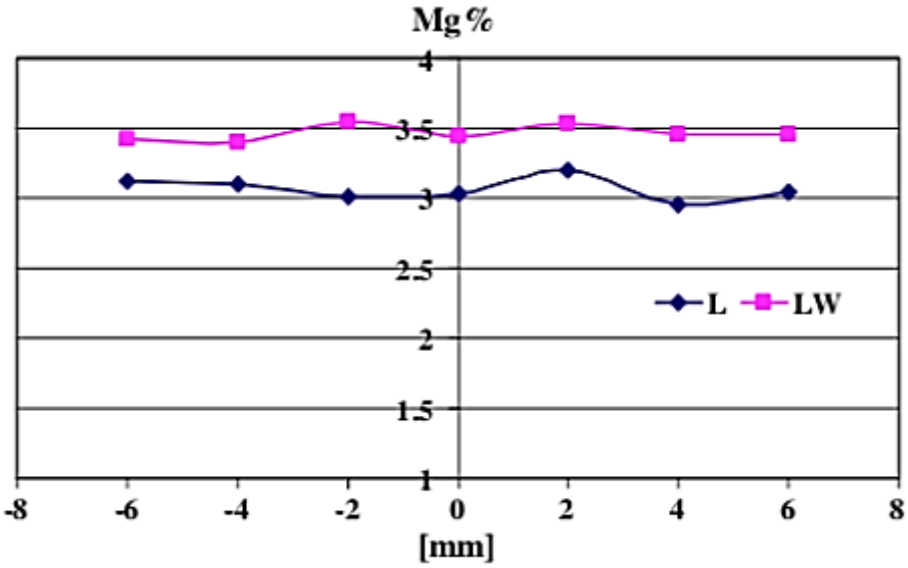

Figure 2.50: Percentage of magnesium in the FSWed AA7075-T6: L indicates the traditional FSW process, the LW the UFSW process [90].

Whang et al. showed that a water-cooling during the processing ensures a clear reduction in temperature, measured with thermocouples inserted in the section of the joints to be welded [91]. In particular, the temperature recorded with an air-cooling system was about 195 °C, while that recorded with a water-cooling system was about 69 °C. For these recordings, the thermocouples were positioned in the advancing side at 13 mm from the welding line.

Figure 2.51 shows the curves of the thermal cycles obtained by measuring a series of temperature values between the points closest to and furthest from the welding line. For the air-cooled joints, the difference in temperature between the advancing side and the

retreating side was evident. On the other hand, this difference in the UFSWed joints was more contained (Figure 2.51c and d) representing the UFSW process [91].

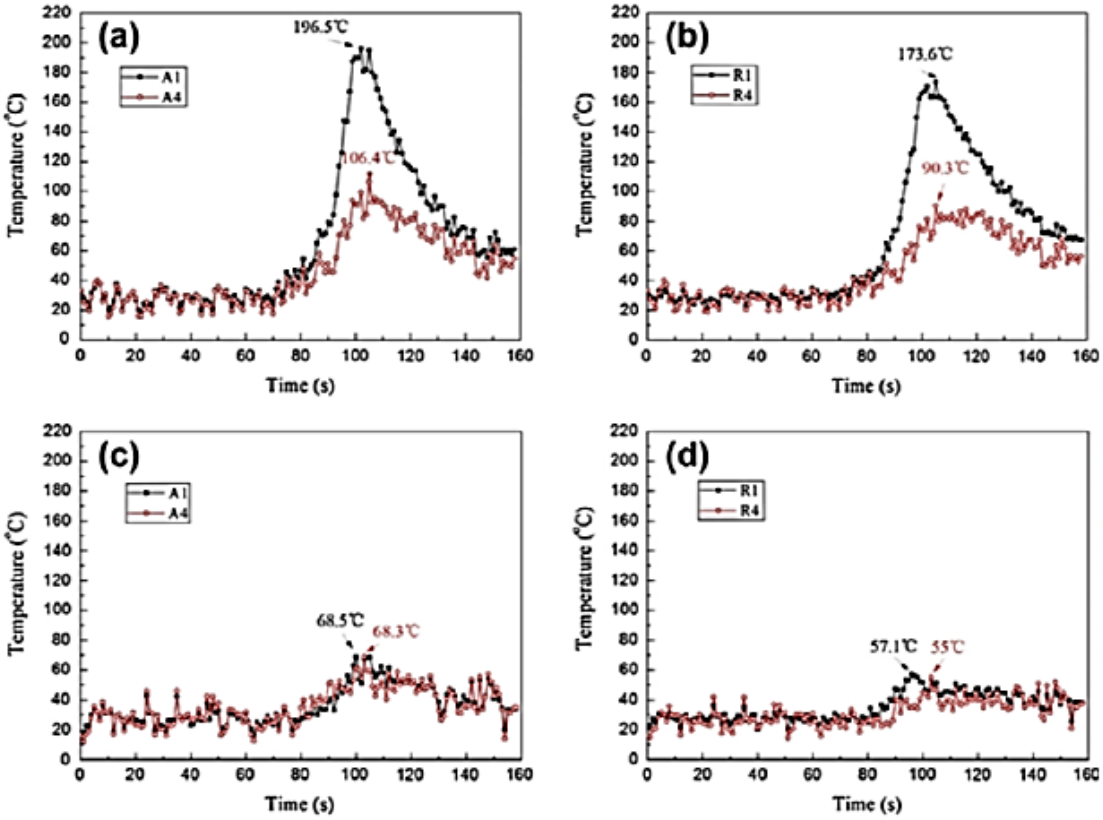

Figure 2.51: Thermal cycle curves measured for FSW advancing side (a) ,FSW retreating side (b), UFSW advancing side (c), UFSW retreating side (d) [91].

In the UFSW process, the advancing side is usually cooled faster. This leads to a better grain refinement and to a more controlled growth of second phases and coarse intermetallics at the nugget. In addition to the microstructure, also the macrostructure of the joint section varies. The typical onion ring structure generated with the FSW is replaced by a V-structure with the UFSW process (Figure 2.52) [87].

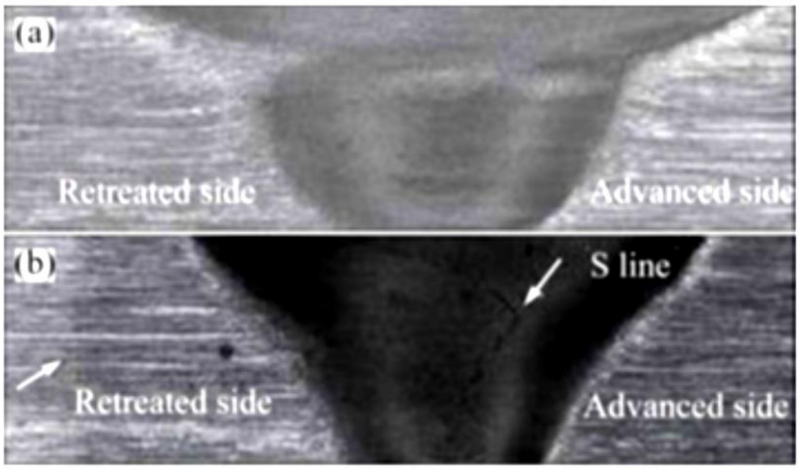

Figure 2.52: Macromorphologies of the welded joint with FSW (a) and UFSW (b) [87].

M. Hosseini and H. Danesh Manesh highlighted the improvement of the mechanical properties of AA1050 water-cooled welded joints, due to smaller grains and second phases in the nugget [92].

The amplitude of the thermo-mechanically affected zone is reduced by the cooler action of the water in the UFSW. In addition, the lower temperature and the high degree of cooling prevents unwanted growth of grains, allowing an improvement of the mechanical performance of the joints [79].

In HAZ, the average grain size is much less affected by the cooling rate of the cooling system, as the average temperature reached in this area (i.e. 250 °C) is not sufficient to trigger the coarsening phenomenon of the grains. On the contrary, the water-cooling system, due to the decrease in temperature, allows to reduce the average size of the precipitates and the width of the free precipitated zones. Furthermore, less dissolution of precipitates in the HAZ in the UFSW process allows to obtain denser areas of precipitates, ensuring an increase in mechanical properties [93].

In the work of F. Heirani et al., the formation of the HAZ was not noted in the section of the UFSWed joints (Figure 2.53). This was attributable to the heat absorbed by the HAZ, that is insufficient for the formation and for the subsequent growth of the grains [88].

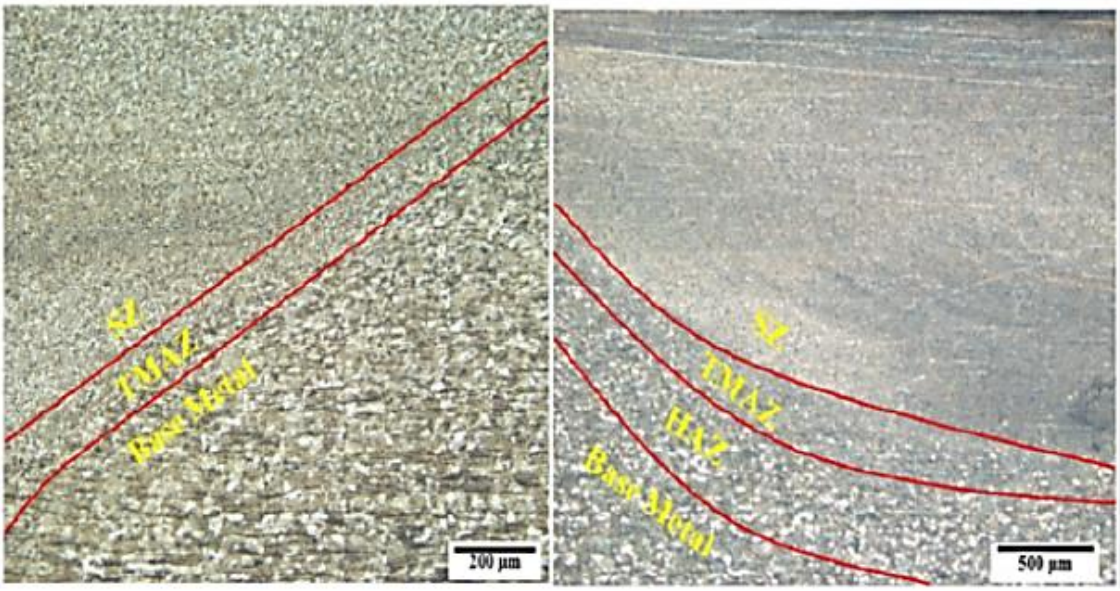

Figure 2.53: Microstructure of the section of UFSWed joint (left) and FSWed joint (right) [88].

Depending on the cooling condition, different kind of typical defects could be detected in the welded joints.

As evidenced by F. Rui-Dong, all the other welding processes being equal, the peak temperature in the nugget is proportional to the rotational speed, while the cooling rate and the time of exposure of the joint to high temperatures is proportional to the feed rate [87]. Therefore, in order to have a close control on the microstructure obtainable from the welding process, it is necessary to consider also to the process parameters in addition to external cooling.

Hence, by combining the cooling action of water and low rotational speed, the formation of grooves occurs, visible respectively on the surface and in the section of the welded joints (Figure 2.54). These kind of defect mainly originate from the inadequate flow of material generated by the roto-translation action of the tool [94].

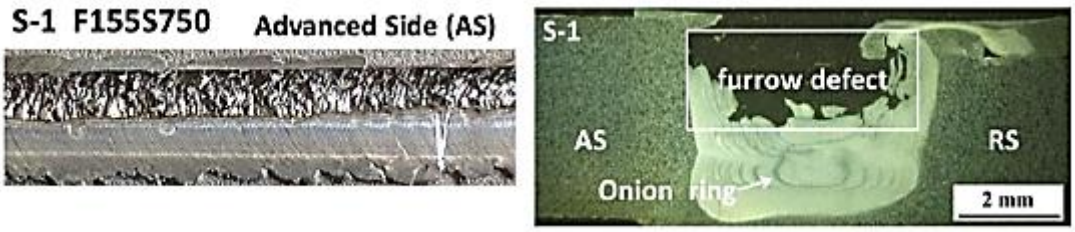

Figure 2.54: Groove defect in an UFSWed AA7055 [94].

By increasing the rotational speed, it is possible to eliminate the groove defect, but the risk of running into tunnel defects in the section of the weld arises (Figure 2.55). The tunnels are originated from the dimensional growth of the micro-voids, since the water is a more effective coolant with respect to the air, slowing down the completion of the welding of the plasticized material.

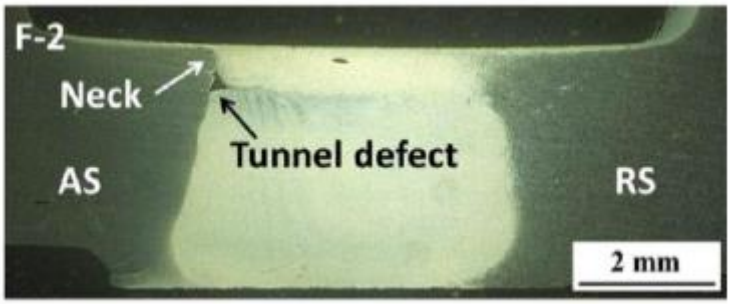

Figure 2.55: Tunnel defect in an UFSWed AA7055 [94].

Despite this, the main benefit in terms of defect elimination was evidenced by Y. Zhao et al. In fact, the authors highlighted the lack of the S-line defect the water-cooled joints [91]. The S-line formation is one of the most frequent defects of the traditional FSWed joints. This kind of defect originates from the breaking and the remixing inside the welding nugget of the aluminum oxide film, caused by the roto-translational movement of the tool. The use of water prevents atmospheric oxidation of the joint during the process and thus the S-line generation.

Figure 2.56: S-line on the section of an AA2024 alloy joint welded with FSW.

Mechanical properties

The tensile strength and ductility of the welded joints are the most affected factors by the presence of a cooling system other than normal air-cooling.

According to Y. Zhao et al., by a water-cooling, the tensile strength of an AA7055 can be increased by more than 10% and its ductility by about 3% compared to the air-cooling case. The reason of this behavior of the UFSWed joints is to be found in the metastable hardening phases precipitation during the welding process. With a water-cooling system, the only hardening phase present within the aluminum matrix is the $MgZn_2$, within the air-cooled joints, a metastable phase $MgCu_2$ is added. This last phase is generated by the exchange reaction of copper with the hardening phase $MgZn_2$. In fact, when the heat generated during processing is very high, copper has an active behavior and induces magnesium to bind preferentially with it than with zinc. Therefore, as already mentioned, with the traditional FSW process the solubility of zinc in the aluminum matrix is reduced and the zinc tends to dissolve, causing a reduction in the percentage of hardening phase present in alloy [91].

The benefit of a water-cooling system in terms of mechanical properties was also confirmed for an AA2219-T62 alloy by W. F. Xu et al. [93]. In particular, the top surface of welded joints exhibited the best values of UTS but the worst values in terms of ductility; the opposite condition occurred in the area in contact with the support plate. However, the main result was that, in comparison with air-cooling, water-cooling during FSW improves both the strength and the ductility.

The same properties were also evidenced for a non-heat-treatable alloy by F. Heirani et al.: the UFSWed AA5083 joints showed higher tensile strength and ductility values with respect to the air-cooled ones (in Figure 2.57 the S1 curve indicates the UFSW results and the S5 curve the FSW values) [88].

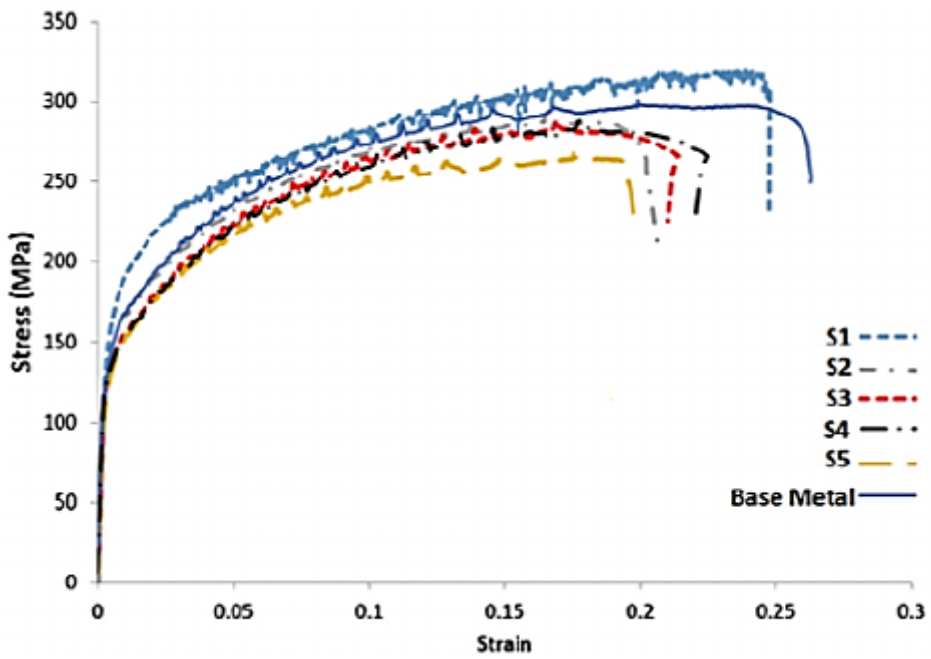

Figure 2.57: Stress-strain curves of AA5083 joints welded with FSW (S5) and with UFSW (S1) [93].

Z. Zhang et al. focused on identifying the area with less resistance in the UFSWed joint [95]. In the heat treatment alloys, the area with the lowest mechanical resistance was the TMAZ, due to the significant dissolution of the hardening elements and to the enlargement of the grains during the process precipitation. This area is called low hardness zone (LHZ), a key-parameter to the mechanical characterization of welded joints. The effect of cooling on these zones depends on the type of alloy taken into consideration: T. W. Nelson et al. demonstrated a marked improvement (10%) in terms of tensile strength for an AA7075-T7351; while, considering an AA2195-T8 alloy, the increase did not exceed 3%, using the same working condition [96].

Regarding the peak temperatures, they vary according to the considered alloy: for an AA2014-T6 was about 340-360 °C, for a AA7075-T6 was 300 °C and for a AA7050-T6 280 °C. The result of these differences in peak temperatures was the change in positioning of the LHZ for the different heat treatment alloys.

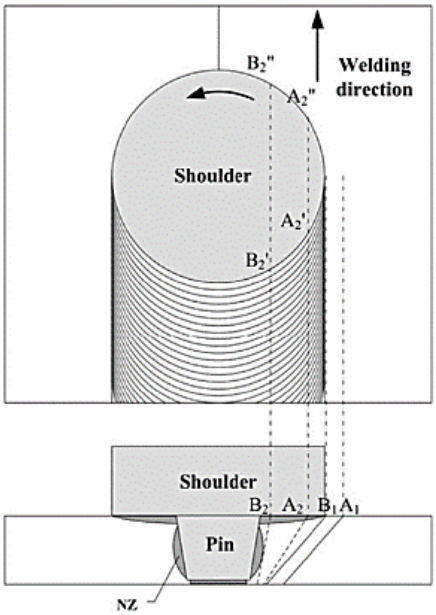

Figure 2.58: Schematic position of the low hardness zones relating to the tool [95].

For AA7050 and AA7075 air-cooled FSWed joints, the LHZ was positioned outside the tool shoulder diameter (graphically represented by point A_1 in Figure 2.58). The action of water exerted a strong cooling on the LHZ, moving it from position A_1 to A_2. This shift of the LHZ indicated that the effect of water significantly reduced the exposure of LHZ to higher temperatures.

Considering the AA2014, the water-cooling system caused the displacement of the low hardness zone from a position B_1, in contact with the shoulder, to the position B_2, near to the pin. But, in this case, the best conductivity of the water was not able to deeply influence the mechanical resistance of the joints. Hence, the conclusion of the authors was that the water-cooling for the 2XXX series did not significantly improve the mechanical resistance values in LHZ, but it caused the movement of the LHZ towards the weld seam.

Finally, a water-cooling system limits the negative effects of the FSW process on residual stress (RSS) of the welded joints. In fact, it is well-known that the RSS is directly related to the cycle thermal, and it causes several problems on the mechanical properties of post weld joints.

H. Papahn et al. showed that the use of water as a coolant can reduce the longitudinal RSS of 80% compared to a normal air-cooled welding system [97].

Y. Zhao et al. highlighted the development of stress compression during UFSW, which guaranteed a better resistance to fatigue in the welded area (Figure 2.59) [91].

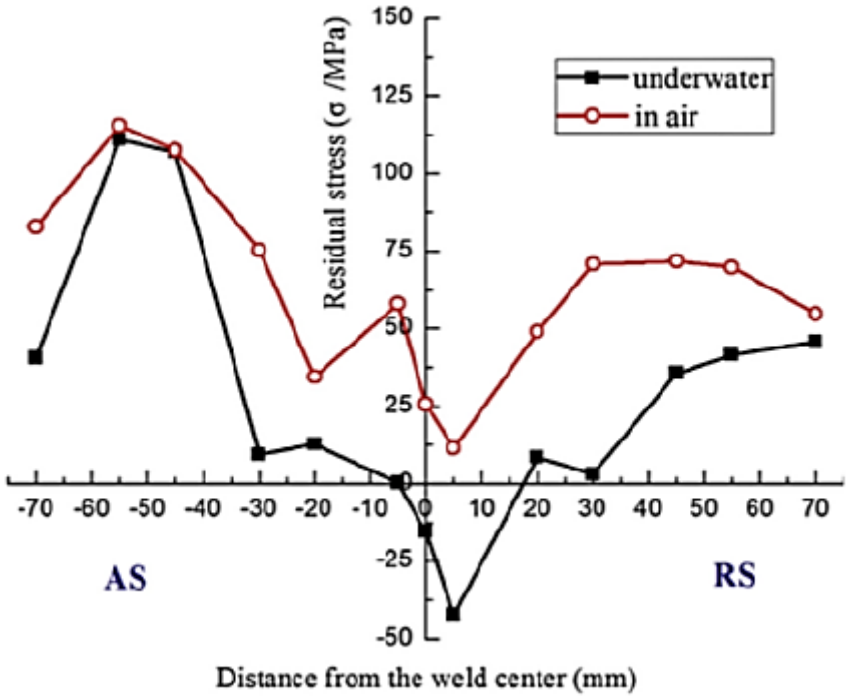

Figure 2.59: .Distribution of residual stress of the plate welded in different media [91].

Hardness profile

The cooling effect of the water is also evident for the recorded micro-hardness values in several studies for different aluminum alloys. For heat treatable alloys, it was observed that, generally, the minimum hardness zone was in the HAZ or TMAZ in the advancing side for FSW. On the contrary, for UFSWed joints the minimum hardness zone was shifted towards the nugget both in the advancing and in the retreating side and the softened region was more contained, guaranteeing an increase in hardness values [79, 87, 91, 94].

In the studies conducted by Y. Zhao et al., the benefit in terms of hardness guaranteed by a water-cooling system was evident [91]. The typical W-pattern distribution of the hardness values along the surface of the AA7055 specimens was less marked and was replaced by a flat pattern at the weld bead, where the typical minimum hardness points at the HAZ were absent.

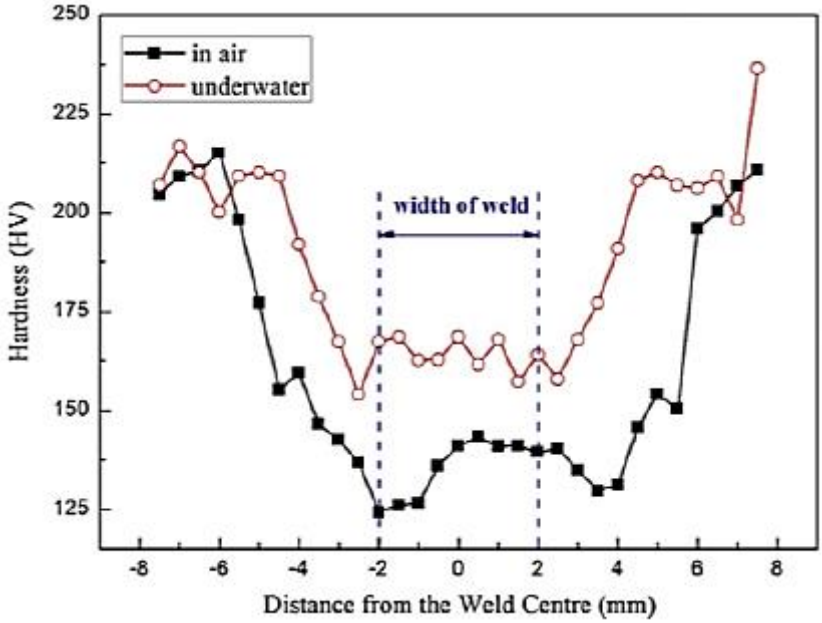

Figure 2.60: Distribution of micro-hardness for FSWed and UFSWed AA7055 [91].

Less noticeable results were observable in an AA2219. The W-shaped trend of the hardness distribution was evident with both the cooling systems. With a UFSW process, the softened area significantly decreased, positioning at the interface between TMAZ and nugget, an area with a greater number of second hardening phases and a greater number of dislocations [93].

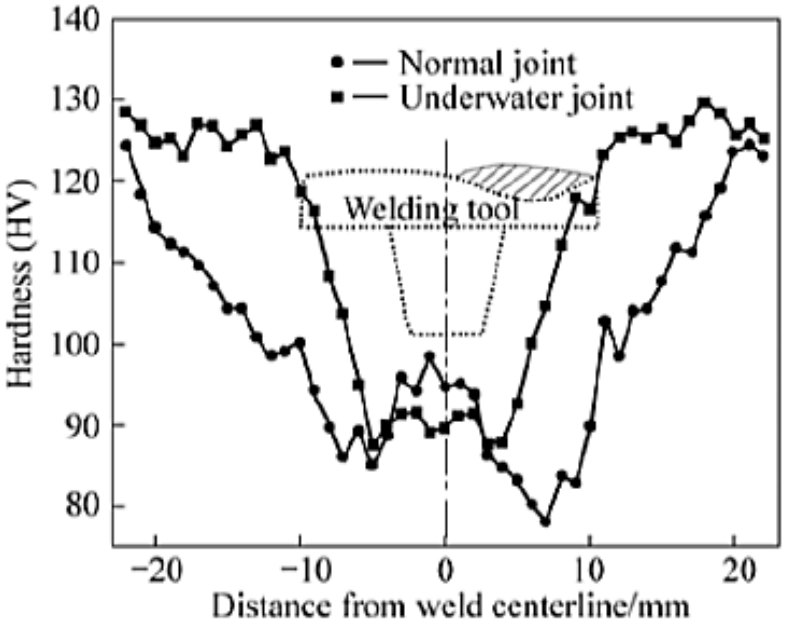

Figure 2.61: Distribution of micro-hardnesses of a FSWed and UFSWed AA2219 joints [93].

The non-heat-treatable alloys showed a different trend in the distribution of the welded joints hardness values. With both cooling systems there was no softened region and the hardness of the tested specimens grew closer to the weld bead. UFSW guaranteed higher hardness values than FSW welding [88, 92].

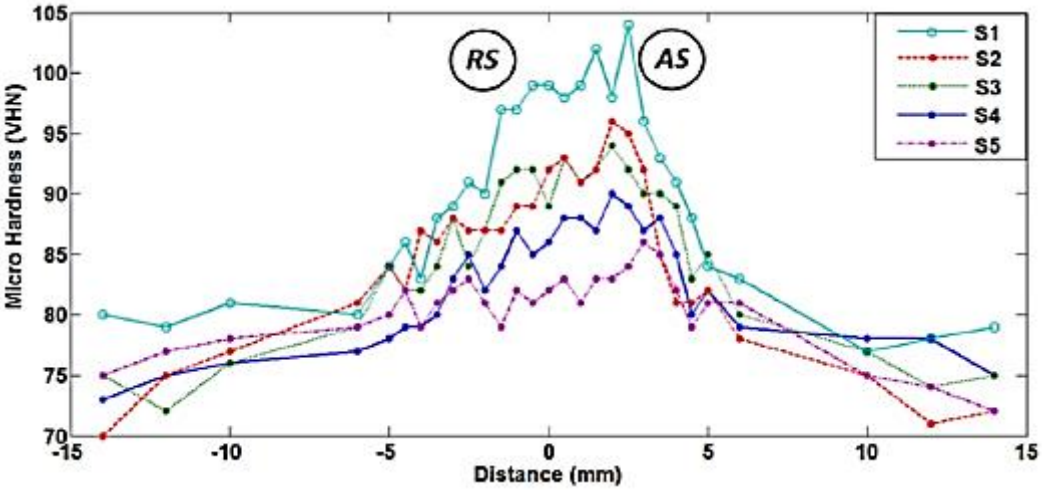

Figure 2.62: Distribution of micro-hardness of a FSWed (S5) and UFSW (S1) AA5083 joint [88].

UFSW possible defects

Despite the benefits on the characteristics of FSWed joints, underwater friction stir welding is perhaps an uncertain process to perform. M. A. Wahid et al. demonstrated that in UFSWed joint more voids affecting the mechanical behavior of the welded pieces were found [89]. This is probably due to the presence of some particles of water trapped in the joint and their evaporation for the temperatures subsequently reached during the process. Indeed, the evaporation, due to the high temperature reached during the process, may results in voids and a consequent reduction of mechanical properties. Another problem strictly related to the under-water process is that the plasticized material is cooled too quickly before completely filling the weld, leaving the already mentioned tunnel defect.

2.4. Finite Element Model

Since FSW is a quite recent process, the development of models and simulation techniques is useful for better understanding its physics [98–100]. In the last decade, some simulative models for the prevision of the FSW process behavior were proposed. These models were based on different formulations and approaches and they were implemented on some well-known commercial codes. For example, Z. Zhang and H. W. Zhang set up a model using the commercial code ABAQUS and an Arbitrary Lagrangian-Eulerian (ALE) formulation with adaptive mesh [101]. This work was focused on the development of a fully coupled thermo-mechanical model of FSW process and the results suggested that the material deformation and the temperature field had a good relationship with the microstructural evolution. C. M. Chen and R. Kovacevic used the commercial finite element package ANSYS to simulate the entire welding process of an AA6061-T6, calculating the thermal impact and the evolution of the stresses in the weld by considering the mechanical effect of the tool [100]. An ANSYS 3D model was used also by N. Contuzzi et al. to understand the influence of the backing plate and the clamping system on the evolution of the thermal flux in an FSWed AA5754-H111 joint [102].

Y. J. Chao et al. studied a steady-state heat transfer analysis for the tool using the commercial finite element analysis code ABAQUS [103]. The model evidenced the high heat efficiency of the FSW process because it has been demonstrated that only about 5% of the heat generated by the friction process flows to the tool and the rest flows to the workpiece. G. Buffa et al., using the FEM commercial package DEFORM, developed a 3D Lagrangian model to predict the non-symmetric nature of the FSW process and the relationships between the tool forces and the variation in the process parameters [104]. The main result was that, although the effective strain distribution was non-symmetric about the welded line, the temperature profile was almost symmetric in the weld zone. Also G. D'Urso et al. used the commercial code DEFORM 3D to analyze how the thermal effects due to the different process parameters may influence the mechanical properties of the joints [105]. The developed method showed a partial matching with the results of a corresponding experimental campaign conducted on a FSWed AA6060 joint.

P. A. Colegrove et al. described a numerical model created in FLUENT for predicting the heat generation in friction stir welding from the material and process characteristics (e.g. process parameters, hot deformation and thermal properties, and the tool and plate

dimensions) in aerospace AA2024, AA6013 and AA7449 [106]. The model was used to demonstrate the sensitivity to key parameters such as contact radius under the shoulder, and the choice of stick or slip conditions.

However, the application of the various FE models does not allow an immediate analysis of the mechanical characteristics of the simulated pieces, except for the stresses generated by the process itself. To fill this gap, it is possible to resort to other types of predictive tools, among which the Artificial Neural Network (ANN) algorithm has stood out in recent years.

2.5. Artificial Neural network

Since the complexity of the process, due to the large number of variables involved, it is difficult to accurately predict and optimize both the process performances and the weld quality considering together the welded materials and the process parameters.

Despite the solution of optimizing the process performance by considering independently each process parameter involved in the FSW process is the simplest method, this approach could restrict the industrial applications of the technology, owing to its very limited validity.

To overcome this limit, several techniques such as multi-objective optimization techniques, Artificial Neural Network (ANN) and regression analysis have recently received great attention, above all by combining different optimization algorithms [107–109].

ANNs are defined as “efficient data-driven modelling tools widely used for nonlinear systems dynamic modelling and identification, due to their universal approximation capabilities and flexible structure that allow to capture complex nonlinear behaviors” [110].

Several researchers developed ANN models to study the effect of welding parameters on the microstructure, thermal, mechanical and metallurgical properties of friction stir welded joints under various conditions [111, 112].

Some authors focused their analysis considering only feed rate and rotational speed as process variables.

M. H. Shojaeefard et al. developed an ANN model to correlate the rotational speed and feed rate to the ultimate tensile stress and the hardness of friction stir welded AA7075-

AA5083 [113]. The application of ANN was integrated with the application of the multi-objective Particle Swarm Optimization (PSO) to obtain the Pareto-optimal set.

An ANN model was used by Sonmez et al. to study the link between the feed rate and rotational speed with the UTS of FSWed AA7075 joints [114]. Dehabadi et al. applied an artificial neural network to predict Vickers micro-hardness of FSWed AA6061 sheets, finding a good correlation between the predicted and experimental results [115].

In a similar study, the tensile strength of AA6061 welded joints was correlated to the number of revolutions per minute of the tool and the feed rate [116].

Other authors also considered the axial force as the input of the ANN model. A. A. Farghaly et al. considered the combined influence of rotational speed, feed rate and the axial force on the tensile strength of AA6061 using an ANN trained and tested using the results of an experimental campaign [117]. In the same way, ANN was used for AA7039 joints [118].

Other researchers used neural networks increasing the number of outputs considered in terms of weld characteristics. For example, H. Okuyucu et al. evaluated the reliability of ANNs in the prediction of the tensile strength, yield strength, elongation and hardness of HAZ of two hot rolled aluminum plates [119]. Correspondingly, other authors considered feed rate and rotational speed as inputs and tensile strength, yield strength, elongation and hardness as outputs in simulating the FSW of several materials (Al1080 [120], AA5754 H111 [121] and AA6063-A319 dissimilar alloys [122]).

R. Ranjith et al. considered also the pin diameter and geometry as inputs whereas the outputs of their modelling were the tensile strength of dissimilar welded joints (AA2014-T651 and AA6063-T651) [123]. M. W. Dewan et al. considered, as the inputs, tool shoulder diameter, feed rate, rotational speed and axial force; UTS, yield strength (YS) and hardness were considered as the output of the model [124]. In the research of E. Maleki, feed rate and rotational speed, axial force, pin and shoulder diameter, as well as the hardness of the tool, were fixed as inputs of the ANNs [125]. YS, UTS, notch-tensile strength and hardness of the welding zone were considered as outputs of neural networks. In all these cited studies, the applied methods showed good reliability and ability in predicting the characteristics of the welds.

Despite the growing interest in these predictive algorithms, to the authors' best knowledge, it seems that the ANN method applied to the friction stir welding process has

primarily focused on the study of a specific link between the input process parameters and the output mechanical behavior.

In fact, from the literature review it is possible to notice that, so far, ANN research applied to the FSW technology has been focusing on the analysis of a specific combination of materials, involving the variation of numerical input parameters and continuous quantitative variables.

3. *Stress enhanced intergranular corrosion of friction stir welded AA2024-T3*

This chapter is derived from the article "Bocchi, S.; Cabrini, M.; D'Urso, G.; Giardini, C.;Lorenzi, S.; Pastore, T (2020). Stress enhanced intergranular corrosion of friction stir welded AA2024-T3. Engineering Failure Analysis, 111, 104483".
DOI: 10.1016/j.engfailanal.2020.104483.

I am immensely grateful to the support received from my co-authors. I am responsible for all the changes in this chapter with respect to the published version.

3.1. Introduction

As reported in the previous chapters, to make FSW technology more applicable, it is necessary to broaden the knowledge concerning the relationship between process parameters and operating behavior of the welded joint.

The literature review reported in Paragraph 2.2 showed that many efforts have been conducted to study the corrosion resistance of the FSWed joints since it is strictly correlated to the behavior of the welded parts in a potential aggressive environment. Despite that, a lack of information can be observed in the correlation between corrosion behavior and welding process parameters.

In this chapter, the evaluation of intergranular corrosion of FSWed AA2024 joints as a function of processing parameters and loading conditions was considered.

Intergranular corrosion assessment, long terms exposure, electrochemical impedance spectroscopy and microstructure were analyzed.

To simulate a potential aggressive environment, the tests were conducted in 0.6 M aerated sodium chloride solution on both unloaded specimens and on four-point beam bending at 80% of the tensile yield stress.

At the end of the tests a clear difference between the behavior of the specimens as a function of the process parameters was evidenced.

On the contrary, loading conditions acted primarily on the corrosion initiation and propagation mechanisms. In fact, stress enhanced intergranular attack was observed only

at the nugget of the loaded specimens, where coalescence of sub-micrometric and continuous copper-rich precipitates at the grain boundary occurred.

3.2. Material and methods

3.2.1. Base material microstructure

The chemical composition and the main mechanical properties of the base material are shown in Table 3.1. The base material has the typical microstructure of rolled aluminum alloys, with α-Al grains oriented along the rolling direction and several intermetallic phases (Figure 3.1a). Coarse round-shaped S-phase (Al-Cu-Mg) particles (Figure 3.1b) and irregularly shaped Al-Cu-Fe-Mn particles (Figure 3.1c) were detected by EDS analysis.

Table 3.1: Chemical composition (%wt) and mechanical properties of the AA2024-T3.

Al	**Cu**	**Mg**	**Si**	**Fe**	**Mn**	**Zn**	**Ti**	**Yield Strength [MPa]**	**Ultimate Tensile Strength [MPa]**	**Elongation %**
Bal	4.4	1.6	0.08	0.10	0.48	0.1	0.04	345	459	17

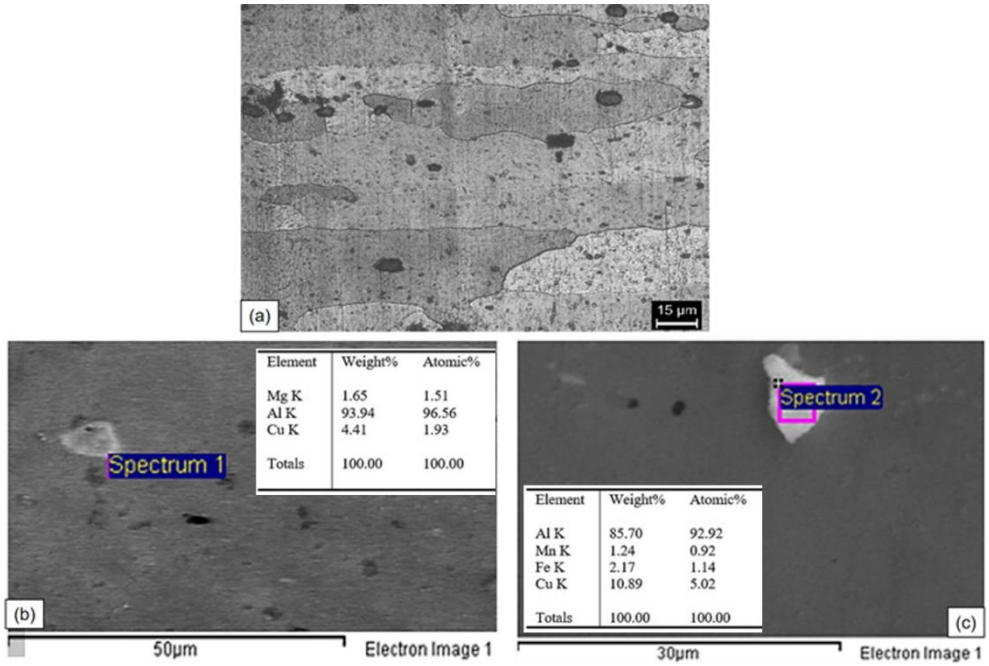

Figure 3.1: α-Al grains oriented along the rolling direction (a). EDS analysis of Al-Cu-Mg intermetallic precipitates (b). EDS analysis of Al-Cu-Fe-Mn intermetallic precipitates (c).

3.2.2. Friction Stir Welding (FSW) process setup

Friction stir welded specimens were taken from a 4 mm alloy sheet perpendicularly to the rolling direction. The dimension of each sheet was 200 x 80 x 4 mm. The sheets were welded two by two resulting in specimens with the rolling direction perpendicular to the welding direction. The welding tool consists of a smooth plane shoulder (16 mm diameter) with a pin having a frustum of cone shape (pin height equal to 3.8 mm with maximum and minimum diameters equal to 6 and 4 mm respectively) [57].

Different rotational speeds (S=1000 and 1500 rpm) and feed rates (F=10 and 35 mm/min) were tested. The parameters were selected according to a previous work, at the boundaries of the technological window [57]. The tool inclination was fixed at 3° and the tool penetration depth into the sheets was almost through the whole thickness of the specimens. For evaluating the process repeatability, three repetitions were carried out for each combination of parameters. The mechanical characterization of the welds is reported in a previous work [57]. The tensile strength of the joints resulted in the range between 280 and 320 MPa.

3.2.3. Intergranular corrosion test

The determination of susceptibility to intergranular corrosion of the FSWed joints was performed according to EN 2716. The tests were carried out on the specimens characterized by the lowest and highest thermal input, such as S=1000-F=35 and S=1500-F=10, respectively. The specimens were degreased in acetone and then they were immersed for one minute in a water solution at 95°C containing 5% vol. HNO_3 at 70% and 0,5% vol. of HF at 40%. Then, the specimens were rinsed in demineralized water and degreased in nitric acid 70% concentrated at ambient temperature.

The intergranular corrosion test consists of the exposure of the specimens for 6 hours at 25°C in 1L of an aqueous aerated solution with 57 g sodium chloride and 10 ml of hydrogen peroxide. After immersion, the specimens were rinsed in demineralized water and then dried. All the surfaces of the samples were observed by means of an optical microscope. According to EN 2716, the specimens were sectioned in the zone that exhibits the more severe corrosion attack to obtain metallographic sections. Microstructures were revealed after grinding up to 4000 grit and then alumina suspension polishing.

3.2.4. Long exposure and SCC corrosion tests

Four-point bending (4PBB) tests were performed according to the ASTM G39 standard to attain uniform tensile strain distribution across the weld. The specimens were loaded up to 80% yield strength (YS) reached during the tensile tests performed for each combination of the welding parameters in a previous work [57]. Four glass cylinders were used to avoid galvanic coupling between the sample and the sample holder. The specimens were exposed for 1000 hours in a cell filled with about 30 L 0.6 M sodium chloride aqueous solution. Another series of specimens was dipped in the same solution without loading, for comparison purposes.

Corrosion potential measurements and electrochemical impedance spectroscopy (EIS) tests were performed during the whole testing period. Tests were carried out by using a custom cell developed to limit the exposed area of the specimen at about 1 cm^2. The EIS spectra were taken by Ivium CompactStat potentiostat, by considering 10 mV amplitude of the sinusoidal signal in the frequency range between 50 kHz and $5x10^{-2}$ Hz. Tests were carried out on both loaded and unloaded specimens.

After exposure, all the specimens were rinsed in distilled water and degreased with acetone in an ultrasonic bath. Metallographic sections were taken by cutting the specimens along the longitudinal direction, perpendicularly to the welding. They were mounted in cold-working resin and then polished with alumina suspension. The microstructure was revealed by means of Keller etchant. The observations were performed through an optical and a scanning electron microscope (SEM) equipped with energy dispersive x-ray analysis (EDS).

3.3. Results and discussion

3.3.1. FSWed joints microstructure and intergranular attack

The analysis of the microstructure of the joints well-evidenced the three different zones typical of FSW joining, i.e. the central zone - called “nugget” – in which complete grain recrystallization occurs, the thermo-mechanically affected zone (TMAZ) and the heat affected zone (HAZ) [10, 70, 72, 126, 127]. No relevant microstructural differences were detected between the advancing and retreating sides of the joint. Fine recrystallized grains surrounded by small precipitates were detected in the nugget. Figure 3.2a and Figure 3.2b show the microstructure of the nugget of joints welded using different process parameters (S=1000 rpm F=35 mm/min, S=1500 rpm F=10 mm/min). Relevant plastic deformation was noticed at the interface between nugget and TMAZ. Microstructures similar to base metal can be found in the TMAZ and in the HAZ, where elongated grains and several precipitates are present (Figure 3.3c and Figure 3.3d).

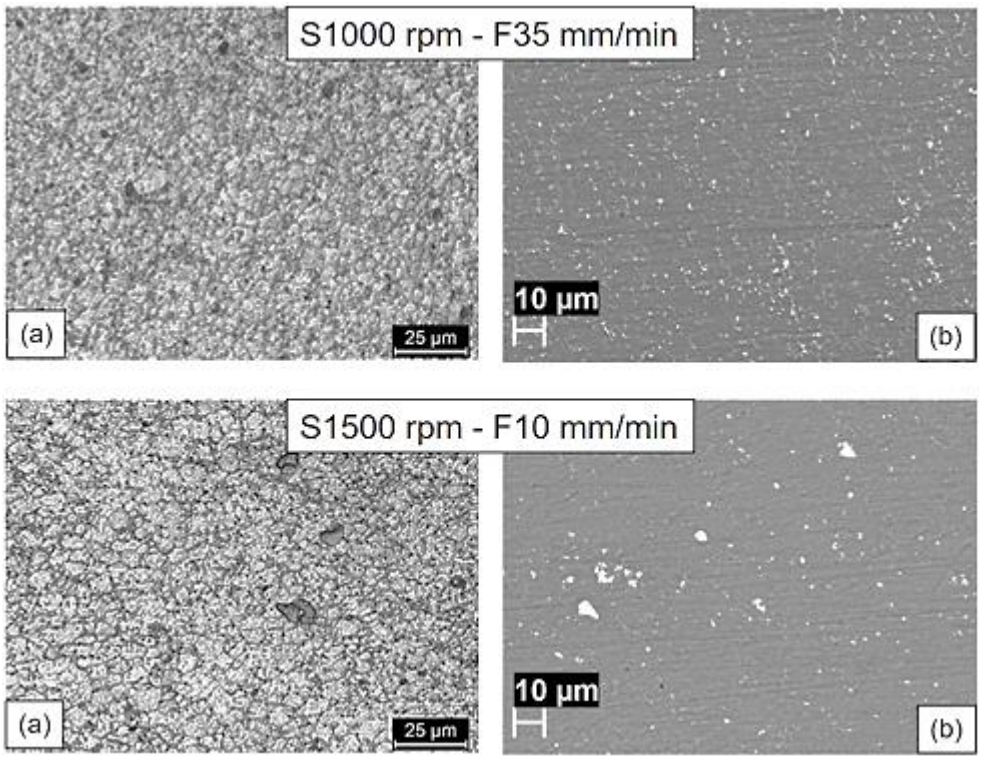

Figure 3.2: The microstructure of the nugget of the specimens - optical images after Keller attack (a) and SEM close up of the precipitates distribution without the metallographic attack (b).

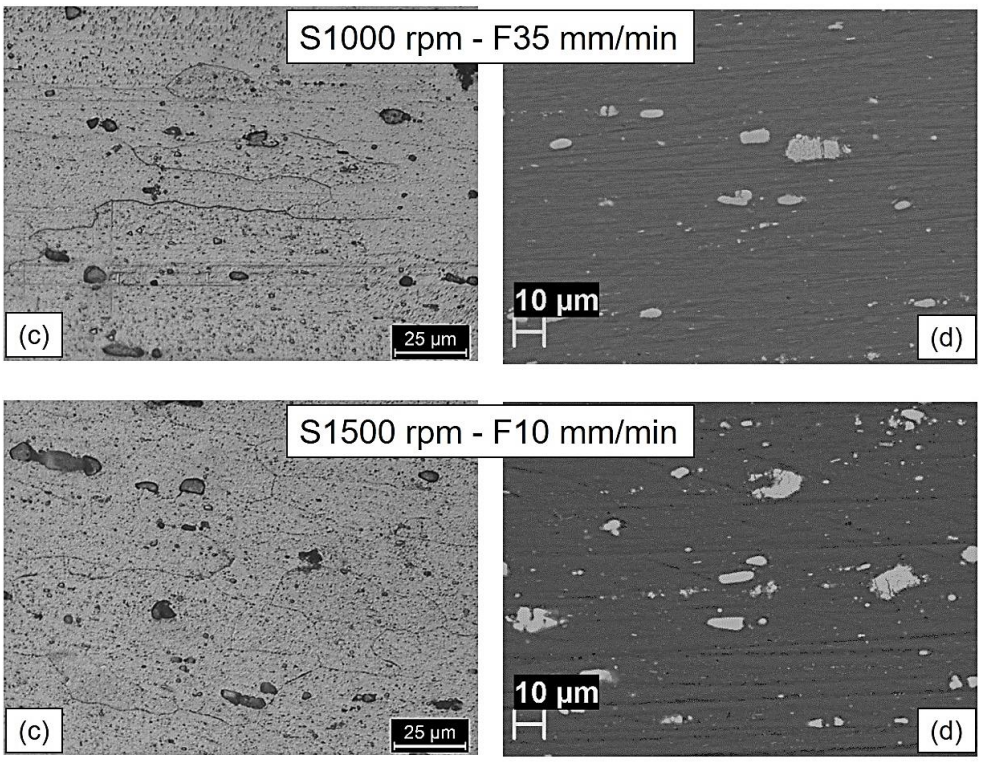

Figure 3.3: The microstructure of the HAZ of the specimens - optical images (c) and SEM close up of the precipitates phases (d).

The commercial aluminum-copper alloy used for testing was furnished in T3 temper, which means that it is heat-treated, cold worked and naturally aged to a substantially stable condition. In the matrix, both homogeneous coherent precipitates and fine precipitates (S-phase) were observed. The amount of GPB zones in the base metal is closely related to the high hardness of the alloy [12]. In the welding zone, dissolution, coarsening of strengthening precipitates and the formation of wide precipitate free zone take place, along with the severe plastic deformation. At the HAZ, close to the base material, softening occurs mainly due to the dissolution of GPB zones and the presence of fine intergranular precipitates. On the contrary, the higher hardness at the nugget is mainly determined by the equilibrium between the very fine microstructure, the presence of GPB zones and the coarsening of S-phase precipitates that can also occur, as evidenced elsewhere by authors [57]. In this previous experimental analysis, the lowest hardness values were found at the interface between nugget and TMAZ and a peak in hardness in the HAZ was noticed. Besides, symmetry with respect to the joint axis was observed and no difference between the advancing and retreating side was advised, consequently. In terms of corrosion behavior, the lowest hardness area was found to correspond to the less noble zones evaluated in terms of corrosion potential by means of a micro-capillary, whereas no corrosion potential modifications were found in the zones with the highest hardness values. The profile of open circuit potential (OCP) showed a decrease of about 100-150 mV among the different regions of the joint (base material, nugget, HAZ and TMAZ). The intergranular corrosion tests carried out according to EN 2716 on the specimens welded at S=1000 and F=35 compared to S=1500 and F=10 evidenced similar attack morphologies on both conditions (Figure 3.4), thus confirming what previously found in [57]. The corrosion attack covered a wide zone at the TMAZ for S=1500, F=10 condition (characterized by the highest heat input) whilst it becomes more intense and restricted at zones closer to the HAZ for S=1000, F=35 condition (Figure 3.4, compare zone B with zone A).

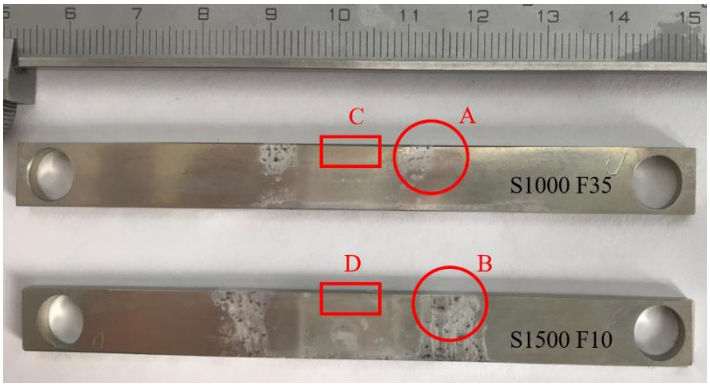

Figure 3.4: Attack morphology of the specimens after six hours of immersion (C and D indicates the center of the welds).

The intergranular corrosion attack morphology was confirmed by an optical microscope analysis on the top of the weld for both the welding conditions at TMAZ/HAZ (Figure 3.5a and b). No relevant intergranular attack was noticed at the nugget, despite the very fine microstructure mainly constituted by recrystallized grains, can be easily distinguished (Figure 3.5c and d).

However, the microstructural examination of the cross-sections taken in the zones A and B of the joint, according to EN 2716, permitted to exclude the penetration of the intergranular attack, which remains only superficial.

The attack morphology found during intergranular corrosion tests is in accordance with the trend of local open circuit potential measurements performed earlier [57], in which the minimum values of the OPC was detectable at the HAZ/TMAZ zones, not at the nugget.

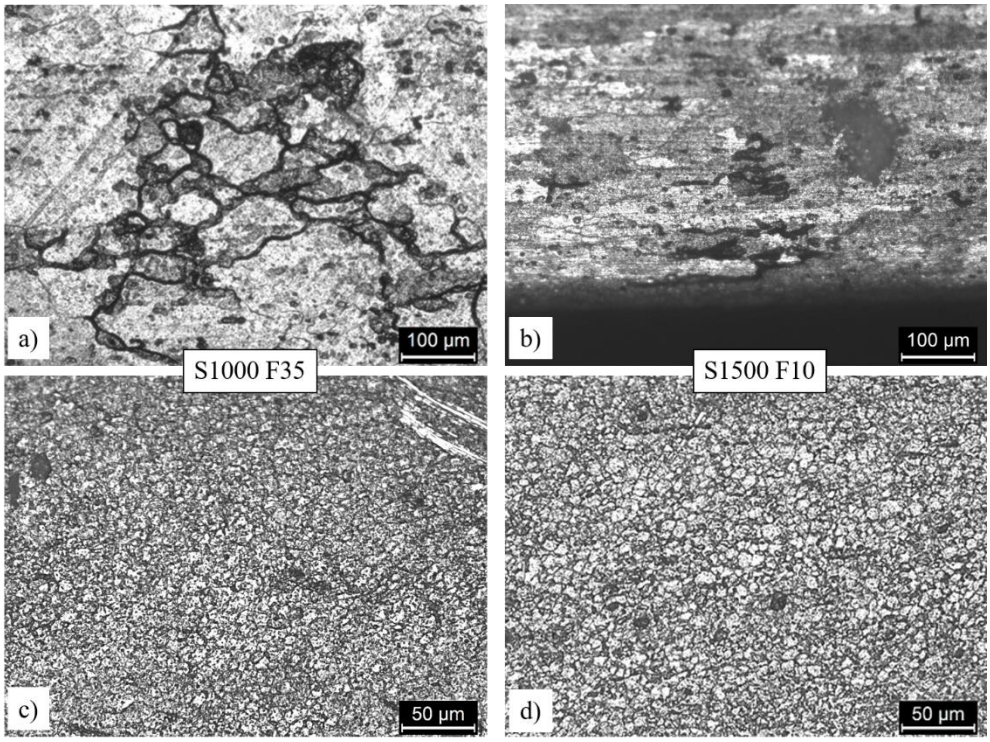

Figure 3.5: The intergranular attack on the top of the specimen welded at S1000 and F35 (a) and of the specimen welded at S=1500 and F=10 (b); nugget images of the specimen welded at S1000 and F35 (c) and welded at S=1500 and F=10 (d).

3.3.2. Long term exposure tests and SCC

Long term exposures of both loaded and unloaded specimens permitted to underline the effect of loading on intergranular corrosion susceptibility of FSWed joints as a function of processing parameters.

Just after immersion, both loaded and unloaded specimens showed an initial sharp decrease in the free corrosion potential and stable similar values for all the conditions can be evidenced after about 700 hours of immersion (Figure 3.6).

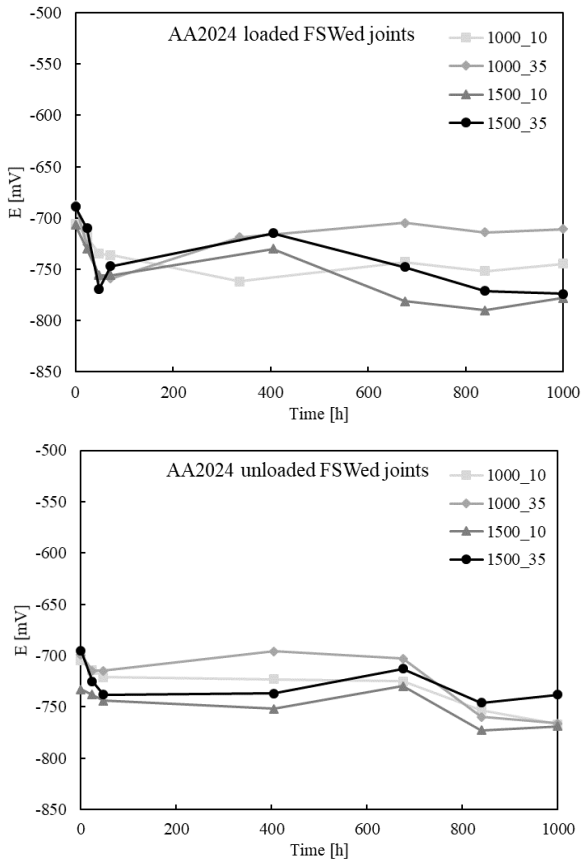

Figure 3.6: Open circuit potential for the loaded and unloaded specimens as a function of the immersion time.

Figure 3.7 and Figure 3.8 show the EIS spectra, in terms of both Nyquist and Bode diagrams, of 4PBB specimens in aerated 0.6 M NaCl solution at different exposures. The results of the two welding conditions at the boundaries of the technological window are shown, i.e. 1000 rpm rotational speed and 35 mm/min feed rate (lowest thermal input) and 1500 rpm and 10 mm/min feed rate (highest thermal input).

The Nyquist diagrams collected just after exposure of the specimens in the solution showed two well-defined capacitive loops (Figure 3.7) and an inductive loop at the lowest frequencies. With increasing immersion time, the radius at the medium frequency capacitive loop decreases, whereas the inductive loop at the low frequency shrinks with the immersion time and then disappears at 48 h, giving rise to diffusive behavior.

The mechanism of localized corrosion initiation and its intergranular propagation can be considered similar to that found by Peng et al. (where the corrosion process in passive systems to the reactions in the interface oxide/electrolyte, producing corrosion product, is discussed) [128]. Thus, in such systems, the oxide/electrolyte response predominates

in the medium frequency range. Hence, the high frequency loop must be associated with the electron transfer process at the metal/oxide interfaces. As to the inductive loop, Keddam et al. indicated that it is more likely promoted by the weakening of the protectively effectiveness of the aluminum oxide layer, due to the anodic dissolution of aluminum alloy [129]. With increasing time, the surface oxide layer becomes progressively less and less protective, due to the action of aggressive anions of the sodium chloride solution. Then, the relaxation of weak points becomes vanishingly small. This explains why the inductive loop vanishes with the immersion period, in agreement with experimental observations. The inductive behavior of electrode impedance is often explained by the relaxation phenomenon of reaction intermediates, but the presence of such a species on an inert aluminum oxide surface is unlikely.

Certain differences can be observed in the medium and very low-frequency inductive loop, between loaded and unloaded specimens. Such differences seem to be mainly noticeable at very early exposures, and the curves overlap already after 48 hours. This can be ascribed to the high chloride content of the solution, which promotes localized corrosion initiation since early exposures. Once localized corrosion occurred, the curves overlap as a huge amount of corrosion products grows on the specimens' surface and diffusive contribution rapidly appears in the EIS spectra, which becomes particularly evident at prolonged exposures.

The same considerations can be drawn by considering the Bode representation (Figure 3.8). The impedance at the lowest frequency can be considered an index of passive film protectiveness of the alloy; an indication of the intensity of the corrosion attack is ever low for loaded specimens compared to unloaded and further decreases in the first 48h, thus denoting active corrosion behavior and the continuous activation of the whole exposed surface. A trend can be also evidenced moving from low thermal input condition (S=1000 F=35) to the highest thermal input considered in this sperimentation (S=1500 F=10). The higher the thermal input of the joining process, the lower the impedance values at very low frequency were detected, thus denoting further weakening of the passive and favoring localized corrosion initiation and propagation.

At 48 hours, Bode-phase plot modifies and a shift to the left can be noticed in the medium frequency range. This change in the capacitance was attributed by Keddam et al. referring to the formation of the intergranular or exfoliation corrosion feature, that occurs more

intensely on specimens joined by considering the highest heat input (S=1500, F=10) [129].

The shapes of the curves further modify at longer exposures, due to the presence of the huge amount of corrosion products on the specimens' surface. A diffusive contribution can be noticed at low frequencies in the curves drawn at 840 hours exposure, which practically hinders the corrosion process.

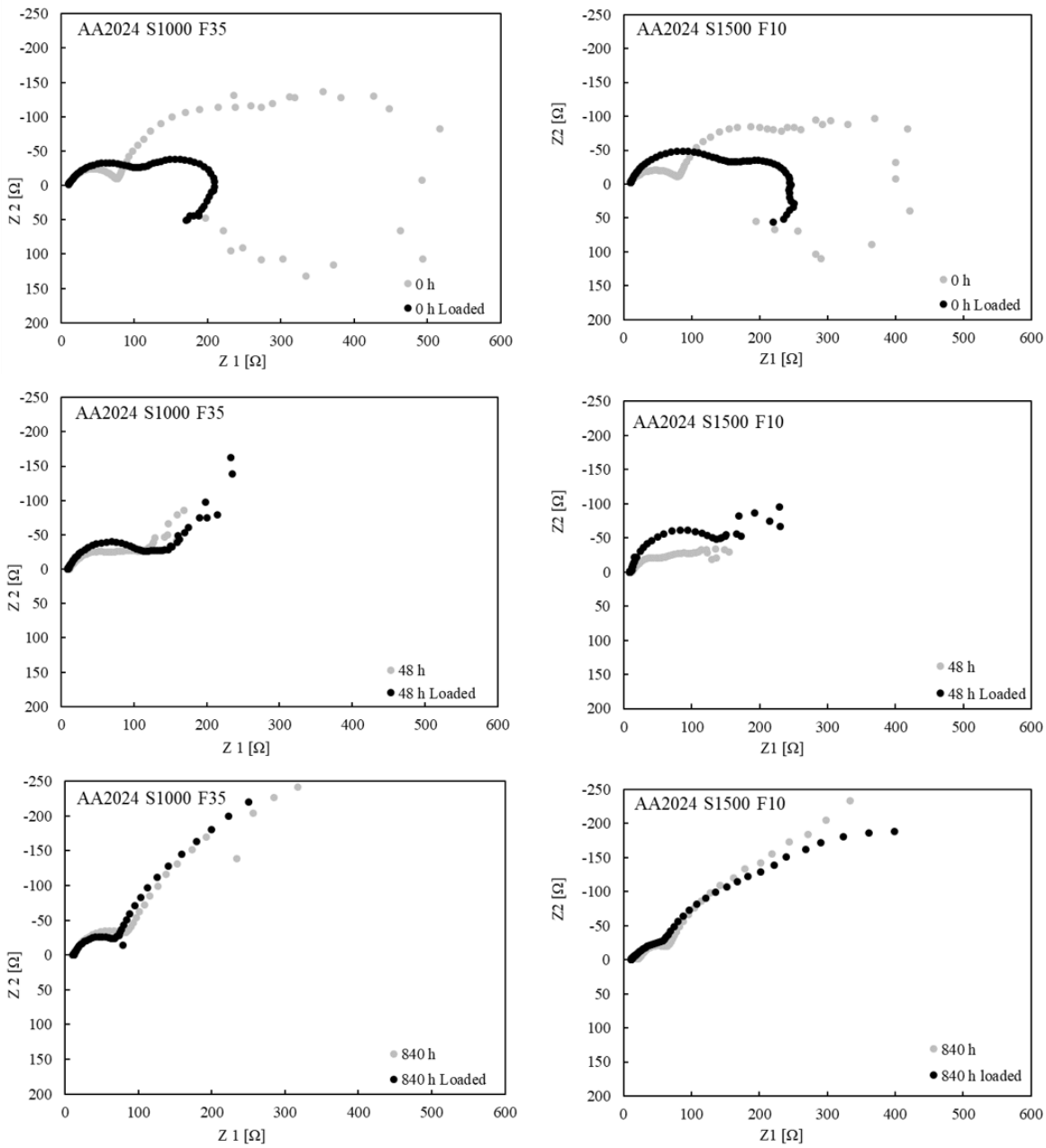

Figure 3.7: Nyquist representations of the EIS spectra for the loaded and unloaded specimens as a function of the immersion time.

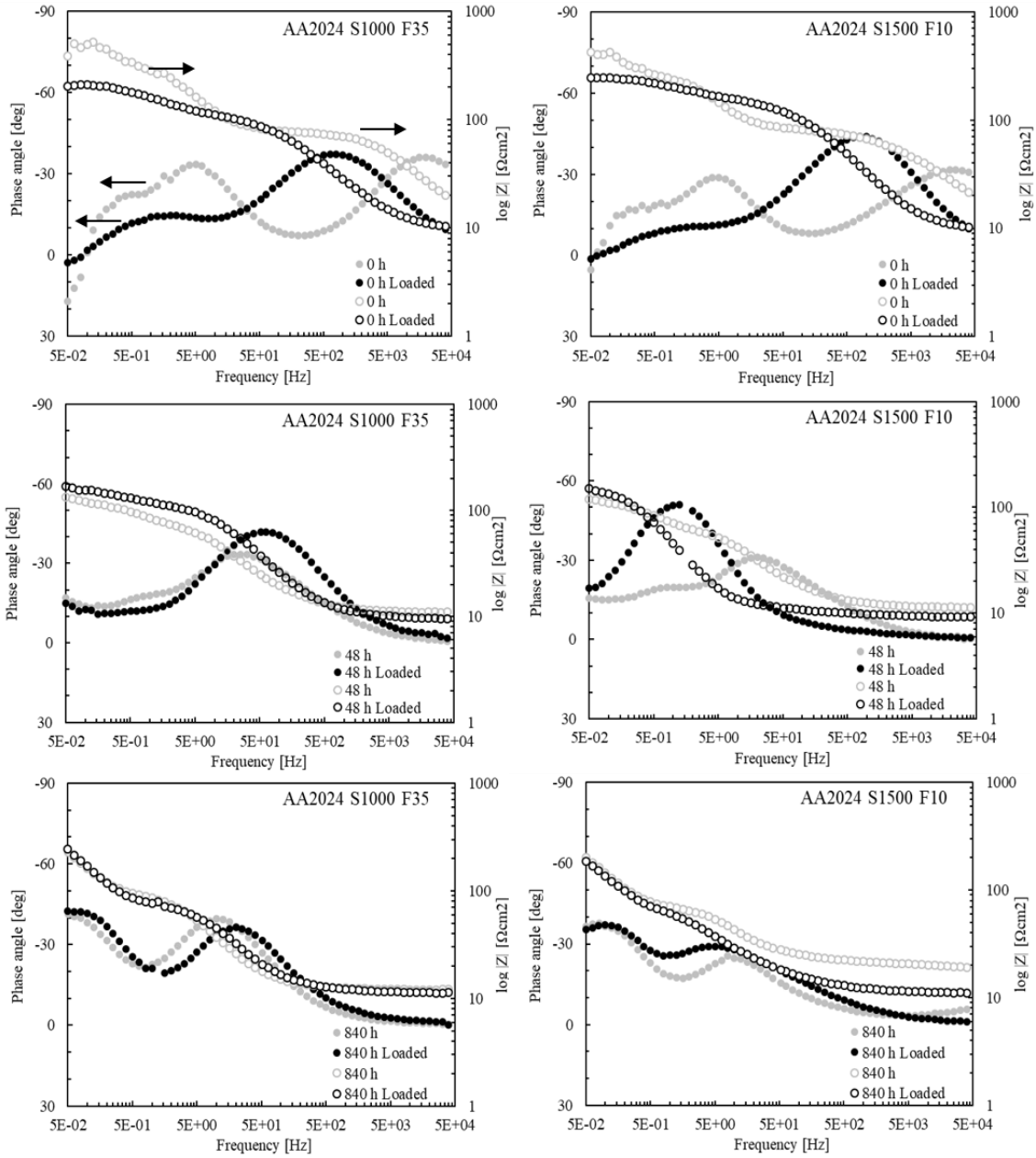

Figure 3.8: Bode representations of the EIS spectra for the loaded and unloaded specimens as a function of the immersion time. Empty markers represent the modulus of impedance and filled ones indicate the phase angle.

Despite the EIS test results evidenced the onset of localized corrosion, no macroscopic stress corrosion cracks were observed at the end of 1000 hours testing period on the loaded specimens. However, the morphology of the attack of the loaded and unloaded samples was very different. The analysis of the metallographic sections (Figure 3.9) of loaded samples showed an intense intergranular attack at the nugget, that grows

perpendicularly to the direction of loading. The attack does not occur on unloaded specimens.

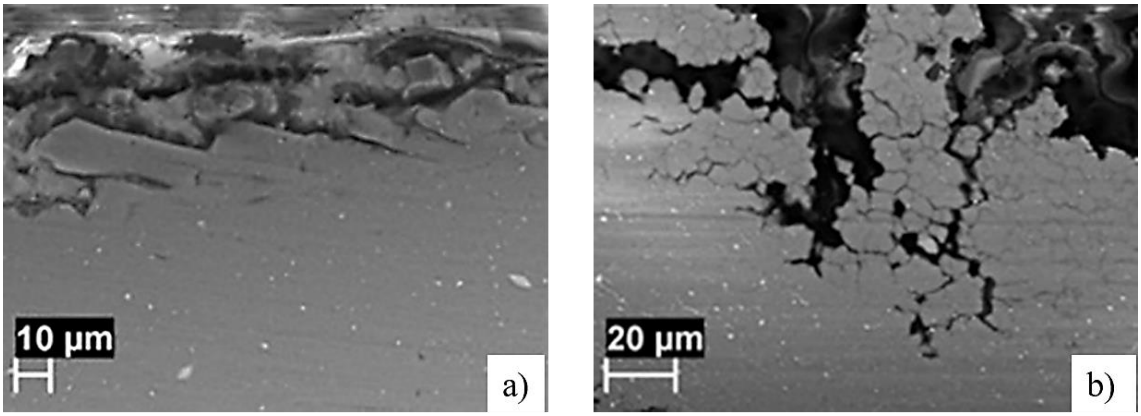

Figure 3.9: Metallographic section of un-loaded (a), loaded (b) 4PBB after 1000 hours of immersion in aerated 0.6 M NaCl solution (a welded at S 1000 rpm and F 10 mm/min, b specimen welded at S 1500 rpm and F 10 mm/min).

In the present study, all the specimens after long term exposure tests preferentially corroded in the zone of the joint, mainly at the nugget, whilst the material not affected by both thermal and mechanical action of the tool exhibit less intense attack. In fact, the different practical nobility of the material seems to be relevant at early exposures, but it becomes far less relevant at longer exposures. This fact can be ascribed to the corrosion process, which promotes the production and re-deposition of corrosion products on the specimens' surface, as demonstrated by EIS tests at longer exposures.

The preferential corrosion of the weld is in agreement with several data reported in the literature [56, 70, 130] and it can be related to the alteration of the microstructure due to the thermomechanical action of the tool. Jariyaboon et al. reported that the presence of an intergranular attack in friction stir welded Al-Cu alloy is due to precipitation of Cu-rich intermetallic particles at grain boundaries in the nugget, which results in the formation of anodically-active Cu-depleted regions at the grain boundaries [56]. The HAZ/TMAZ interface is the zone the most prone to corrosion, as demonstrated by the high variation in microhardness values and stable low potential associated with the presence of several homogeneous anodic sites. This can be due to the presence of both coarse intermetallic compounds and fine intergranular S-phase precipitates, that make this zone susceptible to pitting and intergranular corrosion.

However, unique attack morphology was noticed under loading conditions after long term exposure tests in form of penetrating intergranular attacks at the nugget only on 4PBB specimens (Figure 3.10), whilst no penetrating intergranular attack occurred in absence of loading. At the nugget, localized corrosion mainly occurs at the grain boundary and it follows the path of iron and copper-rich precipitates, which are of micrometric dimensions, but the penetration of such attack is generally not relevant. In the absence of macroscopic cracks, the morphology of corrosion cannot strictly be considered stress corrosion cracking, but rather stress enhanced intergranular corrosion, owing to the microstructural modifications of the alloy due to the FSW process. The role of applied stress on the intergranular corrosion of aluminum-copper alloys is evidenced also under compressive loading, but in a less efficiently way compared to tensile conditions.

Petroyiannis et al. demonstrated that the mechanism of stress corrosion crack growth of 2XXX series aluminum alloys involves either anodic dissolution or hydrogen embrittlement [131]. Galvanic interaction between the particles and the local surrounding matrix can lead to the preferential dissolution of anodic particles or dissolution of the adjacent matrix surrounding noble particles. The evolution of hydrogen always takes place in actively growing localized corrosion sites and cracks. The absorption of hydrogen into aluminum alloy leads to the possibility of crack propagation by hydrogen embrittlement (HE).

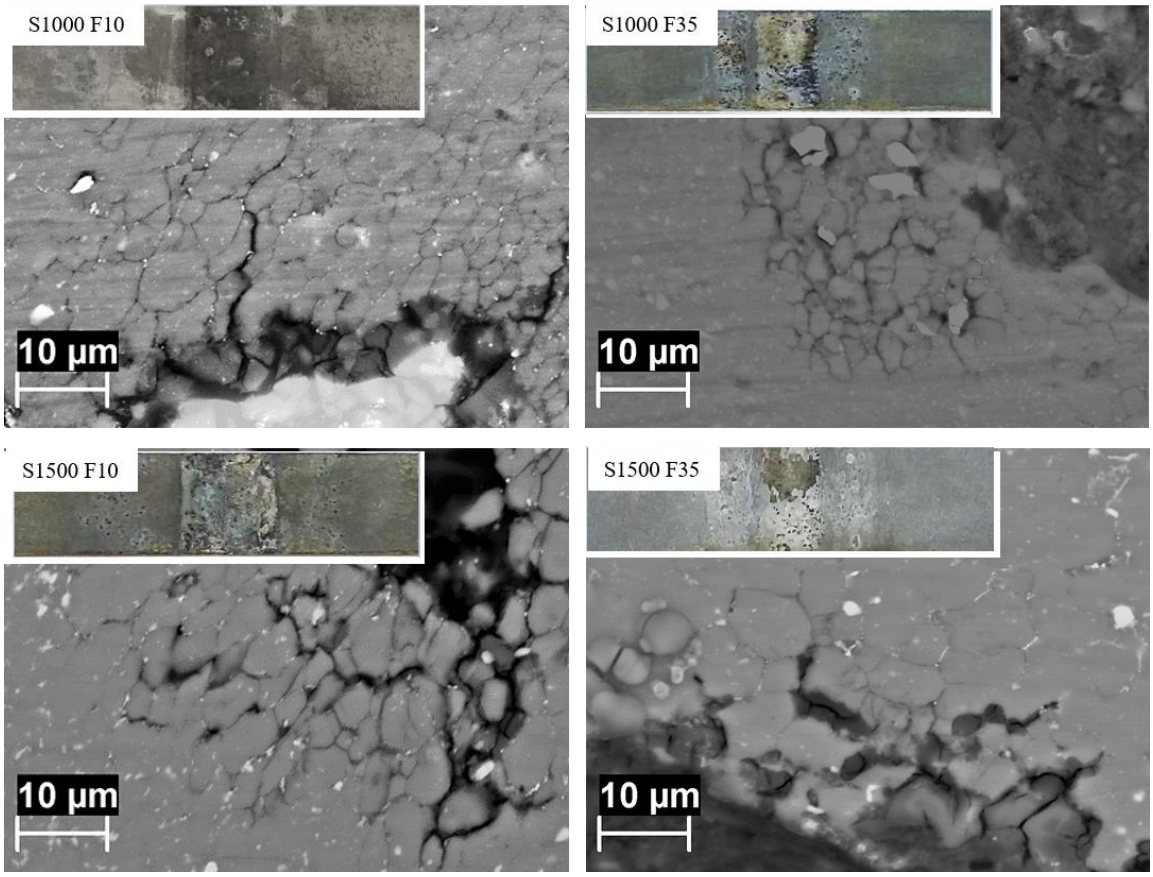

Figure 3.10: Attack morphology for each loaded sample after 1000 h of immersion. In particular, on the upper left, the macro photos of the samples just after dipping are reported.

Corrosion of 2024 aluminum alloys initiates at micrometric second phases. S-phase acted as a cathode and led to the anodic dissolution of the adjacent aluminum matrix [132]. The Fe-containing phase acts as a more efficient cathode, inducing a more severe dissolution of the matrix. Such an effect is limited to the area around precipitates and becomes negligible just after early periods of immersion. In correspondence of the nugget, the precipitation of copper-rich second phases causes the depletion of copper in the aluminum matrix; consequently, the corrosion potential decreases. Besides, it is well known that copper and iron-rich phases are more efficient cathodes, which promote a local increase of pH and the occurrence of passive film destabilization.

In presence of loading, the process is further accelerated because the anodic dissolution rate at the crack tip is enhanced, thus both the mechanisms (i.e. anodic dissolution of the crack tip and hydrogen embrittlement) are promoted. No relevant differences in terms of intergranular corrosion penetration were observed as a function of the process parameters (Figure 3.10).

3.4. Conclusions

This chapter studied the intergranular corrosion behavior of friction stir welded AA2024-T3 joints as a function of manufacturing parameters and loading conditions. Microstructural characterization of the corrosion morphologies and corrosion tests were performed to evaluate the effect of loading on intergranular corrosion initiation and propagation.

EIS data confirmed the presence of active corrosion sites and passive zones but the technique can evidence differences between loaded and unloaded specimens only just after few hours of exposures. At longer exposures, the active corrosion process is hindered by the presence of aluminum corrosion products.

AA2024 FSWed joints are not susceptible to intergranular corrosion because only superficial not penetrating attacks were noticed according to EN 2617 standard.

A more severe corrosion attack after intergranular tests is at the HAZ/TMAZ interface and not in the nugget.

On the contrary, long term corrosion tests evidenced a preferential attack in the zone of the nugget. Despite no stress corrosion cracking occurred, the intergranular corrosion attack became penetrating in the presence of loading, giving rise to stress enhanced intergranular corrosion of the alloy.

The morphology of the penetrating attack was similar for all the joining parameters analyzed in the present study.

4. *Stress corrosion cracking of friction stir-welded AA-2024 T3 alloy*

This chapter is derived from the article "Cabrini, M.; Bocchi, S.; D'Urso, G.; Giardini, C.;Lorenzi, S.; Testa, C.; Pastore, T (2020). Stress corrosion cracking of friction stir-welded AA-2024 T3 alloy. Materials, 13(11), 2610". DOI: 10.3390/ma13112610.

I am immensely grateful to the support received from my co-authors. I am responsible for all the changes in this chapter with respect to the published version.

4.1. Introduction

In literature, many forces have been involved in studying the effect of the tool rotation on both the extension of the characteristic zone of the FSWed joints (nugget, TMAZs and HAZs) and the effects on mechanical properties in function of a single process parameters, i.e., rotational speed or feed rate [133].

In addition to the process parameters, also the environment and the loading conditions strongly influence the mechanical characteristics and thus the behavior of the FSWed joints. In fact, the applied stress and corrosive environment, and above all their combined action, could promote stress corrosion cracking (SCC) in susceptible alloys [134–136]. However, the effect of the modifies induced by the entire FSW process on the intrinsic susceptibility of such alloys is yet far to be completely understood. Most of the available papers focused on the SCC of alloy 7XXX but, in the knowledge of the authors, only few papers reported the SCC behavior of AA2024 FSWed joints.

This chapter is devoted to a deeper analysis of stress corrosion cracking phenomena in friction stir welded AA2024. Constant load cell and slow strain rate tests were carried out in aerated NaCl 35 g/L solution. Open circuit potential and electrochemical impedance spectroscopy were also evaluated in the different zones of the welding.

4.2. Materials and Methods

4.2.1. Preparation of the Welds

Aluminum sheets (size 200 mm × 80 mm × 4 mm thickness) were welded by using a tool with smooth plane shoulder (16 mm diameter) and pin having a frustum of cone shape (pin maximum and minimum diameters equal to 6 and 4 mm, height equal to 3.8 mm) (Figure 4.1). The rotational speed (S) of the tool was fixed at 1500 rpm and feed rate (F) was 10 mm/min. The set-up of the welding process was reported in previous works by authors [38, 57, 135, 137]. The mechanical properties of the base materials and the welded joints are shown in Table 4.1. For the FWSed specimens, only the ultimate tensile strength (UTS) is reported, because it was not possible to evaluate the yield strength (YS) owing to the localization of the plastic straining of the specimens in the TMAZ/HAZ zone. The decrease in the mechanical properties at the thermomechanical and heat affected zones is the result of the modification in the microstructure of the alloy, with solubilization and reprecipitation of the straightening second phases, as reported in previous works by authors [38, 57, 135, 137, 138]. A good reproducibility was observed in the tensile strength of the FSWed joints, thus confirming the absence of macroscopic defects alongside the weld.

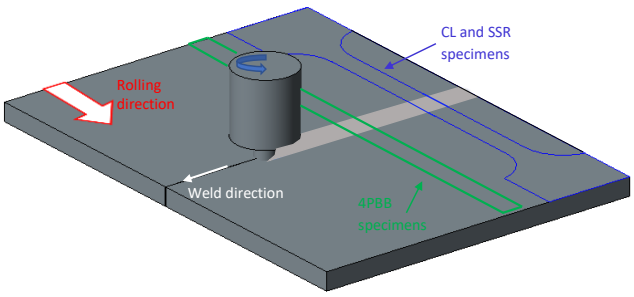

Figure 4.1: Schematic representation of the friction stir welding (FSW) and the machining of the specimens.

Table 4.1: Mechanical properties (yield strength, YS and ultimate tensile strength, UTS) of the base materials and the welded joint.

Alloy	Base Material			FSW Joint	
	YS [MPa]	UTS [MPa]	Max Strain [%]	YS [MPa]	UTS [MPa]
AA2024–T3	345	459	17	-	315

4.2.2. Constant Load Tests

Constant load (CL) tests were carried out on dog bone shaped specimens with 8 mm width, 4 mm thickness, and 82 mm gage length with the weld positioned at the center of the gage length (Figure 4.2). The specimens were inserted in a double compartment cell with a window to expose about 50% of the central area (Figure 4.3a and b). All the compartments were filled with aerated 35 g/L NaCl solution, at 25 °C. The solution was constantly recirculated by means of a pump. The configuration of the cell was chosen in order to monitor one side the open circuit potential (OCP) and carry out the electrochemical impedance spectroscopy (EIS) test on the other side at the same time.

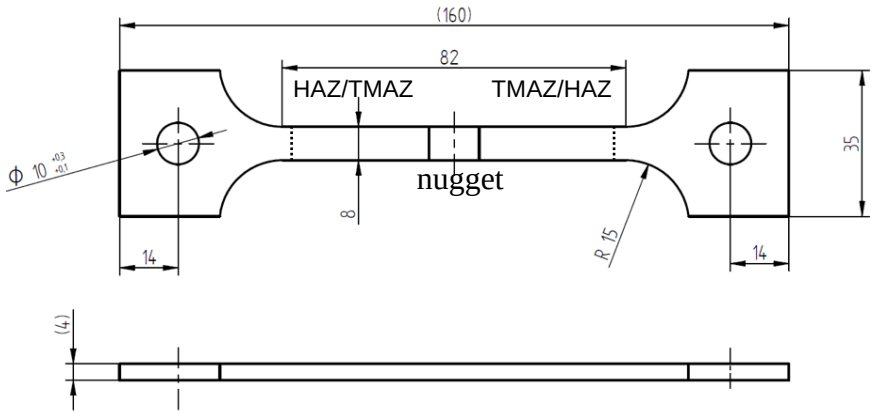

Figure 4.2: FWSed specimen used in constant load (CL) e SSR test; the specimens of the slow strain rate (SSR) test on base materials have the same dimension without weld.

The OCP monitoring was done by means of homemade three Ag/AgCl references electrodes with E = +0.200 V vs. NHE (normal hydrogen electrode). The results were presented after conversion as the saturate calomel electrode (SCE-E = +0.240 V vs. NHE, Amel Instrument, Milano, Italy). The data were registered by a Ivium

CompactStat instrument; the sampling frequency was varied during the experiment from one measurement per second in the initial instants and during the loading phases of the specimen to a 10-h monitoring, with acquisition of one point per minute every 100 or 200 h, during maintenance of the constant load of the specimens. The EIS tests were performed using an Ivium CompactStat instrument. Sinusoidal signal with 0.010 V amplitude in the frequencies range between 10 kHz and 10^{-2} Hz was applied. EIS tests were carried out on the CL specimens just dipped, after 24, 48 (before and after loading the specimen), 480, 504 (before and after increase the load on the specimen), 552, and 650 h (before and after to un-load the specimen).

The specimens were loaded by means of a tensile testing machine with a double lever arm (Figure 4.3c), according to NACE TM 0177-2005 Method A, the loads were imposed by adding weights to the lever, the lever force had previously been calibrated through a calibrated load cell with 10 N accuracy. The testing procedure is as following. The specimen was initially positioned in the cell, the testing solution was inserted, and the first EIS spectrum was registered. The second EIS spectrum was measured after 24 h, the third after 48 h; after the third EIS measurement, the specimen was loaded at 50–55% UTS of the FSWed joints, and the EIS measure immediately repeated. This load was chosen because it is practically in the correspondence of the deviation from the linearity of the stress–strain curve of the weld; it could be assumed that, under this stress, the less resistance zone of the gauge length becomes plastically deformed, while the other parts of the specimen remain in elastic straining. The monitoring of OCP and EIS spectrum continued for 504 h, after these the load was further increased in order to achieve a stress value of about the 80% of the ultimate tensile strength of the weld, thus achieving uniform plastic deformation conditions along the gage length of the specimen. The load was then maintained for 650 h.

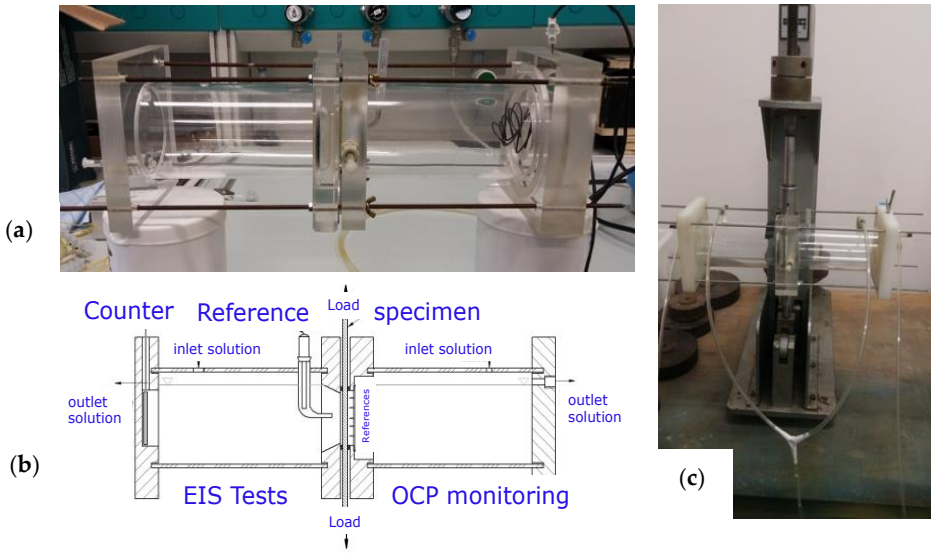

Figure 4.3: (a) Image of the cell used for the CL tests. (b) Schematic illustration of the test apparatus and (c) image of one specimen under the CL testing machine.

At the end of the exposure period, the specimens were unloaded, cleaned, and observed under the scanning electron microscope (SEM, Zeiss EVO 40, Oberkochen, Germany) with energy dispersive spectroscopy (EDS) Oxford X-Act in order to analyze the corrosion products morphology and composition. Metallographic cross sections along the longitudinal direction were also analyzed. The gauge length was cut from the specimen, then longitudinally sectioned using a metallographic cutting machine (Metkon Servocut, Bursa, Turkey) in the central part. The section was embedded in resin and grinded with emery paper and polished with colloid alumina until 0.1 μm of roughness. The metallographic section was observed by a Nikon optical microscope and the SEM without metallographic attack and after attack with Keller reagent.

4.2.3. Slow Strain Rate Tests

The slow strain rate (SSR) tests were carried out by using specimens of the same dimensions as for CL tests. The SSR tests were also performed on AA-2024 T3 base material for comparison.

The tests were carried out by means of a homemade SSR testing machine with four independent loading stations. The load is applied through an electric motor and reduction gears that can impose displacement rates between 5×10^{-7} and 5×10^{-3}

mm/s. The calibration of the cells is performed independently. Acquisition system (spider 8 HBM Italy, Milano, Italy) read the load and a function of time; the displacement of the tensile grip is evaluated multiplying the displacement rate for the time. A displacement rate of 8.2×10^{-4} mm/s, corresponding to 10^{-6} s^{-1} average strain rate along the gage length, was chosen. SSR tests were carried out according to the ASTM 129-00 (2013), exception for the specimen's geometry that was changed to test all the weld. The cell was like those used for the CL tests, with the same configuration of the electrodes, but smaller than that for CL tests, to be settled under the SSR machine, filled with an aerated solution of 35 g/L NaCl. No EIS spectra were obtained during this test because the OCP did not remain constant. At the end of the tests, the specimens were washed in distilled water and rinsed in acetone to permit the observation of the fracture surface under the SEM. Then the specimens were longitudinally sectioned for the metallographic observation with the same procedure illustrated for the CL test.

4.2.4. Electrochemical Characterizations of the Different Zones of the Weld

For comparison, EIS and OCP measurements were performed on the separated different zones of the FSW joints: the nugget, the HAZ/TMAZ (it was not possible to cut the specimens separating these zones), and the base material in unloaded condition. The weld was cut as illustrated in Figure 4.4; the isolate specimens with the nugget, the TMAZ/HAZ zone, and the base material were connected with an external wire and then cold mounted with epoxy resin. The exposed surface of the specimen was 20×20 mm^2. It was grounded with emery paper and then polished with colloidal alumina up to 0.3 μm. The specimens were dipped in separate glass cells in aerated 35 g/L NaCl (Carlo Erba, RPA grade, Cornaredo, Italy) solution. Standard saturated calomel electrode (SCE E = +0.240 V vs. NHE, Amel Instrument, Milano, Italy) was positioned at the surface of the specimens by using a Luggin capillary to compensate the ohmic drop in the electrolyte. Electrochemical impedance spectroscopy (EIS) tests were performed with the same procedure used for on the CL test.

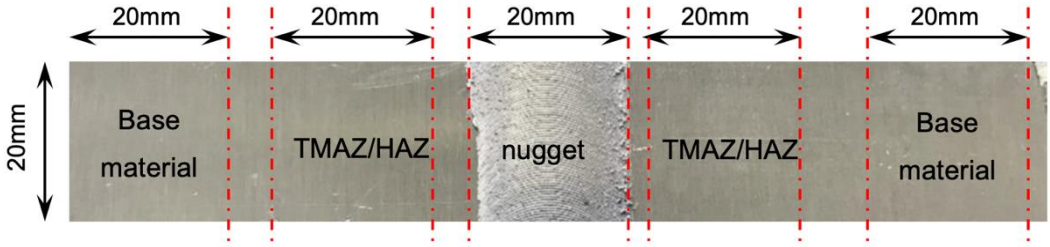

Figure 4.4: Scheme of the sampling of the different areas of the welding and of the base metal for the monitoring of open circuit potential (OCP) and electrochemical impedance spectroscopy (EIS).

4.3. Results and Discussion

Figure 4.5 shows the OCP measurements in aerated NaCl solution at the nugget, the HAZ/TMAZ, and the base material with regard to exposure time.

Similar values of the OCP were measured on the three different zones just after dipping. The nugget showed constant OCP values during all the exposure periods. Different behavior was observed for the base material and the heat-affected zones (HAZ/TMAZ), which showed an initial increase of OPC followed by a decrease of about 150 mV.

Figure 4.6 shows the EIS spectra for the specimens obtained from the different zones of the weld with regard to exposure time. The spectra collected at the nugget are quite different compared to the base material and TMAZ just after dipping. The Nyquist plot shows two overlapped capacitive loops, and an inductive one at very low frequencies, whereas the base material and the TMAZ presented a capacitive loop and diffusive behavior at very low frequencies (Figure 4.6a). The Bode diagram (Figure 4.6b) shows the highest value of the impedance modulus of the base materials, indicating a stable passive condition. Conversely, the values of the impedance modulus of the nugget and the TMAZ decrease at the low frequency, thus indicating activation of the metal surface during low frequency measurements. All the specimens showed two phase constants, one at intermediate frequency and the other at very low frequencies.

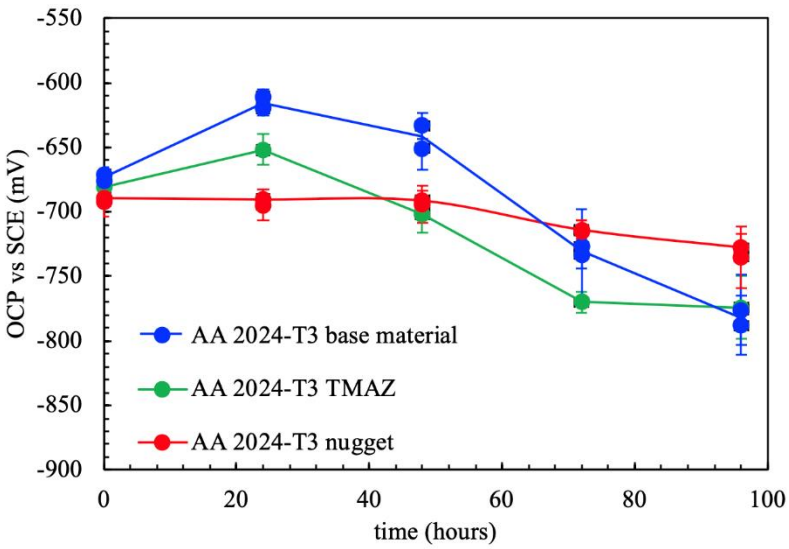

Figure 4.5: OCP in function of exposure time of the different zones of AA-2024 T3 FSWed joint in aerated NaCl 0.6 M at 23 °C.

After only 24 h of immersion, the shape of EIS spectra significantly changed (Figure 4.6c and d). The amplitude of the EIS loops in Nyquist plot decreased significantly for all the different zones of the weld. Diffusive behavior was still observed for the base metal and the TMAZ, while a second capacitive loop can be distinguished for the nugget -but flattened- and the inductive loop disappeared. All the specimens showed only one phase constant, but the frequency range is lower compared to just dipped conditions. An increase in phase can be noticed at very low frequency for the base material and the TMAZ, thus indicating that a second phase constant could be present at very low frequencies. The impedance modulus achieved the values of 10^4 Ωcm^2 for all the zones of the weld, meaning that activation occurred also on base metal and the TMAZ.

After 72 h of immersion, the EIS spectra became practically overlapped, with only a slight difference between the impedance modulus of the nugget with respect to the base material and the TMAZ (Figure 4.6e and f). Well evident diffusive behavior can be noticed at very low frequencies because of the presence of corrosion products deposit.

These results seem to evidence an initial higher activity of the nugget with respect to the other zones, but these differences become negligible at longer exposures. After the tests, all the specimens showed general corrosion morphologies.

The behavior significantly modifies as loading is applied. The corrosion potential showed sudden decrease at the application of monoaxial constant load, as reported in Figure 4.7. The effect is attributable to the breakdown of the thick, porous, and not adherent scale of aluminum oxide formed on specimens after prolonged exposures, which exposes the aluminum matrix directly to the aggressive environment. The potential approached the steady state value -i.e., the value in unloading conditions- because of self-healing effect of corrosion products of aluminum. The decrease in the corrosion potential is more pronounced when the specimens are strained in the plastic field.

Specimens failure was not observed under constant loading for 650-h exposure. The analysis of the specimens after the tests showed an intergranular attack in the nugget near the zone of beginning of the TMAZ (Figure 4.8 and Figure 4.9).

The EIS spectra collected on CL specimens showed certain different behavior just after dipping and after 24 h (Figure 4.10a and b). The spectra mainly approach that of the nugget (compare Figure 4.10a and b with Figure 4.6a and b). It can then be stated that EIS tests carried out during CL tests are mainly affected by the most active zone of the joint -i.e., the nugget. The specimen just after dipping presents two overlapped capacitive loops and an inductive one (Figure 4.10a) -typical of non-stationary OCP values during early exposures EIS tests (Figure 4.10b). After 24 h, the Nyquist diagram presented a well-evident diffusive behavior (compare Figure 4.10c and d to Figure 4.6c and d). The increase in the load does not modify the EIS spectra, that are overlapped to the condition without applied load after 24-h exposure (Figure 4.10c-f), thus confirming that the corrosion process at longer exposures is only limited by the presence of the pseudo-passive film by corrosion products that are able to heal the cracks promoted by loading.

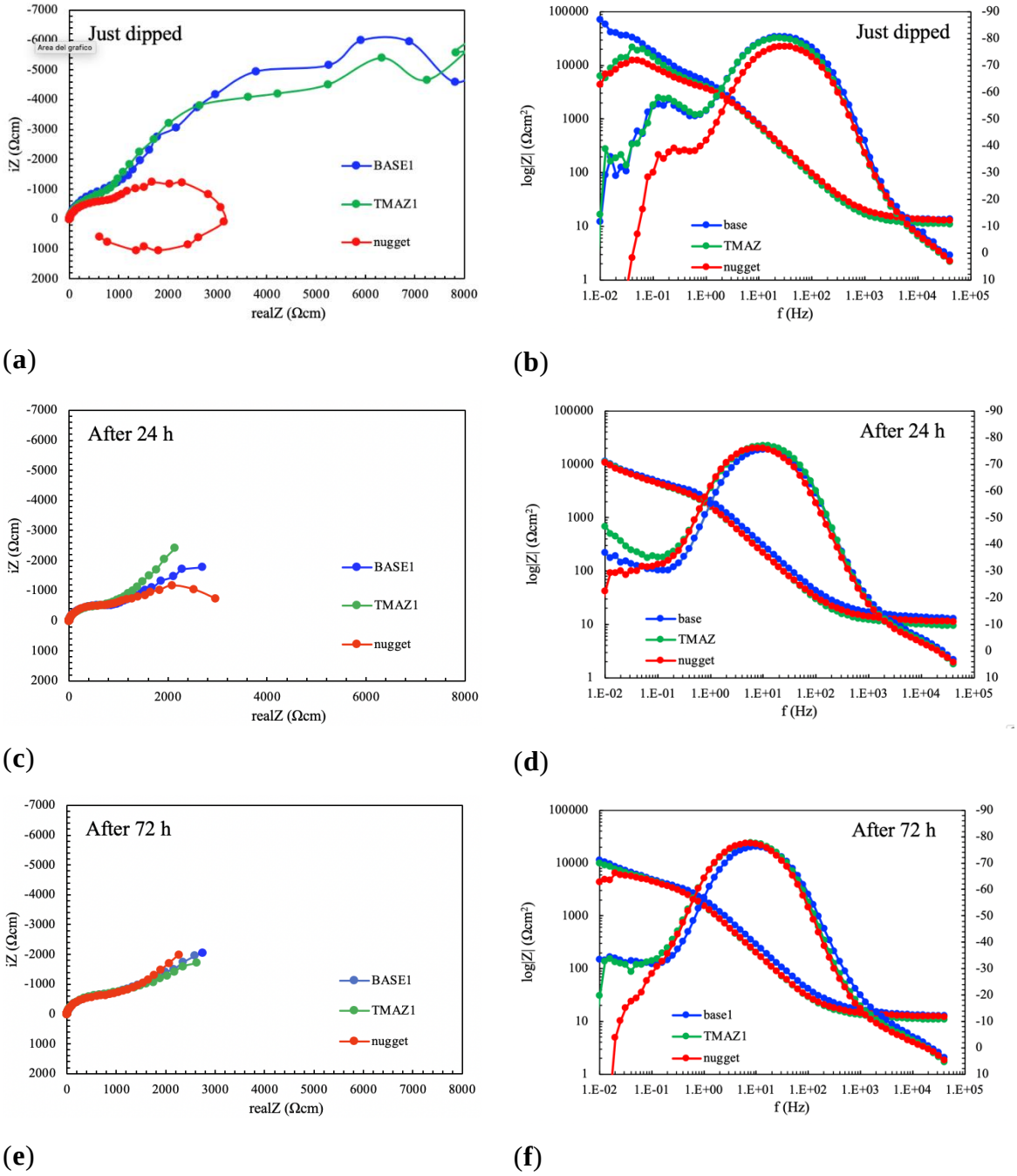

Figure 4.6: EIS spectra (a), (c), and (e) Nyquist and (b), (d), and (e) Bode representation, of the separate different zones of the weld; (a) and (b) just dipped; (c) and (d) after 24 h; (e) and (f) after 72 h of immersion in aerated NaCl 0.6 M solution.

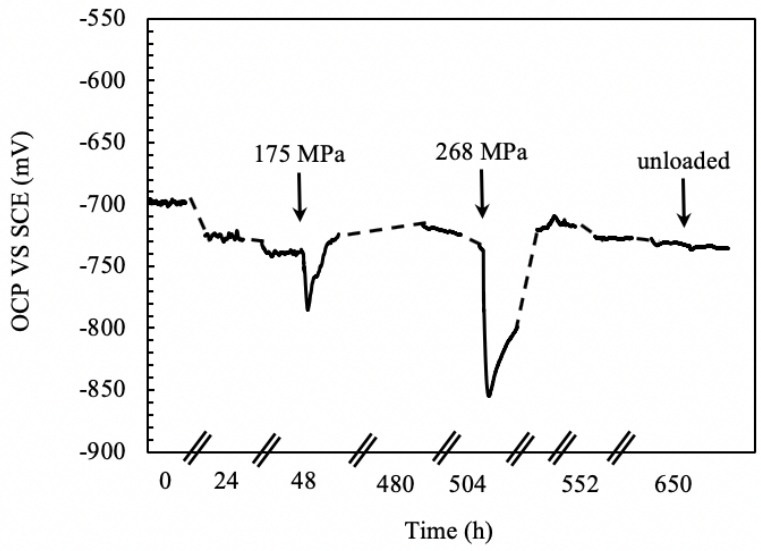

Figure 4.7: OCP measurements during 720 h exposure of CL specimen of the FSWed AA-2024 T3 alloy in aerated NaCl 0.6 M at 23 °C.

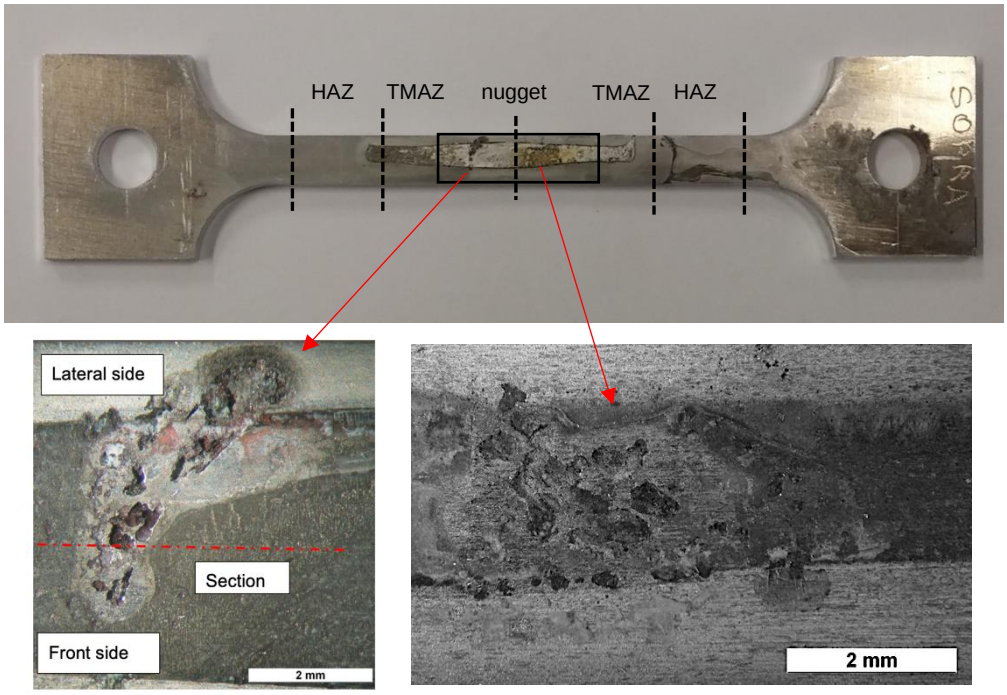

Figure 4.8: Corrosion morphology of FSWed AA-2024 T3 alloy after CL test in aerated 35 g/L NaCl.

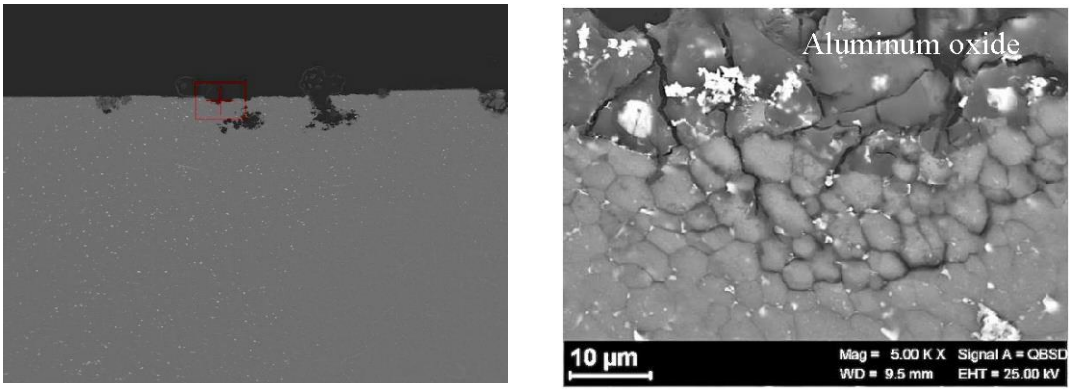

(a) **(b)**

Figure 4.9: Metallographic section of Figure 4.6: (a) Macro image of the nugget with several localized attacks; (b) close-up of the red zone in (a).

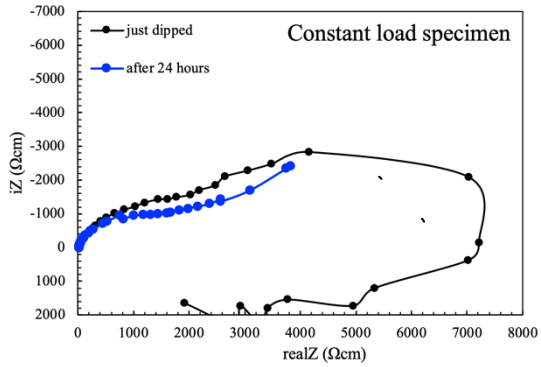

(a)

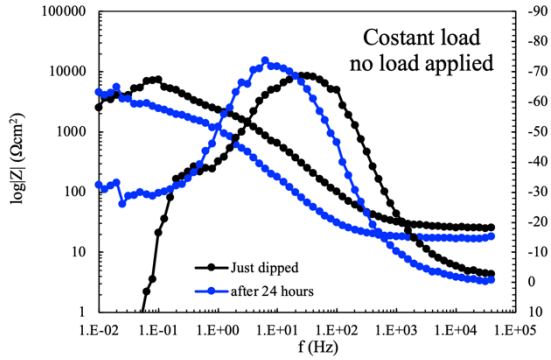

(b)

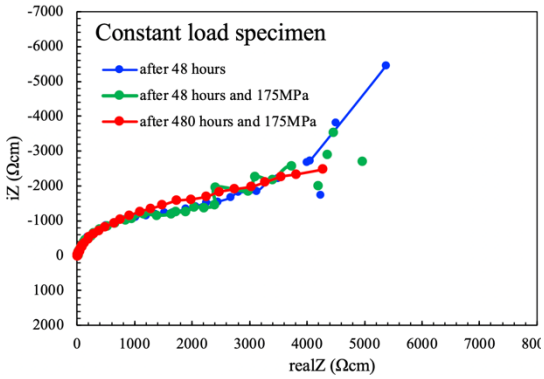

(c)

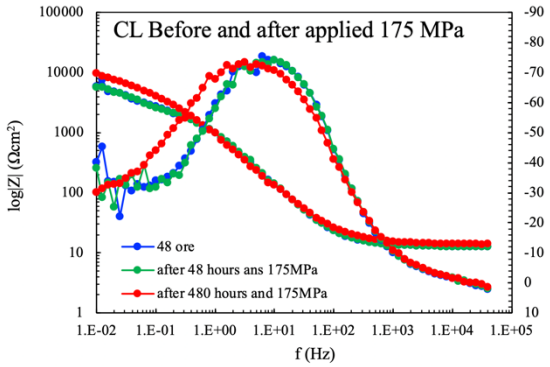

(d)

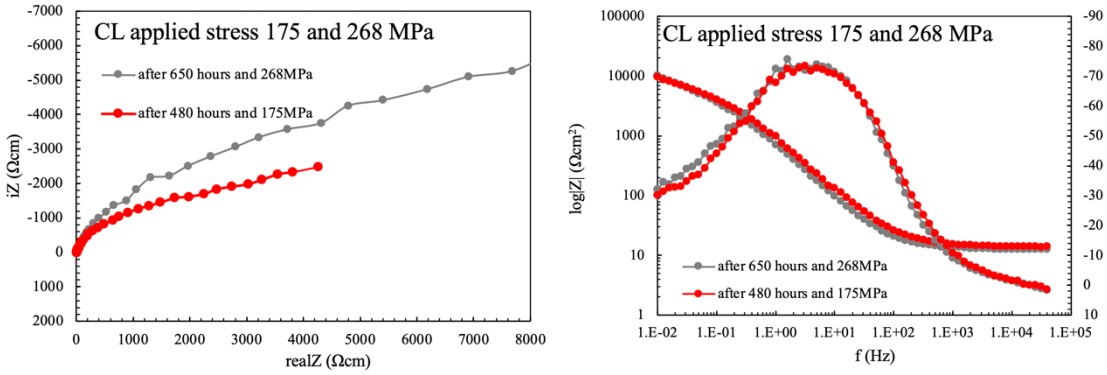

(e) **(f)**

Figure 4.10: EIS spectra (a), (c), and (e) Nyquist representation, (b), (d), and (e) Bode representation of the constant load specimen without load just dipped and after 24 h (a,b), after 48 h without load, and after 175 MPa, and after 480 h loaded at 175 MPa (a,d) and after 480 h at 175 MPa and 650 h at 268 MPa (e,f) in aerated NaCl 0.6 M solution.

These results are in agreement with those obtained in previous works [57, 135, 137]. It was observed that the OCP did not change in four point bent beam (4PBB) specimens in un-loaded or loaded conditions at the 80% of the ultimate tensile strength of the weld (Figure 4.11). The specimens were loaded before the immersion. On the contrary, differences between the EIS spectra of un-loaded and loaded specimens were observed only at very early exposures. This was mainly attributed to the presence of corrosion products scale formed on the surface of the specimens, that hindered the EIS signal response. On 4PBB specimens, the corrosion process was mainly localized at the nugget, with wide and shallow deep morphology on the un-loaded specimens and stress-enhanced intergranular morphology on loaded specimens [135]. The effect of the applied load on intergranular corrosion initiation and propagation in alloy AA-2424 T3 was first highlighted by Zhang and Frankel [68, 139]. However, the entire surface of the specimens is covered with a continuous but porous layer of corrosion products as the exposure time increases. This is well evident in the EIS spectra that are practically overlapped as they are mainly governed by diffusive phenomena occurring at the corrosion products scale [135].

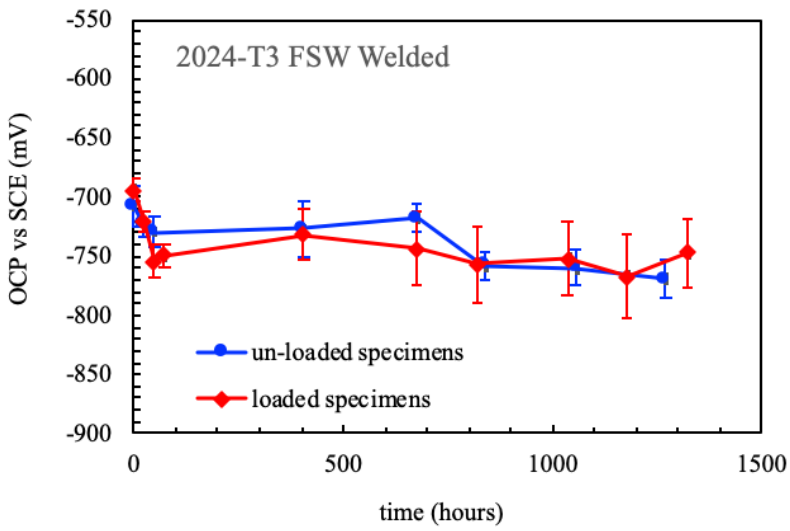

Figure 4.11: Effect of the time of immersion on the OCP of un-loaded and loaded 4PBB specimens of the FWSed alloy AA2024-T3 in aerated NaCl 0.6 M at 23 °C (data obtained by [135]*).*

The OCP of the FSWed AA-2024 T3 alloy under slow strain rate conditions, (Figure 4.12) modifies in function of the applied monotonic tensile stress. A slight decrease in the values can be noticed as the strain values lay in the elastic field. A sharp decrease was noticed -i.e., 100–250 mV- at the YS. Exceeding the YS, the OCP increases up to the values recorded in the elastic field, until the rupture. The specimen breaking did not occur at the nugget that is characterized by higher tensile strength, but in the heat affected zone. Because of this consideration, it can be derived that the attack observed at the nugget (Figure 4.13) did not reach sufficient depth to promote the specimen rupture, as the plastic deformation mainly take place in the softened zones, typical of the HAZ/TMAZ. Consequently, the effect of FSW on the alloy microstructure and on the mechanical properties significantly affects also the stress corrosion cracking susceptibility of the alloy.

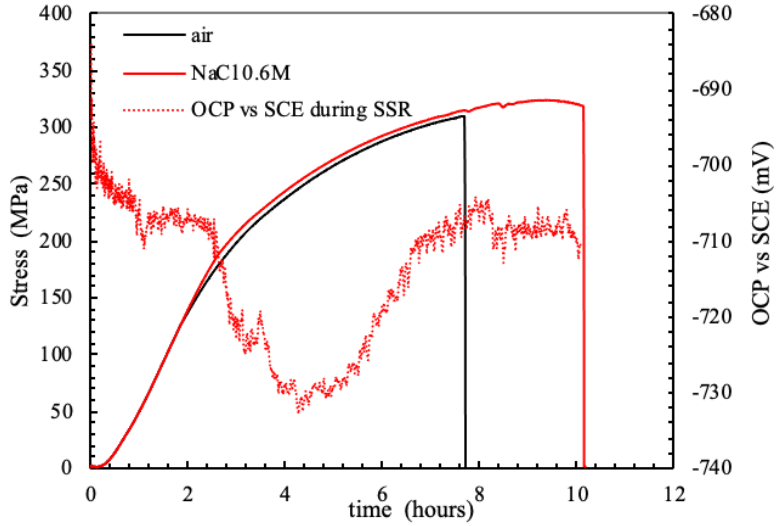

Figure 4.12: Stress vs. strain and OCP FSWed AA2024-T3 alloy during the SSR test in aerated NaCl 0.6 M solution at 23 °C.

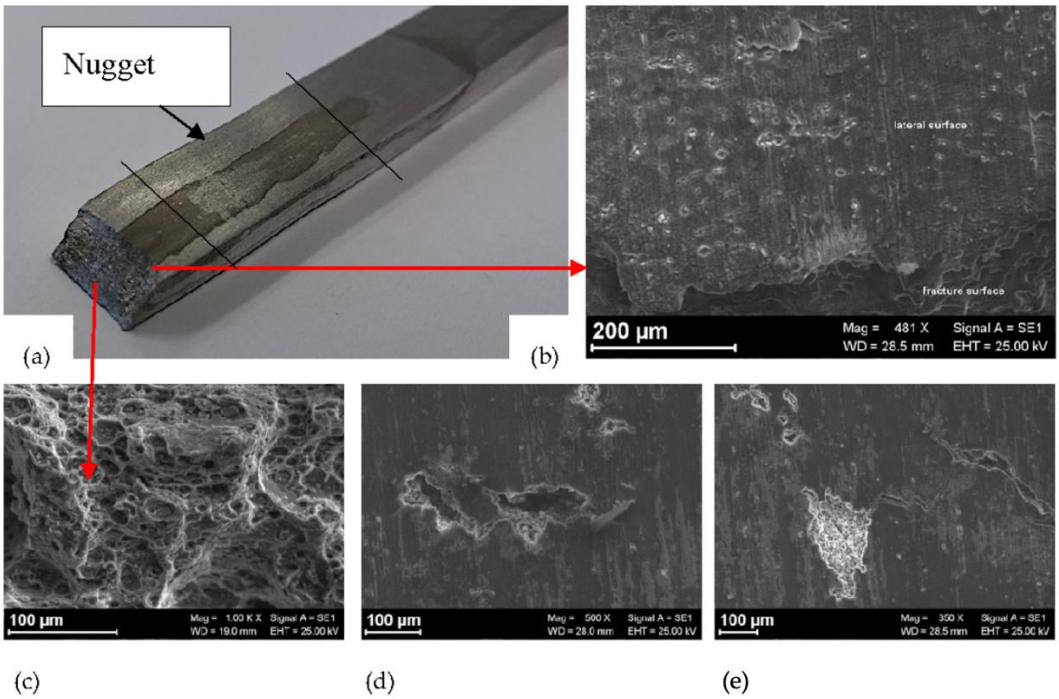

Figure 4.13: (a) Image of a FSWed specimen after the SSR test in NaCl 35 g/L; (b) close-up of the lateral surface in the correspondence of the fracture surface; (c) close-up of the dimples in the fully ductile fracture surface; (d) and (e) SCC microcracks in the nugget of the specimen of the FWSed AA2024-T3.

SSR tests performed on commercial AA-2024 T3 alloy showed a completely different behavior compared to FSWed. The OCP values are stable at more noble values compared to FSWed, without the occurrence of stress corrosion cracks (Figure 4.14).

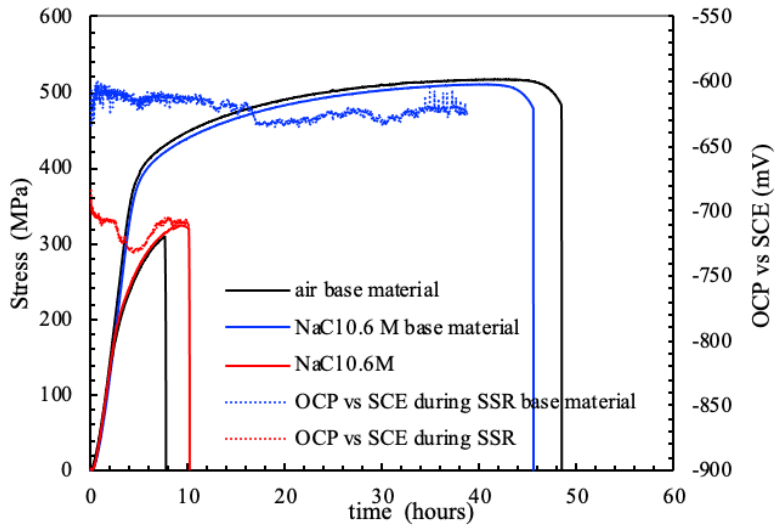

Figure 4.14: Stress vs. strain and OCP of the base and FSWed AA-2024 T3 alloy during the SSR test in aerated NaCl 0.6 M solution at 23 °C.

For both the weld and the commercial AA-2024 T3 alloy, the time-to-failure is longer in NaCl solution compared to air. All the tests were twice repeated with similar results. It could be hypothesized that active corrosion in NaCl solution is stimulated at the dislocations, thus generating vacancies able to accelerate the intrinsic mobility and thus the plastic deformation, as already evidenced by other authors that named this phenomenon as anodic attenuation of strain hardening [140, 141].

FSW modify the microstructure of the alloy and its electrochemical and stress corrosion cracking behavior, consequently. In the base material, both macro-precipitates and nanoprecipitates are present (Figure 4.15) [142, 143]. The last ones are produced because of solution annealing and natural ageing. The macro-precipitates are mainly produced by primary solidification processes and are not solubilized during heat treatment [144]. They are considered to be responsible of the short-term electrochemical behavior of the alloy as it is well-known that the interface between these particles and the matrix is particularly active because of its different practical nobility [132].

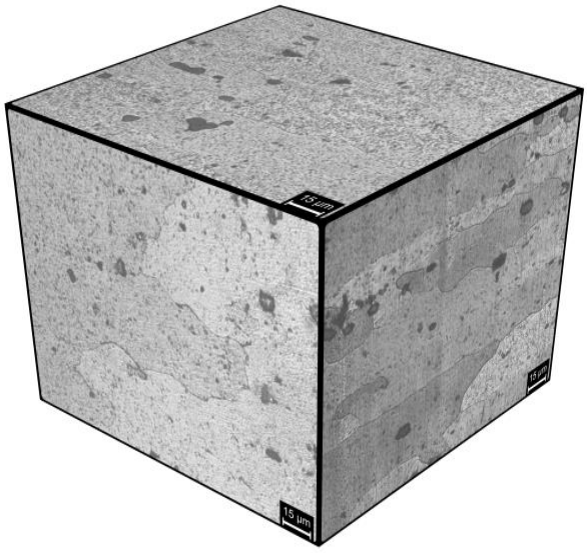

Figure 4.15: Microstructure of the AA2024-T3 alloy (Keller attack).

The main second phases of AA-2024 T3 alloy are S phases (Al_2CuMg) and Al-Cu-Mn-Fe [132, 145]. Generally, the formers are anodic with respect to the aluminum matrix because of the presence of magnesium, while the latter, consisting of more noble elements such as copper, iron, and manganese, are cathodic. S-phase is particularly active and higher amount of this phase is generally present. It quickly reacts with the solution just after dipping, thus leading to the dissolution of magnesium. As a result, the alloy surface becomes richer in copper and the corrosion potential tends to increase. At longer exposures, corrosion initiation occurs in some areas, then propagate in the aluminum matrix. Thick layer of insulating corrosion products then forms on the metal surface, which hinder the corrosion process as a result of the settlement of pseudo-passivation conditions. EIS spectra well evidence the formation of the corrosion products layer as a diffusive behavior at very low frequencies that is compatible with the hypothesized mechanism. The rate-determining step of the corrosion process is then mainly related to the diffusion processes inside the porous non-conductive scale. The phase peaks at low frequencies can be related to the dissolution of the intermetallics at metal/particle interface [146]. During the welding process, recrystallization induced by the thermomechanical action occurs mainly at the nugget. In these zones, dissolution of nanometric S-phase precipitates occurs, which can re-precipitate in form of micrometric particles, clearly detectable at the scanning electron microscope (Figure 4.16). These precipitates are

mainly located at the recrystallized grain boundaries. The presence of copper in the supersaturated solid solution in the aluminum matrix gives rise to initially nobler OCP values compared to the nugget and HAZ. The enriching in copper because of the preferential dissolution of magnesium in S-phase, is responsible for the initial increasing of the OCP, but the rapid activation of corrosion phenomena at precipitate-free zones causes the decrease in the OCP after a few hours of immersion.

The anodic dissolution, catalyzed also by the presence of precipitates along the grain boundaries, is considered to be the main SCC mechanism in high strength 2xxx (Al–Cu–Mg) series alloys [147]. The galvanic interaction between the particles and the surrounding matrix causes the preferential dissolution of the anodic particles or the dissolution of the adjacent matrix surrounding nobler particles. Evolution of hydrogen always occurs in actively growing localized corrosion sites and cracks. The absorption of hydrogen into metals leads to the possibility of crack propagation by hydrogen embrittlement (HE) [131, 147–157].

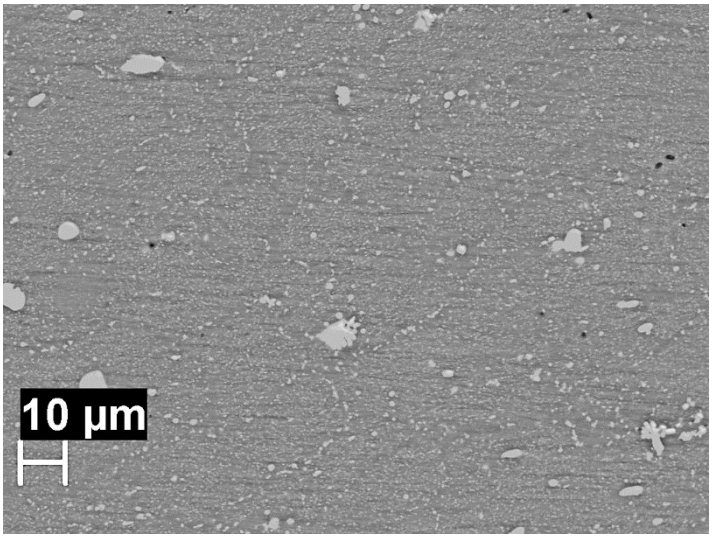

Figure 4.16: SEM image of the nugget without metallographic attack: the bright zones are the macro and micrometric precipitates of S-phase.

In this way, FSW modifies the microstructure of AA2024-T3 alloy, thus making the nugget more susceptible to SCC than the base material. However, the HAZ and TMAZ are characterized by lower tensile strength compared to both the nugget and the base metal. The application of load causes the occurrence of micro-cracks at the nugget which do not propagate as the fracture is localized in zones with lower tensile

strength, i.e., plastic deformation is significantly shifted in the HAZ/TMAZ. Therefore, the strain at the nugget is limited and pseudo-passive film can be restored in such conditions, as demonstrated by the increases in the OCP.

Similar effect was observed on the same alloy by Ferri et al. on 4PBB loaded in elastic field during potentiodynamic tests [158]. This was attributed to dissolution mechanism assisted by the mechanical stress, according to the chemo-mechanical theory of Gutman [159]. The weakening of the effect as load levels approach the YS was ascribed to a barrier action of corrosion products film hindering the exit of dislocations from the surface and thus inhibiting the creation of fresh surfaces [158, 160]. The stress enhanced intergranular corrosion at nugget is inhibited as the specimens are plastically strained in TMAM/HAZ zones. In this way, the SCC phenomena cannot be observed, and the specimen fails in a ductile way in the TMAZ/HAZ, similarly to the test in air.

In other words, the decreasing of tensile properties in TMAZ/HAZ caused a deformation in these zones, counteracting the hypothetically higher stress enhanced intergranular corrosion susceptibility of the nugget.

A similar SCC behavior for joint and base metal of FSWed AA2219-T87 through slow strain rate tests (SSR) is reported by Paglia and Buchheit [71]. On the contrary, intergranular fracture in the interface between the nuggets and TMAZ of welded joints tested in 0.6 M NaCl solution is reported by Wang et al. [72]. The last authors reported that the tests in air showed ductile fracture in the same zone. This different behavior could be attributed to the different welding parameters. The same authors reported that the stress corrosion cracking (SCC) susceptibility of the FSW 2024-T4 aluminum alloy joint increased with feed rate due to the increase of the second phases size.

4.4. Conclusions

This chapter analyzed stress corrosion cracking phenomena in friction stir welding AA2024-T3 joints. Constant load (CL) cell and slow strain rate (SSR) tests were carried out in aerated 35 g/L NaCl solution. During the tests, open circuit potential and electrochemical impedance spectroscopy were measured in the different zones of the welding.

The FSW process significantly modifies the microstructure of the alloy, and therefore, its corrosion and stress corrosion cracking behavior.

The applied load enhances the intergranular corrosion at the nugget of the AA2024-T3 alloy owing to the presence of micrometric copper-rich precipitates at the border of the recrystallized grains. In this zones, no stress corrosion cracking was noticed, but well-evident stress-enhanced intergranular corrosion occurred. Moreover, the applied strain is preferentially localized at HAZ/TMAZ zones which are characterized by lower tensile strength compared to the nugget. Higher strain values are then localized at the heat-affected zones, where softening occurs.

Because of these contrasting effects, it is possible to state that the stress corrosion cracking susceptibility of the FSW-ed alloy is then similar to that of the base metal in the range of processing parameter studied in this experimental work.

5. *Effect of load on the corrosion behavior of friction stir welded AA7075-T6 aluminum alloy*

This chapter is derived from the article "Cabrini, M.; Bocchi, S.; D'Urso, G.; Giardini, C.;Lorenzi, S.; Testa, C.; Pastore, T (2020). Effect of load on the corrosion behavior of friction stir welded AA7075-T6 aluminum alloy. Materials, 13(11), 2600".
DOI: 10.3390/ma13112600.

I am immensely grateful to the support received from my co-authors. I am responsible for all the changes in this chapter with respect to the published version.

5.1. Introduction

As already mentioned in Paragraph 4.1, the corrosion behavior of FSWed joints is clearly linked to the environment and the loading conditions of the samples. In fact, the combination between an aggressive environment and a state of stress applied to the joint could promote different corrosion morphologies depending on the alloy considered.

In order to widely understand the response of the AA7075-T6 to external stimuli, this chapter focuses on the corrosion behavior of FSWed AA7075 joints, in a corrosive environment, as a function of the loading conditions. In particular, four-points bend-beam, constant loading, and slow strain-rate tests were carried out on AA7075 FSWed butt in aerated NaCl 35g/L solution at room temperature.

Regarding the conclusion reported in Paragraph 4.4, it is clear the different corrosion behavior of the AA2024 and AA7075 subjected to FSW process, and this is due, above all, to the very different microstructural and chemical characteristics of the AA2024 and AA7075 base materials.

5.2. Materials and Methods

5.2.1. Welds

Sheets with a thickness equal to 4mmwere considered. Table 5.1 shows the chemical composition of the AA7075-T6 alloy. Sheets of 200 mm × 80 mm were welded by using

a custom-made tool designed with a smooth plane shoulder (16 mm diameter) coupled with a frustum cone-shaped pin (maximum and minimum pin diameters were 6 mm and 4 mm, pin height was 3.8 mm). The rotational speed of the tool (S) was 1500 rpm and feed rate (F) was 10 mm/min. The set-up of the welding procedure was reported in a previous work [57]. The mechanical properties of the base materials and the welded joints are reported in Table 5.2. Good reproducibility was observed in terms of tensile strength of the FSW joints. Owing to non-uniform strain distribution, it was not possible to calculate the yield strength of the welded specimens.

Table 5.1: Chemical composition (% weight) of the alloy 7075-T6.

Al	Si	Fe	Cu	Mn	Mg	Zn	Ti	Cr
bulk	0.05	0.10	1.53	0.008	2.54	5.72	0.04	0.20

Table 5.2: Mechanical properties of the base materials and the welded joint.

Base material			FSW joint		
YS (MPa)	UTS (MPa)	Max Strain (%)	YS (MPa)	UTS (MPa)	Max Strain (%)
512	576	13.5	-	329	11

5.2.2. Metallographic Analysis

The microstructure was revealed through Keller's etchant after grinding by means of emery papers up to 4000 grit, then polishing with 0.1 µm alumina aqueous suspension and finally observed with Nikon (Eclipse MA100N, Tokyo, Japan) optical microscope and SEM (Zeiss EVO 50, Zeiss, Oberkochen, Germany) Oxford x-act sdd (silicon drift detector, nitrogen free) EDX equipment type model (Oxford Instruments, High Wycombe, UK).

5.2.3. OCP Monitoring

OCP was measured on the three different zones of FSW butt welds, i.e., the nugget, the thermomechanical affected zone/heat-affected zone (TMAZ/HAZ -it was not possible to separate the two zones) and the base metal. The specimens were cold-mounted in epoxy resin with an embedded wire to allow electrochemical measurements. A 20 mm × 20 mm

area was grounded with emery paper and then polished with colloidal alumina up to 0.1 µm. After polishing, the specimens were stored at room temperature (23°C) with relative humidity in the range of 25-30% for 48 h before the immersion, to allow the formation of the natural protective film. The specimens were dipped in different testing cells filled with aerated 35 g/L NaCl solution (Carlo Erba RPA reagent, Cornaredo, Italy). The OCP was measured by using a saturated calomel electrode (SCE E=+0.240 V vs Standard Hydrogen Electrode, Amel Instrument, Milano, Italy) positioned close to the surface of the specimens to reduce the ohmic drop in the electrolyte during electrochemical tests.

2.4. Four-Point Bending Tests

Four-point bending (4PBB) tests have been performed according to ASTM G39 on 4 mm × 20 mm × 160 mm prismatic specimens obtained by FSW joints (Figure 5.1). The specimens were polished by emery papers up to 1000 grit and degreased in acetone in ultrasonic bath for 5 min. After polishing, the specimens were left in still air for 48 h to allow the formation of the protective film.

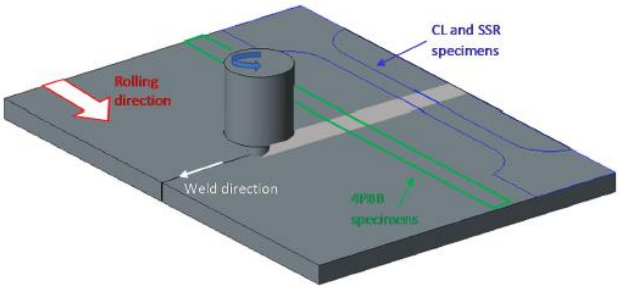

Figure 5.1: Schematic representation of specimens obtained by means of friction stir welding (FSW).

The specimens were positioned inside the bending device to attain a uniform tensile strain distribution over the welded surface. Four glass cylinders were used to avoid galvanic coupling between the stainless-steel specimen holder and the aluminum alloy. Four specimens were loaded up to 80% of the tensile strength of FSW joints derived by tensile tests (refer to Table 5.2). The other four specimens were dipped without loading (unloaded condition). Tests have been performed on four specimens for each condition (loaded and unloaded). All the specimens were exposed in a cell filled with about 30 L water, and 35 g/L sodium chloride (Carlo Erba RPS analytical grade reagents, Cornaredo, Italy) for 1500 h. To avoid the contamination of the testing solution by corrosion products

of aluminum during long-term exposures, the test solution was refreshed after 150 h and 500 h. The amount of water that was substituted was equal to 10 liters. During the procedure, the specimens were always left well below the waterline. The OCP was measured during the exposure. More details about the experimental set-up are reported in a previous work [137].

At the end of the long-term exposure tests, the specimens were unloaded, washed in distilled water, and then rinsed with acetone in an ultrasonic bath. The surfaces were then observed by means of optical microscopy up to 600 times magnification and SEM equipped with EDX.

5.2.4. Constant Load Tests

CL tests were carried out on a specimen of 4 mm × 8 mm × 82 mm gage length, with the weld positioned at the center of each specimen (Figure 5.1). The size of the specimens is reported in Figure 5.2. The specimen was settled in a double compartment cell (Figure 5.3a). All the compartments were maintained at room temperature filled with aerated NaCl 35 g/L solution (Carlo Erba RPS analytical grade reagents, Cornaredo, Italy). Water recirculation in the cell was granted during the tests. The OCP of the specimens was continuously monitored using a SCE positioned close to the metal surface by means of a Lugging capillary.

The specimens in the cell were positioned into the CL machine (no loading), then they were dipped in the test solution. After 120 h of OCP monitoring, the specimens were loaded at 190 MPa, corresponding to 54% of the ultimate tensile strength (UTS) of the weld. This value is slightly lower than the elastic limit of the weld obtained by means of tensile tests. The specimens were left at this value for 350 h and the OCP was measured during all the period. Then, the applied load increased up to 279 MPa, corresponding to 80% of the UTS of the weld (homogeneous plastic deformation field).

The OCP was measured until 720 h of exposure (one month).

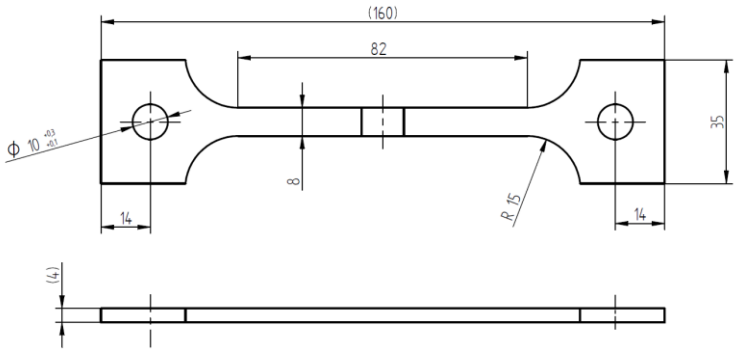

Figure 5.2: CL and SSR specimen: the weld is in the center of the gouge length, the thermomechanical.

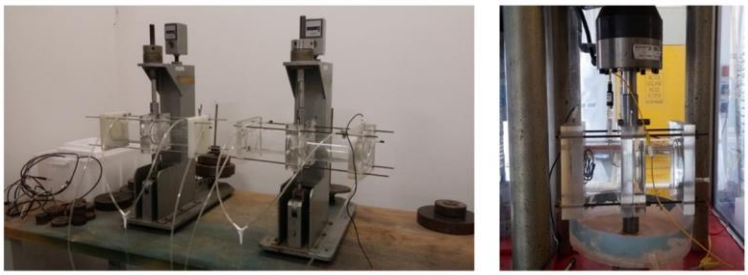

(a) **(b)**

Figure 5.3: CL test device (a) and SSR test device (b).

5.2.5. Slow Strain-Rate Tests

The SSR tests were carried out by using specimens of the same dimensions as the CL tests. The set-up of the tests is shown in Figure 5.3b. The tests were carried out on a 30 kN testing machine at displacement rates varying from $5x10^{-7}$ to $5x10^{-3}$ mm/s. A displacement rate of $8.2x10^{-4}$ mm/s was used in order to have a strain rate of 10^{-6} s^{-1} as average value on all the gage length. During the tests, the load and OCP were measured continuously. At the end of the tests the specimens were washed in distilled water and rinsed in acetone to permit the observation of the fracture surface under the SEM. Then the specimens were longitudinally sectioned for the metallographic observation.

5.3. Results

5.3.1. Metallographic Analysis

The microstructure of the AA7075-T6 alloy has already been presented in [57]. Coarse precipitates along the grain boundaries (Figure 5.4) and micrometric precipitates within

the grains of α-Al, oriented in the rolling direction [144], can be well demonstrated. The strengthening $MgZn_2$ nanoprecipitates are not visible under the optic or SEM microscope, while macro-precipitates are copper and iron-rich phases as Al_2CuMg and Al_7Cu_2Fe or zinc and magnesium rich phases, i.e., undissolved MgZn2 during alloy solution annealing treatment, or MgSi.

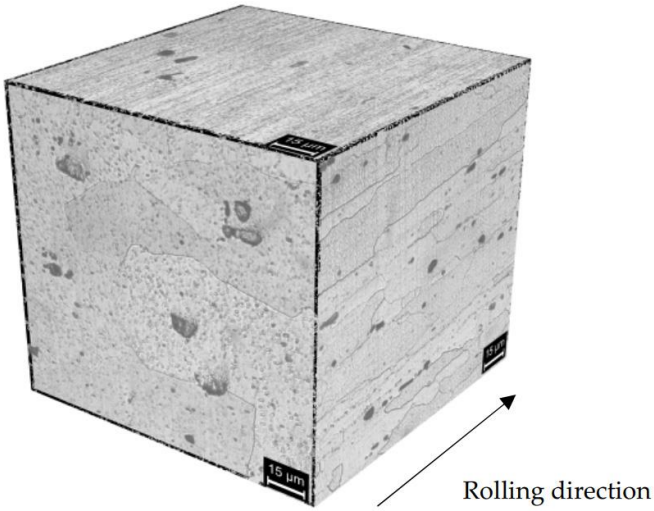

Figure 5.4: Optical image (Keller attack) of the alloy AA7075-T6 (base material). Elongated grains along the rolling direction and the macro-precipitates are visible.

In the nugget, re-crystalized fine equiaxed grain structure can be noticed. In addition, $MgZn_2$ strengthening precipitates are dissolved (T6 artificial ageing temper) into the supersaturated solid solution and reprecipitated after cooling (Figure 5.5). Venugopol et al. affirmed that the temperature obtained during the process is below the melting temperature of the alloy, but above the solutioning temperature, as demonstrated by the re-crystallization of the weld nugget and the redistribution of the precipitates [161]. For the same authors, the absence of fine precipitates in the weld nugget indicates that the cooling rates are such that larger precipitates could nucleate and grow but not the finer ones. In the TMAZ, the precipitates are quite random, and the coarsening of finer precipitates observed in base material can occur during welding [161].

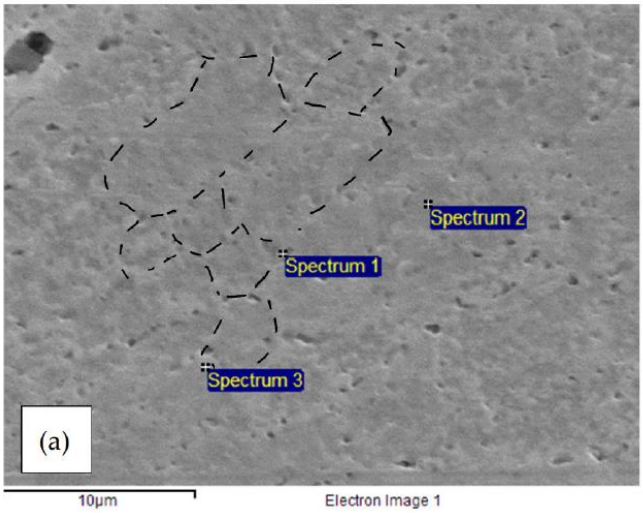

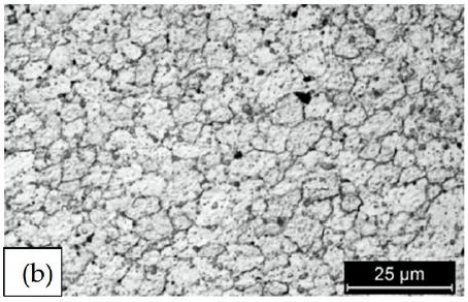

	Mg	Al	Cu	Zn
Spectrum 1	3.24	85.37	2.90	8.48
Spectrum 2	2.49	89.14	1.56	6.82
Spectrum 3	2.64	88.65	1.82	6.90

Figure 5.5: SEM image of the nugget of the FWS 7075 alloy (no metallographic attack) the rounded recrystallized grains are visible owing to the precipitates of MgZn2 on their grain borders and EDX spectra in which is visible an enrichment of zinc and copper in the correspondence of the precipitates. In the image the grain border is demonstrated; (b) optical image of the nugget with metallographic attack (Keller's reagent) that better demonstrated the rounded recrystallized grains.

The size of the precipitates at the grain boundaries of the HAZ (Figure 5.6) is unfortunately too small to permit their observation under the SEM, but many transmission electron microscope (TEM) observations were reported in the literature and they demonstrated that these smaller precipitates play a fundamental role in the intergranular corrosion and the SCC of these alloy series [76].

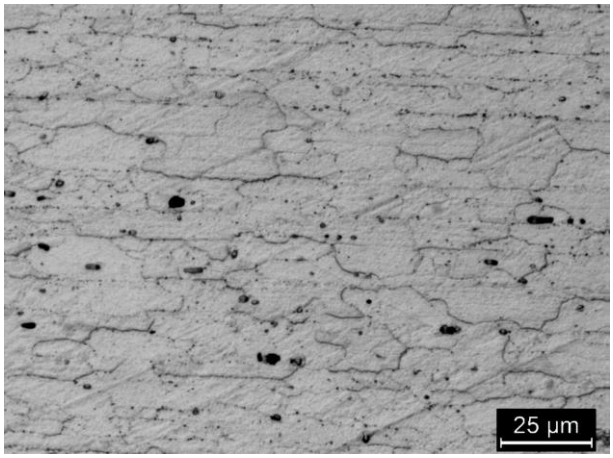

Figure 5.6: Optical image (Keller attack) of the HAZ of the FWS AA7075 alloy. The grains appear elongated along the rolling direction; presence of macro-precipitates is evident.

5.3.2. 4PBB Specimens

The OCP measurements (average values of four specimens) did not show any evident differences between 4PBB loaded and unloaded specimens (Figure 5.7). The corrosion potentials generally were in the range of -870÷-840 mV vs SCE; the corrosion potential showed a sharp decrease during the solution refresh owing to the partial removal of non-adherent scale of corrosion products that exposes the corroded surface on the fresh solution; after this, the corrosion potential increases to the same potential values detected prior to the partial substitution of the testing solution. This effect was more marked for specimens without loading compared to loaded specimens. The corrosion potential of the loaded specimens decreases after 1300 h, then it increases again. Compared to the values obtained by the analysis of the three different zones (nugget, TMAZ/HAZ and base materials - Figure 5.8) similar results can be outlined in both the TMAZ/HAZ and the nugget. The base metal showed slightly nobler potential values.

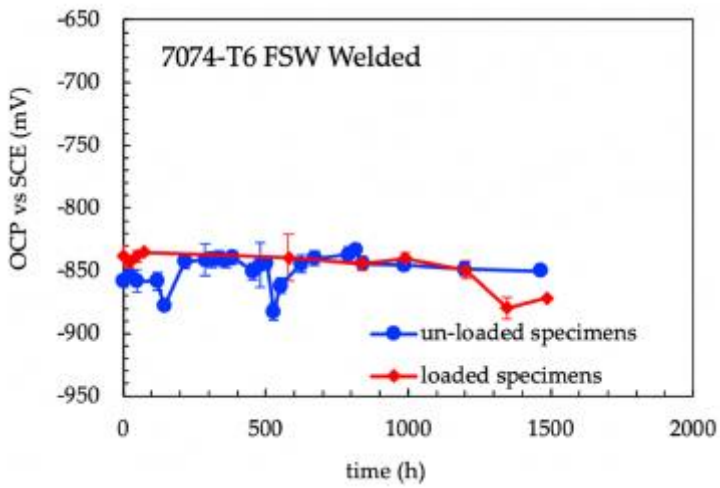

Figure 5.7: Open circuit potential (OCP) vs time for loaded and unloaded 4PBB specimens. The decreasing of the OCP of the specimens in the correspondence of the partial refresh of the test solution that breaks the aluminum oxide scale and exposes fresh metal surface to the aggressive solution.

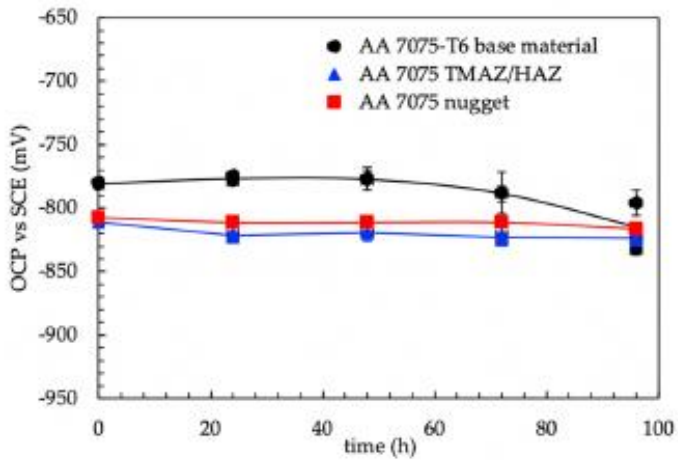

Figure 5.8: OCP vs time of the different zones (base materials, TMAZ and nugget) of the alloy AA7075-T6.

Figure 5.9a shows the corrosion morphology of the specimens at the end of the 4PBB tests.

No differences in the corrosion morphology were observed between the loaded and unloaded specimens. The HAZ is preferentially corroded. The attack propagates along the grain boundaries, following the rolling direction (Figure 5.9b). The EDX analysis (Figure 5.9c) demonstrated the depletion of zinc and copper in the corroded zone (Spectrum 1) with respect to the un-corroded zones (Spectrum 2).

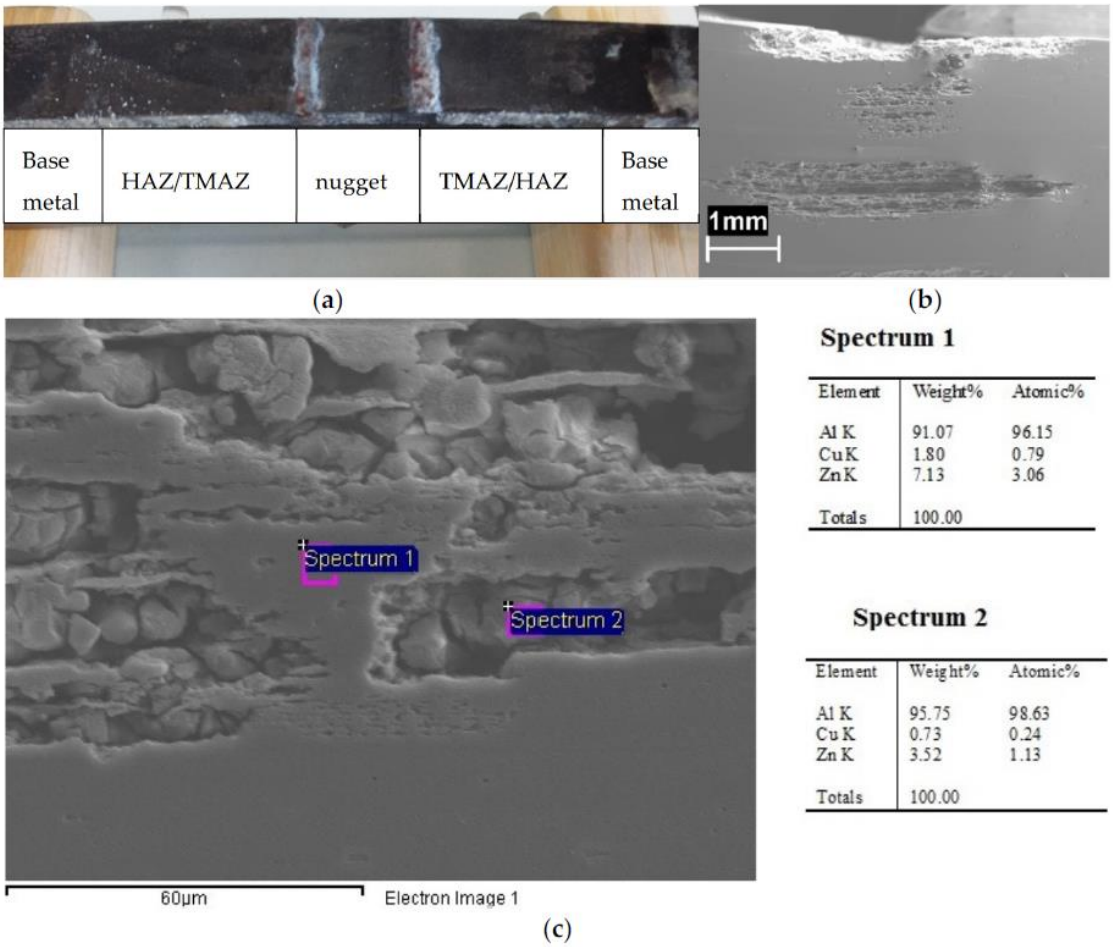

Spectrum 1

Element	Weight%	Atomic%
Al K	91.07	96.15
Cu K	1.80	0.79
Zn K	7.13	3.06
Totals	100.00	

Spectrum 2

Element	Weight%	Atomic%
Al K	95.75	98.63
Cu K	0.73	0.24
Zn K	3.52	1.13
Totals	100.00	

Figure 5.9: (a) Image of a 4PBB specimens after the test: an intense localized attack in the attack in the correspondence of the TMAZ and (b) SEM image of the metallographic longitudinal section of the loaded specimen in which is visible the deviation of the attack along the rolling direction, (c) particular of the attack and EDX analysis.

5.3.3. Constant Loading (CL) Tests

Figure 5.10 shows the effect of the applied load on the OCP of the CL specimen. The OCP of the unloaded specimens rapidly stabilized between -850 and -800 mV vs SCE. The fluctuations are mainly ascribable to the removal of corrosion products of aluminum formed at very early exposures, due to the recirculation of the testing solution. When the specimen is loaded in elastic field, a decrease in the OCP was noticed but the potential values stayed in the same range measured in unloaded condition.

Conversely, at strain level exceeding the yield stress -i.e., in the plastic field- 100 mV decrease in the OCP occurred due both to the rupture of the thick corrosion product scale of aluminum and the plastic straining exposes the very active metal to the aggressive

environment. The OCP came back to the initial value after about 24 h. This value remained almost constant, until the end of the tests.

The specimen did not break during the tests but showed a corrosion attack mainly localized at the HAZ (Figure 5.11). Differently from the 4PBB specimens, the attack appears wider, and positioned perpendicularly to the loading direction coinciding with the rolling direction (Figure 5.11c and Figure 5.12a).

Some small ramifications along the grain boundaries were observed (Figure 5.12b).

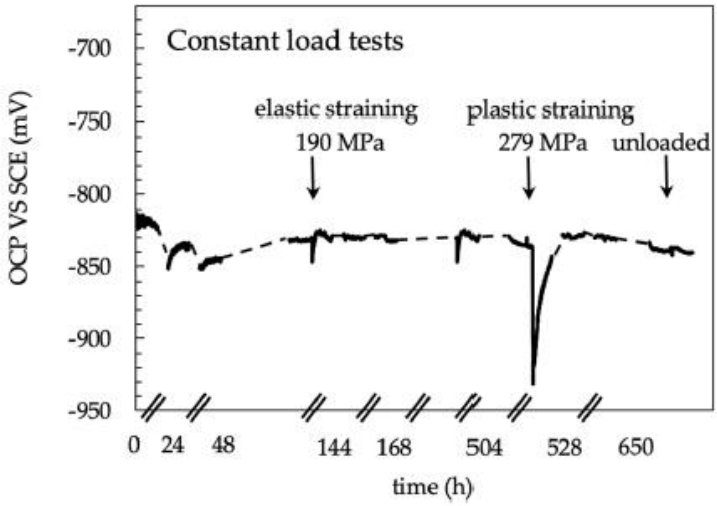

Figure 5.10: Open circuit potential measurements of the specimen loaded at different values during CL test. The decrease in the OCP mainly occurs as loading increase due to aluminum corrosion products cracking.

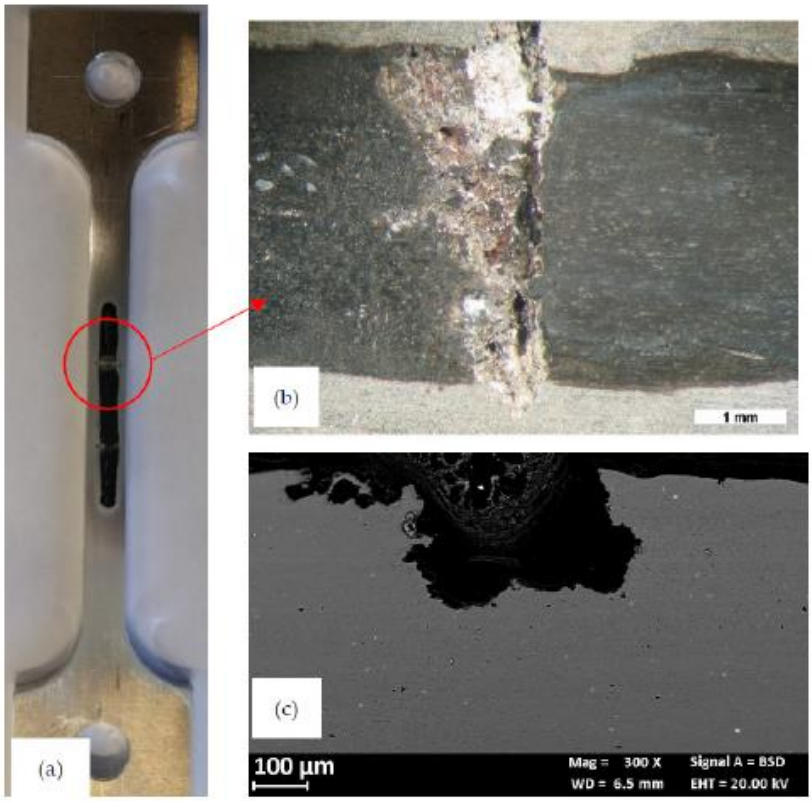

Figure 5.11: Aspect of the specimen at the end of the constant load test. (a) Macro image: the dark zone in the central part exposed to the NaCl 0.6 M solution; (b) close-up of the red circle with the selective attack of the TMAZ; (c) metallographic section of localized attack.

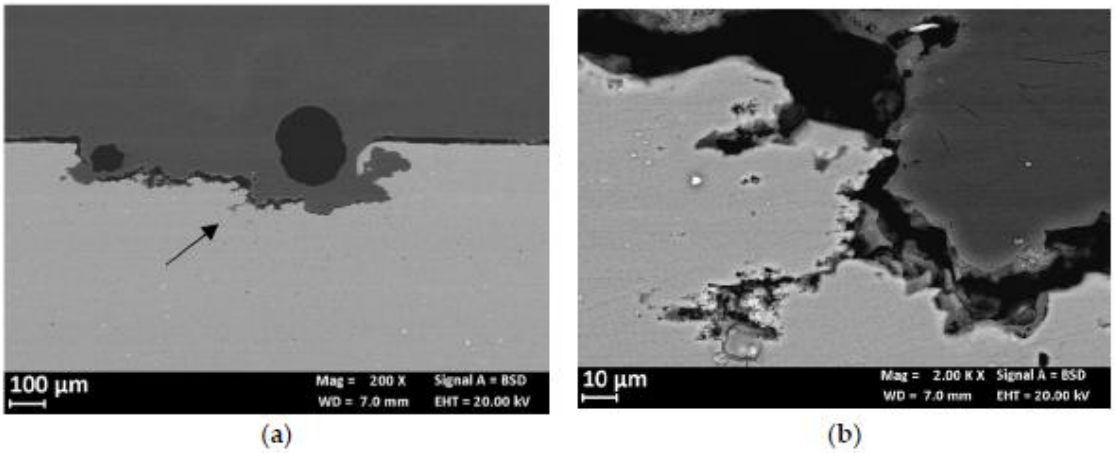

Figure 5.12: (a) Metallographic section of the enlarged localized attack in the TMAZ zone of the CL specimen. Close-up of the arrow in (b) in which is evident the change the morphology of attack that allows the rolling direction.

5.3.4. Slow Strain-Rate (SSR) Tests

Figure 5.13 reports the load and OCP measurements performed during the SSR tests of the AA7075-T6 base materials and the FSW joints. The tests were twice repeated, but only one curve for each condition is reported in the graph for simplicity. The tensile curves of the base material and the weld obtained in air or in NaCl 0.6 M are practically overlapped. The time to failure of the base material is close to the mean value with a very small deviation of 7%. 25% deviation was observed for the welded specimens. No stress-corrosion crack occurrence was noticed for the base metal and the time to failure in 0.6 M NaCl solution is even longer compared to the value measured at air. The role of active corrosion in NaCl solution can be hypothesized to enhance dislocation mobility and thus the plastic deformation, as reported by Jones et al. [144, 162]. The authors named this phenomenon anodic attenuation of strain hardening.

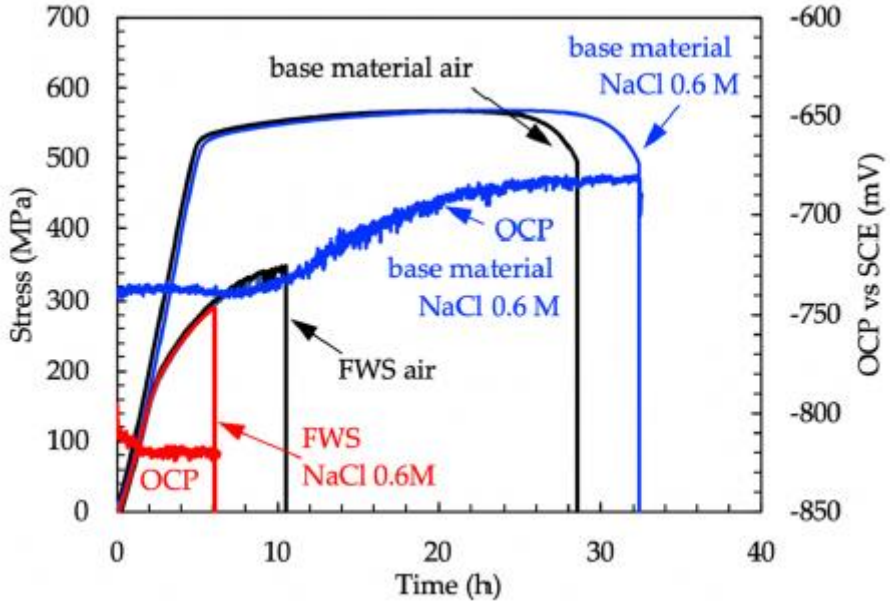

Figure 5.13: Stress vs. time and OCP of the specimens during the slow strain-rate tests.

Figure 5.14 compares the fracture surface of the SSR specimens after the test in air and in 0.6 M NaCl solution. The fracture surface at air (Figure 5.14a) showed a shearing failure, typical of the prismatic specimens, while the fracture surface of the specimen after the SSR test in 0.6 M NaCl solution exhibits an initial flat area (Figure 5.14b) due to the presence of microdefects able to trigger localized corrosion initiation. These microcracks are mainly at macro-precipitates (black arrows in Figure 5.15a) and have depth less than

100 μm. In the correspondence of these microcracks, the fracture surface is heavily corroded (Figure 5.15b) and it is possible to observe the presence of several micro-precipitates. The flat zone of the fracture surface (Figure 5.16b) is mixed brittle/ductile as some small dimples and quasi cleavage areas were observed, similarly to the fracture surface at air (Figure 5.16a). The presence of very small zones with typical SCC morphology, indicated with the arrows in Figure 5.16b [162] was also confirmed; the final shearing fracture of these specimens was similar to that in air.

No macroscopic SCC phenomena were observed probably due to the strain rate (10^{-6} s^{-1}) value adopted and very aggressive NaCl solution. Results presented in other works [141] confirmed the absence of stress corrosion on this alloy during the SSR tests at the OCP and strain rate of 10^{-6} s^{-1}.

The OCP remains constant in the elastic field, but it increases with the plastic deformation, probably due to the enrichment in iron and copper due to the dissolution of the surrounding aluminum matrix. This observation is supported by back-scattered electron (BSE) image and EDX spectrum (Figure 5.17).

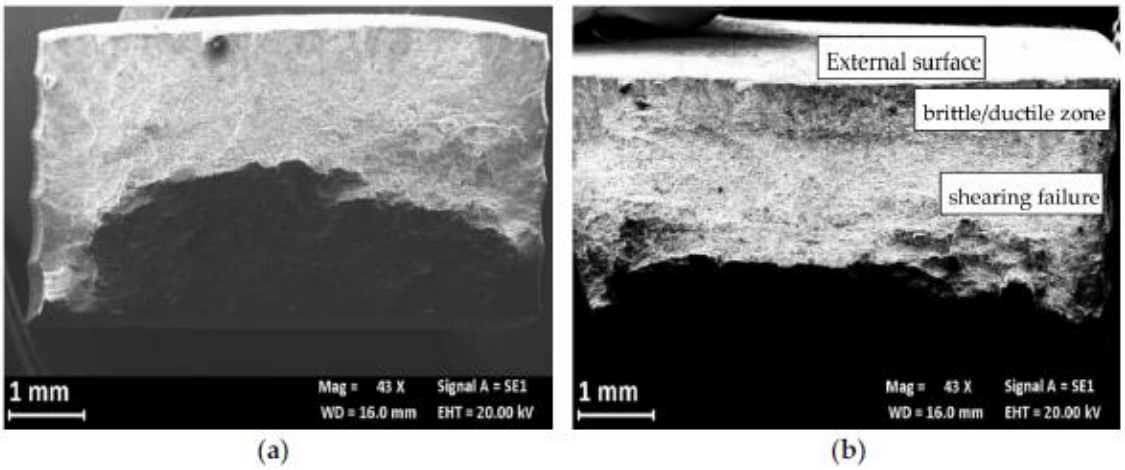

Figure 5.14: SEM image of the fracture surface of the AA7075-T6 specimen after the SSR test (a) macro at air, (b) macro in 0.6 M NaCl solution.

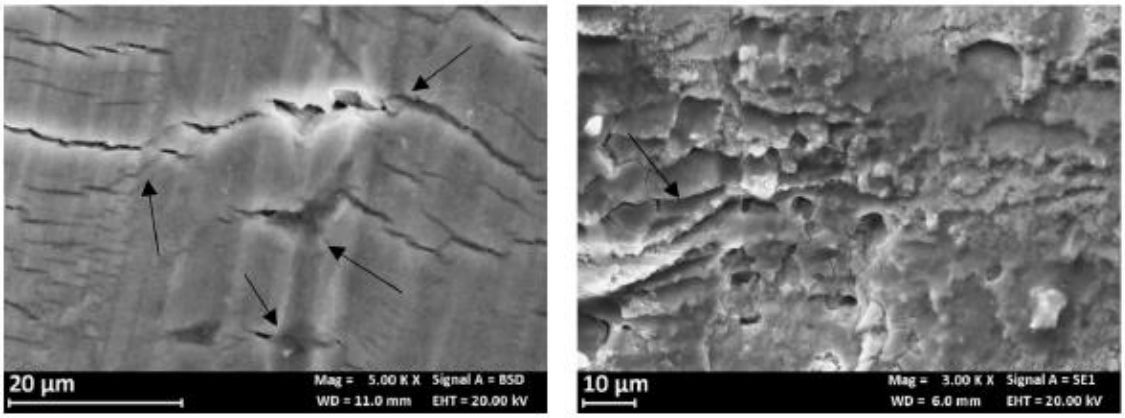

(a) (b)

Figure 5.15: SEM image of the fracture surface of the AA7075-T6 specimen after the SSR test (a) specimen surface with corrosion products of aluminum and several microcracks at macro-precipitates (black arrows); (b) particular of fracture initiation zone after SSR test in 0.6 M NaCl solution.

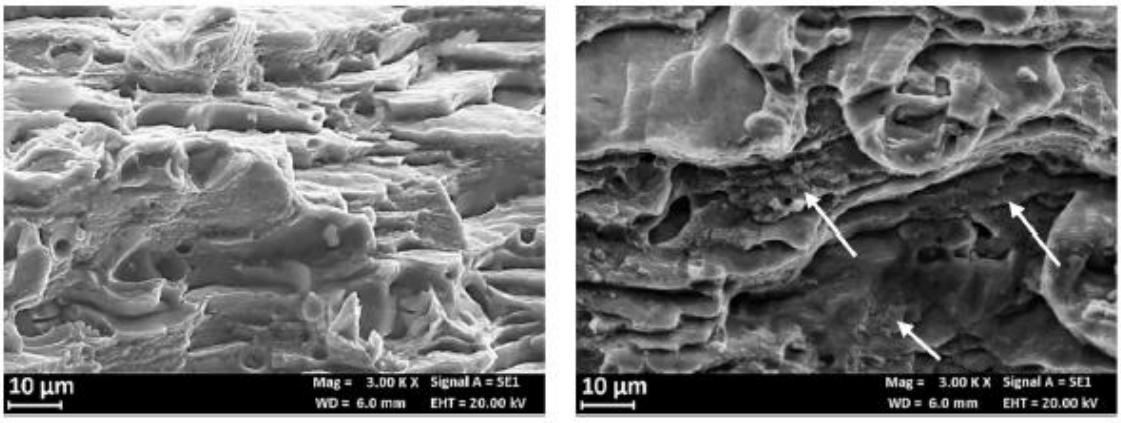

(a) (b)

Figure 5.16: SEM image of the fracture surface of the AA7075-T6 specimen after the SSR test: (a) particular of the fracture surface at air and (b) in 0.6 M NaCl solution (the arrows indicate small areas with typical SCC morphology).

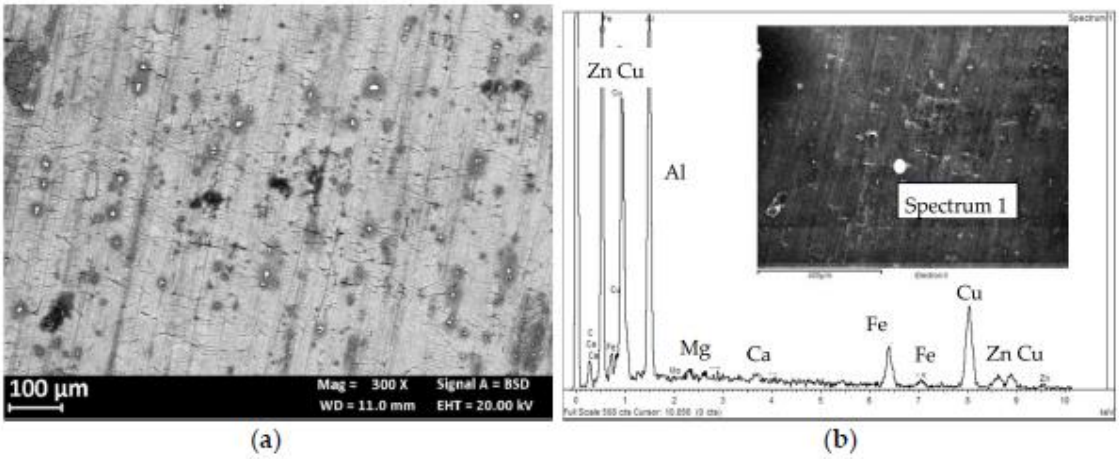

Figure 5.17: Backscatter electron detector (BSD) image of the external surface of a base material specimen after the SSR test in NaCl 0.6 M, the bright zone indicates precipitates with higher atomic weight than the aluminum matrix; (b) EDX spectrum of one of these particles.

The curves of the FSW joints exhibit time-to-failure values lower than the base material. This can be mainly ascribable to the decrease in the tensile properties at the joint TMAZ/HAZ zone, as observed also elsewhere [38, 57, 135, 163]. Consequently, the hardness and then the UTS of the alloy decrease due to microstructural modifications [24, 164].

Figure 5.18a reports the hardness profile of the longitudinal section of the weld. The hardness sharply decreases at the TMAZ/HAZ and, therefore, the plastic deformation mainly occurs at this point, thus decreasing the total elongation at break and the time of failure. Despite the high strain rate due to plastic strain localization at TMAZ/HAZ, slight decrease in the time to failure in 0.6 M NaCl solution was noticed compared to air -i.e., 10±0.5 h -thus denoting SCC occurrence. Bala Srinivasana et al. reported about SCC phenomena in the HAZ of the AA7075 of mixed FWS joints of AA7075 and AA6056, when the specimens were tested at strain rate 10^{-7} s^{-1} in NaCl solutions, but only localized corrosion in the tests carried out at 10^{-6} s^{-1} was detected [165]. The SEM observation of the surfaces demonstrate a flat zone at fracture initiation with maximum depth of 1mm (Figure 5.18b and c). The presence of non-coherent corrosion products of aluminum and several precipitates was also noticed (Figure 5.19a).

EDX analysis detected the presence of zinc, aluminum, and copper, as well as magnesium depletion (Figure 5.20). The final fracture is by shearing (Figure 5.18b) and its

morphology is characterized by elongated dimples and a few brittle areas (Figure 5.19b), similarly to the base material (Figure 5.16).

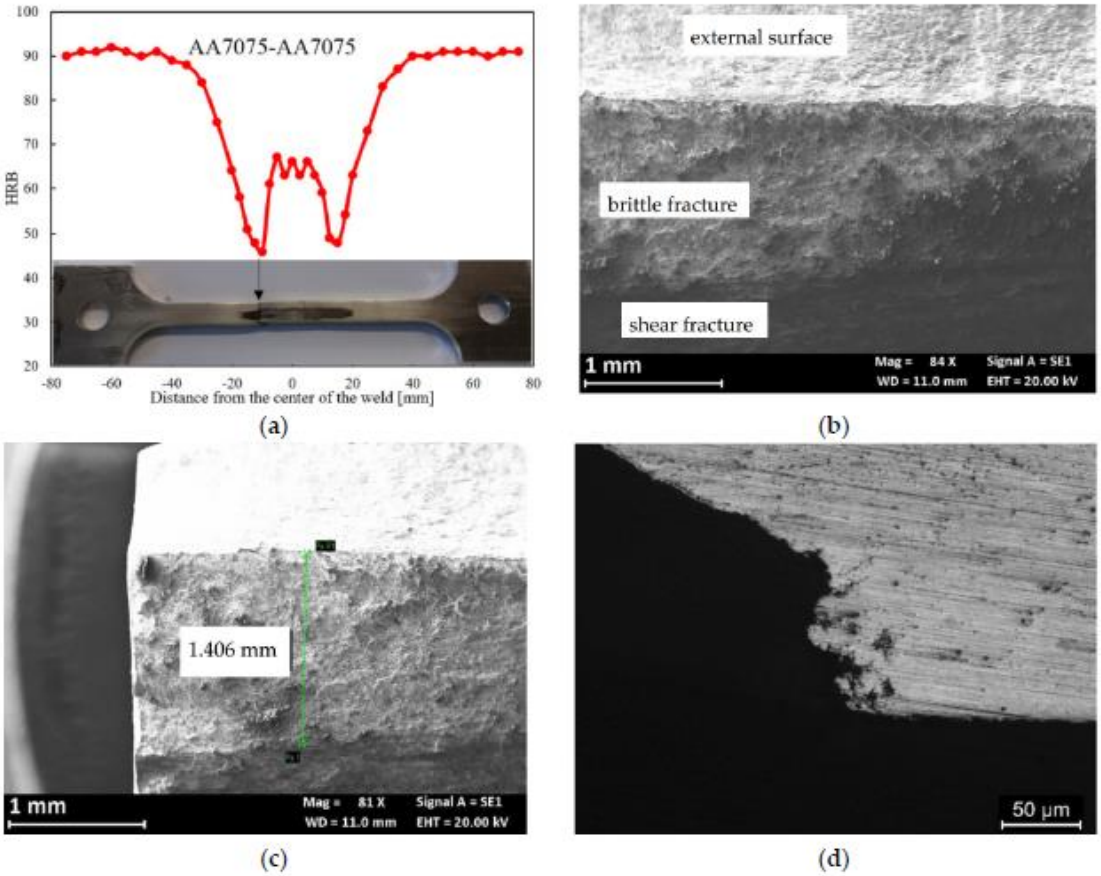

Figure 5.18: (a) Hardness profile along the FSW butt joint; (b) SEM image of the fracture surface, a flat zone of about 1 mm of growth (close-up in (c) is highlighted in (d)) metallographic section of the fracture surface in which is visible the flat zone and the small ramifications.

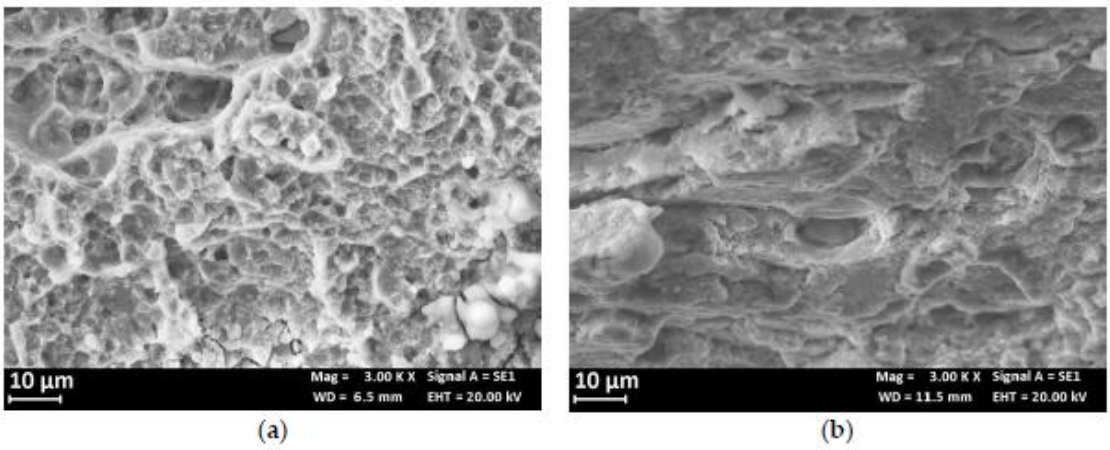

Figure 5.19: (a) Particular of the mixed ductile/brittle fracture zone and (b) of the ductile shearing. final rupture.

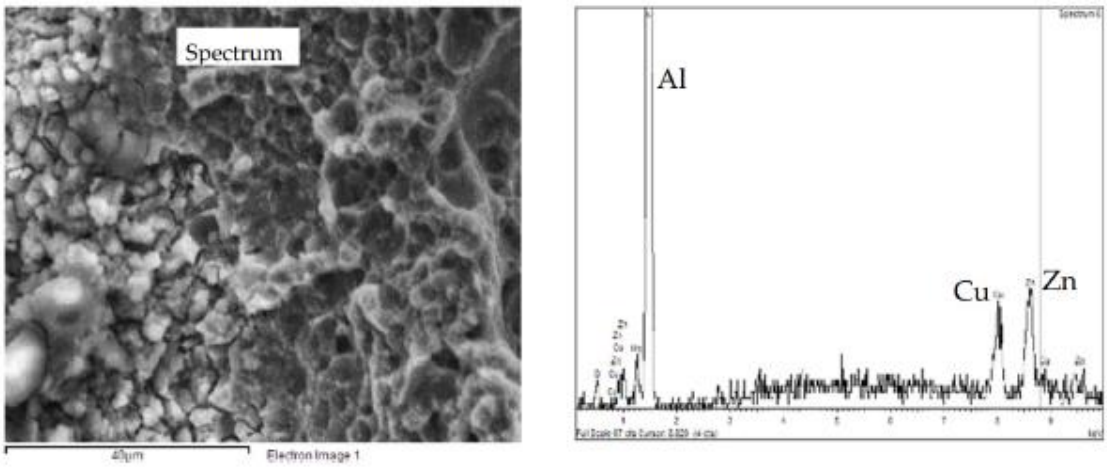

Figure 5.20: EDS spectrum of the precipitates present on the mixed ductile/brittle zone of the fracture surface of the FWS specimen after the SSR test in 0.6 M NaCl solution.

The OCP of the FSW butt joints lies in the range of -820÷-810 mV vs SCE and it is less noble than the base material, whose potential was in the range between -725 and -670 mV vs SCE. The OCP of the FSW alloy decreases during the elastic deformation. Conversely, constant values were detected once the specimen was strained in the plastic field. The values of the OCP of the FSW specimens during SSR tests are close to that measured during 4PBB tests and CL tests (Figure 5.7 and Figure 5.10), corresponding to the OCP of the TMAZ/HAZ and the nugget (Figure 5.8). The very low OCP potential indicates that these zones are more susceptible to corrosion than the base material, as confirmed by the intense attack observed on the specimens at the end of the test.

5.4. Discussion

These results confirmed the higher corrosion susceptibility of the TMAZ/HAZ of the AA7075 FSW joints with respect to the nugget and the base material, but there is no agreement between the different geometries of the specimens.

No SCC occurrence was noticed after 4PBB tests, but severe localized attack along the rolling direction at TMAZ/HAZ. Shallow defects at TMAZ/HAZ were observed after CL and SSR tests, which direction was perpendicular respect to the applied load. The higher corrosion susceptibility of the TMAZ/HAZ can be attributed to the microstructure modification produced by the FSW process. The presence of

precipitates at the grain boundaries less noble than the matrix promotes the intergranular corrosion of the alloy [166]. Different mechanisms were proposed to explain their effect, Maitra and English affirmed that the grain boundaries have a more active breakdown than the matrix and preferentially initiated the pitting [167], while other authors consider the effect of acidification generated by the preferential dissolution of the anodic particles as the cause of the continuous grain-boundary attack [168, 169]. The intergranular attack through thickness direction (short transverse -S) is much lower than that in either longitudinal (L) and transverse (T) directions for rolled plates owing to the microstructural anisotropy while the breakdown potentials were independent of sample orientations [170].

Similar mechanisms have been formulated to explain the SCC mechanism of aluminum 7XXX alloys, mainly hypothesizing hydrogen embrittlement [76, 134], but also slip-dissolution mechanism [171].

Naijar et al. proposed a mixed mechanism, in which the SCC phenomena were initiated from localized attacks at macro-precipitates present on the alloy surface (i.e., Al_7Cu_2Fe or Al_2CuMg) or on grain boundaries [171]. The hydrolysis of the produced cations induces the local acidification of the occluded cell and, as consequence, the possibility to electrochemical evolution of hydrogen. These authors suggested that localized dissolution at precipitates or at the grain boundary corresponds to the formation of critical defects, which is the first step of the SCC. The deterioration of the passive film and the anodic dissolution of the metal promotes hydrogen uptake and diffusion inside the metal lattice.

As the defects act as local stress intensifier, intergranular fracture are promoted, especially in the short-transverse direction for which grain boundaries are favorably oriented to the applied tensile stress [172]. Vasudevan and Sadananda [173] reported the decrease in the crack propagation rate in NaCl solution with the increasing of the precipitates size at the grain boundaries, and the depletion in copper of the aluminum matrix. The positive effect of precipitates size was also underlined by other authors [174].

On the contrary, the results of Ashai et al. on smooth specimens of Al-4.3Zn-1.7Mg alloys in 3.5% NaCl+0.2% H2O2 solution, demonstrated an inverse correlation between the time to failure (failure rate) and the size of precipitates at the grain

boundaries [175]. This can be ascribed to the preferential dissolution of the MgZn2 precipitates at the grain boundaries [159].

Talianker and Cina demonstrated a clear relationship between the presence of dislocations aside to grain boundaries and the susceptibility to stress corrosion of AA7XXX. [176].

The fractographic analysis of the specimens demonstrated the microcracks initiation preferentially at larger precipitates. The nugget and the TMAZ/HAZ showed lower OCP, thus indicating higher susceptibility to corrosion than the base material. No SCC microcracks propagation was noticed at the nugget due to the large size of the strengthening MgZn2 micro-precipitates -that decreased the SCC susceptibility- and the higher tensile strength compared to the TMAZ/HAZ zones. Under constant deformation tests, such as 4PBB tests, the applied stress naturally decreases during the exposure as localized attack propagate toward the specimen thickness. In addition, the tensile stress acts on these specimens in the direction of the elongated grains, and therefore the SCC cracks should propagate in the perpendicular direction. For these reasons, corrosion takes place in form of localized attacks at the elongated grain boundaries along the rolling direction (Figure 5.9).

In SSR and CL tests, the localized attacks and the plastic strain mainly occurred at TMAZ/HAZ, thus triggering the formation of SCC crack embryos. Based on the abovementioned mechanism, hydrogen embrittlement should promote SCC microcracks propagation. Hydrogen supplied by both the cathodic reaction and the anodic dissolution of the matrix/precipitate interphase can diffuse in the high stressed zone and promotes brittle crack propagation. The SEM analysis confirms the presence of several submicrometric precipitates in the correspondence of the brittle areas of the fracture surface.

The iron-rich phases can consequently enhance the hydrogen evolution mechanism because the hydrogen overpotential on these phases is lower than that on aluminum. Conversely, the applied plastic strain enhanced the corrosion rate by means of the chemo-mechanical effect underlined by Gutman. This effect is higher at the interface between the matrix and second phases, which acts as an obstacle to the movement of the dislocations [144, 158]. In these zones, the very high dissolution rate of the alloy is prevalent, and hydrogen cannot reach the critical concentration to produce

cracking. In the CL tests the attack becomes enlarged and no failure of the specimens were observed. On the other hand, the only small propagation of microcracks noticed after SSR tests suggests that the final rupture quickly occurred with a shear mechanism because of the high strain rate at the TMAZ/HAZ. For this reason, no evident stress-corrosion cracking phenomena were observed.

5.5. Conclusions

This chapter studied the stress-corrosion cracking behavior of AA7075-T6 aluminum joints made by FSW as a function of loading conditions. SCC tests were performed by considering constant deformation (4PBB and CL) conditions and SSR conditions in aerated NaCl 35g/L solution at room temperature.

Certain susceptibility to SCC was demonstrated for AA7075 FSW butt joints tested in this work mainly at the TMAZ/HAZ as nucleation of crack embryos occurred during both CL and SSR tests. However, high dissolution rate of the metal inside the localized attack prevents the achievement of critical crack size to promote its propagation up to rupture.

Slight decrease in the free corrosion potential was noticed because of the modification of the microstructure introduced by the welding process mainly at the TMAZ/HAZ and the nugget with respect the base material. As the TMAZ/HAZ zone is characterized by low tensile strength compared to both the nugget and the base material, it is preferentially strained under loading conditions. The plastic strain then enhances the active dissolution rate of the metal matrix and severe attack takes place, thus hindering SCC crack propagation.

The penetration depth of the intergranular attack was deeper after the four-point bent-beam tests compared to all the other testing techniques. Preferential dissolution along the grain boundaries was found in heat-affected zones and the attack follows the elongated grain structure along the rolling direction.

6. *Effects of cooling conditions on microstructure and mechanical properties of friction stir welded butt joints of different aluminum alloys*

This chapter is derived from the article "Bocchi, S.; D'Urso, G.; Giardini, C.; Maccarini, G. (2019). Effects of cooling conditions on microstructure and mechanical properties of friction stir welded butt joints of different aluminum alloys. Applied Sciences, 9(23), 5069".
DOI: 10.3390/app9235069.

I am immensely grateful to the support received from my co-authors. I am responsible for all the changes in this chapter with respect to the published version.

6.1. Introduction

As reported in Paragraph 1.1, the aluminum has proven to be a material characterized by good mechanical properties, which could be even excellent in precipitation hardening alloys. However, these high-strength alloys are also characterized by a poor response to the high temperatures reached during traditional welding melting processes. In the FSW process, despite never melting, it has been shown in the previous chapters that the temperatures reached in a FSW process are able to modify the microstructure and the metallurgical characteristics of the alloy leading to a worsening of the mechanical properties, especially in the HAZ.

The main goal of research in recent years is to further limit these microstructural changes. This necessarily means operating on the thermal cycle to which the joints are subjected to during the FSW process. To do this, possible post welding heat treatments have been studied by various authors, as reported in Paragraph 2.3. However, this type of post treatments was not satisfactory because they limited the size of the treatable pieces and increased energy outflow, characteristics that make two of the main strengths of the FSW process disappear. However, the technique that allows to control the thermal cycle without the negative aspects of post-process heat treatments is to use alternative to air-cooling systems during the welding process itself. For this purpose, different cooling fluids can be used, as reported in Paragraph 2.3.

The research reported in this chapter is aimed at the evaluation of the difference between the properties of several FSWed aluminum alloys joints welded with the traditional air-cooled process and others obtained by the combination of the traditional friction stir welding setup with a water-cooling system.

This analysis is primarily focused on the investigation of the effects of a water-cooling system on the mechanical properties and the microstructural characteristics of the joints for all the studied alloys to compare the effects and to identify the optimal working conditions for each material.

6.2. Materials and Methods

The chemical composition and the mechanical properties of the base aluminum alloys used in the experimental procedure are reported in Table 6.1 and Table 6.2.

Table 6.1: Chemical composition (% weight) of the base materials.

Alloy	Al	Si	Fe	Cu	Mn	Mg	Zn	Ti	Cr
AA2024 - T3	bulk	0.06	0.09	4.50	0.46	1.40	0.08	0.04	0.03
AA6082 – T6	bulk	0.9	0.36	0.07	0.42	0.8	0.05	0.03	0.02
AA7075 - T6	bulk	0.05	0.10	1.53	0.008	2.54	5.72	0.04	0.20
AA5754 - H111	bulk	0.103	0.34	0.059	0.318	2.808	0.019	0.009	0.019

Table 6.2: Mechanical properties of the base materials.

Alloy	YS [MPa]	UTS [MPa]	Max strain [%]
AA2024 – T3	344	464	16
AA6082 – T6	281	326	16
AA7075 – T6	512	576	13.5
AA5754 – H111	84	212	25.9

Both air-cooled and water-cooled FSW tests were carried out for each material on 200 x 80 x 4 mm sheets using a FAMUP MC60 CNC machine equipped with a suitable tool for the Friction Stir Welding. The tool was characterized by a smooth

flat shoulder (16 mm diameter) and a frustum of cone pin (maximum and minimum diameters equal to 6 and 4 mm, height equal to 3.8 mm) (Figure 6.1).

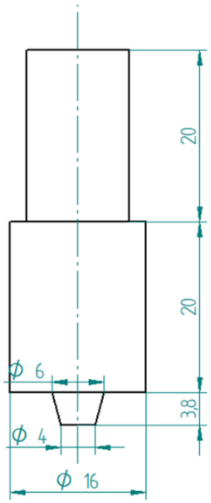

Figure 6.1: FSW tool geometry (dimensions unit: mm).

Due to the considerable forces generated during a FSW welding, it was necessary to fix the sheets to be welded on a support plate through 6 grips, as reported in Figure 6.2.

Figure 6.2: Support plate for the FSW process.

The welding parameters have been defined through a detailed bibliographic analysis, to obtain the best combination of rotational speed and feed rate for each alloy maximizing the mechanical characteristics of the welded joints [21, 28, 30, 48, 90, 93, 177, 178].

Table 6.3 shows the parameters used in the experimental campaign.

Table 6.3: Parameters used for the experimental setup.

Aluminum alloy	Rotational speed [rpm]	Feed rate [mm/min]	Tool inclination	Tool penetration depth into the sheets [mm]
AA2024-T3	1200	100	3°	3.99
AA6082-T6	2400	375	3°	3.99
AA7075-T6	1500	40	3°	3.99
AA5754-H111	1200	250	3°	3.99

To realize the water-cooled welded joints, a cooling system was appropriately designed and implemented that allows a continuous and controlled flow of water at room temperature in the welding area. To ensure that no particles of water remain blocked in the joint during the welding process, the water has been kept away from the sheets not yet welded by the presence of a bulkhead fixed near the pin (Figure 6.3).

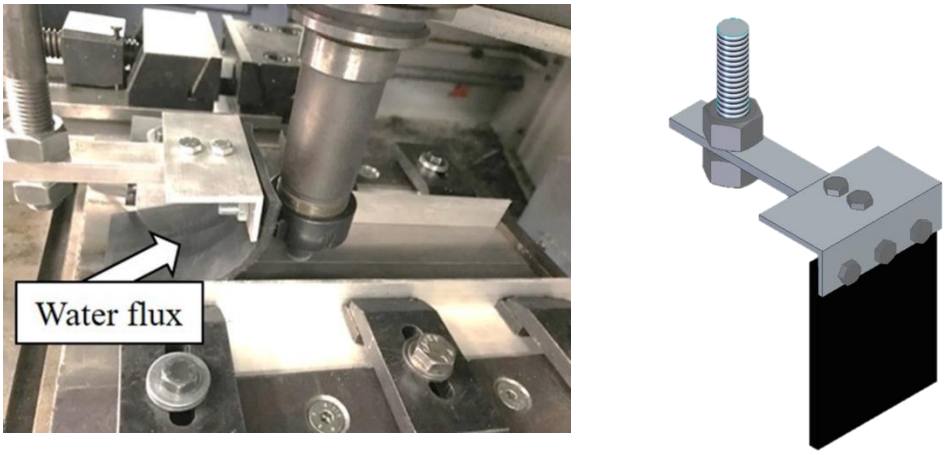

(**a**) (**b**)

Figure 6.3: Water-cooling system (a) and the used bulkhead (b).

The appearance and morphology of the cross-section of a typical welded joint are shown in Figure 6.4.

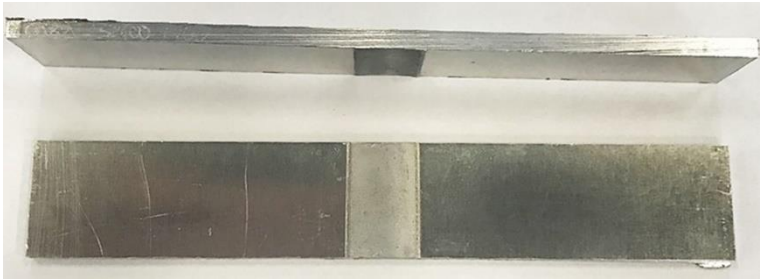

Figure 6.4: Appearance and morphology of a FSWed joint.

The mechanical characteristics of both air-cooled and water-cooled joints were evaluated by means of hardness and tensile tests of the joints.

Rockwell tests (HRB) were executed using a 5 mm spaced grid on the top of the specimen according to ISO 6508, while Vickers tests (HV) were executed using a 1 mm spaced grid on the transversal section of the specimen according to ASTM E92-17 and using a load of 1000 gf to limit the elastic recovery of the material that could modify the measured values. Both hardness tests were carried out moving from the center of the welded joints until the hardness of the base material was reached.

Tensile tests (5 repetitions) were conducted according to UNI EN ISO 6892-1:2016 using a testing machine Galdabini with a load cell of 50 kN. The tests were carried out orthogonally to the welding direction, with the welding center placed in the middle of the specimen, according to EN 10002-1:2001, under speed control (7.6 mm/min) and with a pre-load equal to 0.5 kN.

The microstructure of base materials and of longitudinally cut specimens were observed at the optical microscope only for precipitation hardening alloys since it is on their microstructure that the welding process is more damaging. The samples were mounted in a cold-working resin, polished up to 0.05 μm with alumina suspension and etched by Keller (for AA2024 and AA7075) and Weck solutions (for AA6082).

The average size of the grain in the base materials and also in correspondence of both the nugget and the Thermo Mechanically Altered Zones (TMAZs) was determined according to the Heyn lineal intercept procedure (ASTM E 112-13) on images obtained with an optical microscope with 400x magnification for the nugget and 200x for the TMAZs.

For each line drawn, the intercepted grain boundaries were counted and then the final average size of the single grain was calculated according to equation 2.

$$d = A_{int}/M \quad (2)$$

$$A_{int} = l_{line}/n_i \quad (3)$$

Where:

d: average grain diameter;

A_{int}: average line length intersected;

M: image magnification;

l_{line}: length of the line;

n_i: average numbers of grain boundaries intersected by the line.

To consider the anisotropy of TMAZ, three lines of 300 mm parallel to the rolling direction and three lines of 200 mm perpendicular to the rolling direction were drawn. Due to the presence of equiaxial grains in the nugget zone, the evaluation of the average grain size in this zone was performed by tracing three parallel lines having a length equal to 100 mm.

6.3. Results

6.3.1. Microstructure analysis

The microstructures of AA2024, AA6082 and AA7075 base metal are reported in Figure 6.5.

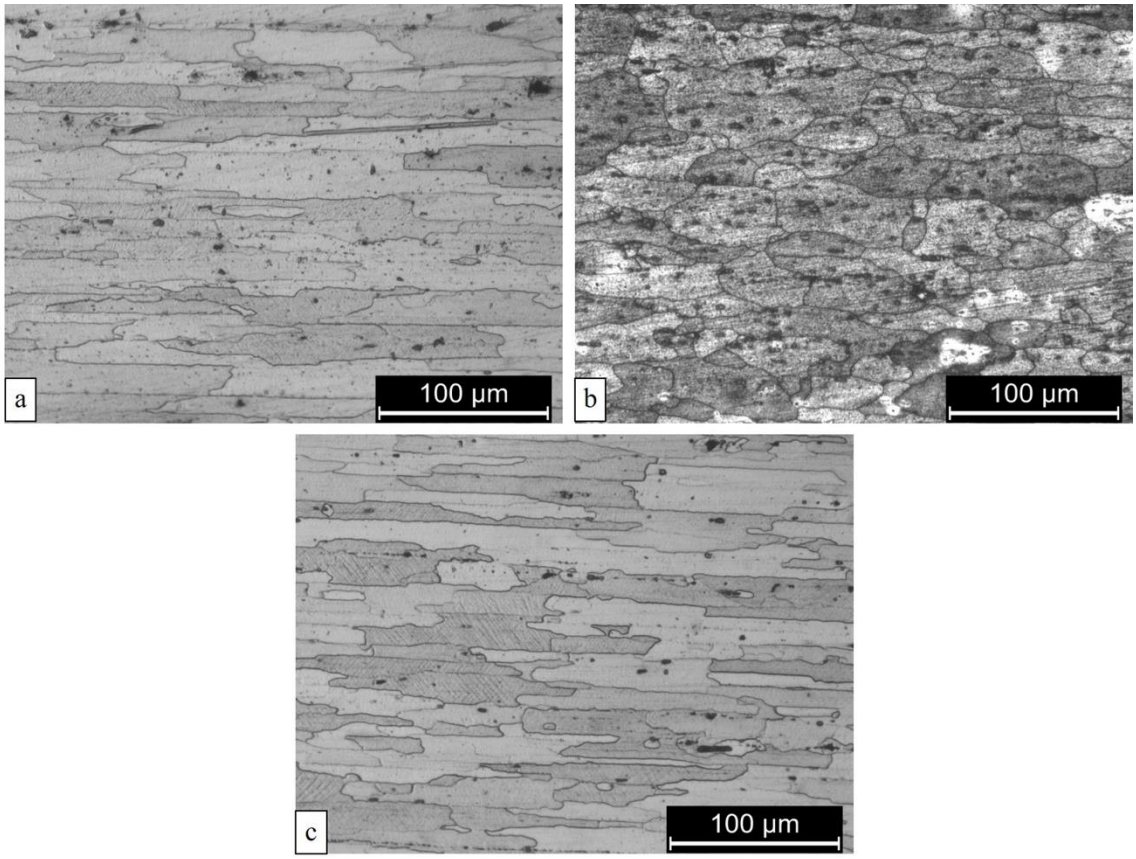

Figure 6.5: Microstructure of the base alloys: a) AA2024, b) AA6082 and c) AA7075.

The microstructures of both nugget and TMAZ areas for AA2024, AA6082 and AA7075 under air-cooled and water-cooled conditions are reported in Figure 6.6, Figure 6.7 and Figure 6.8. For all the alloys and for both the cooling conditions it is possible to detect the typical microstructure characterizing the joints friction stir welded. In particular, in the nugget (Figure 6.6a and b, Figure 6.7a and b and Figure 6.8a and b), fine and equiaxial grains are present due to the thermo-mechanical action of the pin, which causes the crushing of the elongated grain detectable along the rolling direction in the base alloy. At the same time, with the breaking of the grain, even the precipitates are crushed. These particles are responsible for the mechanism that causes the reinforcement in precipitation hardening aluminum alloys. The smaller crushed precipitates are usually distributed preferentially on the grain boundary, weakening the structure of the nugget, since the reinforcing particles are no longer uniformly distributed.

On the contrary, in TMAZ (Figure 6.6c and d, Figure 6.7c and d and Figure 6.8c and d) the elongated grains in the rolling direction present in the base metal are still

detectable, due to the lack of direct mixing and the limited amount of heat reaching the area.

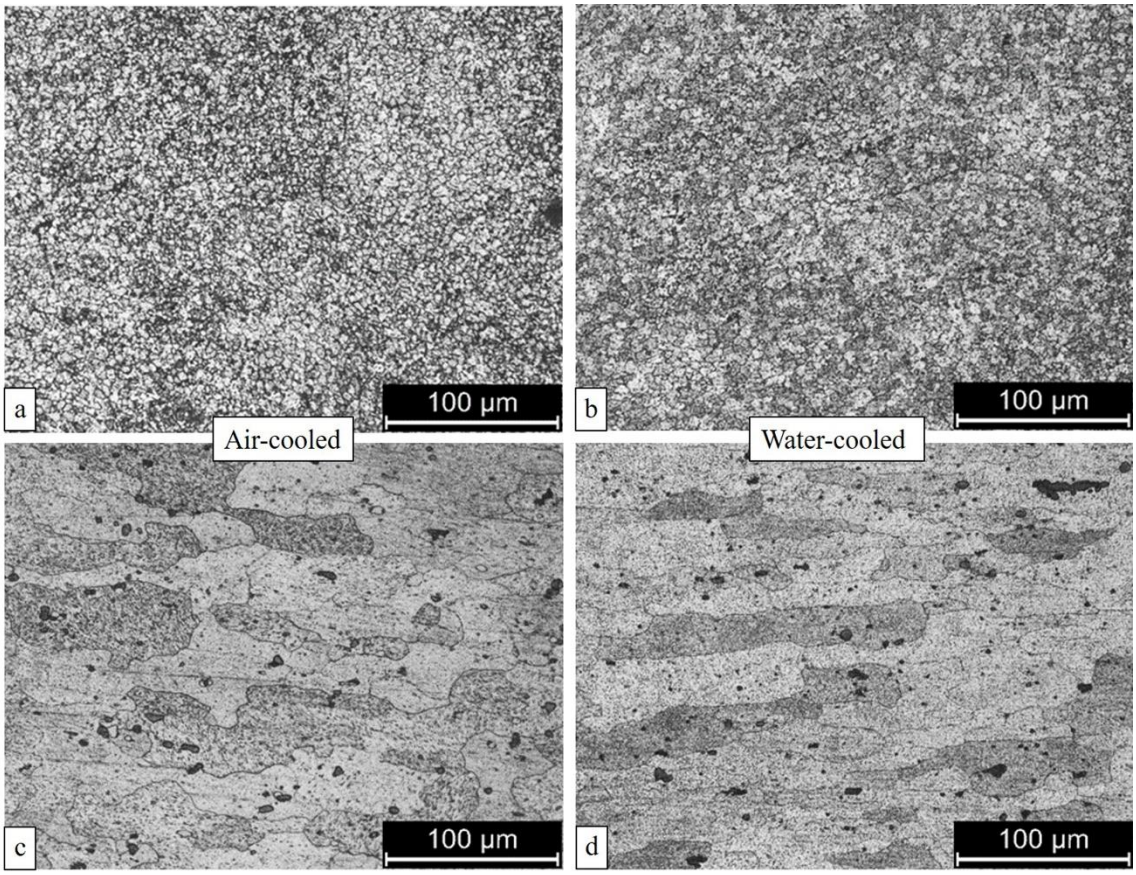

Figure 6.6: Microstructure of the nugget (a-b) and the TMAZ (c-d) of AA2024 air-cooled (on the left) and water-cooled (on the right) welded joints.

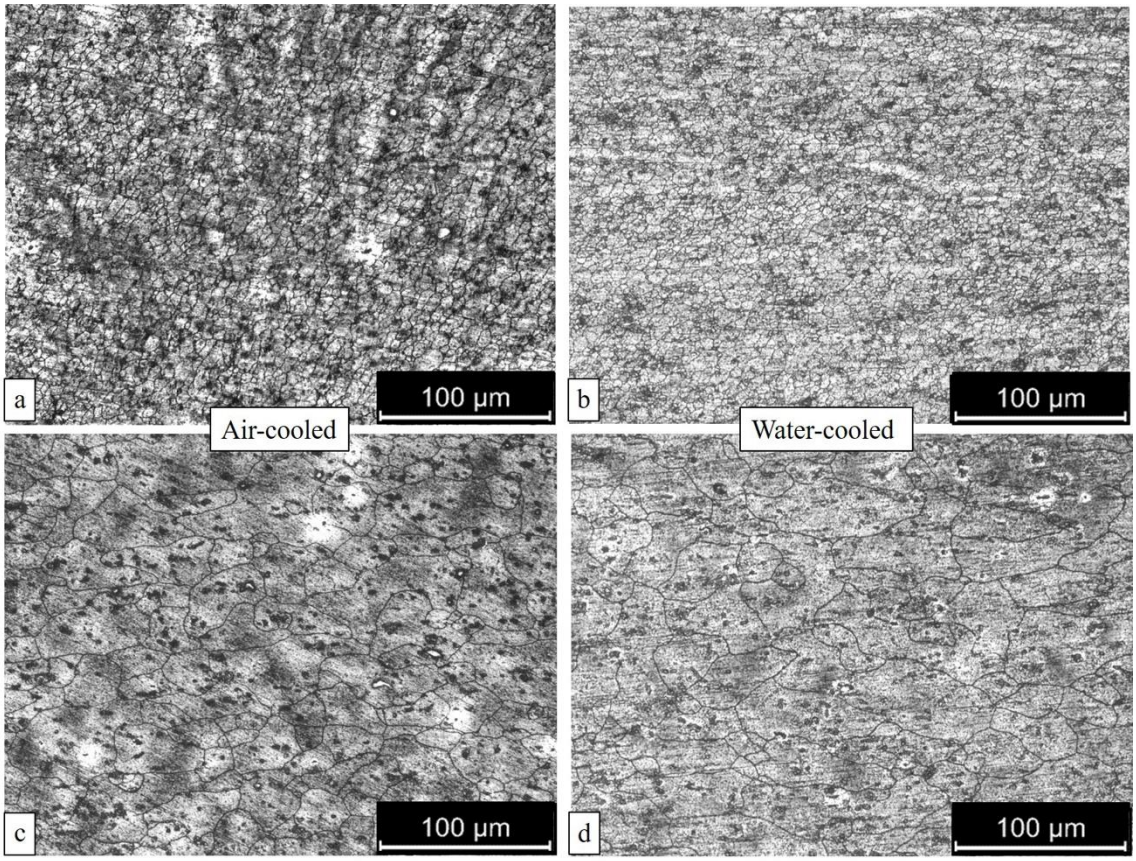

Figure 6.7: Microstructure of the nugget (a-b) and the TMAZ (c-d) of AA6082 air-cooled (on the left) and water-cooled (on the right) welded joints.

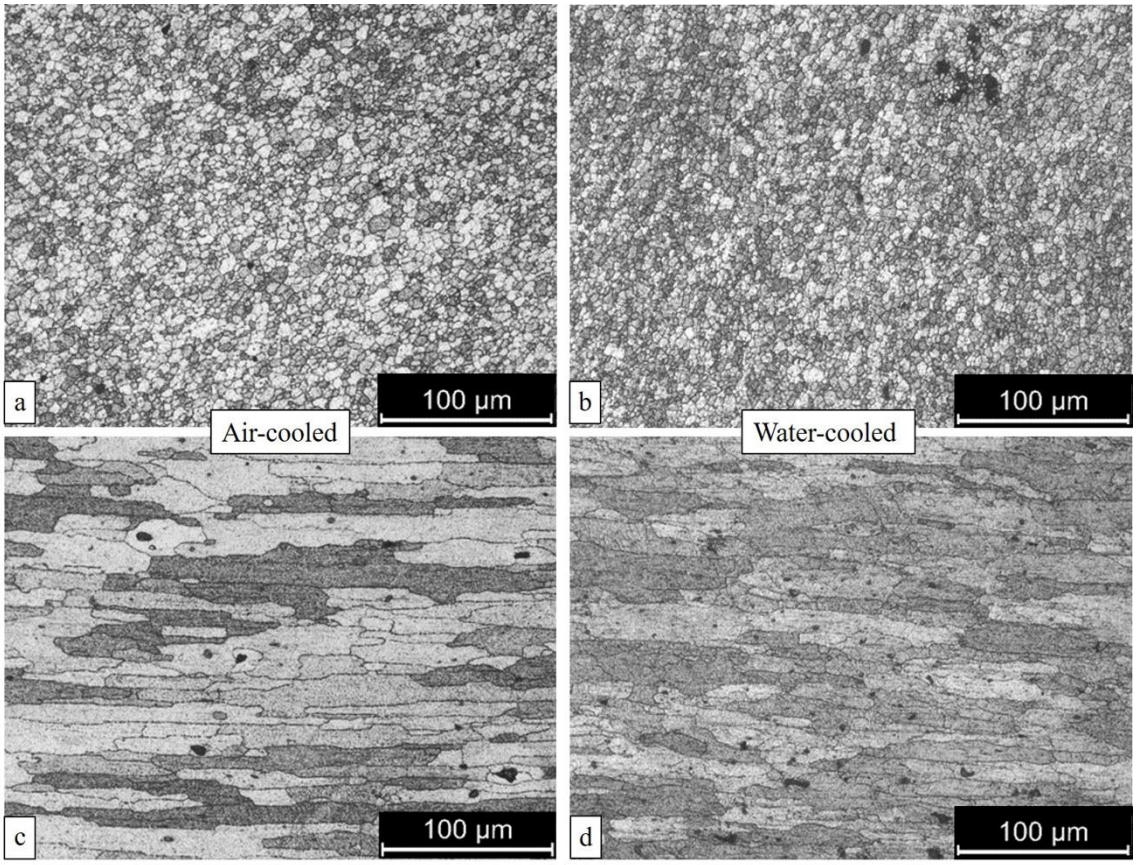

Figure 6.8: Microstructure of the nugget (a-b) and the TMAZ (c-d) of AA7075 air-cooled (on the left) and water-cooled (on the right) welded joints.

As already said, the grain size has been determined according to Heyn lineal intercept procedure. For each line drawn, the intercepted grain boundaries were counted, and the results are reported in Table 6.4.

Table 6.4: Counts of the grain boundary intersections with the drawn line for each alloy.

AA2024

	Base alloy		**FSW**					
			Air-cooled			**Water-cooled**		
			Nugget	TMAZ		Nugget	TMAZ	
	//	⊥		//	⊥		//	⊥
Line 1	3	22	46	10	11	39	7	10
Line 2	6	19	45	12	11	38	9	18
Line 3	4	16	44	9	11	41	11	19

AA6082

	Base alloy		**FSW**					
			Air-cooled			**Water-cooled**		
			Nugget	TMAZ		Nugget	TMAZ	
	//	⊥		//	⊥		//	⊥
Line 1	8	13	41	12	16	35	12	14
Line 2	9	16	51	12	18	37	13	12
Line 3	11	14	44	10	16	30	14	13

AA7075

	Base alloy		**FSW**					
			Air-cooled			**Water-cooled**		
			Nugget	TMAZ		Nugget	TMAZ	
	//	⊥		//	⊥		//	⊥
Line 1	4	21	43	9	31	37	12	25
Line 2	6	20	36	13	25	35	17	26
Line 3	9	21	39	9	22	37	12	22

The average grains sizes in correspondence of both the nugget and the TMAZs for all the precipitation hardening alloy and for both the cooling conditions are reported in Table 6.5, Table 6.6 and Table 6.7.

Table 6.5: Average grain size in the base alloy, in the nugget and in the TMAZ of air-cooled and water-cooled AA2024 welds.

AA2024

	Base alloy		**FSW**					
			Air-cooled			**Water-cooled**		
			Nugget	TMAZ		Nugget	TMAZ	
	//	⊥		//	⊥		//	⊥
n_i	4.33	19	45.00	10.33	11.00	39.33	9.00	15.67
A_{int}	69.28	10.52	2.22	29.03	18.18	2.54	33.33	12.77
d [µm]	**346.42**	**52.63**	**5.56**	**145.16**	**90.91**	**6.36**	**166.67**	**63.83**

Table 6.6: Average grain size in the base alloy, in the nugget and in the TMAZ of air-cooled and water-cooled AA6082 welds.

AA6082

	Base alloy		**FSW**					
			Air-cooled			**Water-cooled**		
			Nugget	TMAZ		Nugget	TMAZ	
	//	⊥		//	⊥		//	⊥
n_i	9.33	14.33	45.33	11.33	16.67	34.00	13.00	13.00
A_{int}	32.15	13.96	2.21	26.47	12.00	2.94	23.08	15.38
d [µm]	**160.77**	**69.78**	**5.51**	**132.35**	**60.00**	**7.35**	**115.38**	**76.92**

Table 6.7: Average grain size in the base alloy, in the nugget and in the TMAZ of air-cooled and water-cooled AA7075 welds.

AA7075

Base alloy	**FSW**

			Air-cooled			Water-cooled		
			Nugget	TMAZ		Nugget	TMAZ	
	//	⊥		//	⊥		//	⊥
n_i	6.3	20.67	39.33	10.33	26.00	36.33	13.67	24.33
A_{int}	47.62	9.68	2.54	29.03	7.69	2.75	21.95	8.22
d [μm]	**238.10**	**48.38**	**6.36**	**145.16**	**38.46**	**6.88**	**109.76**	**41.10**

6.3.2. Rockwell and Vickers hardness distributions

The hardness test samples were obtained by cutting the welded sheet in the area shown in Figure 6.9 obtaining a 160x20 mm sample as shown in Figure 6.10.

Figure 6.9: Part of the welded sheet on which the hardness tests were carried out.

Figure 6.10: Specimen surface on which Rockwell hardness tests were performed.

The distributions of Rockwell hardness measured on the top of the specimens are reported in Figure 6.11.

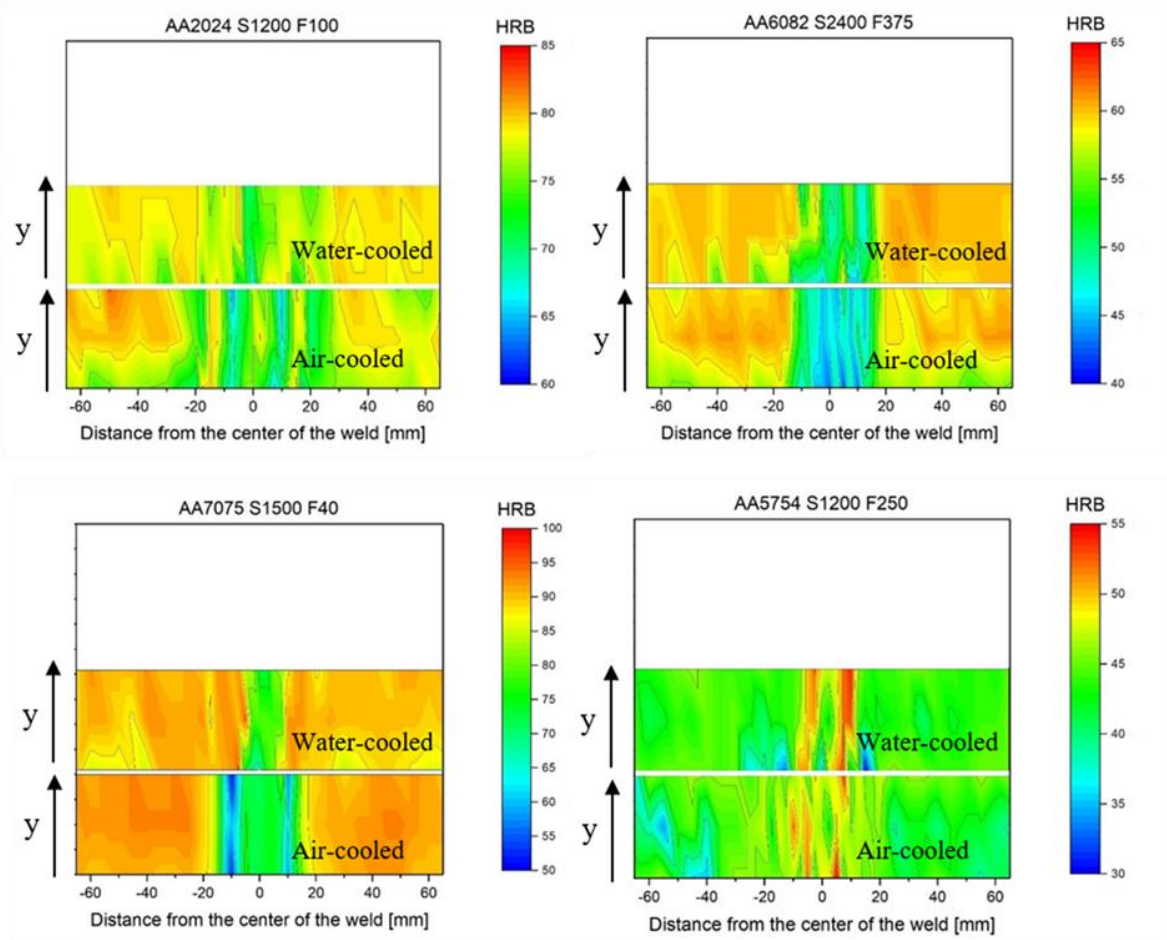

Figure 6.11: Rockwell hardness maps.

Figure 6.12 shows the area where the Vickers hardness has been measured. The distributions of the hardness measured along the transversal section for the different cases considered are reported in Figure 6.13.

Figure 6.12: Specimen surface on which Vickers hardness tests were performed.

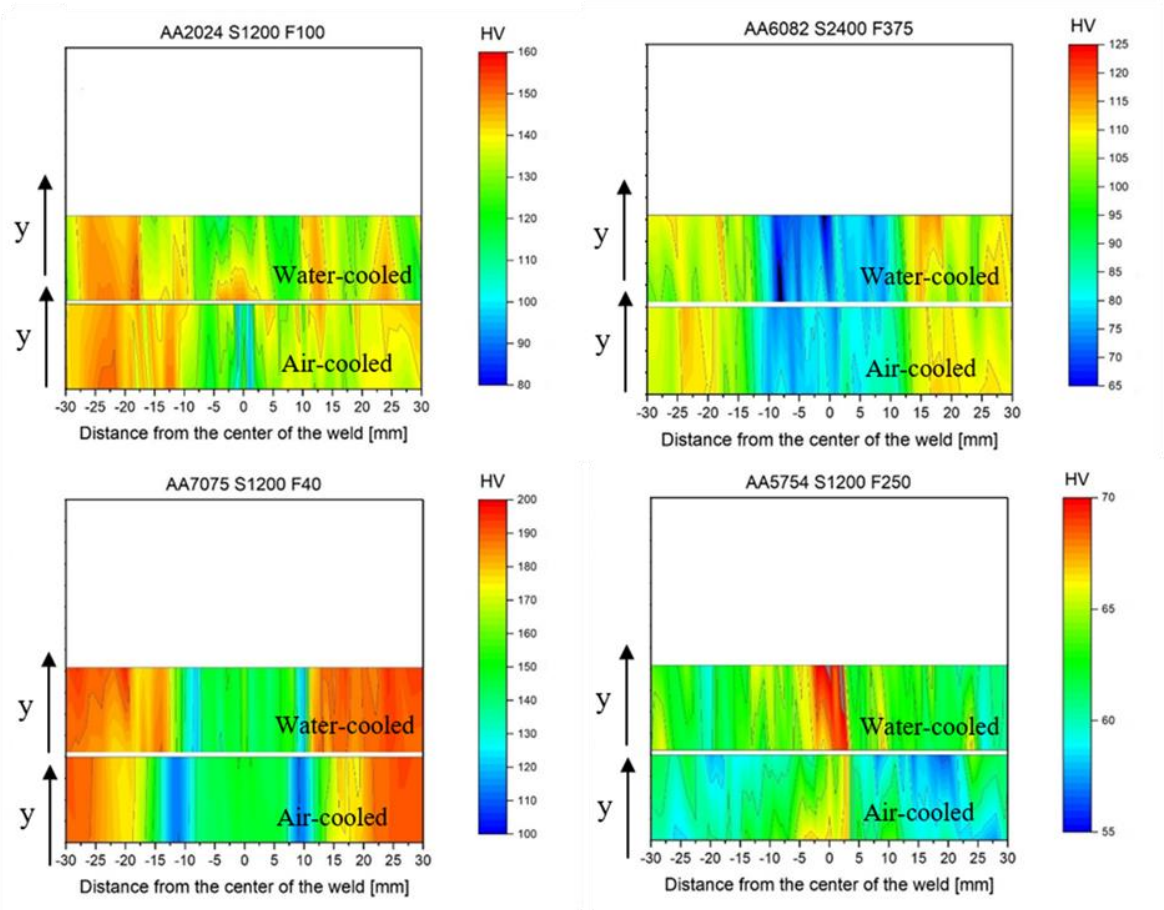

Figure 6.13: Vickers hardness maps.

6.3.3. Tensile tests

The ultimate tensile strength (UTS), elongation (A) [%] and their standard deviation, calculated for all the alloys and for all the tested conditions according to the type of cooling, are reported in Table 6.8.

Table 6.8: Average UTS data, real elongation A and standard deviations of all the tested conditions.

Alloy		UTS [MPa]	UTS std. dev. [MPa]	A [%]	A std. dev.
AA2024	Air-cooled	289.59	17.24	0.91	**0.28**
	Water-cooled	278.23	22.79	1.11	**0.31**
AA6082	Air-cooled	220.73	3.62	3.91	**0.47**
	Water-cooled	217.27	6.06	2.62	**0.21**
AA7075	Air-cooled	352.46	44.02	0.96	**0.87**
	Water-cooled	370.33	40.71	2.16	**1.34**
AA5754	Air-cooled	198.80	8.07	14.11	4.47
	Water-cooled	201.21	4.39	17.36	2.01

The UTS and A data obtained from the tensile tests for the different cases are reported in Figure 6.14 for analyzing the effect of the cooling system.

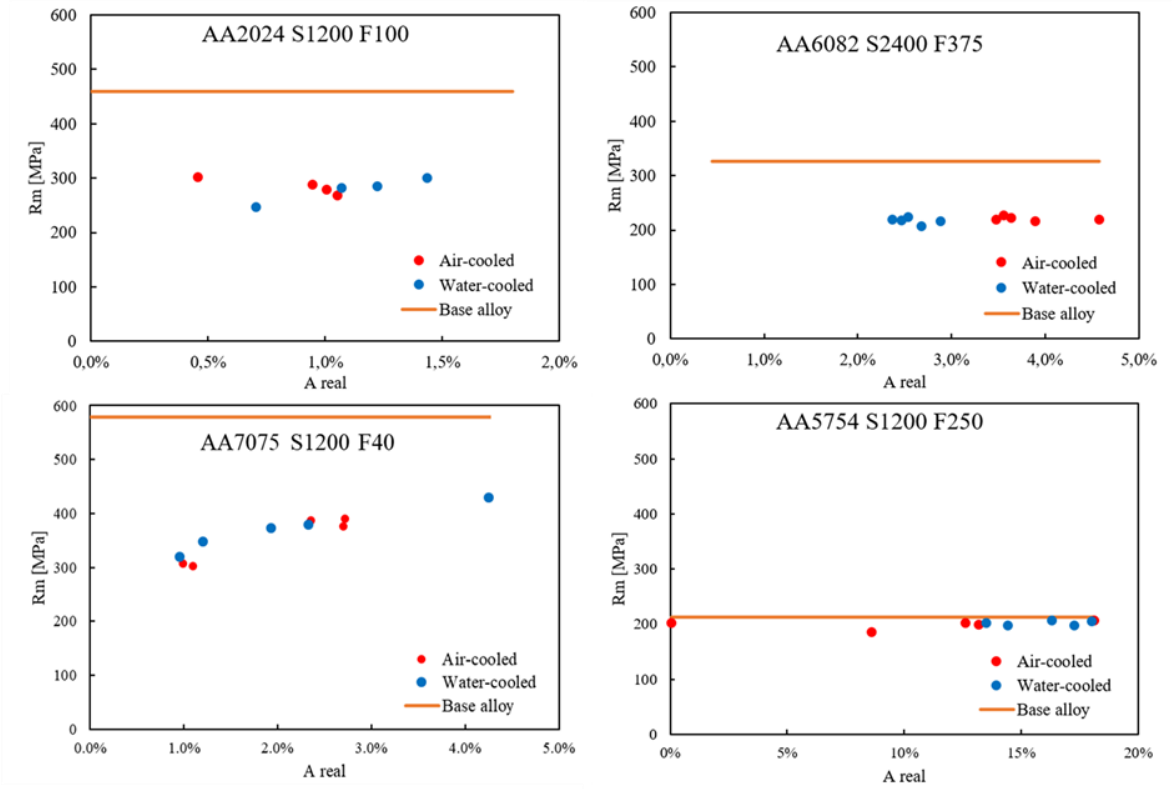

Figure 6.14: Ultimate tensile strength vs. elongation [%] data obtained from tensile tests for all the alloys and for all the tested conditions. The continuous line indicates the UTS value of the base alloy.

Figure 6.15 reports the fracture locations on the tensile test specimens for each alloy and for each cooling condition. The reported images refer to the most representative situation of each condition drawing a direct comparison between the different cooling methods.

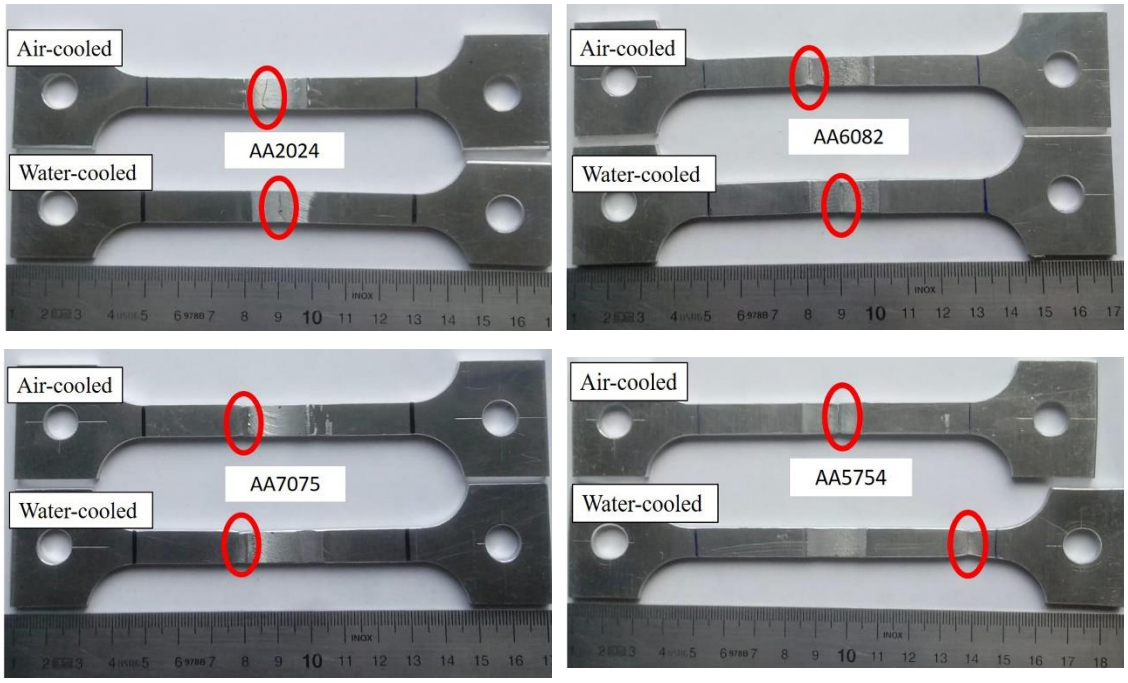

Figure 6.15: Fracture location for each alloy and for each cooling condition.

6.4. Discussion

The alloys belonging to the 2xxx series are normally supplied in the T3 or T4 state, abbreviations indicating respectively solubilization and natural ageing heat treatment. The T3 heat treatment involves a cold processing step between solubilization and ageing. An intermediate cold plastic deformation allows to obtain superior mechanical properties compared to ageing alone.

Natural ageing involves maintaining the alloy for a long period of time, at room temperature or at a slightly higher temperature. During this period, there is the spontaneous formation of a structure characterized by the presence of Guinner-Preston zones (G.P.), which are areas of the crystalline matrix in which the clusters of precipitates and solutes are aggregated. The areas thus formed oppose greater resistance to the path of the dislocations than the crystalline matrix of the base metal, generating the desired increase in mechanical strength.

Natural ageing appears to be an extremely slow process and, for some alloys, such as those belonging to the 6xxx and 7xxx series, does not guarantee the achievement of stable conditions.

For this reason, the AA6082 to AA7075 alloys are usually supplied in the T6 state, which provides solubilization, tempering and artificial ageing.

Artificial ageing involves exposing the alloy to temperatures above room temperature for obtaining the transition phase starting from the equilibrium precipitates; this form of transition remains consistent with the matrix of the solid solution and therefore contributes to precipitation hardening. However, as the ageing temperature increases, the precipitate particles grow and reconvert to the state of equilibrium, which is generally inconsistent. These changes produce a loss of mechanical characteristics with respect to the untreated base metal. This phenomenon is called over-ageing.

The control of the temperatures to which these alloys are subjected is therefore of fundamental importance for the mechanical properties of both the base material and the friction stir welded one. Therefore, the presence of a water-cooling system plays a key role in controlling the thermal cycle to which these alloys are subjected during welding. Furthermore, each point of the weld, in relation to its distance from the center of the nugget, has a microstructure strongly influenced by the welding process. Consequently, in the weld region, where the material is stirred at solid-state, dissolution, coarsening of strengthening precipitates and formation of wide precipitate free zone take place.

From the measurements made on the joints, a clear dependence of the average grain size from the cooling system is detectable. In particular, in the water-cooled nugget, the grains are characterized by an increase in the average size compared to the air-cooled nugget being 14% in AA2024 (Table 6.5), 33% in AA6082 (Table 6.6) and 8% in AA7075 (Table 6.7). It is possible to notice how the percentage growth of the average dimensions present in the nuggets of the single alloys, is considerably different from each other. This is attributable to the mechanical characteristics of the base alloys. In fact, hardness and mechanical strength of AA7075 result in a greater resistance to the breakage action of the grains by the pin. This is also reflected by the average size of the grains present in its air-cooled welded nugget, which are already on average larger than those present in the other two alloys (Figure 6.8).

On the contrary, the alloy with the highest percentage growth is the AA6082, which has the mechanical characteristics on average lower than the other two alloys and it

is also characterized by grains with average lower dimensions in the air-cooled welded nugget (Figure 6.7).

Regarding the TMAZs, AA6082 and AA7075 show grains characterized by smaller average dimensions in the rolling direction in water-cooled welds. On the contrary, perpendicularly to the rolling direction, in water-cooled joints, the grains are slightly larger (Figure 6.7 and Figure 6.8). The percentage decrease was around 13% in AA6082 and 25% in AA7075 parallel to the rolling direction. On the contrary, the percentage increase perpendicularly to the rolling direction was about 28% in AA6082 and 7% in AA7075 (Table 6.6 and Table 6.7). These dimensional variations make the grains present in water-cooled welds smaller than those present in the same position for air-cooled welds.

On the contrary, in AA2024 the average grain size increases by 15% in the direction parallel to the rolling direction and decreases by 30% in the perpendicular direction (Table 6.5).

As a general observation, it can be seen that in each alloy, the grain size in the TMAZ is much closer to that of the base material in the direction perpendicular to the rolling direction in water-cooled welds. In the case of AA6082, perpendicularly to the rolling direction, the water-cooled TMAZ grains are characterized by an average size even greater than those of the base alloy. This is further a proof of how the material responds differently to the cooling system in microstructural terms and, consequently, in the mechanical characteristics.

In fact, from the mechanical tests data, it is possible to observe a behavior common to all the precipitation hardening alloys (AA2024, AA6082 and AA7075). In particular, for all the welded conditions, the specimens have specific zones characterized by hardness lower than the one of the base materials. This characteristic trend of the hardness values in precipitation hardening alloys is mainly due to the thermo-mechanical action of the pin that acts on the alloy modifying its microstructural characteristics.

In fact, for these alloys, it is possible to identify a clear microstructural change caused by the welding process (Figure 6.6, Figure 6.7 and Figure 6.8). The heat generation and the mechanical action of the stirring generate a dynamic recrystallization that particularly affects the nugget. In TMAZs, the dynamic action of the pin and the heat

generated are not sufficient to modify the microstructure of the base material. Therefore, in these zones, the grains are similar to the original ones (Figure 6.5) maintaining an elongated shape along the rolling direction (Figure 6.6c and d, Figure 6.7c and d and Figure 6.8c and d).

Even the precipitates are influenced by the FSW process in two ways. In fact, depending on the action of the pin and the heat input, it is possible to have both the crushing of large precipitates by the mechanical action and the coalescence of the precipitates in sub-micrometric dimensions.

These are the reasons why the lower hardness areas are concentrated in the TMAZs, where the grain recrystallization is not complete and where the alloy-hardening-precipitates are partially crushed. On the other hand, in the nugget, the dynamic recrystallization is complete and the precipitates are fully crushed reaching the sub-micrometric dimensions suitable for strengthening the matrix formed by the micrometric grains (Figure 6.6a and b, Figure 6.7a and b and Figure 6.8a and b).

In addition, AA5754 presents a completely different behavior and a different hardness map. In fact, since AA5754 is a work-hardening alloy, the thermo-mechanical action of the pin has led to a hardness increase in the nugget area, where the solid-state mixing has completely taken place.

By comparing the hardness maps measured on air-cooled and water-cooled welds, it is possible to observe how the effect of water-cooling is twofold on each alloy (Figure 6.11 and Figure 6.13). The first effect can be traced in the numerical value of the hardness achieved in the TMAZs as regards the three precipitation hardening alloys and in the nugget for the work-hardening alloy. In these areas, for all the alloys and for all the considered conditions, the hardness is higher than those measured in air-cooled welds. This effect is less noticeable on AA2024 joint. Moreover, 6082 Rockwell tests showed an increase in the hardness values at the nugget in water-cooled welds.

The second effect is the narrowing of the area characterized by the lower hardness values. Regarding the precipitation hardening alloys, the extent of the zone characterized by the lower hardness is considerably reduced in the water-cooled specimens. On the contrary, in AA5754 the extent of the area characterized by a

greater hardness is almost constant for air-cooled and water-cooled welds (Figure 6.11 and Figure 6.13).

These effects are mainly due to the presence of the local water-cooling during the welding process that leads to a better dimensional control of the grains in the joints, which is closely related to the mechanical properties of the piece.

Also the hardness is closely related to the microstructure of the materials. As a consequence, it is possible to correlate the increase in hardness in the TMAZ of AA6082 and AA7075 welded with the water-cooling system to the smaller dimensions of the grain present in these areas. Contrariwise, it has already been noted that the AA2024 has mitigated the effect in increasing the hardness in the TMAZ of water-cooled welds. This characteristic of AA2024 finds its explanation in the further elongation that the grains undergo in the TMAZ of water-cooled welds, as reported in section 6.3.1.

By observing the Vickers hardness maps (Figure 6.13), it is possible to draw the same considerations made for the Rockwell hardness maps (Figure 6.11). In fact, it is possible to notice, also in the cross-section of the specimens, an increase in the hardness in the central areas of the specimens, with the exception of AA6082, and a reduction in the extent of the area characterized by lower hardness values for the hardening alloys. Concerning the AA6082, the decrease in Vickers hardness recorded in the cross-section could be related to the considerable increase in the average grain size at the nugget of the water-cooled welds. In fact, this alloy has proved to have the highest average percentage growth rate of the grains present in the water-cooled weld nugget, as already reported in Table 6.6. Finally, it is possible to observe, for AA5754, a significant increase in the hardness values in correspondence of the nugget.

Also in the tensile tests, it is possible to observe different behaviors between the studied alloys (Figure 6.14 and Figure 6.15). In particular, for the AA2024, the values of ultimate tensile strength and percentage of elongation are almost comparable for both cooling methods and are much lower than those of the base metal. Both cooling conditions led to breakages in the nugget during the tensile tests.

As regards the tensile tests of the AA6082, the average values of UTS and percentage elongation are comparable between air-cooled and water-cooled welds. But the

cooling system seems to affect the fracture locations of the tested joints. In fact, the air-cooled joints showed fractures at the interface between the nugget and TMAZ, while the water-cooled joints broke especially at the nugget. Moreover, the AA7075 have shown a benefit in water-cooling in the UTS but both cooling conditions led to breakages in the interface between the nugget and TMAZ during the tensile tests.
However, it is possible to recognize the welding obtained from the AA5754 joints as the welding that has reached the value of UTS and of percentage elongation closer to those of the base alloy both in the air-cooled and water-cooled process. Finally, for this work-hardening alloy, the percentage elongation was found to be on average higher for water-cooled welds than those air-cooled and, in particular, it was possible to observe that in the water-cooled joints the point of failure is placed in the base material, away from the welded area. On the contrary, in the air-cooled joints, the breakages were found in the nugget.

6.5. Conclusions

This chapter reports the results of the investigations of the effect of a water-cooling system on the mechanical properties and microstructural characteristics on FSW joints made of different alloys: precipitation hardening alloys AA2024-T3, AA6082-T6 and AA7075-T6 and work-hardening alloy AA5754-H111. All these alloys have shown a different behavior. In fact, AA2024 has proved to be the least affected by the cooling system. Moreover, a dependence between the cooling systems and the average value of percentage elongation was detectable in AA6082, despite the Rockwell tests showed an increase in the hardness values at the nugget in water-cooled welds. The AA7075 alloy was characterized by an increase in hardness distributions and an improvement in the breaking load in water-cooled welded joints. Regarding the AA5754, it reached the value of UTS and of percentage elongation closer to those of the base alloy both in the air-cooled and water-cooled process; it was possible to observe that only in the water-cooled joints the point of failure is placed in the base material, away from the welded area.

7. *The effect of heat generated on mechanical properties of friction stir welded aluminum alloys*

This chapter is derived from the article "Bocchi, S.; D'Urso, G.; Giardini, C.; (2021). The effect of heat generated on mechanical properties of friction stir welded aluminum alloys. International Journal of Advanced Manufacturing Technology, 112(5-6), 1513-1528".
DOI: 10.1007/s00170-020-06462-9.

I am immensely grateful to the support received from my co-authors. I am responsible for all the changes in this chapter with respect to the published version.

7.1. Introduction

It has been demonstrated that the choice of both the process parameters and the welding process setup are fundamental for the quality of the welding, as they strongly influence the thermal input of the process and, therefore, the microstructural characteristics of the joint.

In the last years, the scope of the researcher is focused on the control of the thermal cycle to which the FSWed joints are subjected to further limit their microstructural changes, as reported in Paragraph 6.1. As already demonstrated in Chapter 6, a faster cooling rate could lead to a better control of microstructural changes, limiting phenomena such as solubilization, re-precipitation and coarsening of precipitates and hence the local strength of each area of the weld zone.

In the study reported in Chapter 6, an analysis was conducted to qualitatively correlate the temperature cycle to the microstructure alterations and, consequently, to the mechanical resistance of the joints. Starting from the good correlation founded between the cooling conditions and the obtained results, it was clear that a deeper analysis was necessary. For this reason, a new experimental campaign involving a quantitative evaluation of both the maximum reached temperature and the cooling rate obtained with and without the water-cooling systems has been conducted.

So, in this study, the temperature distribution in both temporal and spatial terms during the FSW process were measured by a thermo-camera and by three type K thermocouples

positioned near to the nugget, in the thermo-mechanically affected zone and in the heat-affected zone.

7.2. Materials and methods

7.2.1. Materials

The experimental campaign was conducted on three precipitation-hardening alloys (AA2024-T3, AA6082-T6 and AA7075-T6) and on a work-hardening alloy AA5754-H111. Chemical composition, mechanical properties and microstructure of the base materials are reported in Table 7.1, Table 7.2 and Figure 7.1.

Table 7.1: Chemical composition (wt. %) of the base materials.

Alloy	Al	Si	Fe	Cu	Mn	Mg	Zn	Ti	Cr
AA2024-T3	bulk	0.06	0.09	4.50	0.46	1.40	0.08	0.04	0.03
AA5754-H111	bulk	0.103	0.34	0.059	0.318	2.808	0.019	0.009	0.019
AA6082-T6	bulk	0.9	0.36	0.07	0.42	0.8	0.05	0.03	0.02
AA7075-T6	bulk	0.05	0.10	1.53	0.008	2.54	5.72	0.04	0.20

Table 7.2: Mechanical properties of the base materials.

Alloy	Yield Strength (YS) [MPa]	Ultimate Tensile Strength (UTS) [MPa]	Max strain [%]
AA2024 – T3	344	464	16
AA5754 – H111	84	212	25.9
AA6082 – T6	281	326	16
AA7075 – T6	512	576	13.5

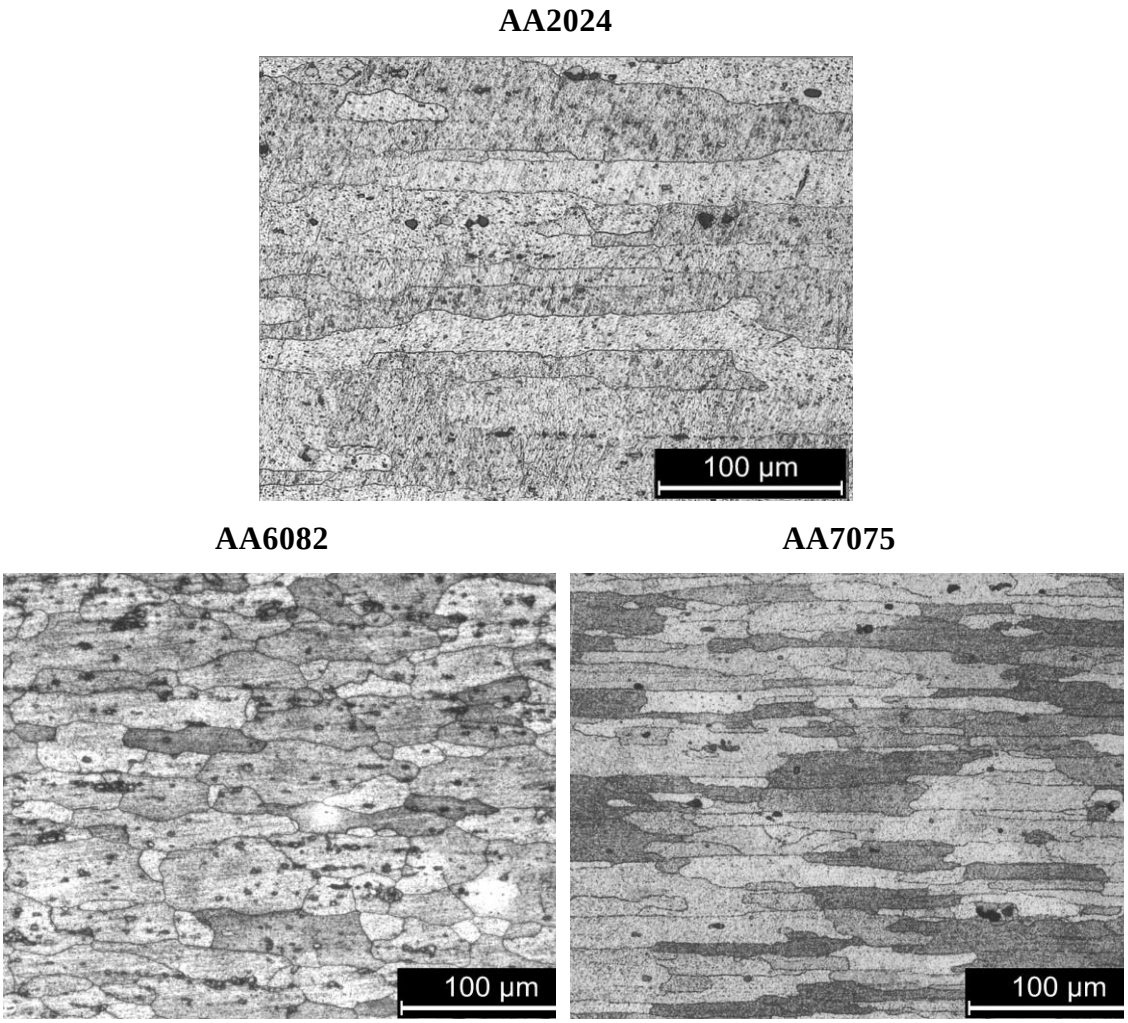

Figure 7.1: Microstructure of the base alloys.

7.2.2. FSW experimental setup

The aluminum sheets were friction stir welded perpendicularly to the rolling direction. The FSW process was performed using a CNC machine tool (complete information about CNC are reported in Table 7.3). A tool characterized by a smooth plane shoulder (16 mm diameter) and a frustum of cone pin shape (pin maximum and minimum diameters equal to 6 and 4 mm, pin height equal to 3.8 mm) was used (see Figure 7.2). The tool was realized from a drawn bar of carbon steel C40 without any heat treatment.

Table 7.3: Complete information about CNC machine employed.

Brand;	Famup	**Spindle Cone (DIN 69871):**	ISO 40
Model:	Mc 60 Evolution	**Spindle Power:**	7,5 kW
Control Type:	Fanuc 18 M	**Spindle Speed:**	50-10 000 rpm
Table Useful Surface:	800×370 mm	**X - Y - Z Rapid Feeds:**	18 m/min
Length Stroke X Axis:	600 mm	**Installed Total Power:**	15 kW
Cross Stroke Y Axis:	400 mm	**Maxi Weight With Distributed Load:**	250 kg
Vertical Stroke Z Axis:	570 mm		

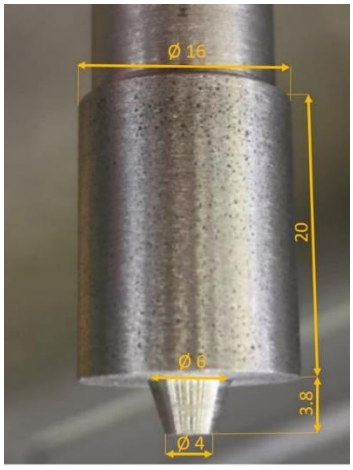

Figure 7.2: FSW tool geometry.

Couples of sheets having a dimension of 300×80 mm were used for each alloy. Different rotational speeds and feed rates were considered based on the optimal process parameters identified in a previous work, where the effect of the process parameters on both the mechanical and the corrosion behavior of butt joints obtained by FSW process, on the same aluminum alloys considered in this paper, were deeply analyzed [57] (Table 7.4).

Table 7.4: Parameters set-up for each alloy.

Aluminum alloy	Rotational speed [rpm]	Feed rate [mm/min]
AA2024-AA2024	1500	35
AA5754-AA5754	1200	250
AA6082-AA6082	2400	375
AA7075-AA7075	1500	40

All the other process parameters, such as the clamping system for the sheets, the tool inclination (fixed at 3°) and the tool penetration depth into the sheets (fixed at 3.99 mm) were kept constant. In order to evaluate the process repeatability, three repetitions were performed for each combination of the welding parameters.

The cooling system used consists of a continuous water jet at room temperature, which immediately cools the welded area. To prevent water particles from being incorporated in the welding during the process (causing micro-defects in the nugget), a bulkhead was fixed to the spindle (Figure 7.3).

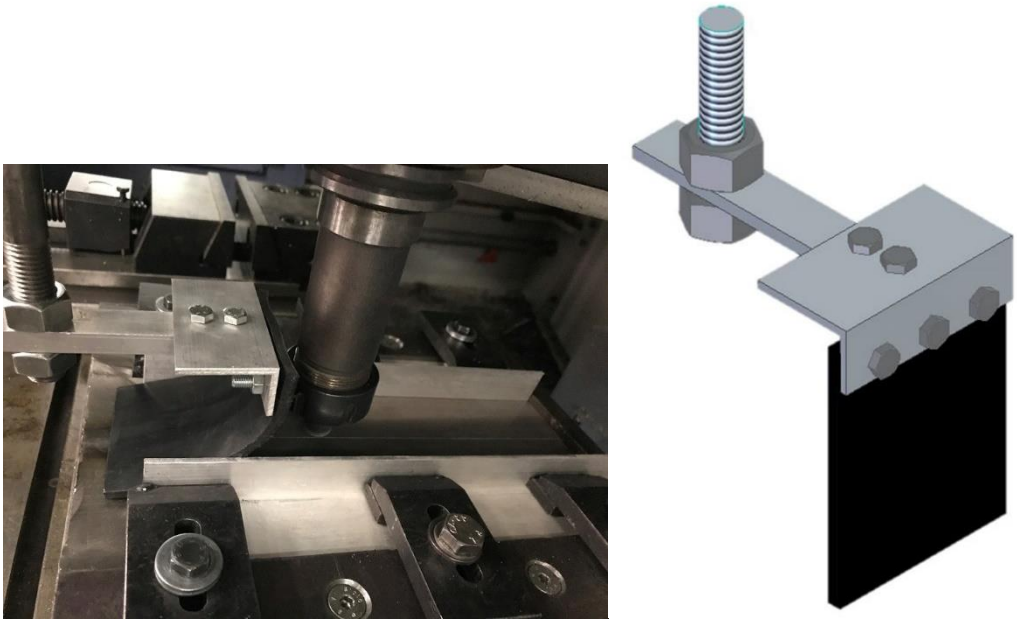

a) b)

Figure 7.3: Water-cooling system (a) and Bulkhead particular (b) [138].

The thermocouples (Figure 7.4) were housed in three 2 mm diameter holes with different depths realized in the advancing side of the weld.

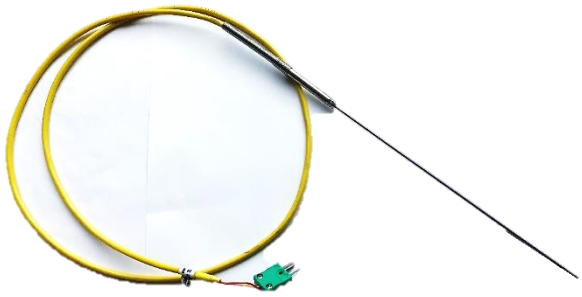

Figure 7.4: Type-K thermocouple.

The hole depths were chosen to detect the temperature in the three fundamental welding zones, i.e. nugget proximity, TMAZ and HAZ, as shown in Figure 7.5.

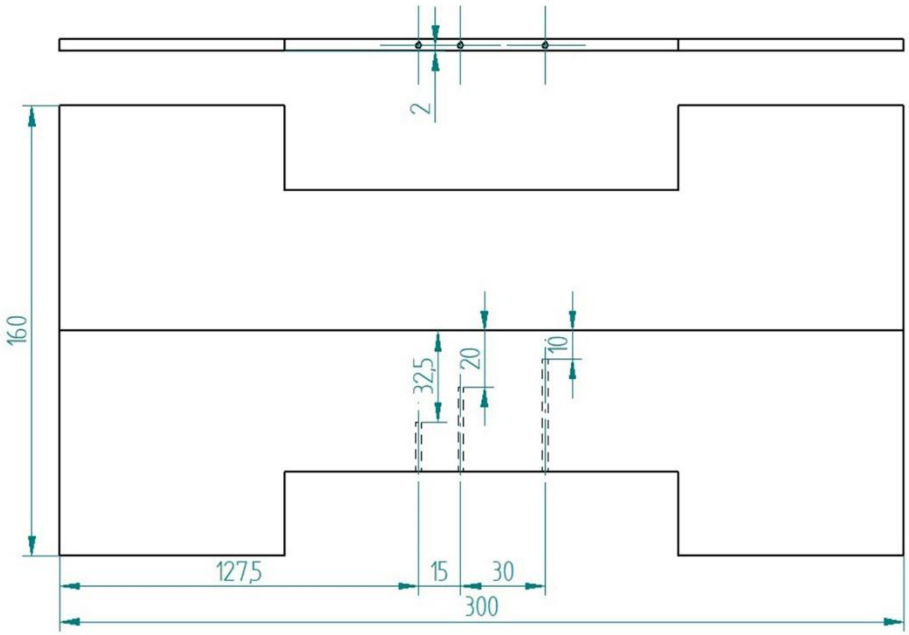

Figure 7.5: Thermocouples housings inside the plates to be welded.

The temperature data were sampled at a frequency of 3 Hz using an A/D board.
A Flir System ThermoVision A40 infrared camera (Figure 7.6) was used to measure the temperature reached in correspondence of the nugget, where it is not possible to locate the thermocouples.

Figure 7.6: Flir System ThermoVision A40 infrared camera.

7.2.3. Microstructure analysis and Mechanical testing of the joints

An analysis of the microstructure of the welding zones was conducted with the use of an optical microscope. This characterization was executed only on precipitation hardening alloys since it is on their microstructure that the mixing action of the pin and the heat generated by the welding process are more damaging. The samples, after being mounted in a cold-working resin, were polished up to 0.05 μm with alumina suspension and etched by Keller (for AA2024 and AA7075) and Weck solutions (for AA6082).

The influence of the cooling system was studied by measuring the mechanical properties (tensile tests and hardness distributions) of the joints. Tensile tests were executed orthogonally to the welding direction on specimens having the welding nugget placed in the middle of gage length, according to UNI EN ISO 6892-1:2016. A testing machine Galdabini with a load cell of 50 kN was used. The tests were carried out under speed control (1.2 mm/min) and a pre-load equal to 0.5 kN. Three specimens for each alloy and each condition were tested.

The hardness tests (HRB) were performed for all the welding conditions, following a 5 mm spaced grid in the central zone of the top of the specimen, to avoid border effects, according to ISO 6508. Three profiles of indentations were carried out moving from the joint axis to the base material.

7.3. Results and discussion

7.3.1. Temperature analysis

The temperature cycles of all the air-cooled and water-cooled welded alloys are reported in Figure 7.7. It was arbitrarily chosen to impose the achievement of 50°C in all three monitored areas as end of acquisition criterion.

It is important to remark that, due to this end of acquisition criterion and the different parameters used for each alloy (Table 7.4), the time within each alloy reaches 50°C strongly depends on the tool feed rate. For this reason, the x-axes of the graphs were adapted to the scale of the single alloy, in order to have more readable curves.

AA2024-AA2024

Air-cooled

a)

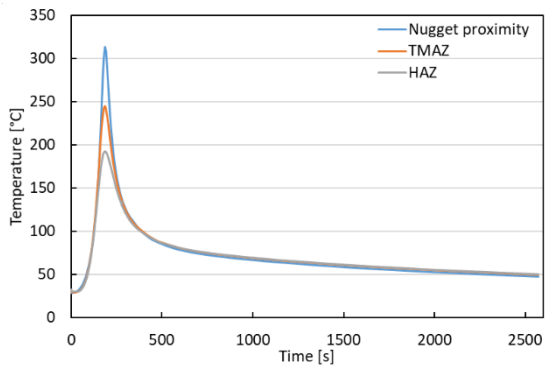

Water-cooled

b)

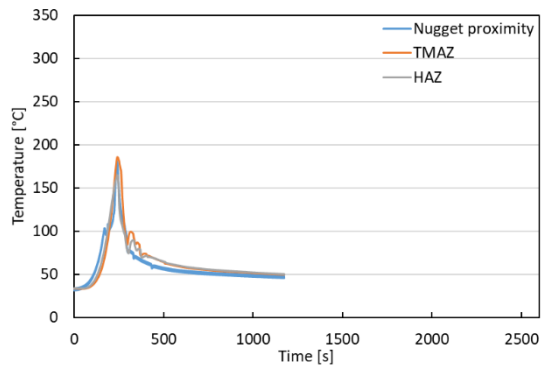

AA5754-AA5754

Air-cooled

c)

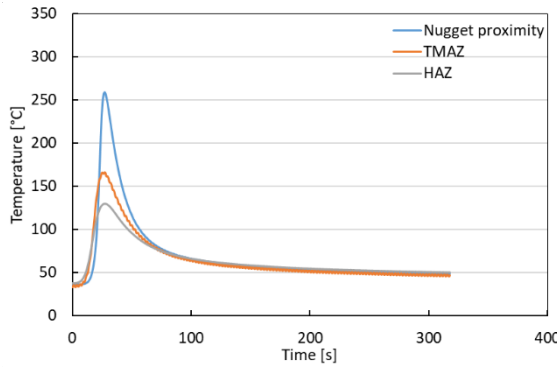

Water-cooled

d)

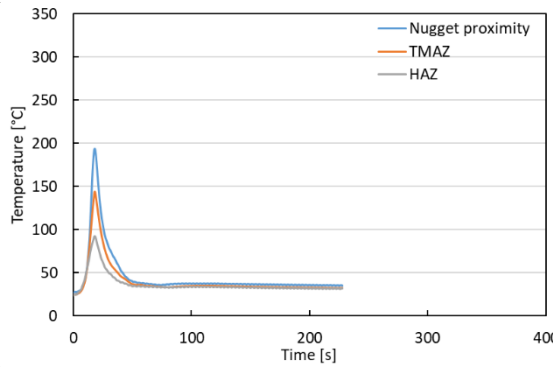

AA6082-AA6082

Air-cooled

e)

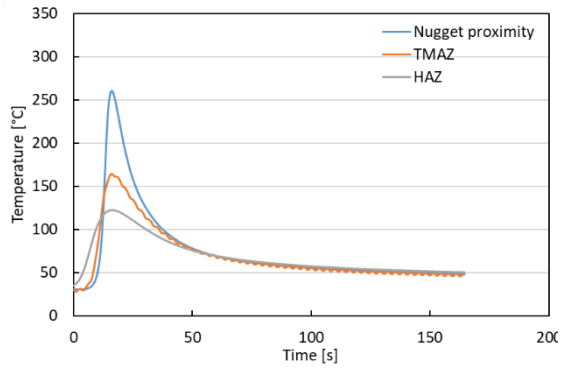

Water-cooled

f)

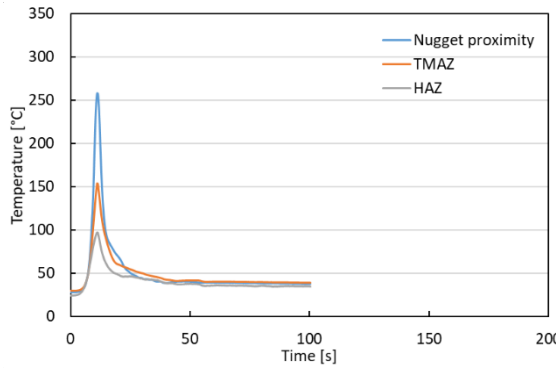

AA7075-AA7075

Air-cooled

g)

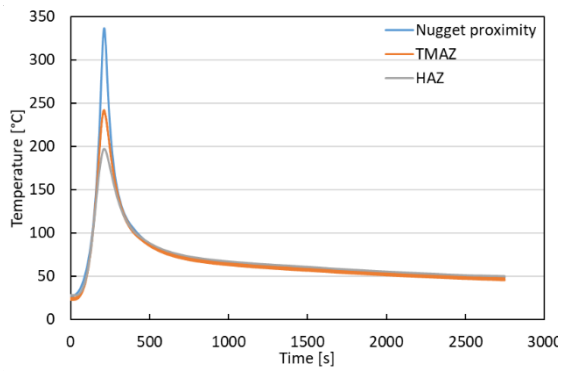

Water-cooled

h)

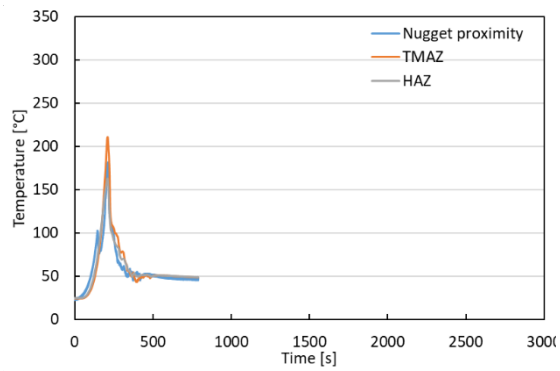

Figure 7.7: Temperature cycles showing thermal gradients in all the welded alloys with and without water-cooling system. In the legend "nugget proximity" indicates the measurements executed at 10 mm from the center of the weld.

From the graphs shown in Figure 7.7 it is possible to notice that the water-cooling system has a twofold effect on the thermal cycles:

- the peak temperatures reached in the three different areas are always higher for the air-cooling condition, with the exception of the AA6082-AA6082 weld which is characterized by similar maximum peak temperature values in the presence and absence of cooling (Figure 7.7e and f);
- it is evident that all three areas in water-cooling conditions return to temperatures below 50 °C in a shorter time than for air-cooled conditions. The effect just described is even more visible in the two alloys welded with

the higher feed rates: AA5754 (Figure 7.7c and d) and AA6082 (Figure 7.7e and f).

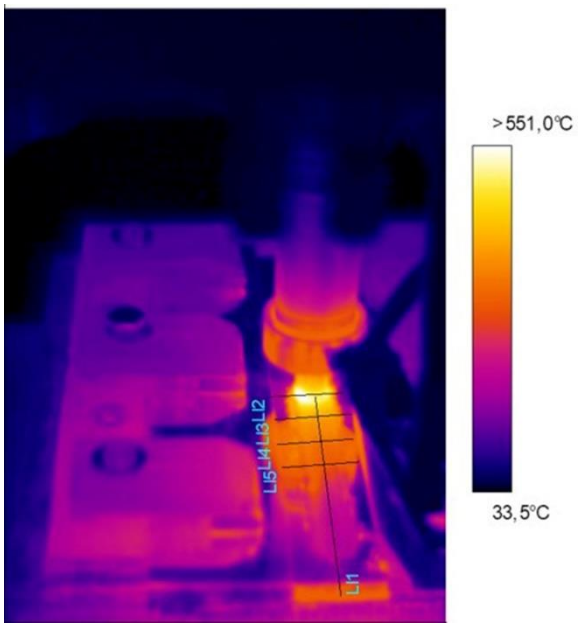

Figure 7.8: Example of thermo-vision of the infrared camera (AA2024 S1500-F35).

From the image shown in Figure 7.8, taken with the thermo-camera, the maximum temperature point at the interface between the welded joint and the tool results to be about 550 °C. Frigaard et al. showed that a temperature of 555 °C is a reasonable compromise for the maximum temperature reached in the nugget [19]. Furthermore, this temperature seems to be independent of both the alloy and the welding parameters considered, as it is caused by the thermo-mechanical action of the pin which acts similarly in any applied condition.

Starting from the peak temperatures obtained from the curves reported in Figure 7.7 and the peak temperature in the nugget, it was possible to build the regression lines of the thermal distribution of each individual condition studied, as reported in the Figure 7.9.

It is important to underline that the ln function was chosen because it proved to fit very well, without losing the physical meaning of the regression curve.

AA2024-AA2024

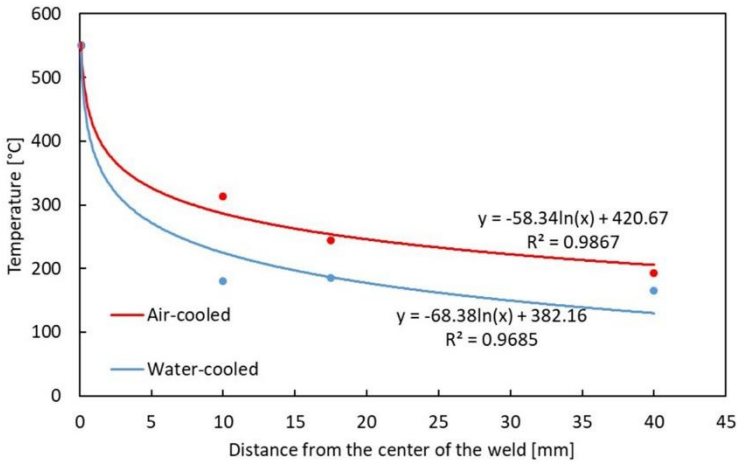

a)

AA5754-AA5754

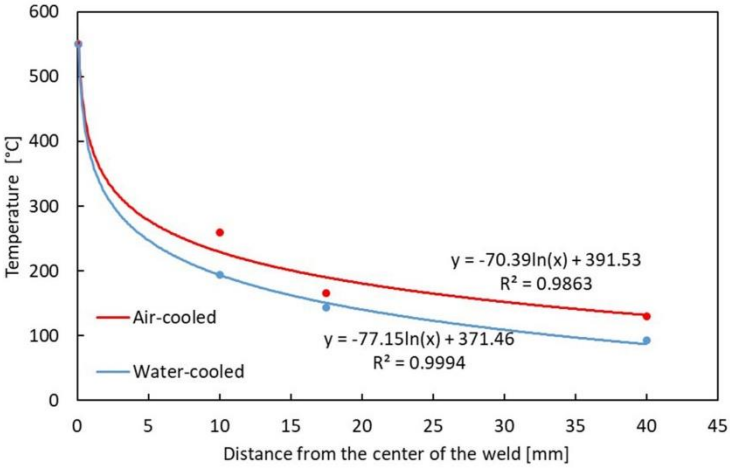

b)

AA6082-AA6082

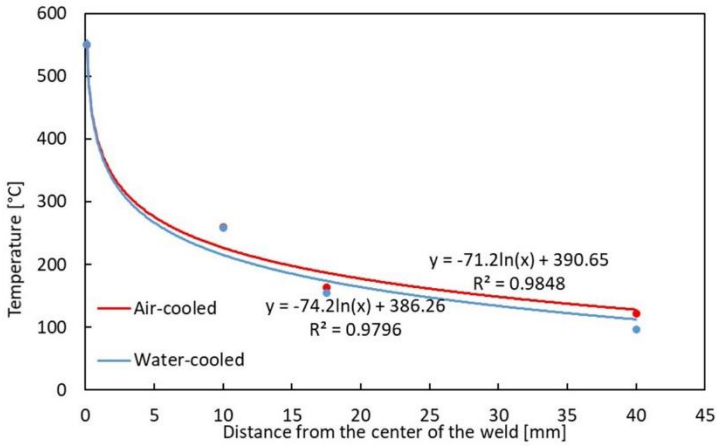

c)

AA7075-AA7075

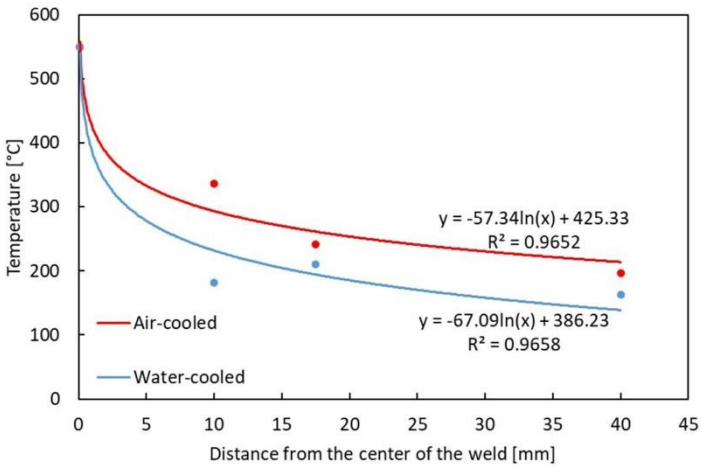

d)

Figure 7.9: Logarithmic regression function of air-cooled and water-cooled AA2024-AA2024 (a), AA5754-AA5754 (b), AA6082-AA6082 (c) and AA7075-AA7075 (d).

All the regression functions are characterized by very high R^2 values ranging from a minimum of 0.9652 to a maximum of 0.9994. This means that regressions well approximate the actual trend of the measured peaks. In all cases, the red line (indicating the trend of air-cooled tests) is always positioned above the blue line (indicating the trend of water-cooled tests).

Moreover, it is possible to highlight two different behaviors for the AA2024 and AA7075 welds (Figure 7.9a and d) with respect to the AA5754 and AA6082 welds (Figure 7.9b and c). This confirms what already discussed in relation to the graphs in Figure 7.7: considering only the thermal history of the welds, the actual cooling depends almost exclusively on the parameters used and not on the alloy considered. AA5754 and AA6082 alloys have, in fact, the higher feed rates, a condition that implies a lower quantity of heat entered in the sheets during FSW. This is also demonstrated by the lower temperature peaks reached during the welding (about 250 °C in air-cooled welds; Figure 7.7c and e) if compared to those of AA2024 and AA7075 welds (exceeding 300 °C; Figure 7.7).

7.3.2. Rockwell hardness distributions

The graphs shown in Figure 7.7 and Figure 7.9 permits to consider the thermal evolution of the welded joints. In order to analyze more in detail the effect of the

cooling conditions, it is necessary to study the mechanical characteristics of the obtained welds.

Figure 7.10 shows the average trends of the Rockwell B hardness obtained by repeating three different series of measurements for each type of welded alloy and cooling condition.

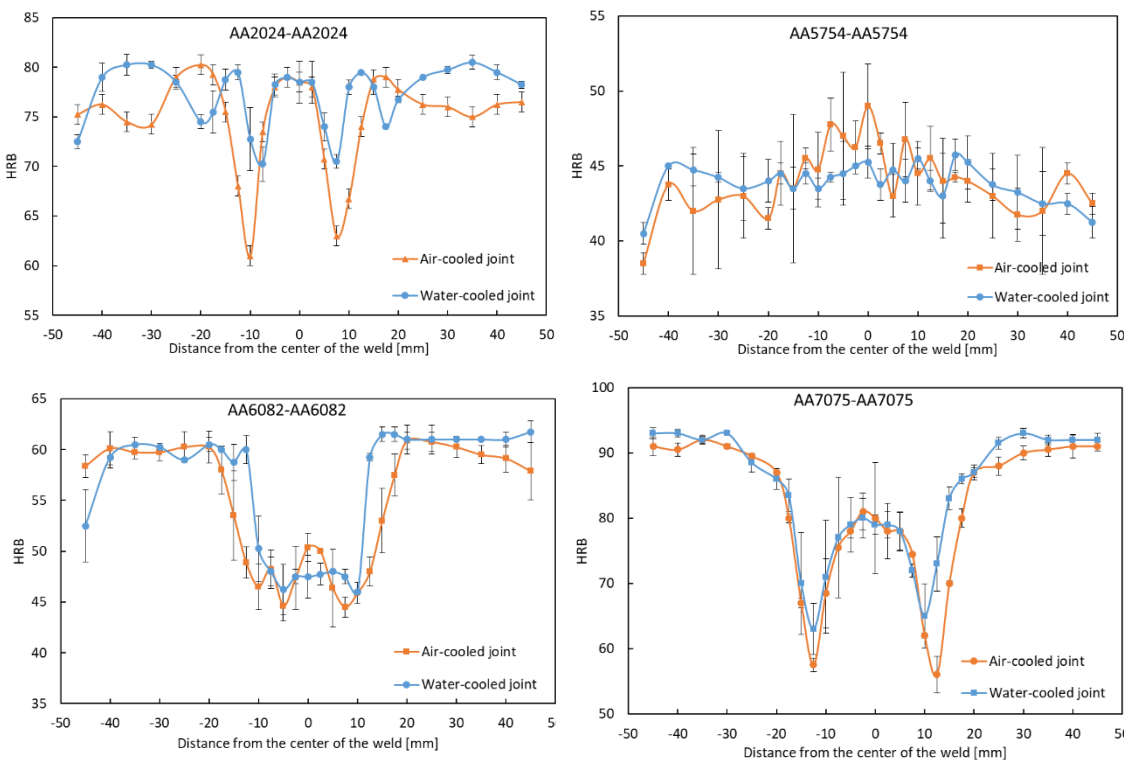

Figure 7.10: Rockwell harness diagrams for each alloy and for each cooling conditions. In each diagram the advancing side is on the right and the retreating side on the left.

From the graphs shown in Figure 7.10, a different behavior can be observed depending on whether the alloy is precipitation-hardening or work-hardening. Indeed, all precipitation-hardening alloys have the typical W-shape graph that characterizes the hardness maps of the FSWed joints, since the heat generated during processing acts on the microstructure of the material, changing its characteristics. On the contrary, the AA5754 alloy (that is a work-hardening alloy) has a different hardness distribution, in which the maximum hardness of the joint is traceable at the nugget, especially in the case of air-cooled welding. This is because the AA5754 bases its reinforcement on the mechanical processing and not on the precipitation

mechanism; therefore, the heat input does not play an unfavorable role on the hardness in the nugget.

For the precipitation-hardening alloys, the temperature reached in the various areas plays a fundamental role, since it is strictly connected to the quantity of hardening precipitates present in the matrix. If the temperature exceeds the solubilization temperature of the hardening precipitates, their density within the aluminum metal matrix undergoes a drastic reduction, leading to the softening of the interested area. This is particularly true for TMAZ and HAZ, because in the nugget the hardness is higher thanks to the effect of the mechanical action of the tool that causes the formation of fine and equiaxial grains.

For these reasons, in precipitation-hardening alloys, two effects of the cooling system on TMAZ/HAZ hardness values are visible. First, there is a benefit in terms of lower hardness peaks, since it can be seen that the hardness values are higher in the water-cooling conditions. The second effect regards the width of the area within the two minimum peaks: in water-cooled welds this area is more limited than in air-cooled welds. Furthermore, even from these tests, it is evident that water-cooling is more effective on the precipitation-hardening alloys.

The most pronounced effect of cooling system can be found in the TMAZ and HAZ because in these areas only the effects of the thermal cycle act without having the benefit of the mechanical action of destroying the grains. In these areas low temperatures and high thermal cooling gradient, given by the use of water, reduce the tendency of coalescing of precipitates and decrease the size of the grains, leading to an improvement in mechanical properties. On the other hand, if the temperature in those areas reaches and exceeds the reversion temperature of the hardening precipitates, the mechanical properties of the weld decrease.

The reversion temperatures are different according to the alloy and indicate the two temperatures at which the dissolution takes place before the hardening phase and subsequently the dissolution of the non-hardening phase. For the AA2024-T351 alloy these characteristic temperatures are 230 °C and 270 °C; at 230 °C corresponds the reversion of the hardening phase θ' and the beginning of the formation of the non-hardening phase θ, whose complete reversion takes place around 270 °C [179]. For the AA6082-T6 and AA7108-T6 alloys (also valid for the AA7075-T6 alloy), the

reversion temperatures are shown in Figure 7.11, as reported by Frigaard et al. [19]. The θ', β" and η' are hardening phase, whose presence within the alloy improves its mechanical properties. On the contrary, θ, β' and η are non-hardening precipitates and their presence within the joints worsen proves the mechanical properties.

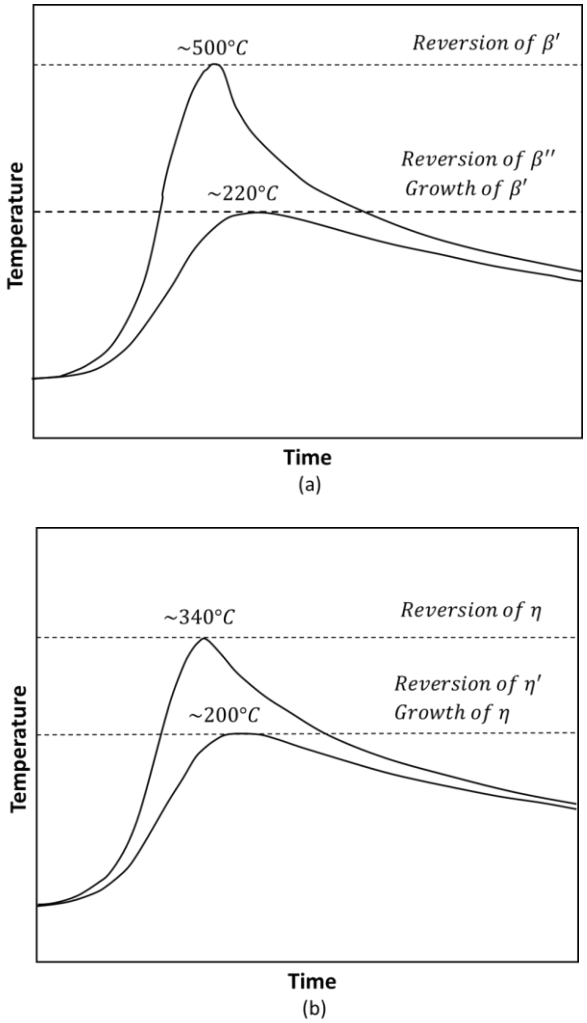

Figure 7.11: Schematic diagram showing the microstructure evaluation of the AA6082-T6 (a) and AA7108-T6 (b) during the welding [19].

Figure 7.12, Figure 7.13 and Figure 7.14 show the correlation between the logarithmic regression of air-cooled and water-cooled joints and the HRB maps as a function of the reversion temperature (indicated by the green line) of the hardening phases of each precipitation hardening alloy.

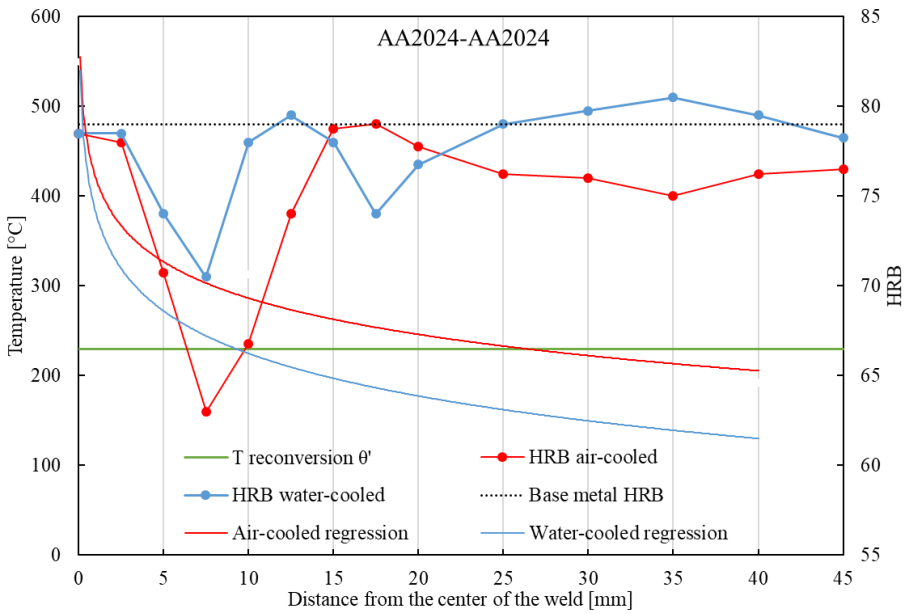

Figure 7.12: Correlation between logarithmic regression of air-cooled and water-cooled AA2024-AA2024 and Rockwell harness map in function of the temperature of reversion of θ' phase.

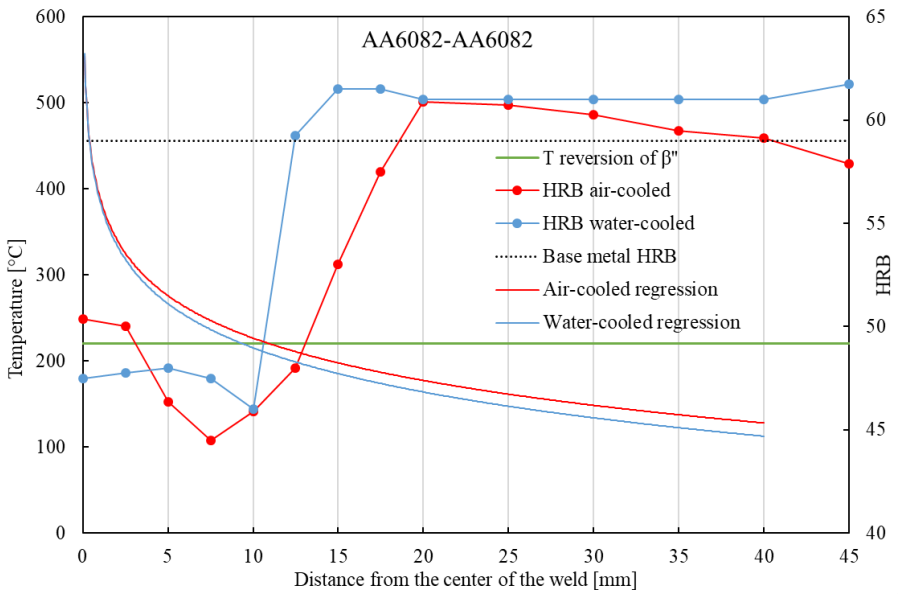

Figure 7.13: Correlation between logarithmic regression of air-cooled and water-cooled AA6082-AA6082 and Rockwell harness map in function of the temperature of reversion of β" phase.

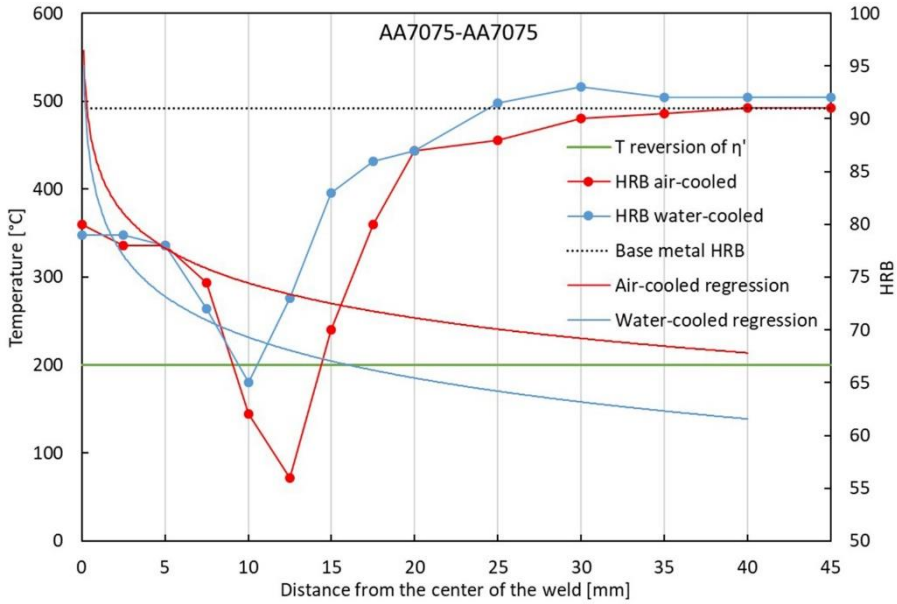

Figure 7.14: Correlation between logarithmic regression of air-cooled and water-cooled AA7075-AA7075 and Rockwell harness map in function of the temperature of reversion of η' phase.

The hardening phases θ', β" and η' are present in the base metal of all the precipitation hardening alloys subjected to heat treatment, in the supply conditions T3 or T6. However, these phases are certainly absent in the nugget because they are completely dissolved in the matrix during the welding process, since in this area the reversion temperatures of all the hardening precipitates are abundantly exceeded (Figure 7.15).

AA2024-AA2024

Air-cooled Water-cooled

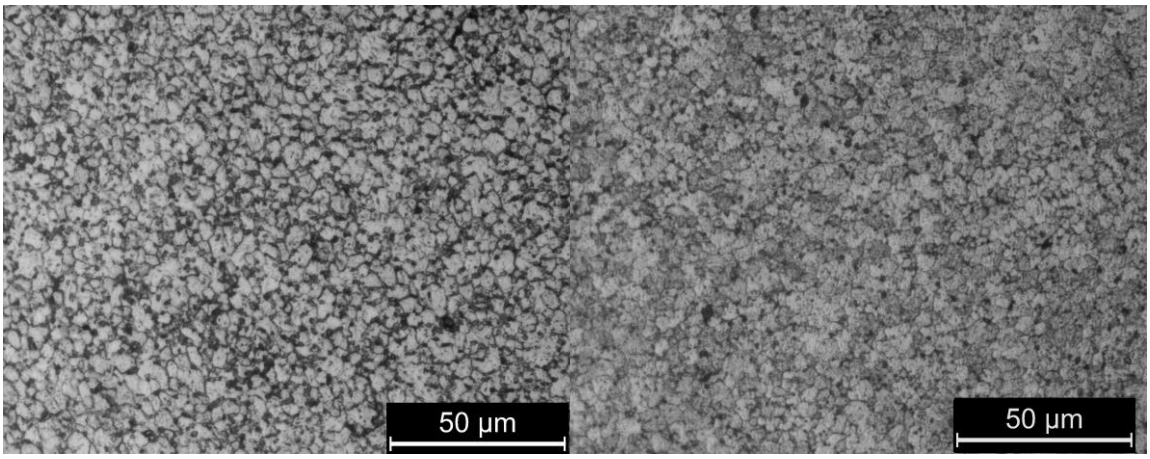

AA6082-AA6082

Air-cooled Water-cooled

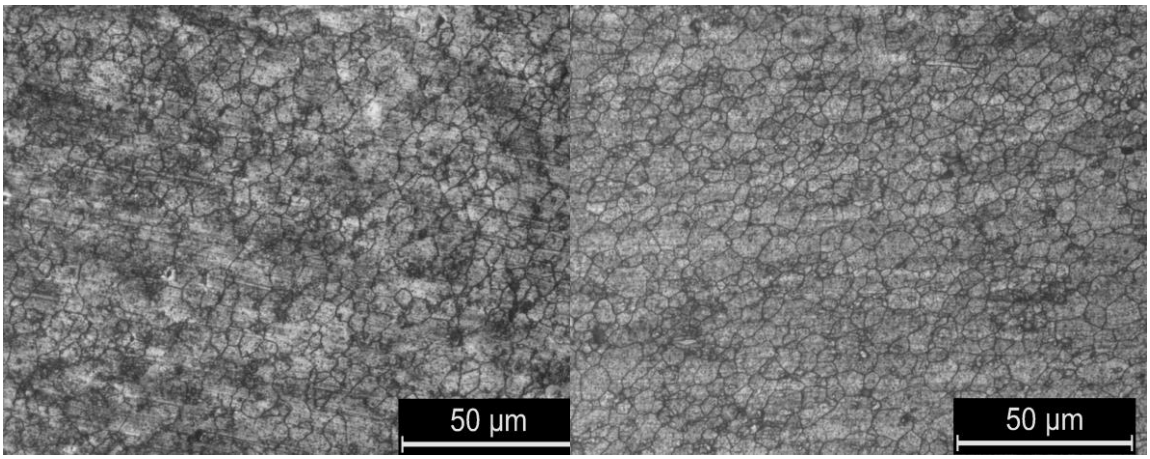

AA7075-AA7075

Air-cooled Water-cooled

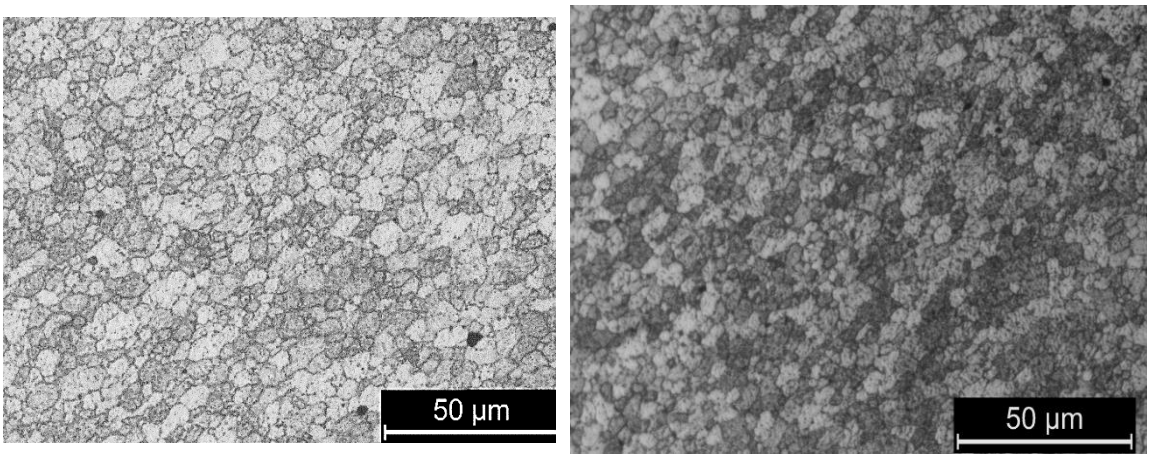

Figure 7.15: Microstructure of the welding zones of each cooling condition and for each alloy.

Due to these high temperatures, an over-saturated solution is created and cools as the process progresses, causing heterogeneous nucleation of the precipitates. At the same time, the mechanical action of the tool causes important plastic deformations that lead to the generation of dislocations. The dislocations are preferential points for the nucleation of non-hardening phases, especially at the grain boundaries, due to their high energy at the interface.

Subsequently, the precipitates begin to increase in dimension favored by the heat, thus giving coalescence.

This process leads to a decrease in mechanical properties, and this is what occurs especially in air-cooled welds. In water-cooled welds, on the other hand, the heat is removed faster and therefore the non-hardening precipitates, which are however present because they are inevitably generated by the process itself, do not have the possibility of coalescing and then are present with smaller dimensions. Hence, the benefit of cooling is evident, especially in welds characterized by a low feed rate and therefore by a prolonged time in which the important thermal flow causes the non-hardening precipitates to coalesce. This is evident in Figure 7.14 where the temperature regression (red line) of the air-cooled weld never drops below the green line that indicates the temperature above which the hardening precipitates disappear in favor of the non-hardening ones.

Table 7.5, Table 7.6 and Table 7.7 show the time (in seconds) during which the FSW zones have remained above the characteristic reversion temperature of the hardening phase for each alloy.

Table 7.5: Time in which the welding zones have remained above the phase transition temperature characteristic of the A2024 (230 °C).

AA2024-AA2024		
Time with T>230°C [s]		
	Air-cooled	Water-cooled
Nugget	50.4	0
TMAZ	27.9	0
HAZ	0	0

Table 7.6: Time in which the welding zones have remained above the phase transition temperature characteristic of the AA6082 (220 °C).

AA6082-AA6082		
Time with T>220°C [s]		
	Air-cooled	Water-cooled
Nugget	4.8	1.5
TMAZ	0	0
HAZ	0	0

Table 7.7: Time in which the welding zones have remained above the phase transition temperature characteristic of the AA7075 (200 °C).

AA7075-AA7075		
Time with T>200°C [s]		
	Air-cooled	Water-cooled
Nugget	82.8	0
TMAZ	62.4	11.1
HAZ	0	0

7.3.3. Tensile tests

In Table 7.8 average UTS data of the FSWed joints and their real percentage elongation (A%) are reported together with the ratio between the UTS of joints and base material.

Table 7.8: Average UTS data, real elongation A and ratio between the average ultimate tensile strength of joints and base material (UTSb) for all the tested conditions.

Alloy		UTS [MPa]	UTS [MPa] std.dev.	UTS/UTSb [%]	A [%]	A [%] std.dev.
AA2024-AA2024	Air-cooled	383.51	8.74	83.55	4.25	0.34
	Water-cooled	349.98	2.33	76.25	2.62	2.62
AA5754-AA5754	Air-cooled	213.94	1.76	100.91	19.96	1.55
	Water-cooled	214.36	1.42	101.11	16.78	2.13
AA6082-AA6082	Air-cooled	220.30	3.46	67.58	4.23	0.37
	Water-cooled	228	6.14	69.94	4.02	0.99
AA7075-AA7075	Air-cooled	374.04	3.33	64.71	3.28	0.31
	Water-cooled	392.76	20.34	67.95	2.59	0.83

It is possible to note that only AA5754, being a work-hardening alloy, has an improvement in the FSWed joints UTS with respect to the base material. This data also confirms the increase in hardness in the welded area compared to the base metal of the same alloy.

A common element for all alloys, both work-hardening and precipitation-hardening, is the reduction in the real percentage elongation of the water-cooled welded joints. This occurs because the increase in the amount of hardening precipitates at the expense of the non-hardening phase increases the hardness of the joints, as reported in Paragraph 7.3.2, but on the other hand decreases the ductility of water-cooled joints.

With reference to precipitation hardening alloys, in all alloys except for AA2024, a higher UTS is observed in water-cooled joints, although this benefit is less evident in AA6082. The response of the different alloys to the cooling system in terms of UTS can be explained by the failure points of the specimens shown in Figure 7.16. It is important to underline that the reported image refers to the most representative situation of each condition.

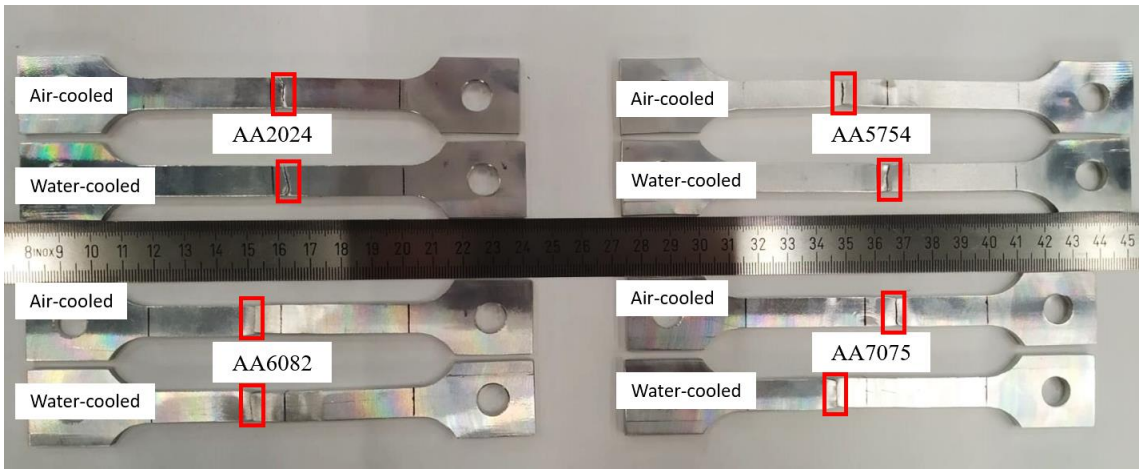

Figure 7.16: Fracture location for each cooling condition and for each alloy.

In AA6082 it is evident that the failure occurred in the same points for both cooling conditions and in particular at 8-10 mm from the center line of the weld. In these points it is possible to observe from Figure 7.13 that there is little difference in terms of hardness values and this is also the reason for the limited difference in UTS.

Similarly, in the AA7075 the breakage took place in the proximity of the TMAZs but, unlike the AA6082, it is possible to notice from Figure 7.14 a clear difference between the values corresponding to the TMAZ of the air-cooled weld compared to the air-cooled one. This difference is then reflected in the UTS value, thus achieving a benefit in the water-cooled condition.

On the contrary, a particular behavior was detectable in the welded AA2024, since in both cooling conditions the points of least resistance are near the nugget. As already mentioned in Paragraph 7.3.3, the pin mixing action prevails in this area, causing significant plastic deformations. Therefore, since near to the nugget, the grains and hardness values are similar in both the cooling conditions (Figure 7.12 and

Figure 7.15), the benefit of cooling is not perceptible from the UTS values; on the contrary, cooling proves to be harmful to the mechanical behavior of the joint.

The reason why, with the same grain size and hardness values, the AA2024 alloy proved to be more resistant in the air-cooled condition has to be found in the microstructural modifications caused by the welding process of the alloy, which must be considered as the only natural aged among the studied alloys.

The micrometric hardening precipitates present in the matrix are formed during solidification and they are not redissolved in the matrix, even during the solubilization hardening treatment, but they can be only mechanically crushed. Due to the natural ageing, the alloy is subjected to the formation of a solid supersaturated solution, that separates in magnesium and copper-rich nanometric precipitates, mainly at the dislocations created by mechanical processing of the pin. Following the thermo-mechanical action of the welding process, these precipitates are firstly dissolved in the matrix and then they precipitate again in micrometric dimensions on the edge of the recrystallized grain of the nugget. Vice versa, in correspondence with the TMAZs and HAZs there is no the thermomechanical dissolution of the precipitates, but only their coalescence to give larger particles. For this reason, in these zones, there is a significant lowering of the mechanical properties compared to both the base metal, were the hardening precipitates are still present.

As already mentioned in Paragraph 3.2, these hardening precipitates begin to increase in dimension favored by the heat, thus giving coalescence. With the water-cooling system, the heat is removed faster and therefore the non-hardening precipitates do not have the possibility of coalescing and then are present with smaller dimensions and, for a naturally aged alloy this leads to less benefit in terms of mechanical strength in the nugget area.

Being a naturally aged alloy, usually with very long ageing times, the temperatures reached lead to an over-ageing (probably interrupted in the case of water-cooling) of the area with a consequent depletion and redistribution of the hardening precipitates rich in copper.

In order to better comprehend the joint behavior, one-way ANOVA analysis was carried out on both the recorded UTS and the real percentage elongation data reported

in Table 7.8. Table 7.9 reports the interval plots, the F-values and the P-values about the effects of the cooling condition on UTS and A%.

Table 7.9: Interval plots, the F-values and the P-values about the effects of the cooling condition on UTS and A%.

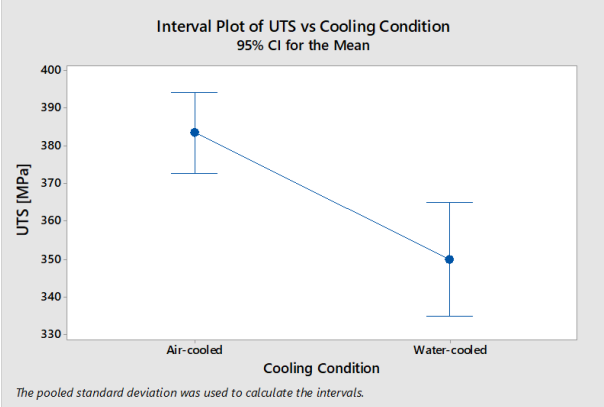

UTS	
F-Value	25.55
P-value	0.007

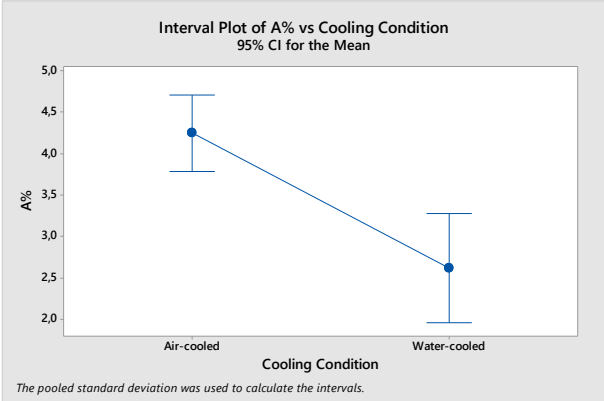

A%	
F-Value	31.75
P-value	0.005

It is important to remark that, in general, a factor was considered to have a relevant influence if its P value is lower than the cut off limit (in this case set equal to 0.05). For this reason, a clear dependence of the cooling system especially on the UTS and A% for the AA2024 values can be observed.

7.4. Conclusions

This chapter reports the results of a study about the effects of the heat generated in joints obtained by FSW technology. Four different aluminum alloys were considered, three precipitation-hardening alloy (AA2024, AA6082 and AA7075) and a work-hardening alloy (AA5754).

The results suggest that the thermal gradient of air-cooled welds is always lower than the thermal gradient of water-cooled joint. Moreover, considering only the thermal history of the welds, the actual cooling depends almost exclusively on the parameters used and not on the alloy considered. In fact, the alloys with the highest thermal gradient are those with the lower feed rates (AA2024 and AA7075 alloys).

From the mechanical point of view, it was observed that the change in hardness in precipitation-hardening alloys depends on the distribution of the hardening precipitates, on the density of the dislocations and on the size of the grains.

In TMAZ and HAZ the temperatures reached (lower than the reversion temperature characteristic of each precipitation-hardening alloy) allow to consider the presence of hardening precipitates in water-cooled welds. This leads to a benefit in terms of hardness and UTS of the water-cooled joints, with a consequent real elongation percentage systematically lower with respect to air-cooled ones.

In conclusion, the cooling acts on mechanical and metallurgical phenomena, reducing the formation of non-hardening precipitates and consequently increasing the mechanical properties of the TMAZ and HAZ.

Although it is important to act on the temperature of the different areas, it should not be forgotten that the mechanical contribution of the process, which acts especially in the nugget, cannot be modified. Therefore, the effects of cooling are certainly more appreciable in areas where there is no physical mixing of the material but only where there is a heat input due to the high conductivity of aluminum, i.e. TMAZ and HAZ.

8. *FSW optimization through Particle Swarm Algorithm and Artificial Neural Network*

This chapter is derived from the under-review article "Quarto, M.; Bocchi, S.; D'Urso, G.; Giardini, C.; (2021). FSW optimization through Particle Swarm Algorithm and Artificial Neural Network. Journal of Mechanical Science and Technology.

I am immensely grateful to the support received from my co-authors. I am responsible for all the changes in this chapter with respect to the published version.

8.1. Introduction

In the previous chapters the effects of the process parameters and of the cooling conditions have been analyzed both on the mechanical properties and on the corrosion behavior of the joints. It was evident that the FSW process is characterized by a variety of parameters and factors that make it rather complex to outline by optimizing the overall performance considering only one parameter at a time. Furthermore, all the data collected so far derived from rather long experimental campaigns in which different resources have been used (i.e., materials, equipment, particular instrumentation). These aspects could discourage the effective application of this process, that is a still recent technology, in the industrial field.

To overcome this problem, the present chapter took a step forward through the development of a methodology based on an ANN that analyzes and optimizes the FSW process considering also qualitative and uncountable variables, such as the welded material and the cooling type. Furthermore, the proposed method can be defined as a bidirectional method since it used the trained ANN to optimize a multi-objective function, defined on the base of the process outputs. The multi-objective optimization was carried out by using the Particle Swarm Optimization (PSO) algorithm. The ANN training and the PSO algorithm were obtained by customized routines written in Matlab environment. The developed model can be used successfully to identify the most suitable process parameters that allow to obtain certain characteristics of the joints. In the same way, it can be also used when limitations in terms of cooling conditions and/or materials are

imposed. In this case, it is possible to force in the model one or more inputs, so identifying the best combination of the remaining unknown inputs and outputs.

Indeed, the approach proposed in this research could efficiently respond to different industry needs, since the technicians are free to set factors from both process parameters and process outputs while the other process variables are automatically optimized.

8.2. Artificial Neural Network modelling

ANN is a general mathematical model inspired by the brain's structure and attempts at simulating its processing capabilities using the interconnection of elementary computational elements (neurons). ANN learns from experiences and then it is able to solve non-linear problems easily and quickly. The ANN is composed of an oriented network that is built by several layers identified as input, output and one or more hidden layers, each of them containing a certain number of nodes called neurons. Each neuron of a layer is linked to those of the following layer through weighted connections (Figure 8.1), which, together with the activation functions, store the knowledge acquired during the training phase. The connection weights and the activation functions are unknown until training is performed. As already said, the first layer of the net is represented by the input layer (IN) and its number of neurons is defined by the number of data enclosed in the input array. The external data are collected by the IN and then are sent to the neurons of the hidden layers (HN) through the activation function and the connections weight. The data elaborated through the connections reach the neurons of the output layer (ON), defined by the items included in the output array.

The most common training technique is the backpropagation, an iterative procedure that minimizes the error forcing the network to work in a back direction. After that, some other examples are used to test and validate the net which is able to compute the error between the forecast and the actual output values, working in the forward direction. The validation is conducted for defining the validity and reliability of the net, evaluating the deviation between the predicted output and the targets.

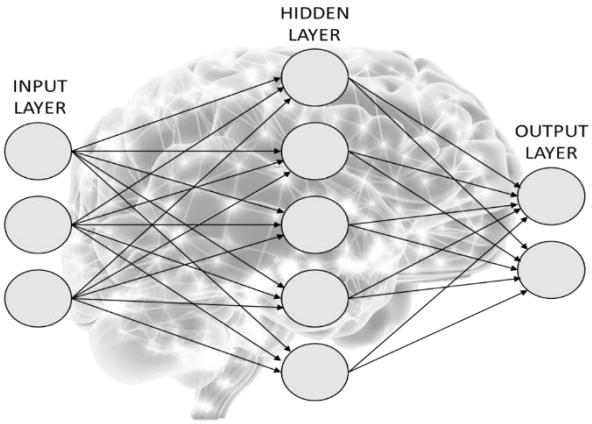

Figure 8.1: Artificial Neural Network.

8.2.1. Input and Output Layers structure

In this work, the IN is selected considering the following process parameters: tool rotational speed and feed rate, welding material and cooling type; for the ON the main mechanical characteristics of the welded joint are selected, such as the ultimate tensile strength and the hardness of the different areas of the weld. It is evident that the same methodology here proposed can be applied also considering a wider set of variables like pin geometry, other materials and so on. Table 8.1 reports the input and output neurons considered in this specific case. Materials and cooling type are represented by codes, while the other parameters are continuous variables. The whole dataset is normalized between 0 and 1 to simplify the net activity since inputs and outputs are characterized by large differences in terms of absolute value and unit of measure.

Table 8.1: Summary of Input and Output.

Inputs (IN)						
Material	M	Coded	AA2024: 1	AA5754: 2	AA6082: 3	AA7075: 4
Rotational speed	s	rpm				
Feed rates	*f*	mm/min				
Cooling	Cool	Coded	Air: 1	Water: 2		
Outputs (ON)						
Ultimate tensile strength	UTS	MPa	Obtained following the UNI EN ISO 6892-1:2016			
Hardness Rockwell Nugget	HRB	Average of the values collected in each zone following the international standard ISO 6508				
Hardness Rockwell TMAZ advancing	HRBa					
Hardness Rockwell TMAZ retreating	HRBr					

8.2.2. Hidden Layer structure

The most challenging aspect of the definition of ANN structure is the selection of the right number of hidden layers and the respective neurons (HN). Referring to the literature, the best ANN structure is characterized by one or two hidden layers; in fact, overfitting or underfitting scenarios can be described by a net structure defined by too many or too few hidden layers respectively. Empirical tests performed through the backpropagation algorithm show that there are no significant advantages in using two hidden layers instead of one [180–182]. The Kolmogorov's Theorem has applied to a neural network, demonstrating that a network with a single hidden layer can compute any arbitrary function of its input [183]. In 1987, a clear intuitive geometric argument that two hidden layers are sufficient to compute any decision has provided [184]. Further studies, based on empirical tests using a backpropagation algorithm,

have demonstrated that no significant advantages are using two hidden layers with respect to a single hidden layer [180–182]. According to the literature, the use of a single layer and a sigmoidal activation function is enough to define arbitrary decision boundaries for the outputs [181]. For this reason, in the present research, a single hidden layer network was chosen and the optimal network architecture was identified by varying the HN in a range defined by applying different heuristic methods as a function of the number of IN and ON. In particular, the lower bound MTI was defined according to Eq. 1 [185, 186].

$$MTI = \frac{(IN + ON)}{2} \qquad \text{Eq. 1}$$

For the definition of the upper bound it was considered the maximum value between three heuristics methods called Kolmogorov (Eq. 2) [183], Lippmann (Eq. 3) [184] and Kudrycky (Eq. 4) [186]:

$$KOL = 2 \cdot IN + 1 = 9 \qquad \text{Eq. 2}$$

$$LIP = ON \cdot (IN + 1) = 20 \qquad \text{Eq. 3}$$

$$KUD = 3 \cdot ON = 12 \qquad \text{Eq. 4}$$

In conclusion, the tested ANN configurations are reported in Table 8.2.

Table 8.2: Main characteristics of applied Heuristics approach.

Input (IN)	**Hidden Nodes (HN)**	**Output (ON)**	**Heuristics**
4	4	4	MTI
	5		…
	6		
	7		
	….		
	20		LIP

For testing the ability of the ANN and selecting the optimal number of HN, the Coefficient of Variation CV_i, a statistical indicator independent from the distribution, was considered. CV_i is expressed as a percentage so allowing a comparison of the variability between datasets described by different units of measure and order of magnitude. In particular, it is expressed as the ratio between the standard deviation (σ_{RMSE_i}) and the average value of the distribution (μ_{RMSE_i}) multiplied by 100 (Eq. 5).

$$CV_i = \frac{\sigma_{RMSE_i}}{\mu_{RMSE_i}} \cdot 100 \qquad \text{Eq. 5}$$

CV_i is calculated for each iteration i (where i indicates the tested value of HN) and for each output.

σ_{RMSE_i} and μ_{RMSE_i} describe the distribution of the Root Mean Square Error ($RMSE_i$) of each iteration, obtained comparing predicted outputs and desired targets (Eq. 6).

$$RMSE_i = \sqrt{\frac{\sum_{k=1}^{n}\left(Target_{i,k} - Output_{i,k}\right)^2}{n}} \qquad \text{Eq. 6}$$

Where k is the number of cases included in the dataset used for the training step; i corresponds to HN, varying between 4 and 20; $Target$ is a vector containing the experimental output recorded in the training dataset; $Output$ is a vector containing the output calculated by the trained ANN.

For each iteration, correspondent to the number of tested HN, the total value of CV_i is calculated as the sum of the CV_i of single output ($CV_i\ total$). The lowest value of $CV_i\ total$ identifies the optimal net structure allows to generate the minimum error in the forecast. Table 8.3 reports the value of CV_i estimated as a function of the number of tested neurons for each output node. The optimal value is equal to 20 neurons.

This procedure allowed the definition of the optimal ANN configuration, as reported in Figure 8.2.

Table 8.3: CV comparison using different hidden neurons.

HN i	CV_i UTS	CV_i HRB	CV_i HRBa	CV_i HRBr	CV_i total
4	26.52	92.87	25.41	46.57	191.36
5	37.10	80.41	56.44	67.21	241.16
6	29.92	63.80	24.01	37.34	155.07
7	30.10	88.09	37.63	49.19	205.01
8	20.09	50.26	19.10	32.51	121.96
9	19.16	43.57	15.51	23.27	101.51
10	22.17	62.16	22.33	37.23	143.90
11	23.86	48.54	15.33	24.83	112.55
12	18.84	48.09	14.77	27.50	109.20
13	20.17	48.57	14.84	28.64	112.22
14	24.96	49.91	20.46	27.94	123.27
15	21.36	54.64	22.00	34.52	132.52
16	41.97	85.22	32.44	56.39	216.02
17	35.14	86.36	12.16	24.49	158.14
18	12.41	51.41	11.83	23.30	98.95
19	8.96	18.69	7.34	19.33	54.32
20	3.93	21.51	7.23	18.42	51.08

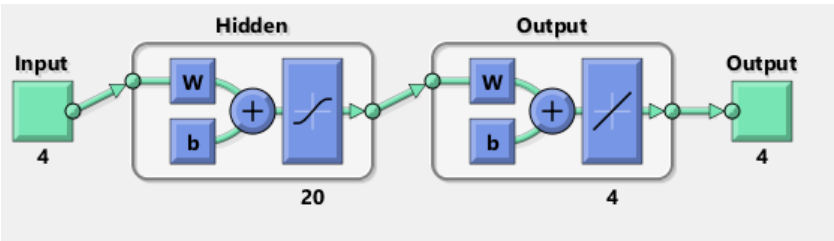

Figure 8.2: The structure of the ANN.

8.2.3. Training, Validation, and Testing of the ANN

A Matlab code was developed and implemented for training, validating and testing the ANN.

The data used for the analysis were collected through experimental FSW tests performed on a CNC machine. Tools with a smooth plane shoulder (16 mm diameter) and a frustum of cone pin shape (pin maximum and minimum diameters equal to 6 and 4 mm, pin height equal to 3.8 mm) were used; the tests were carried out by varying the feed rate and the rotational speed. The cooling system used consists of a continuous water jet at room temperature, which immediately cools the welded area. With regard to the output, tensile tests were executed on the FSWed specimens according to UNI EN ISO 6892-1:2016, using a Galdabini testing machine with a load cell of 50 kN. The hardness tests (HRB) were performed for all the input combination according to ISO 6508. 70% of input combinations and the corresponding outputs were used for the training, 15% for the validation and 15% for the test.

Figure 8.3, Figure 8.4, Figure 8.5 and Figure 8.6 show how the trained ANN predictions fit well the experimental values for the different terms considered.

Such a trained network can now be used to reliably forecast the process performance once the working conditions are defined.

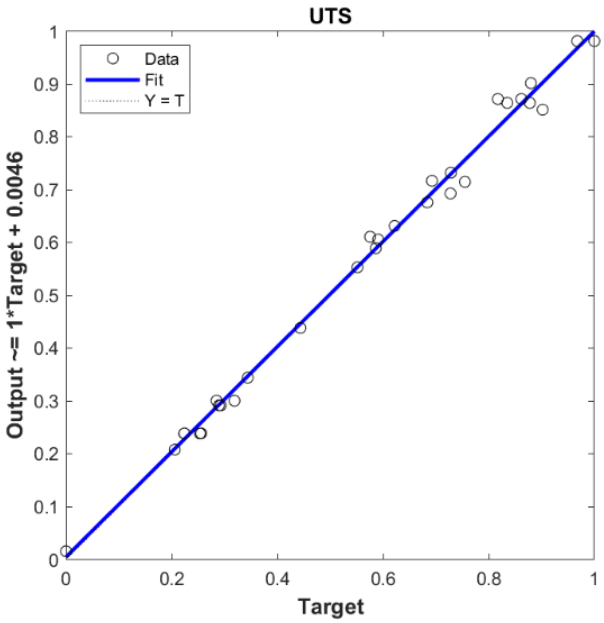

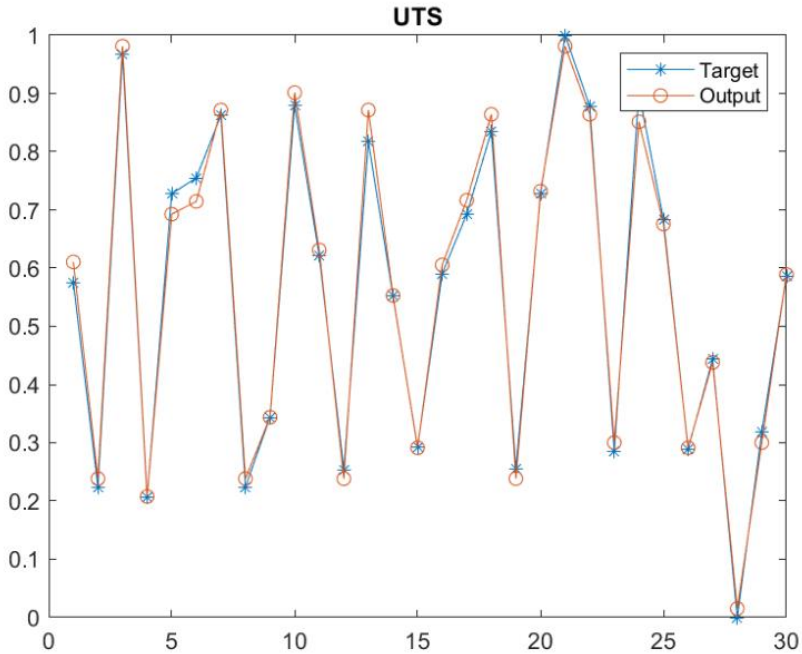

Figure 8.3: Prediction test data and actual values of UTS.

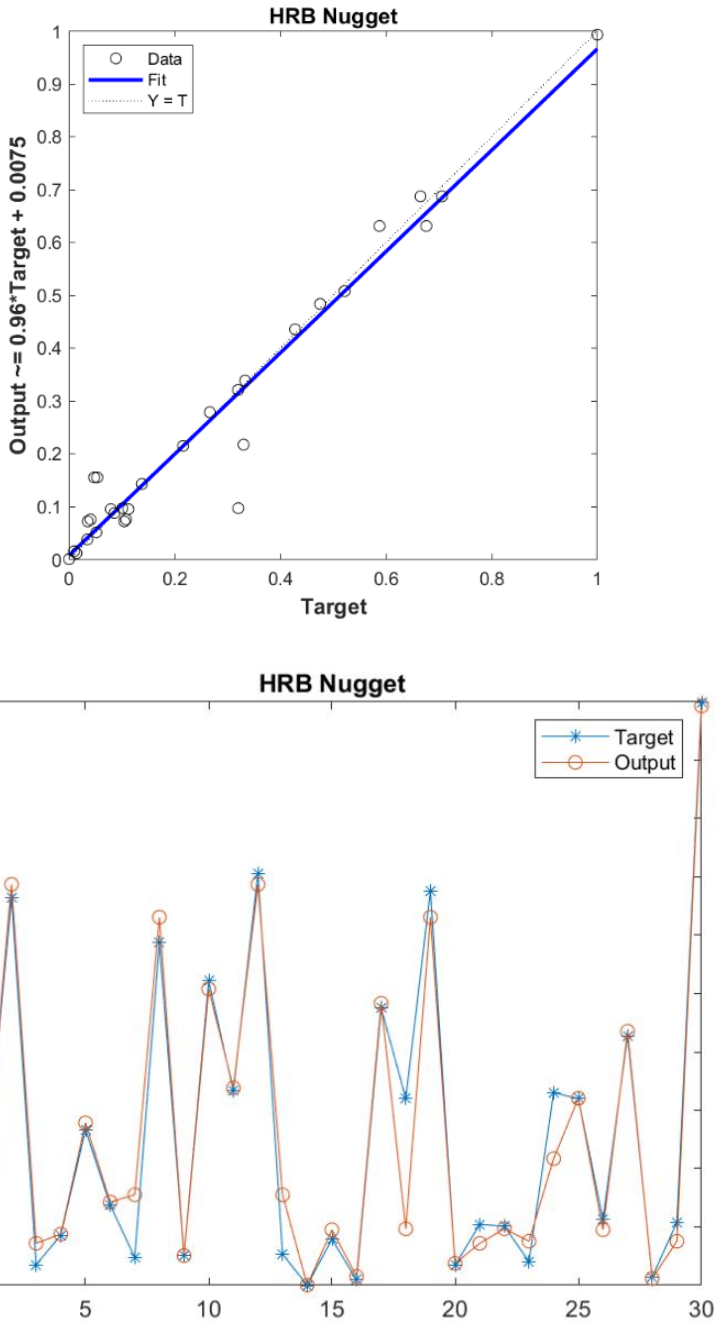

Figure 8.4: Prediction test data and actual values of HRB in the nugget.

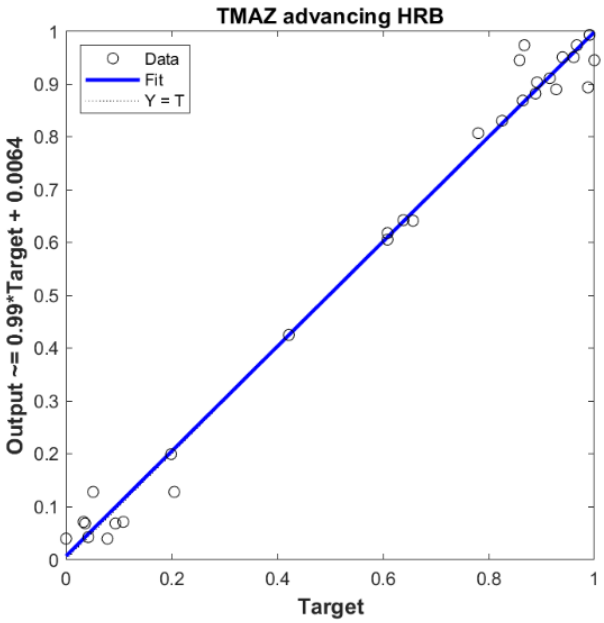

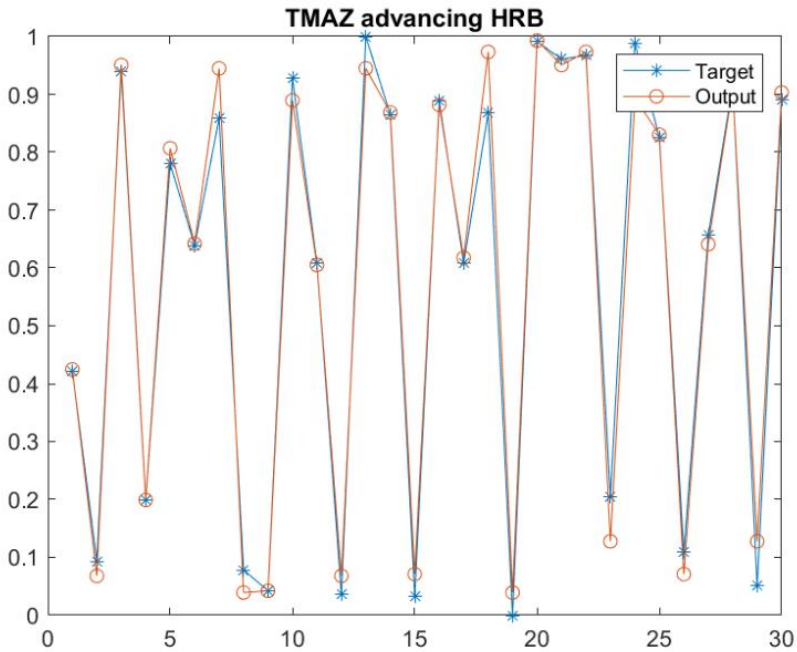

Figure 8.5: Prediction test data and actual values of HRB in the TMAZ, advancing side.

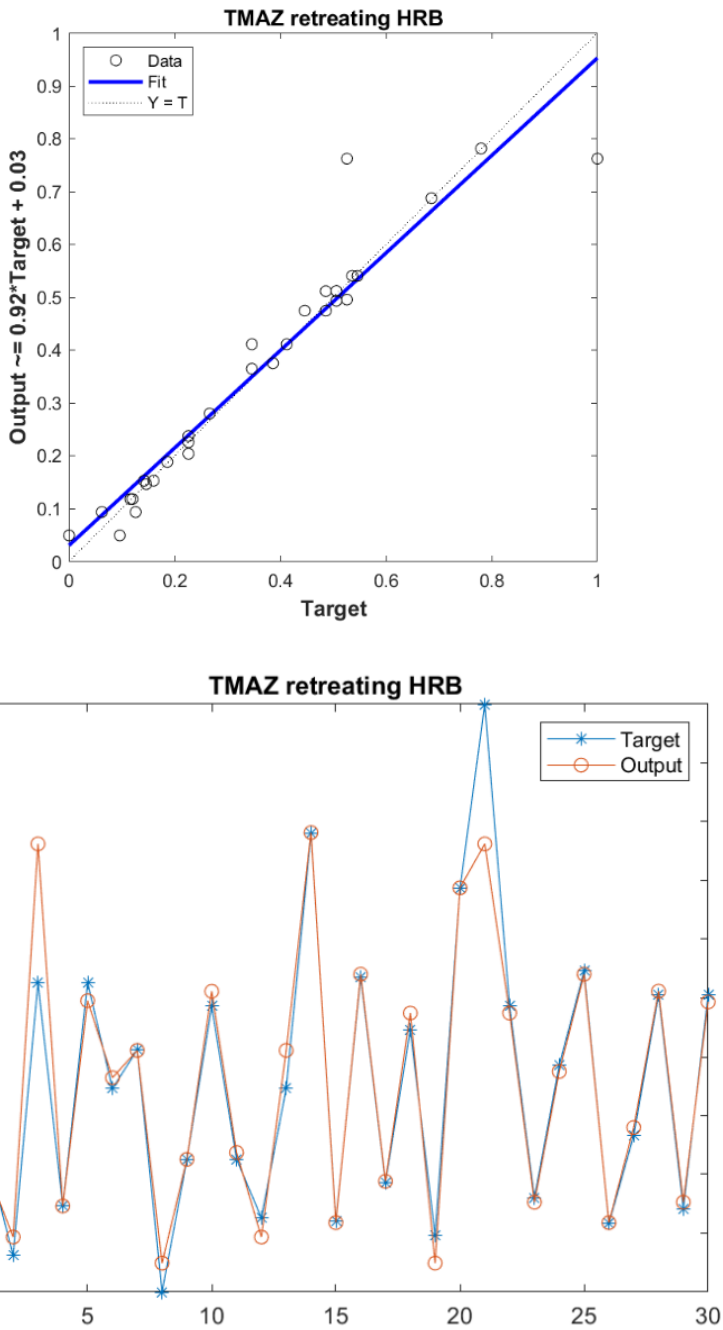

Figure 8.6: Prediction test data and actual values of HRB in the TMAZ, retreating side.

8.3. PSO algorithm

Even if the ANN is well trained, it does not work as an optimization tool. For this reason, the Particle Swarm Optimization (PSO) was chosen in this research.

In PSO the potential solutions are called particles and simulate a flock of birds. These particles move in the multidimensional problem space and each of them represents a combination of variable values. For each particle, the objective function can be calculated and stored. The algorithm moves iteratively the particles (partially in a random way) towards those values that correspond to the maximum values of the objective function (the so-called optimum particles). Some constraints in the problem space definition can also be defined.

In this specific case, the objective function is defining in relation to the ANN outputs, trying to maximize the mechanical characteristics involved in the ANN training. All the outputs are related to the ANN inputs, whose possible values represent the problem space. The objective function is defined in a limited range through some boundaries related to the normalization applied in the definition of the training matrix during the ANN definition. The PSO algorithm aims to find the combination of these values that optimize the objective function. The trained ANN was used to define the range in which the PSO can find the optimal solution, and at the same time, the identified solution must be satisfied the activation function established through the training of the ANN.

In practice, the PSO algorithm is characterized by an initialization procedure that defines a population of random solutions (the particles). For each of them, the objective function is calculated and a new position of the single particle is defined by an algorithm that calculates its new velocity and position towards the optimum particles. This procedure is iteratively repeated until, respecting the imposed constraints, the optimal value of the objective function is found. The process of PSO algorithm is summarized in the flowchart reported in Figure 8.7 and it was translated in Matlab code for the application of PSO coupled to the trained ANN.

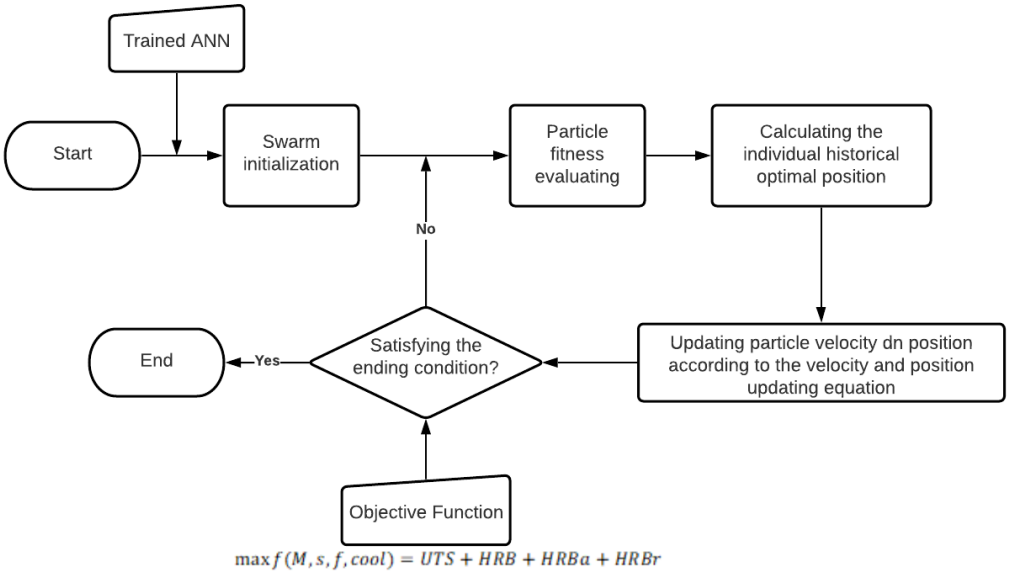

Figure 8.7: Flowchart of the PSO algorithm.

8.4. Application of PSO algorithm to FSW process optimization

8.4.1. Objective function definition and PSO application

In the present research, the objective function is defined through the maximization of both the UTS and the hardness values (Eq. 7).

$$\max f(M, s, f, cool) = UTS + HRB + HRBa + HRBr \qquad \text{Eq. 7}$$

Where, $f(M, s, f, cool)$ is an unknown function that is substituted by the trained ANN.

To keep the input values $(M, s, f, cool)$ within the technological limits and the ANN knowledge learnt through the network training (i.e. the values of the examples used for training it), it is necessary to limit the problem space imposing upper and lower bounds for each of them. The limits are set in normalized units between 0 and 1:

$$0 \leq M \leq 1 \qquad 0 \leq s \leq 1 \qquad 0 \leq f \leq 1$$

$$0 \leq cool \leq 1$$

With this configuration, the PSO algorithm works by changing recursively the ANN input values until the objective function is optimized. In industrial practice, some of the input values are fixed (e.g. material); in other cases, mechanical characteristics are defined by the technical specifications for the functionality that the product must satisfy. In the first case, it is necessary to force some of the ANN input values, while, in the second case, it is necessary to impose some limits for the ANN output values. The developed Matlab code is able to respond to these needs so that it is possible to fix both ANN inputs and outputs. For example, defining a priori the material, the MATLAB code uses the PSO algorithm to return the missing process parameters ($s, f, cooling\ type$) which guarantee the optimization of the objective function. Similarly, the operator may wish to base the optimization on the design specifications by forcing the values of the required mechanical characteristics of the joint; also in this case, the developed code can provide the optimal values of the missing process parameters.

8.4.2. Validation of optimization methodology

The validation was performed considering a possible industrial scenario where the operator needs to identify the optimal process parameters starting from the material and the desired level of UTS. In this way, it was possible to investigate/demonstrate the reliability of the method forcing both input and output at the same time. Specifically, the material as input and the UTS as output were considered into the optimization procedure. The optimization algorithm was used to identify the optimal process conditions in terms of $s, f, cooling\ type$ optimizing the objective function, while forcing one term (UTS).

Table 8.4 reports the input values suggested by the algorithm for welding four specific materials and obtaining the desired UTS (as closest as possible to the basic material UTS). The only forced imposed input in the algorithm was the material alloy, in this way it was possible define the best welding parameters set and, at the same, predict the mechanical characteristics. Considering these combinations, it is possible to observe that cooling with water is the preferred solution; the only exception is for the AA2024 alloy. This piece of evidence agrees with what emerged from a previous study on the effects of the cooling solution on the microstructure of FSW joints [138]

where it has been shown that the AA2024 alloy is the material least affected by cooling performed with water. Subsequently, using these process parameters, experiments were conducted on a CNC machine to verify the system reliability by comparing the predicted outputs and the experimental results in terms of UTS and hardness in different areas of the joint. The percentage of errors are shown in Figure 8.8. From the bar chart, the ability of the proposed optimization method in forecasting the actual behaviour of FSW process is evident; in fact, the maximum identified error is lower than 5%. The combination of PSO and ANN, managed by the code developed in Matlab for the definition of both solution space and constraints, has proven to be effective in satisfactorily identifying the process parameters as experimentally confirmed.

Table 8.4: Forced input and predicted optimal process parameters.

Case	**Imposed Material**		**Normalized Suggested Input**	**Suggested Input**
01	**AA2024**	***s***	1	2400
		f	0.0362	35
		Cool	0	Air
02	**AA5754**	***s***	0.1485	1200
		f	0.3478	250
		Cool	1	Water
03	**AA6082**	***s***	0.1918	1200
		f	0	10
		Cool	1	Water
04	**AA7075**	***s***	0.1728	1200
		f	0	10
		Cool	1	Water

Table 8.5 reports the predicted output, normalized and its actual value, and the experimental value obtained from the execution of welded tests performed applying

the welding parameters suggested by the algorithm. It is important to underline that the absence of decimal places in the experimental outputs values (HRB, HRBa and HRBr) is exclusively due to the sensitivity of the instrument used for the detection of these results. Nevertheless, it has been chosen to consider also the decimal places of the predicted values of the hardness outputs because, as predicted, they are not strictly bound to the smallest value of the quantity that the instrument can detect.

Table 8.5: Predicted and experimental output.

Case		Normalized Predicted Output	Predicted Output	Experimental Output
01	**UTS**	0.8779	394.57	394.57
	HRB	0.9178	75.27	76
	HRBa	0.5233	64.87	63
	HRBr	0.4290	60.89	61
02	**UTS**	0.2557	215.75	215.75
	HRB	0.0321	45.87	45
	HRBa	0.0714	42.27	44
	HRBr	0.0384	42.15	44
03	**UTS**	0.4827	280.98	281.61
	HRB	0.0914	47.83	47
	HRBa	0.1491	46.16	46
	HRBr	0.1391	46.98	48
04	**UTS**	0.9693	420.85	429.00
	HRB	0.9767	77.23	78
	HRBa	0.3764	57.52	56
	HRBr	0.3616	57.66	58

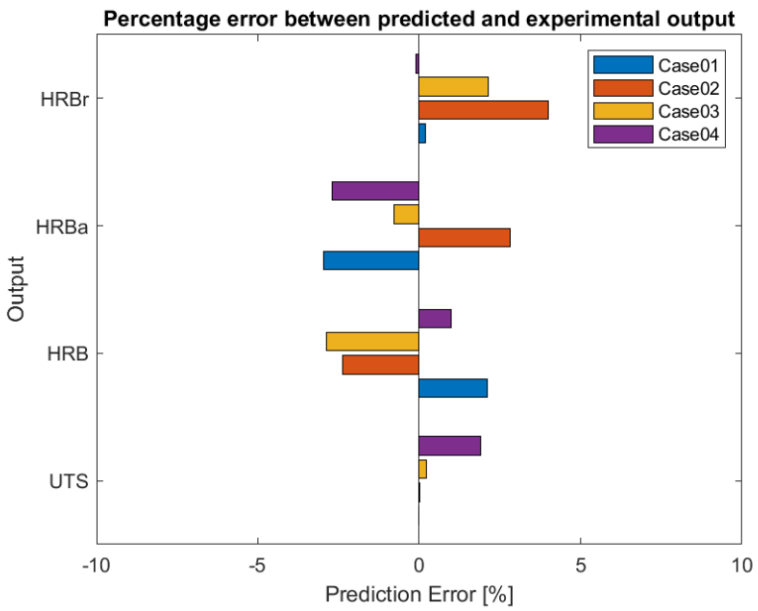

Figure 8.8: Percentage error between predicted and experimental process performances.

8.5. Conclusions

An optimization methodology for FSW process was developed combining artificial neural network (ANN) and particle swarm optimization (PSO). The developed algorithm can satisfy different requirements of industrial scenarios; in fact, it is able to suggest the best process conditions for a defined material or for respecting the mechanical characteristics required by a product design. The first step concerned the design and training of an ANN relating the most influencing process parameters as inputs and the main mechanical characteristics of the joint as outputs. The neural network was trained by a backpropagation algorithm, considering a dataset based on the historical data, the 70% of which were used for training and the remaining for testing and validating the network. The second step involved the PSO algorithm implemented in a Matlab code in order to use the trained ANN for identifying optimal process parameters under different multi-objective function and by introducing several constraints in the definition of the solution space. The method was successfully validated by executing actual FSW experiments and comparing the results with the process performances forecasted by the model in terms of actual mechanical properties of the joints. The good results coming out from the validation allow to state that the proposed method is effective when constraints are fixed not

only for the ANN inputs but also for the ANN outputs, respecting the multi-objective function imposed.

9. *Hybrid FEM-ANN approach for hardness prediction of AA6082 Friction Stir Welded joints*

This chapter is derived from the submitted article "Quarto, M.; Bocchi, S.; D'Urso, G.; Giardini, C.; (2021). Hybrid FEM-ANN approach for hardness prediction of AA6082 Friction Stir Welded joints. International Journal of Mechatronics and Manufacturing Systems.

I am immensely grateful to the support received from my co-authors. I am responsible for all the changes in this chapter with respect to the published version.

9.1. Introduction

As already demonstrated, the surface hardness is a very interesting characteristic that allows to understand the trend of the mechanical properties of a FSWed joints. One of the main aspects to consider is the different achieved surface hardness as a function of the area of the sample, due to the peak of temperature reached during the welding process. These disparities between the different characteristic zones of the weld could strongly affect the service quality and the component life. The problem becomes more evident if the aim is the determination of the surface hardness in correspondence to a specific peak of temperature.

This chapter presents a hybrid model based on the Finite Element Method (FEM) and ANN that can be used for predicting the final hardness of the single points of the welding as a function of the maximum reached temperature.

Since FSW is a quite recent process, the development of models and simulation techniques is useful for better understanding its physics [98–100].

Indeed, a virtual model was set up to predict the temperatures reached locally by the joint and consequently the overall mechanical properties. Sensitivity analysis has been conducted to study the relationship between the input and the output variables for creating a robust model.

The FEM model was set-up and validated starting from numerical investigations on the peak of temperature experimentally reached in the different areas of the welded sample, reported in Chapter 7, considering a forecasting error of about 15%. The output data of

the simulation was a temperature map of the sample introduced into the ANN together with experimental results for the ANN training. The hybrid approach FEM-ANN provides a robust framework for forecasting aluminum hardness after the FSW process without experimentally investigating each welding.

9.2. Proposed Hybrid FEM-ANN approach

The FEM-ANN approach proposed in this paper is sketched in Figure 9.1. Once the model has reached a satisfactory level of accuracy and robustness, the simulated results were used to generate the dataset suitable for the ANN training step.

The numerical simulation already represents a suitable tool for forecasting process results, but its integration with the neural network can result in an improvement of a prediction model.

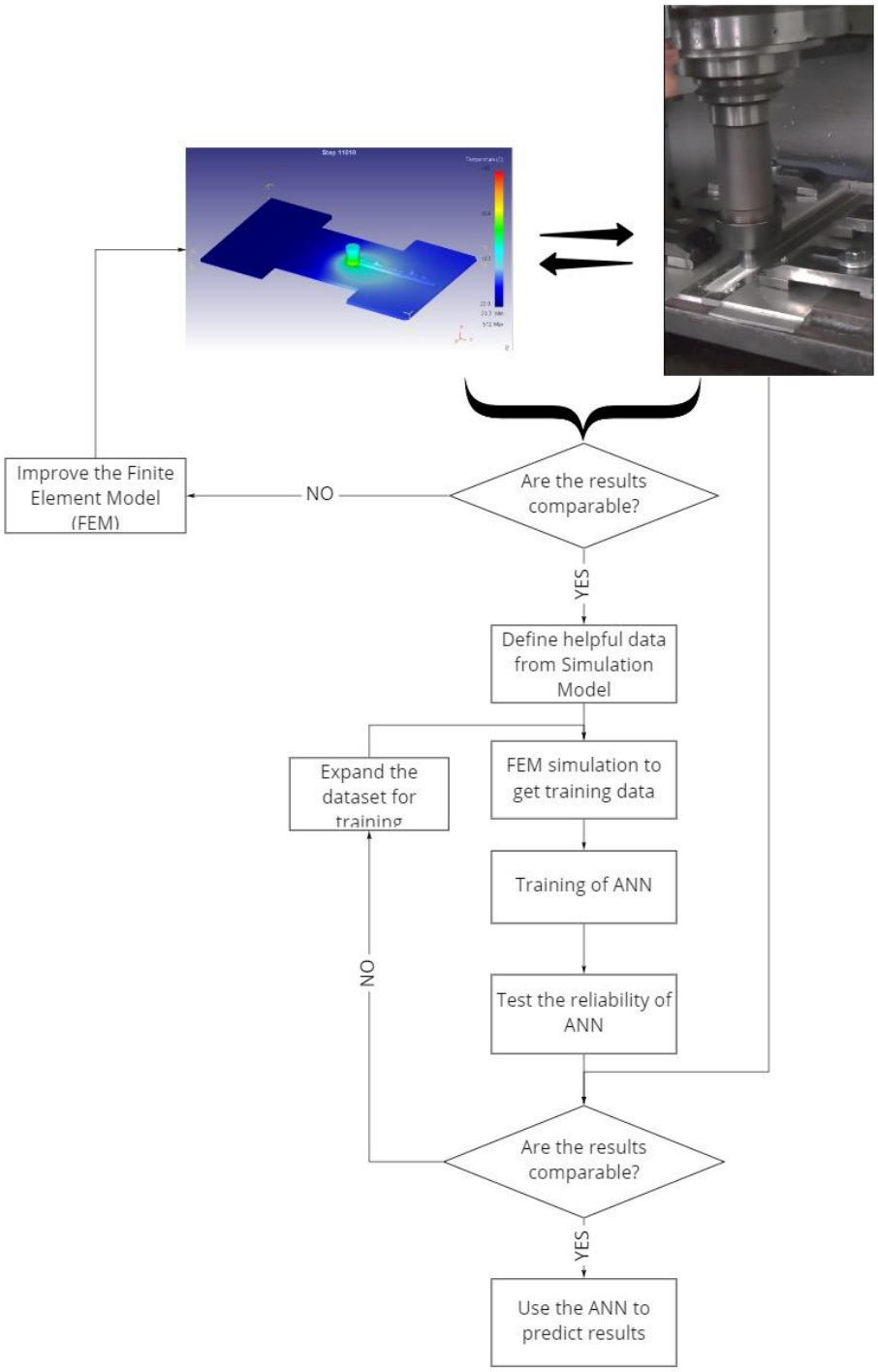

Figure 9.1: Hybrid FEM-ANN approach flowchart.

9.3. FSW simulation model setup

A 3D FEM Lagrangian model was set up using the commercial software DEFORM 3D™. The tool was modelled as a rigid object using AISI-1045 steel as reference material

(defined between 20°C and 1100°C). The plates to be welded were modelled as a single plastic workpiece made of Aluminum-6061 (defined between 250°C and 480°C). Both aluminum and steel with their material flow stress data were chosen among those available in the Deform library database (with their related material constitutive and physical properties).

The assumption to consider the tool as a rigid object and the workpiece as plastic is reasonable because of the significantly lower yield strength of the aluminum with respect to the yield strength of the steel tool. Finally, the workpiece was discretized using 100000 tetrahedral elements, as shown in Figure 9.2.

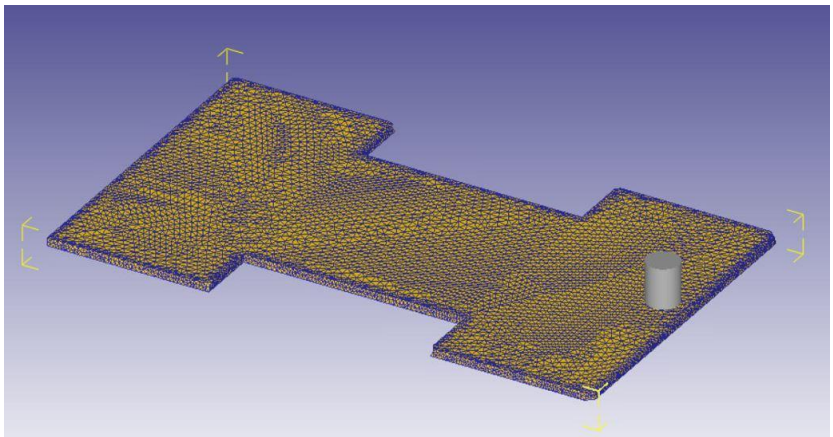

Figure 9.2: Mesh of the aluminum workpiece.

In order to better simulate the entire friction stir welding process, the process was divided into three main steps. In the first one, the tool, which is not yet in contact with the workpiece, starts to rotate and translate in the vertical direction until the tool shoulder is completely in contact with the aluminum workpiece. In the second phase, the advancing stage, the tool moves forward along the welding line, until the entire length of the sheet has been involved in the process. The last step involves ascent and the detachment of the tool from the workpiece. For the whole process, the rotational speed and the feed rate were set equal to 2400 rpm and 375 mm/min respectively, which are the optimal welding parameters obtained from previous work [138].

Regarding the thermal part of the simulation, the heat exchange with the environment was kept constant. In particular, the heat exchange with the environment was set equal to 0.02 N/(mm·s·°C) for the air-cooled FSWed joints. For the water-cooling condition, three

levels were tested (0.3 - 0.4 – 0.6 N/(mm·s·°C)) to obtain the better match with the experimental results.

After identifying the best coefficient, the heat exchange with the environment for the water-cooling condition was maintained constant only within a local window moving with the tool only during the advancing stage. This choice was done to get closer to the experimental campaign, where the flux of water hit only the already welded part of the joint. Into the local window, the water temperature was maintained constant at 20°C.

During the last stage of the process, the mentioned local window remains in the reached position at the end of the welding advancing step until the entire simulation process stops. This choice was made to obtain a model as close as possible to the experimental conditions. A sensitivity analysis, involving the parameters reported in Table 9.1, was carried out following an inverse characterization method.

Table 9.1: Parameters and their range considered for the sensitivity analysis.

Parameters	**Value**	
	Min	**Max**
Friction coefficient aluminum-tool	0.1	1
Thermal conductivity	100 N/(mm·s·°C)	600 N/(mm·s·°C)
Aluminum emissivity	0.2	1
Heat transfer coefficient aluminum-tool	11 N/(mm·s·°C)	10000 N/(mm·s·°C)

9.3.1. FEM model validation

For validating the FEM model, the simulated results were compared with the experimental data. The experimental campaign was performed using a CNC machine. Butt joints were carried out on AA6082-T6 sheets having a thickness equal to 4 mm. A simple tool with a frustum of cone pin shape (pin minimum and maximum diameters equal to 4 and 6 mm, pin height equal to 3.9 mm) and flat shoulder (diameter equal to 16 mm) was considered. The adopted values of tool rotation speed and feed rate are the same applied in the simulations [138].

Two cooling conditions were taken into account:

1. the traditional with air;

2. room-temperature water, insolating the area still to be welded through a bulkhead mounted on the spindle.

In order to quantitatively measure the temperature variation reached in the joint with and without the water-cooling system, three type K thermocouples were positioned in the cross-section of the plates at different depths to be able to detect the temperature at the three fundamental zones of the welding: nugget, TMAZ and HAZ, as shown in Figure 9.3.

It was chosen to position the thermocouples in the advancing side because, although the process is almost symmetrical in terms of hardness and mechanical properties achieved, this part has proved to be hotter than the retreating side, as demonstrated by G. Sorger et al. [43].

A Flir System ThermoVision A40 infrared camera was used in order to measure the peak temperature reached by the nugget, where the remixing of the material prevents the contact measurement.

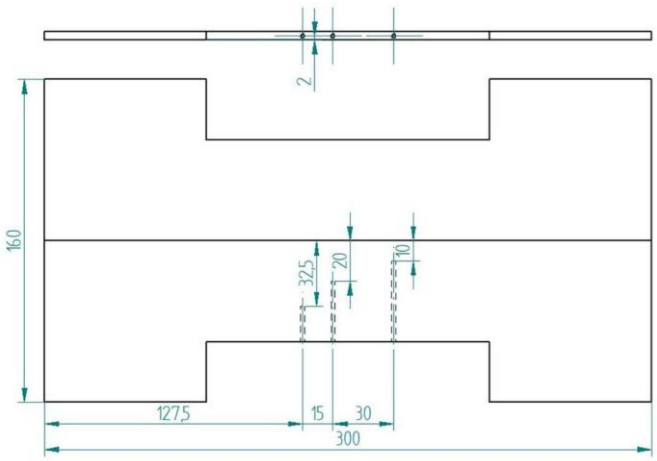

Figure 9.3: Thermocouples housings inside the plates to be welded [187].

The combinations of parameters used in the FEM simulations are shown in Table 9.2 and Table 9.3. The columns relating to the outputs show the percentage differences with respect to the reference temperatures experimentally measured by the thermocouples. In the tables, the friction coefficient between aluminum and tool is indicated by A, the thermal conductivity of aluminum by B, the aluminum emissivity by C and the heat transfer coefficient between the aluminum and tool by D. The main difference among the

two models is represented by the presence of a fifth parameter for the water-cooled process, the heat exchange with the environment, represented in Table 9.3 by the letter E. As results from the several simulations conducted, the optimal combinations able to better reproduce the process behavior and the temperature distribution are highlighted in Table 9.2 for air-cooled joints and in Table 9.3 for water-cooled butt.

Table 9.2: Considered combination of inputs and relating outputs for the air-cooled joints.

Air-cooled joints							
	INPUT				**OUTPUT**		
	A	**B [N/(mm·s·°C)]**	**C**	**D [N/(mm·s·°C)]**	ΔT_{nugget} **[%]**	ΔT_{TMAZ} **[%]**	ΔT_{HAZ} **[%]**
#1	0.4	180.181	0.7	11	-52.40%	-44.40%	-40.20%
#2	0.4	180.181	0.7	110	-37.10%	-33.60%	-27.40%
#3	0.4	180.181	0.7	1100	-37.20%	-31.60%	-26.70%
#4	0.4	180.181	0.7	1100	-21.60%	-21.60%	-13.60%
#5	0.4	180.181	0.2	1100	-25.30%	-19.40%	-12.20%
#6	0.4	180.181	1	1100	-28.80%	-28.90%	-21.90%
#7	0.4	100	0.7	1100	-46.30%	-48.20%	-43.30%
#8	1	100	0.7	10000	-29.80%	-36.10%	-33.90%
#9	1	300	0.7	10000	-26.40%	-19.20%	-7.10%
#10	1	600	0.7	10000	-27.70%	-9.80%	9.10%
#11	1	450	0.7	10000	-19.60%	0.90%	17.60%
#12	0.4	100	0.2	8000	-10.90%	-42.90%	-41.70%
#13	1	450	0.7	10000	2.60%	-0.10%	15.90%

Table 9.3: Considered combination of inputs and relating outputs for the water-cooled joints.

Water-cooled AA6082								
	INPUT					OUTPUT		
	A	**B** [N/(mm·s·°C)]	**C**	**D** [N/(mm·s·°C)]	**E** [N/(mm·s·°C)]	ΔT_{nugg} [%]	ΔT_{TMAZ} [%]	ΔT_{HAZ} [%]
#1	1	450	0.7	10000	0.3	-7.90	-15.20	-3.70
#2	1	450	0.7	10000	0.4	-4.30	-9.10	-2.10
#3	1	450	0.7	10000	0.6	-8.60	-23.90	-15.80

To validate the model, the temperature values predicted by the model (registered in the corresponding positions) were compared to the maximum temperatures experimentally measured by the thermocouples. It was observed that the predicted peak temperature matches the experimental maximum peak values very well, as demonstrated in Figure 9.4 and Figure 9.5. In fact, as reporting by X. K. Chu et al and by H. S. Arora et al., the simulated values are considered in close agreement with the experimental ones, and thus trustable for the further phases of the analysis, if the forecasting error value is around 15% [188, 189].

Air-cooled

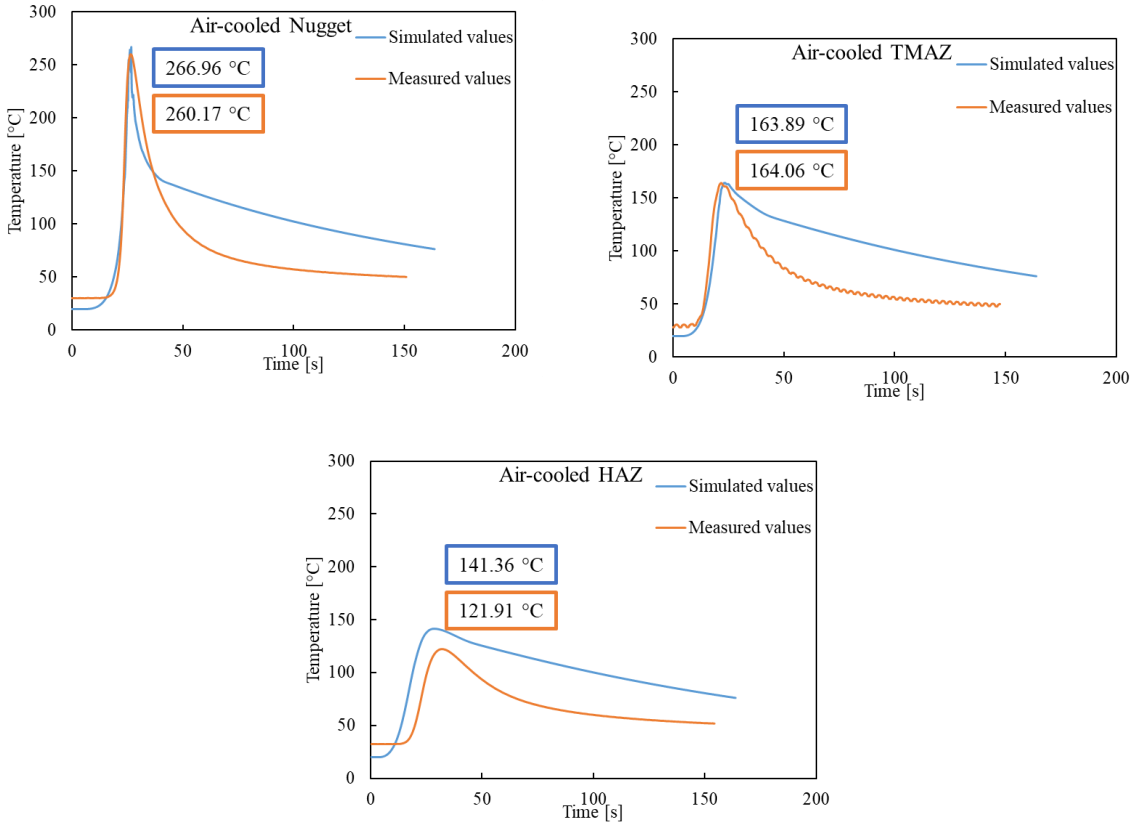

Figure 9.4: Simulated and measured values of temperature reached in air-cooled joint.

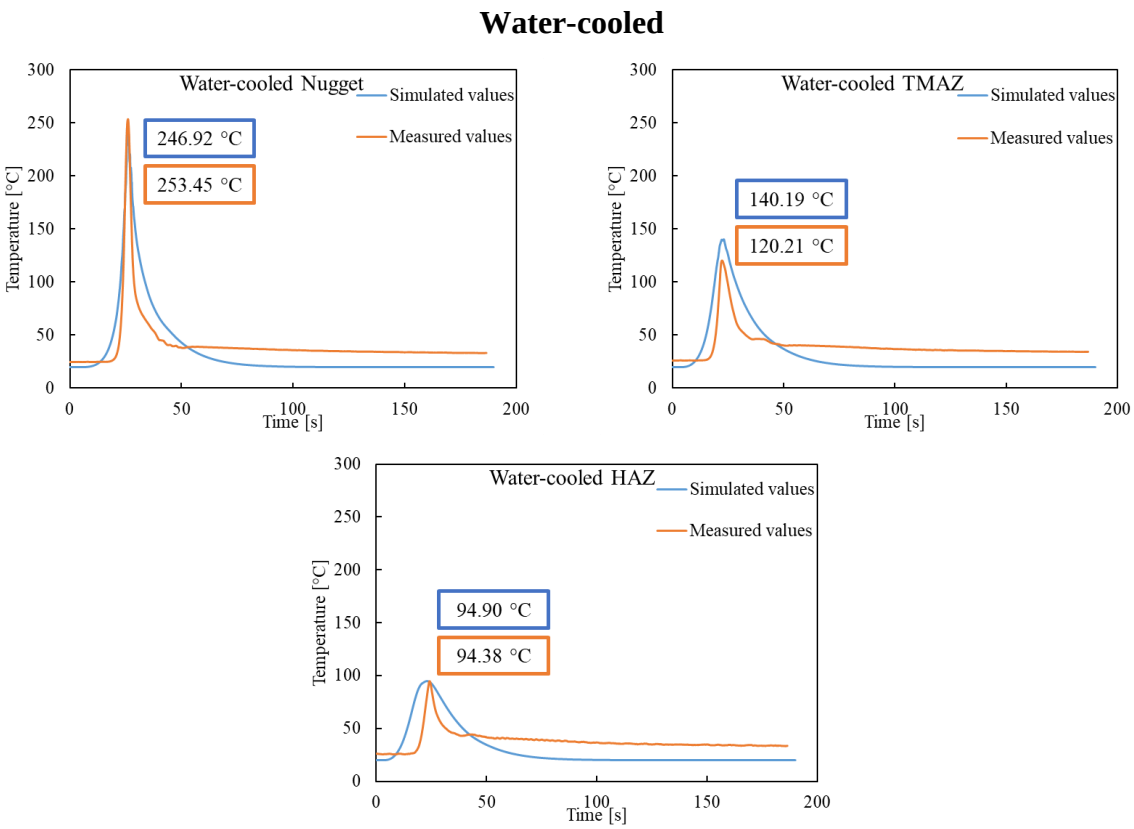

Figure 9.5: Simulated and measured values of temperature reached in water-cooled joints.

From the graphs shown in Figure 9.4 and Figure 9.5, it is possible to state that the simulative model is able to predict the reached maximum temperatures better than the cooling thermal gradient, especially in the case of air-cooled welds. Specifically, the cooling thermal gradient is considered as the time required to decrease the sheet temperature until the 50°C. This different temperature trend in the air-cooling phase (Figure 9.4) is probably due to the presence of the support plate on which the sheets to be welded are strongly constrained during the experimental campaign.

The support plate is made of steel and for this reason, represents an important thermal mass capable of absorbing a large amount of heat. For simplicity, the simulation model has been assumed without taking into account the thermal constraints due to the weld clamping system (used in the experiments). This aspect can lead to notable differences in the cooling phase between the simulated curves and the measured curves in air-cooled joints. On the other hand, this difference is much less evident in water-cooled welds (Figure 9.5) where the useful time for transferring heat between the aluminum and the

steel plate is significantly reduced thanks to the presence of water which is able to quickly remove most of the heat developed by the process.

As far as the FEM model (Figure 9.6), following several experimental tests, the proposed model was calibrated.

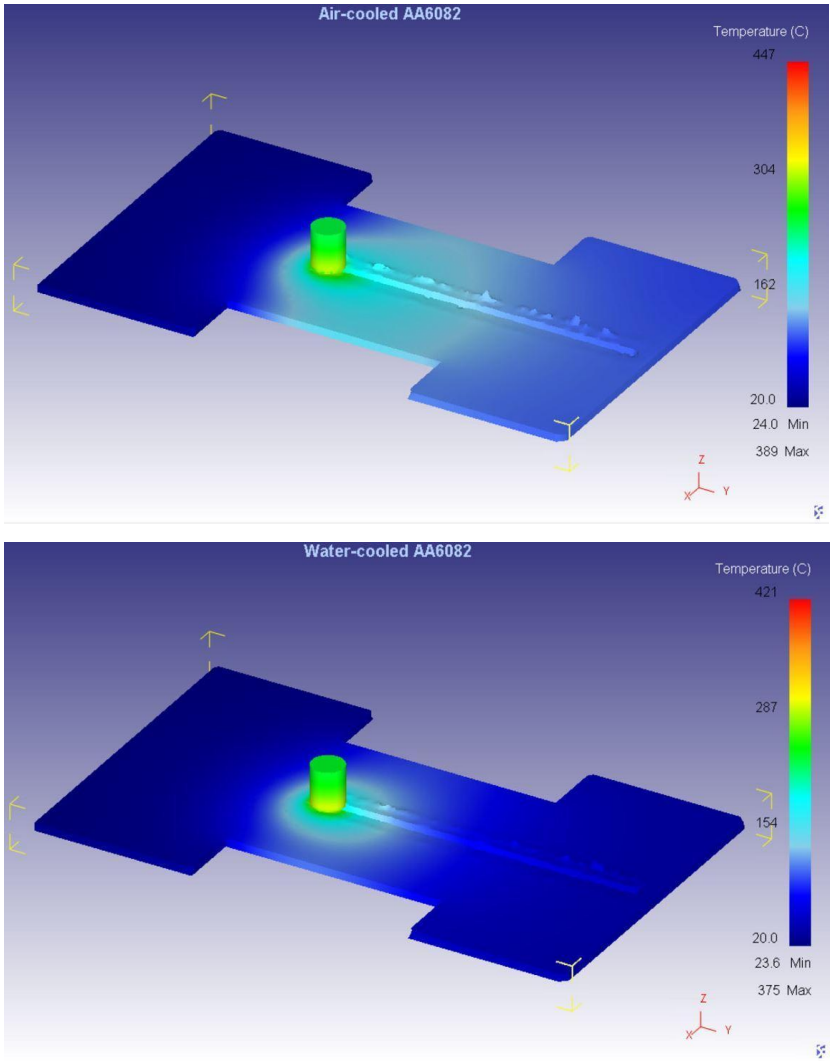

Figure 9.6: FEM model.

The model was successfully validated in different process conditions through the comparison with the corresponding experimental cases. Although the model was built using an AA6061, it is possible to assert that the validity of the thermal model is not linked to the use of a particular aluminum alloy, since there is no significant difference in thermal properties for 6000 and the other aluminum alloy series [104].

9.4. Implementation and validation of ANN

The neural network approach is one of the most powerful computer analysis techniques, based on the statistical regression, currently used in many fields of engineering for modelling complex relationships which are difficult to describe using physical models. The ANN utilized in the present study consists of three layers: input, hidden and output layers. The input layer information is derived from the output and main characteristics of the FE model. Specifically, temperature (T) and its acquisition point, in terms of x and y, derived from the FEM simulation and the type of cooling applied (Cool) were considered. The ANN aims to predict the value of hardness simply by knowing the temperature reached at a certain point during the welding process, since as it is reported by S. Bocchi et al. [187], the temperature reached in the various areas plays a fundamental role, due to the fact that it is strictly connected to the quantity of hardening precipitates present in the matrix.

Since the literature supports the idea of introducing few hidden layers to avoid an unnecessary complexity of the network, a single hidden layer was introduced. The number of hidden nodes (HN) is the most critical aspect for the neural network architecture definition since too few or too many nodes could generate an underfitting or overfitting. In this case, a trial and error approach was applied in a specific interval of nodes. The bounders of the hidden nodes interval hypothesis were defined through the most common heuristic technique developed in [185] for the lower bound and, based on the hypothesis and suggestion of [190], the upper bound was calculated based on the dimension of the training dataset.

$$MTI = \frac{IN + ON}{2} \qquad \text{Eq. 8}$$

$$N = \frac{R}{\alpha(IN + ON)} \qquad \text{Eq. 9}$$

Where:

- MTI is lower bound is heuristically defined by Her Majesty's Department of Trade and Industry
- IN is the number of input nodes.
- ON is the number of output nodes.
- R is the dimension of the training dataset.
- α is an arbitrary scaling factor usually 2-10. In this case, it was assumed $\alpha = 2$.

The trial and error procedure was performed through a Matlab code developed by the authors working as reported in Figure 9.7. Based on this procedure, for each HN hypothesis, a comparison between the provided output and the target values defined in the dataset is made. Since the dataset contains a single output, for evaluating the prevision error between the imposed target and the predicted output, the Mean Square Error (MSE) was considered. Specifically, for each iteration, performed fixing the hypothetical value of HN, the MSE was calculated and the configuration described by the lower value of MSE was selected as the optimal one.

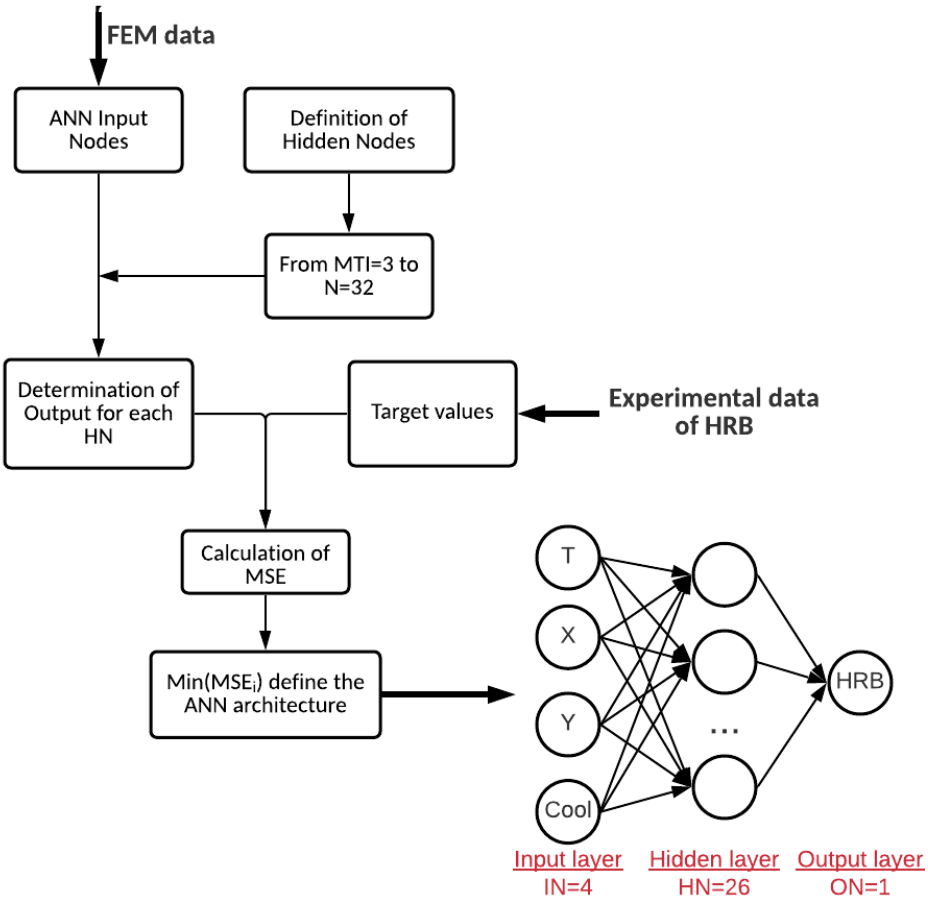

Figure 9.7: ANN structure definition flowchart.

The dataset was built based on the FEM and experimental results. Specifically, the temperature map was extracted from the FE model indicating the temperature reached in several specific positions (x; y shown in Figure 9.8). For each combination, the hardness was experimentally measured as a target of the training dataset.

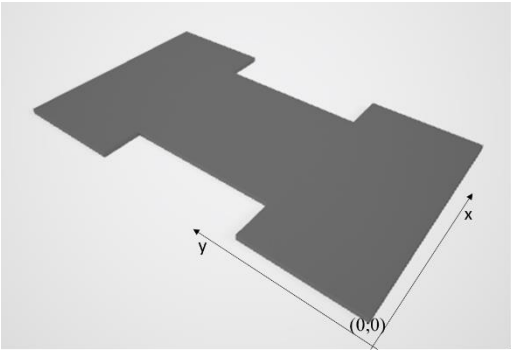

Figure 9.8: Reference system for identifying ordered pairs of points.

70% of the entire dataset (318 cases) was used for the training activity, while the validation and tests stages exploited 15% each of the available data. As it is possible to observe from Figure 9.9, after the ANN training, the difference between the targets and the forecast outputs is very low and it is possible to observe that the defined ANN was properly trained. This means that the network will be able to predict, with an acceptable level of tolerance, the hardness of a specific area of the welded sheets allowing to identify the mechanical characteristic and the main behavior of the surface after the heat transfer due to the welding process.

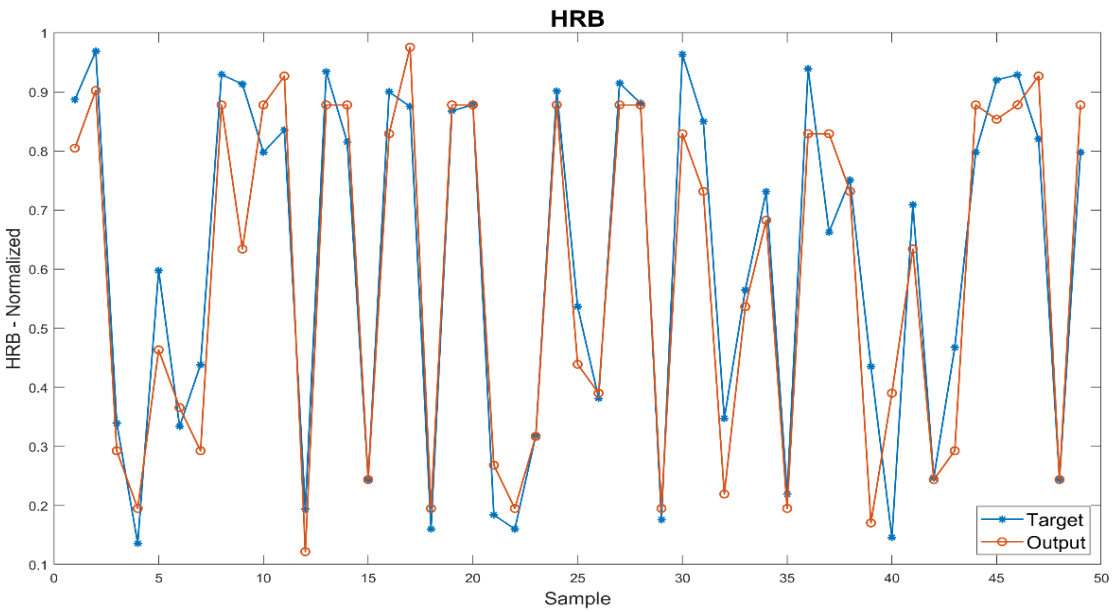

Figure 9.9: ANN validation.

9.5. Results and discussion

The results obtained through the application of the developed FEM-ANN hybrid methodology fit very well the experimental data. As an example, the comparison between the experimental curve and the curve of predicted values obtained at y = 45 mm and y = 135 mm is shown in Figure 9.10 (air-cooled) and Figure 9.11 (water-cooled).

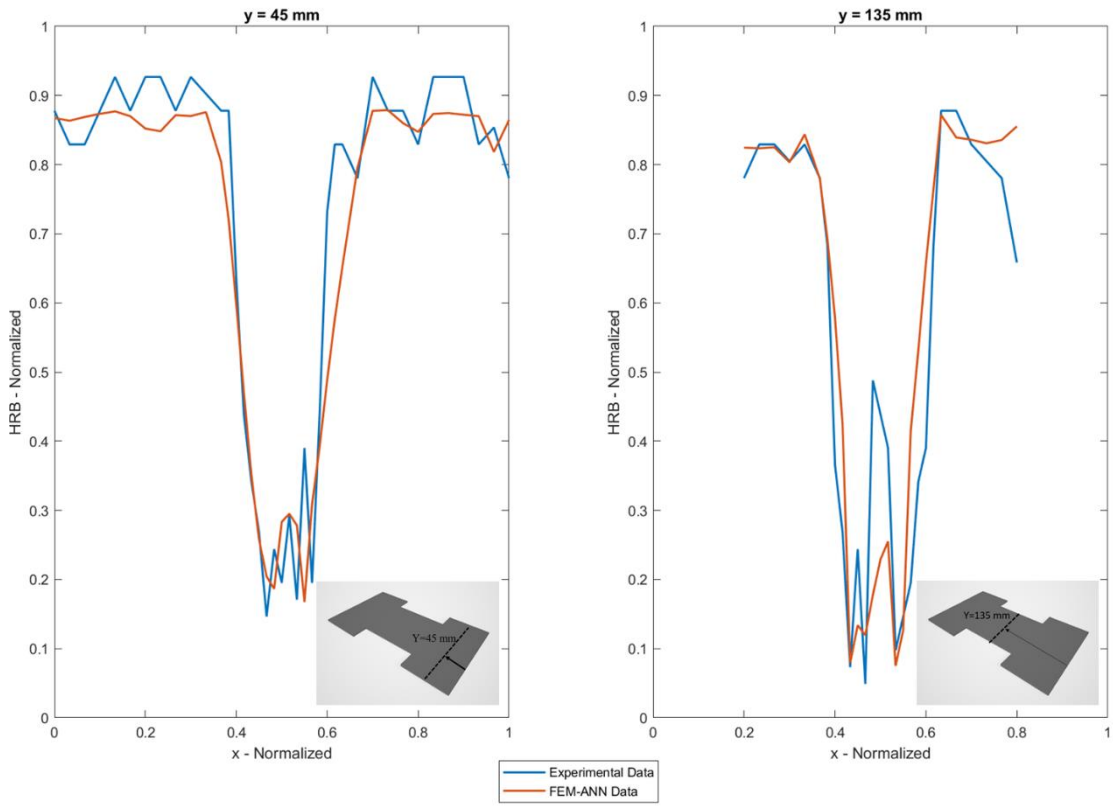

Figure 9.10: Application of hybrid FEM-ANN model to air-cooled FSW.

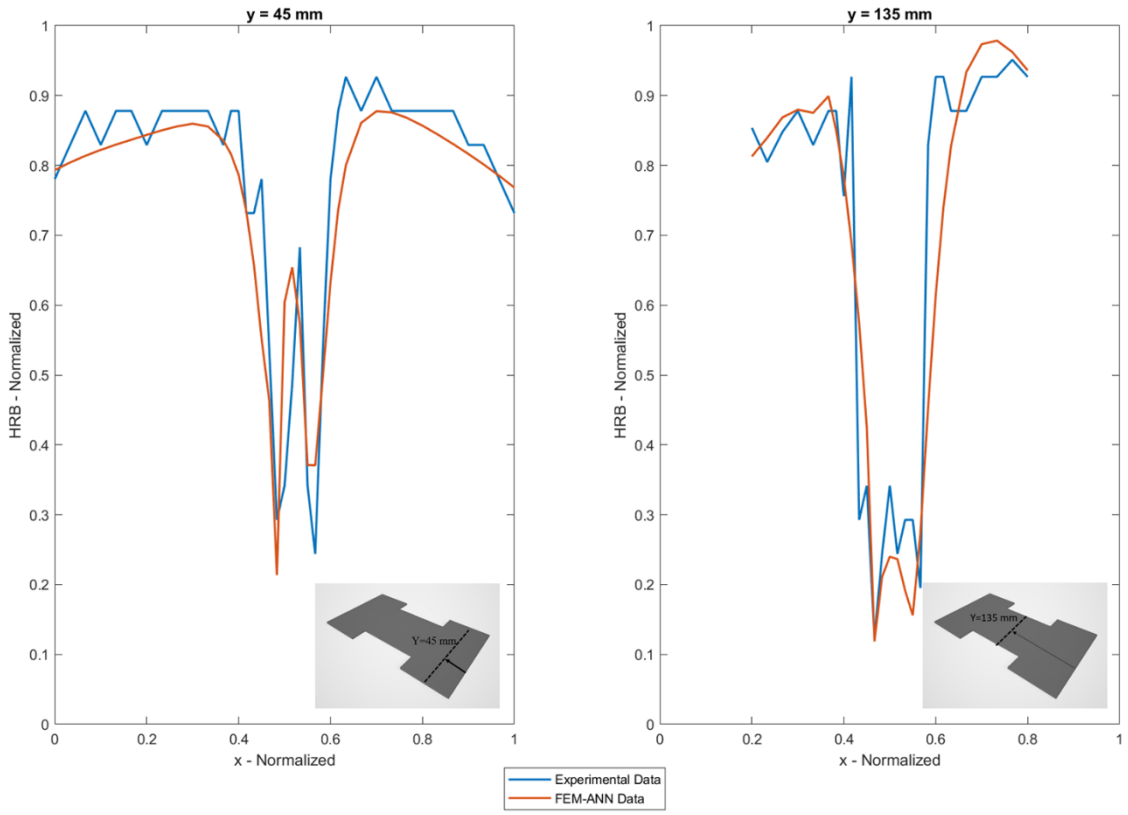

Figure 9.11: Application of hybrid FEM-ANN model to water-cooled FSW.

From the graphs, it is possible to see how the W shape, typical of the junctions obtained with FSW technologies, is maintained in the trend representation of the predicted values. It is important to underline that to apply the proposed model, the developed hybrid approach must be capable of adequately predict the lower peak of hardness since it indicates the point where the break may occur. Such as possible to observe in Figure 9.10 and Figure 9.11, the model is able to very well approximate the minimum peak hardness values, identifying the typical points of failure of the FSW welds, mostly located near the interface between TMAZ and HAZ.

The search for the relationship between the maximum temperature reached during the process and the final hardness corresponding to that exact point arises from the relationship between the metallurgical phenomena occurring in the alloy and the mechanical behavior of the joint. In particular, since AA6xxx is a precipitation hardening aluminum alloy, it is possible to state that the local mechanical characteristics of the piece, including therefore the hardness, are strongly linked to the microscopic state of the alloy

structure, i.e. to the quantity and size of the hardening precipitates dispersed within the aluminum matrix.

These hardening precipitates, present in all precipitation hardening aluminum alloys, albeit formed by different alloying elements, give the alloy the highest level of mechanical behavior only if present under specific conditions. The best hardening conditions occur only within a certain range of temperatures, characteristics for each alloy but well known and defined. These characteristic temperatures are linked to the presence of a transition temperature of the hardening precipitates above which the precipitates begin to coalescence and the matrix strengthening function is lost. Because of the described characteristic behavior of precipitation hardening alloys, a systematic correlation between maximum temperatures and relative reached hardness was developed.

Finally, it is necessary to underline that the minimum hardness is reached at the interface between TMAZ and HAZ and not at the nugget, where the temperatures measured are the highest, because in the nugget the thermal effect of processing and the mechanical action of the pin coexist. The mechanical action of the pin acts on the material by mechanically breaking up the grains and hardening precipitates present in the matrix, thus ensuring a better mechanical response compared to the welding points where only the thermal contribution of the process acts without mixing the material.

9.6. Conclusions

The objective of this study was to develop a robust hybrid FEM-ANN approach that can be used for predicting the surface hardness in FSW for different cooling types starting from the peak of temperature reached during the welding process.

The Finite Element model set-up for the welding process cooled by air or water can supply a good prediction of the peak of temperature reached during the process on the entire surface of the samples. The neural network can exploit this information in order to have a quick prediction of the hardness of the specific point which is useful for identifying the mechanical characteristics of the part as a function of the area of interest. Specifically, it was shown how, once the hybrid approach was set-up and trained, the trends of predicted hardness fit very well with the corresponding experiments. In fact, it was possible to identify the different behavior related to the different areas of the joint.

Finally, even if the developed hybrid FEM-ANN approach has been proposed for AA6082, it can be used for determining the final characteristics for welded joints of also all other precipitation hardening alloys, in order to forecasting the final characteristics and comparing them with the required data.

10. General conclusions

FSW is an attractive solution for the welding of materials difficult to weld by conventional technologies. In order to improve its characteristics and enhance the application of this kind of technology is very important to increase the knowledge not only of the process performance but also of the mechanical aspects and the joint behavior. The complete evaluation of a process is very important for the industries, because it allows to distribute in the best way the resources, but it is equally important to optimize the process parameters to obtain the best performances in terms of process and product characteristics.

In the first part of this work, the microstructure and the corrosion behavior of the precipitation-hardening alloys as a function of the process parameters and loading conditions were studied.

Regarding the AA2024 FSWed joints, the results evidenced a more severe corrosion attack after intergranular tests at the TMAZ/HAZ interface and not in the nugget. On the contrary, long term corrosion tests showed a preferential attack in the zone of the nugget. If the welded were subjected to an applied load, an intergranular corrosion at the nugget, owing to the presence of micrometric copper-rich precipitates at the border of the recrystallized grains, was detected. Despite no stress corrosion cracking was noticed, in the presence of loading, the intergranular corrosion attack became penetrating, giving rise to a stress enhanced intergranular corrosion. Moreover, the AA2024 joints showed the same corrosion behavior regardless of the process parameters involved.

Otherwise, a specific susceptibility to SCC was demonstrated for FSWed AA7075 joints mainly at the TMAZ/HAZ as nucleation of crack embryos occurred during both CL and SSR tests. However, high dissolution rate of the metal inside the localized attack prevents the achievement of critical crack size to promote its propagation up to rupture. Preferential dissolution along the grain boundaries was found in HAZ and the attack follows the elongated grain structure along the rolling direction.

Once studied the corrosion behavior, the analysis was focused on evaluating the effect of the heat input generated by the welding process. As well as the metallurgical and microstructural modification, this factor is strongly dependent on the process parameters, and in particular on the ratio between rotational speed and feed rate.

All the tested air-cooled and water-cooled FSW alloys (both precipitation-hardening and work-hardening alloys) showed different behaviors:

- AA2024 proved to be the least affected by the cooling system.
- AA6082 showed increased hardness values at the nugget in water-cooled welds.
- AA7075 revealed a benefit both in hardness distribution and in UTS in water-cooled welded joints.
- AA5754 reached UTS and percentage elongation values closer to the base alloy both in the air-cooled and water-cooled process; in the water-cooled joints the failure occurred in the base material, away from the welded area.

The quantitative analysis showed that the thermal gradient of air-cooled welds was always lower than the water-cooled joint. Moreover, a clear dependence between the process parameters and the thermal history of the FSWed joints was found. In fact, the cooling rate depends almost exclusively on the parameters used and not on the material considered: the alloys with the highest thermal gradient were those with the lower feed rates.

Once the characterization of the effect of the welding parameters and of the cooling conditions has been completed, the main objective has become the applicability of the technology in the industrial field.

Since the now proven complexity of the process, all the data experimentally collected were used to set-up a combined artificial neural network and particle swarm optimization model. The developed algorithm can satisfy different requirements of industrial scenarios; in fact, it was able to suggest the best process conditions for a defined material or for respecting the mechanical characteristics required by a product design. The validation of the algorithm showed satisfactory results; this allowed to state that the proposed method was effective when constraints were fixed not only for the ANN inputs (material, rotational speed, feed rate and cooling type) but also for the ANN outputs (UTS and hardness values at the different zones of the joint), respecting the multi-objective function imposed.

In the last part of this work, a mathematical model to correlate the temperatures reached during the welding process to the surface hardness in the FSWed joint was improved. This was made developing firstly a robust FEM model and then using both

the experimental reached temperatures presented in Chapter 7 and the simulated values deriving from the FEM model to build an artificial neural network. The purpose of the ANN was to have a quick prediction of the hardness of the specific point which was useful for identifying the mechanical characteristics of the part as a function of the area of interest.

Finally, it was shown that the trends of predicted hardness fit very well with the corresponding experiments and it was also possible to identify the different behavior related to the different areas of the joint.

The developed hybrid FEM-ANN approach can be used for determining the final characteristics for welded aluminum for forecasting the final characteristics and comparing them with the required data, without executing experimental campaign and limiting the use of external resources.

Future steps are going to involve a wide range of materials and parameters to deepen the comprehension of the Friction Stir Welding process.

11. References

1. International Aluminium Institute (2015) World Aluminium: Primary Aluminium Production. In: World Alum. https://www.world-aluminium.org/statistics/primary-aluminium-production/#data. Accessed 2 Aug 2021
2. Baker H, Okamoto H, Henry SD, et al (1992) ASM Handbook Volume 3 Alloy Phase Diagrams Prepared under the direction of the ASM International Alloy Phase Diagram and Handbook Committees
3. Chen R, Xu Q, Guo H, et al (2017) Modeling the precipitation kinetics and tensile properties in Al-7Si-Mg cast aluminum alloys. Mater Sci Eng A 685:403–416. https://doi.org/10.1016/j.msea.2016.12.042
4. Alexopoulos ND, Velonaki Z, Stergiou CI, Kourkoulis SK (2017) Effect of ageing on precipitation kinetics, tensile and work hardening behavior of Al-Cu-Mg (2024) alloy. Mater Sci Eng A 700:457–467. https://doi.org/10.1016/j.msea.2017.05.090
5. ASM International. Handbook Committee (2008) ASM Handbook, Volume 15. ASM International
6. Wang W, Wang G, Hu Y, et al (2016) Temperature-dependent constitutive behavior with consideration of microstructure evolution for as-quenched Al-Cu-Mn alloy. Mater Sci Eng A 678:85–92. https://doi.org/10.1016/j.msea.2016.09.090
7. Feng Z, Yang Y, Huang B, et al (2010) Precipitation process along dislocations in Al-Cu-Mg alloy during artificial aging. Mater Sci Eng A 528:706–714. https://doi.org/10.1016/j.msea.2010.09.069
8. Shercliff HR, Ashby MF (1990) A process model for age hardening of aluminium alloys-I. The model. Acta Metall Mater 38:1789–1802. https://doi.org/10.1016/0956-7151(90)90291-N
9. Armstrong RW (1970) The influence of polycrystal grain size on several mechanical properties of materials. Metall Mater Trans 1:1169–1176. https://doi.org/10.1007/BF02900227
10. Thomas WM, Nicholas ED, Needham JC, et al (1991) GB Patent application no. 9125978.8. Int. Pat. Appl. No. PCT/GB92/02203
11. Thomas WM, Murch MG, Nicholas ED, et al (1992) Improvements relating to friction welding. 11

12. Cao X, Jahazi M (2011) Effect of tool rotational speed and probe length on lap joint quality of a friction stir welded magnesium alloy. Mater Des 32:1–11. https://doi.org/10.1016/j.matdes.2010.06.048
13. Kitamura K, Fujii H, Iwata Y, et al (2013) Flexible control of the microstructure and mechanical properties of friction stir welded Ti-6Al-4V joints. Mater Des 46:348–354. https://doi.org/10.1016/j.matdes.2012.10.051
14. Lee SJ, Shin SE, Sun Y, et al (2018) Friction stir welding of multi-walled carbon nanotubes reinforced Al matrix composites. Mater Charact 145:653–663. https://doi.org/10.1016/j.matchar.2018.09.033
15. Adibeig MR, Hassanifard S, Vakili-Tahami F, Hattel JH (2018) Experimental investigation of tensile strength of friction stir welded butt joints on PMMA. Mater Today Commun 17:238–245. https://doi.org/10.1016/j.mtcomm.2018.09.009
16. Martinsen K, Hu SJ, Carlson BE (2015) Joining of dissimilar materials. CIRP Ann - Manuf Technol 64:679–699. https://doi.org/10.1016/j.cirp.2015.05.006
17. Tabasi M, Farahani M, Givi MKB, et al (2016) Dissimilar friction stir welding of 7075 aluminum alloy to AZ31 magnesium alloy using SiC nanoparticles. Int J Adv Manuf Technol 86:705–715. https://doi.org/10.1007/s00170-015-8211-y
18. Mishra RS, Ma ZY (2005) Friction stir welding and processing. Mater Sci Eng R Reports 50:1–78. https://doi.org/10.1016/j.mser.2005.07.001
19. Frigaard, Grong, Midling OT (2001) A process model for friction stir welding of age hardening aluminum alloys. Metall Mater Trans A Phys Metall Mater Sci 32:1189–1200. https://doi.org/10.1007/s11661-001-0128-4
20. Sivakumar, Bose V, Raguraman D, Muruganandam D (2014) Review Paper on Friction Stir Welding of various Aluminium Alloys. J Mech Civ Eng 46–52. https://doi.org/10.17485/ijst/2015/v8i35/86774
21. Mishra RS, De PS, Kumar N, et al (2014) Fundamentals of the Friction Stir Process. In: Friction Stir Welding and Processing. Springer International Publishing, Cham, pp 13–58
22. El-Danaf EA, El-Rayes MM (2013) Microstructure and mechanical properties of friction stir welded 6082 AA in as welded and post weld heat treated conditions. Mater Des 46:561–572. https://doi.org/10.1016/j.matdes.2012.10.047
23. Sonne MRR, Tutum CCC, Hattel JHH, et al (2012) The effect of hardening laws

and thermal softening on modeling residual stresses in FSW of aluminum alloy 2024-T3. J Mater Process Technol 213:477–486. https://doi.org/10.1016/j.jmatprotec.2012.11.001

24. Rhodes CG, Mahoney MW, Bingel WH, et al (1997) Effects of friction stir welding on microstructure of 7075 aluminum. Scr Mater 36:69–75. https://doi.org/10.1016/S1359-6462(96)00344-2
25. Johnson R, Threadgill PL (2003) Progress in Friction Stir Welding of Aluminium and Steel for Marine Applications. In: RINA Conference: Advanced Marine Materials: Technology and Applications
26. Heinz A, Haszler A, Keidel C, et al (2000) Recent development in aluminium alloys for aerospace applications. Mater Sci Eng A 280:102–107. https://doi.org/10.1016/S0921-5093(99)00674-7
27. Thomas WM, Nicholas ED (1997) Friction stir welding for the transportation industries. Mater Des 18:269–273. https://doi.org/10.1016/s0261-3069(97)00062-9
28. Threadgill PL, Leonard AJ, Shercliff HR, Withers PJ (2009) Friction stir welding of aluminium alloys. Int Mater Rev 54:49–93. https://doi.org/10.1179/174328009X411136
29. Istituto Italiano della Saldatura Processi di saldatura ad energia concentrata. In: Dispense per la qualifica di International Welding Engineer
30. Mishra RS, Ma ZY, Mahoney MW, et al (2005) Friction stir welding and processing. Mater Sci Eng R Reports 50:1–78. https://doi.org/10.1016/j.mser.2005.07.001
31. Nandan R, DebRoy T, Bhadeshia HKDH (2008) Recent advances in friction-stir welding - Process, weldment structure and properties. Prog. Mater. Sci. 53:980–1023
32. Garg A, Raturi M, Bhattacharya A (2019) Influence of additional heating in friction stir welding of dissimilar aluminum alloys with different tool pin profiles. Int J Adv Manuf Technol 105:155–175. https://doi.org/10.1007/s00170-019-04186-z
33. Biswas P, Kumar DA, Mandal NR (2012) Friction stir welding of aluminum alloy with varying tool geometry and process parameters. Proc Inst Mech Eng Part B J

Eng Manuf 226:641–648. https://doi.org/10.1177/0954405411424111

34. Kumar K, Kailas S V., Srivatsan TS (2008) Influence of tool geometry in friction stir welding. Mater Manuf Process 23:189–195. https://doi.org/10.1080/10426910701774734
35. Rai R, De A, Bhadeshia HKDH, DebRoy T (2011) Review: Friction stir welding tools. Sci Technol Weld Join 16:325–342. https://doi.org/10.1179/1362171811Y.0000000023
36. Ren SR, Ma ZY, Chen LQ (2007) Effect of welding parameters on tensile properties and fracture behavior of friction stir welded Al-Mg-Si alloy. Scr Mater 56:69–72. https://doi.org/10.1016/j.scriptamat.2006.08.054
37. Lee WB, Yeon YM, Jung SB (2004) Mechanical properties related to microstructural variation of 6061 Al alloy joints by friction stir welding. Mater Trans 45:1700–1705. https://doi.org/10.2320/matertrans.45.1700
38. Lorenzi S, Cabrini M, D'Urso G, et al (2017) The Effects of Process Parameters on Mechanical Properties and Corrosion Behavior in Friction Stir Welding of Aluminum Alloys. Procedia Eng 183:270–276. https://doi.org/10.1016/j.proeng.2017.04.038
39. Kumar SS, Murugan N, Ramachandran KK (2020) Effect of tool tilt angle on weld joint properties of friction stir welded AISI 316L stainless steel sheets. Meas J Int Meas Confed 150:107083. https://doi.org/10.1016/j.measurement.2019.107083
40. Zhai M, Wu CS, Su H (2020) Influence of tool tilt angle on heat transfer and material flow in friction stir welding. J Manuf Process 59:98–112. https://doi.org/10.1016/j.jmapro.2020.09.038
41. Rajendran C, Srinivasan K, Balasubramanian V, et al (2019) Effect of tool tilt angle on strength and microstructural characteristics of friction stir welded lap joints of AA2014-T6 aluminum alloy. Trans Nonferrous Met Soc China (English Ed 29:1824–1835. https://doi.org/10.1016/S1003-6326(19)65090-9
42. Vimalraj C, Kah P (2021) Experimental review on friction stir welding of aluminium alloys with nanoparticles. Metals (Basel) 11:1–28. https://doi.org/10.3390/MET11030390
43. Sorger G, Wang H, Vilaça P, Santos TG (2017) FSW of aluminum AA5754 to steel DX54 with innovative overlap joint. Weld World 61:257–268.

https://doi.org/10.1007/s40194-016-0412-y

44. Lin H, Wu Y, Liu S, Zhou X (2018) Effect of cooling conditions on microstructure and mechanical properties of friction stir welded 7055 aluminium alloy joints. Mater Charact 141:74–85. https://doi.org/10.1016/j.matchar.2018.04.029
45. Benavides S, Li Y, Murr LE, et al (1999) Low-temperature friction-stir welding of 2024 aluminum. Scr Mater 41:809–815. https://doi.org/10.1016/S1359-6462(99)00226-2
46. Mahmoud TS, Khalifa TA (2014) Microstructural and mechanical characteristics of aluminum alloy AA5754 friction stir spot welds. J Mater Eng Perform 23:898–905. https://doi.org/10.1007/s11665-013-0828-0
47. Conserva M, Bonollo F, Donzelli G (2005) Alluminio : manuale degli impieghi. Edimet
48. Radisavljevic I, Zivkovic A, Radovic N, Grabulov V (2013) Influence of FSW parameters on formation quality and mechanical properties of Al 2024-T351 butt welded joints. Trans Nonferrous Met Soc China (English Ed 23:3525–3539. https://doi.org/10.1016/S1003-6326(13)62897-6
49. Su JQ, Nelson TW, Mishra R, Mahoney M (2003) Microstructural investigation of friction stir welded 7050-T651 aluminium. Acta Mater 51:713–729. https://doi.org/10.1016/S1359-6454(02)00449-4
50. Jata K V., Sankaran KK, Ruschau JJ (2000) Friction-stir welding effects on microstructure and fatigue of aluminum alloy 7050-T7451. Metall Mater Trans A Phys Metall Mater Sci 31:2181–2192. https://doi.org/10.1007/s11661-000-0136-9
51. Sato YS, Kokawa H, Enomoto M, Jogan S (1999) Microstructural evolution of 6063 aluminum during friction-stir welding. Metall Mater Trans A Phys Metall Mater Sci 30:2429–2437. https://doi.org/10.1007/s11661-999-0251-1
52. Aissani M, Gachi S, Boubenider F, Benkedda Y (2010) Design and optimization of friction stir welding tool. Mater Manuf Process 25:1199–1205. https://doi.org/10.1080/10426910903536733
53. D'Urso G, Giardini C, Lorenzi S, Pastore T (2014) Fatigue crack growth in the welding nugget of FSW joints of a 6060 aluminum alloy. J Mater Process Technol 214:2075–2084. https://doi.org/10.1016/j.jmatprotec.2014.01.013
54. Ghosh M, Kumar K, Kailas S V., Ray AK (2010) Optimization of friction stir

welding parameters for dissimilar aluminum alloys. Mater Des 31:3033–3037. https://doi.org/10.1016/j.matdes.2010.01.028

55. Heurtier P Characterising Texture Variations in A Friction Stir Welded Aluminium Alloy | Welding | Construction

56. Jariyaboon M, Davenport AJJ, Ambat R, et al (2007) The effect of welding parameters on the corrosion behaviour of friction stir welded AA2024–T351. Corros Sci 49:877–909. https://doi.org/10.1016/j.corsci.2006.05.038

57. Bocchi S, Cabrini M, D'Urso G, et al (2018) The influence of process parameters on mechanical properties and corrosion behavior of friction stir welded aluminum joints. J Manuf Process 35:1–15. https://doi.org/10.1016/j.jmapro.2018.07.012

58. Di S, Yang X, Luan G, Jian B (2006) Comparative study on fatigue properties between AA2024-T4 friction stir welds and base materials. Mater Sci Eng A 435–436:389–395. https://doi.org/10.1016/j.msea.2006.07.009

59. El Rayes MM, Soliman MS, Abbas AT, et al (2019) Effect of Feed Rate in FSW on the Mechanical and Microstructural Properties of AA5754 Joints. Adv Mater Sci Eng 2019:. https://doi.org/10.1155/2019/4156176

60. Taavitsainen T, Vilaça P, Mutanen T (2016) Production by FSW of free-shape hollow box profile in AA5754 for automotive application. Weld World 60:1121–1131. https://doi.org/10.1007/s40194-016-0382-0

61. Serio LM, Palumbo D, De Filippis LAC, et al (2016) Effect of friction stir process parameters on the mechanical and thermal behavior of 5754-H111 aluminum plates. Materials (Basel) 9:. https://doi.org/10.3390/ma9030122

62. Sato YS, Kokawa H (2001) Distribution of tensile property and microstructure in friction stir weld of 6063 aluminum. Metall Mater Trans A Phys Metall Mater Sci 32:3023–3031. https://doi.org/10.1007/s11661-001-0177-8

63. Sato YS, Kokawa H, Enomoto M, Jogan S (1999) Microstructural evolution of 6063 aluminum during friction-stir welding. Metall Mater Trans A Phys Metall Mater Sci 30:2429–2437. https://doi.org/10.1007/s11661-999-0251-1

64. Pang JJ, Liu FC, Liu J, et al (2015) Friction stir processing of aluminium alloy AA7075: Microstructure, surface chemistry and corrosion resistance. Corros Sci 106:217–228. https://doi.org/10.1016/j.corsci.2016.02.006

65. Gholami S, Emadoddin E, Tajally M, Borhani E (2015) Friction stir processing of

7075 Al alloy and subsequent aging treatment. Trans Nonferrous Met Soc China (English Ed 25:2847–2855. https://doi.org/10.1016/S1003-6326(15)63910-3

66. Navaser M, Atapour M (2017) Effect of Friction Stir Processing on Pitting Corrosion and Intergranular Attack of 7075 Aluminum Alloy. J Mater Sci Technol 33:155–165. https://doi.org/10.1016/j.jmst.2016.07.008
67. Ralston KD, Brunner JG, Virtanen S, Birbilis N (2011) Effect of processing on grain size and corrosion of AA2024-T3. Corrosion 67:1–10. https://doi.org/10.5006/1.3647762
68. Zhang W, Frankel GS (2003) Transitions between pitting and intergranular corrosion in AA2024. Electrochim Acta 48:1193–1210. https://doi.org/10.1016/S0013-4686(02)00828-9
69. Yasakau KA, Tedim J, Montemor MF, et al (2013) Mechanisms of localized corrosion inhibition of AA2024 by cerium molybdate nanowires. J Phys Chem C 117:5811–5823. https://doi.org/10.1021/jp3124633
70. Bousquet E, Poulon-Quintin A, Puiggali M, et al (2011) Relationship between microstructure, microhardness and corrosion sensitivity of an AA 2024-T3 friction stir welded joint. Corros Sci 53:3026–3034. https://doi.org/10.1016/j.corsci.2011.05.049
71. Paglia CS, Buchheit RG (2006) Microstructure, microchemistry and environmental cracking susceptibility of friction stir welded 2219-T87. Mater Sci Eng A 429:107–114. https://doi.org/10.1016/j.msea.2006.05.036
72. Wang W, Li T, Wang K, et al (2016) Effect of Travel Speed on the Stress Corrosion Behavior of Friction Stir Welded 2024-T4 Aluminum Alloy. J Mater Eng Perform 25:1820–1828. https://doi.org/10.1007/s11665-016-1979-6
73. Lumsden JB, Mahoney MW, Pollock G, Rhodes CG (1999) Intergranular Corrosion Following Friction Stir Welding of Aluminum Alloy 7075-T651. Corrosion 55:1127–1135. https://doi.org/10.5006/1.3283950
74. Holroyd NJH, Scamans GM (2013) Stress corrosion cracking in Al-Zn-Mg-Cu aluminum alloys in saline environments. In: Metallurgical and Materials Transactions A: Physical Metallurgy and Materials Science. Springer, pp 1230–1253
75. Loto CA, Cottis RA (1989) Electrochemical noise generation during stress

corrosion cracking of the high-strength aluminum AA 7075-T6 alloy. Corrosion 45:136–141. https://doi.org/10.5006/1.3577831

76. Knight SP, Birbilis N, Muddle BC, et al (2010) Correlations between intergranular stress corrosion cracking, grain-boundary microchemistry, and grain-boundary electrochemistry for Al-Zn-Mg-Cu alloys. Corros Sci 52:4073–4080. https://doi.org/10.1016/j.corsci.2010.08.024

77. Park JK, Ardell AJ (1984) Effect of retrogression and reaging treatments on the microstructure of Ai-7075-T651. Metall Trans A 15:1531–1543. https://doi.org/10.1007/BF02657792

78. Andreatta F, Terryn H, De Wit JHW (2004) Corrosion behaviour of different tempers of AA7075 aluminium alloy. In: Electrochimica Acta. Pergamon, pp 2851–2862

79. Fonda RW, Bingert JF (2004) Microstructural evolution in the heat-affected zone of a friction stir weld. Metall Mater Trans A Phys Metall Mater Sci 35 A:1487–1499. https://doi.org/10.1007/s11661-004-0257-7

80. Priya R, Subramanya Sarma V, Prasad Rao K (2009) Effect of post weld heat treatment on the microstructure and tensile properties of dissimilar friction stir welded AA 2219 and AA 6061 alloys. Trans Indian Inst Met 62:11–19. https://doi.org/10.1007/s12666-009-0002-4

81. Safarbali B, Shamanian M, Eslami A (2018) Effect of post-weld heat treatment on joint properties of dissimilar friction stir welded 2024-T4 and 7075-T6 aluminum alloys. Trans Nonferrous Met Soc China (English Ed 28:1287–1297. https://doi.org/10.1016/S1003-6326(18)64766-1

82. Baghdadi AH, Rajabi A, Selamat NFM, et al (2019) Effect of post-weld heat treatment on the mechanical behavior and dislocation density of friction stir welded Al6061. Mater Sci Eng A 754:728–734. https://doi.org/10.1016/j.msea.2019.03.017

83. Sakurada D, Katoh K, Tokisue H (2002) Underwater friction welding of 6061 aluminum alloy. Keikinzoku/Journal Japan Inst Light Met 52:2–6. https://doi.org/10.2464/jilm.52.2

84. Peng G, Yan Q, Hu J, et al (2019) Effect of forced air cooling on the microstructures, Tensile strength, and Hardness distribution of dissimilar friction

stir welded AA5A06-AA6061 Joints. Metals (Basel) 9:304. https://doi.org/10.3390/met9030304

85. Upadhyay P, Reynolds AP (2010) Effects of thermal boundary conditions in friction stir welded AA7050-T7 sheets. Mater Sci Eng A 527:1537–1543. https://doi.org/10.1016/j.msea.2009.10.039

86. Sharma C, Dwivedi DK, Kumar P (2012) Influence of in-process cooling on tensile behaviour of friction stir welded joints of AA7039. Mater Sci Eng A 556:479–487. https://doi.org/10.1016/j.msea.2012.07.016

87. Rui-dong F, Zeng-qiang S, Rui-cheng S, et al (2011) Improvement of weld temperature distribution and mechanical properties of 7050 aluminum alloy butt joints by submerged friction stir welding. Mater Des 32:4825–4831. https://doi.org/10.1016/j.matdes.2011.06.021

88. Heirani F, Abbasi A, Ardestani M (2017) Effects of processing parameters on microstructure and mechanical behaviors of underwater friction stir welding of Al5083 alloy. J Manuf Process 25:77–84. https://doi.org/10.1016/j.jmapro.2016.11.002

89. Wahid MA, Khan ZA, Siddiquee AN (2018) Review on underwater friction stir welding: A variant of friction stir welding with great potential of improving joint properties. Trans Nonferrous Met Soc China (English Ed 28:193–219. https://doi.org/10.1016/S1003-6326(18)64653-9

90. Fratini L, Buffa G, Shivpuri R (2010) Mechanical and metallurgical effects of in process cooling during friction stir welding of AA7075-T6 butt joints. Acta Mater 58:2056–2067. https://doi.org/10.1016/j.actamat.2009.11.048

91. Zhao Y, Wang Q, Chen H, Yan K (2014) Microstructure and mechanical properties of spray formed 7055 aluminum alloy by underwater friction stir welding. Mater Des 56:725–730. https://doi.org/10.1016/j.matdes.2013.11.071

92. Hosseini M, Danesh Manesh H (2010) Immersed friction stir welding of ultrafine grained accumulative roll-bonded Al alloy. Mater Des 31:4786–4791. https://doi.org/10.1016/j.matdes.2010.05.007

93. Xu WF, Liu JH, Chen DL, et al (2012) Improvements of strength and ductility in aluminum alloy joints via rapid cooling during friction stir welding. Mater Sci Eng A 548:89–98. https://doi.org/10.1016/j.msea.2012.03.094

94. Wang Q, Zhao Z, Zhao Y, et al (2015) The adjustment strategy of welding parameters for spray formed 7055 aluminum alloy underwater friction stir welding joint. Mater Des 88:1366–1376. https://doi.org/10.1016/j.matdes.2015.09.038
95. Zhang Z, Xiao BL, Ma ZY (2014) Influence of water cooling on microstructure and mechanical properties of friction stir welded 2014Al-T6 joints. Mater Sci Eng A 614:6–15. https://doi.org/10.1016/j.msea.2014.06.093
96. Nelson TW, Steel RJ, Arbegast WJ (2003) In situ thermal studies and post-weld mechanical properties of friction stir welds in age hardenable aluminium alloys. Sci Technol Weld Join 8:283–288. https://doi.org/10.1179/136217103225011005
97. Papahn H, Bahemmat P, Haghpanahi M (2016) Effect of cooling media on residual stresses induced by a solid-state welding: underwater FSW. Int J Adv Manuf Technol 83:1003–1012. https://doi.org/10.1007/s00170-015-7653-6
98. Assidi M, Fourment L, Guerdoux S, Nelson T (2010) Friction model for friction stir welding process simulation: Calibrations from welding experiments. Int J Mach Tools Manuf 50:143–155. https://doi.org/10.1016/j.ijmachtools.2009.11.008
99. He X, Gu F, Ball A (2014) A review of numerical analysis of friction stir welding. Prog. Mater. Sci. 65:1–66
100. Chen CM, Kovacevic R (2003) Finite element modeling of friction stir welding - Thermal and thermomechanical analysis. Int J Mach Tools Manuf 43:1319–1326. https://doi.org/10.1016/S0890-6955(03)00158-5
101. Zhang Z, Zhang HW (2008) A fully coupled thermo-mechanical model of friction stir welding. Int J Adv Manuf Technol 37:279–293. https://doi.org/10.1007/s00170-007-0971-6
102. Contuzzi N, Campanelli SL, Casalino G, Ludovico AD (2016) On the role of the Thermal Contact Conductance during the Friction Stir Welding of an AA5754-H111 butt joint. Appl Therm Eng 104:263–273. https://doi.org/10.1016/j.applthermaleng.2016.05.071
103. Chao YJ, Qi X, Tang W (2003) Heat Transfer in Friction Stir Welding—Experimental and Numerical Studies. J Manuf Sci Eng 125:138. https://doi.org/10.1115/1.1537741
104. Buffa G, Hua J, Shivpuri R, Fratini L (2006) A continuum based fem model for

friction stir welding - Model development. Mater Sci Eng A 419:389–396. https://doi.org/10.1016/j.msea.2005.09.040

105. D'Urso G, Longo M, Giardini C, Ceretti E (2012) Quality analysis of friction stir welded butt joints by means of experiments and simulations. In: Key Engineering Materials. Trans Tech Publications Ltd, pp 759–764

106. Colegrove PA, Shercliff HR, Zettler R (2007) Model for predicting heat generation and temperature in friction stir welding from the material properties. Sci Technol Weld Join 12:284–297. https://doi.org/10.1179/174329307x197539

107. Katherasan D, Elias J V., Sathiya P, Haq AN (2014) Simulation and parameter optimization of flux cored arc welding using artificial neural network and particle swarm optimization algorithm. J Intell Manuf 25:67–76. https://doi.org/10.1007/s10845-012-0675-0

108. Xu L, Huang C, Li C, et al (2021) Estimation of tool wear and optimization of cutting parameters based on novel ANFIS-PSO method toward intelligent machining. J Intell Manuf 32:77–90. https://doi.org/10.1007/s10845-020-01559-0

109. Gaitonde VN, Karnik SR (2012) Minimizing burr size in drilling using artificial neural network (ANN)-particle swarm optimization (PSO) approach. J Intell Manuf 23:1783–1793. https://doi.org/10.1007/s10845-010-0481-5

110. Shokry A, Espuña A (2018) The Ordinary Kriging in Multivariate Dynamic Modelling and Multistep-Ahead Prediction. In: Computer Aided Chemical Engineering. Elsevier, pp 265–270

111. Deepandurai K, Parameshwaran R (2016) Multiresponse Optimization of FSW Parameters for Cast AA7075/SiCp Composite. Mater Manuf Process 31:1333–1341. https://doi.org/10.1080/10426914.2015.1117628

112. Mallieswaran K, Padmanabhan R, Balasubramanian V (2018) Friction stir welding parameters optimization for tailored welded blank sheets of AA1100 with AA6061 dissimilar alloy using response surface methodology. Adv Mater Process Technol 4:142–157. https://doi.org/10.1080/2374068X.2017.1410690

113. Shojaeefard MH, Behnagh RA, Akbari M, et al (2013) Modelling and pareto optimization of mechanical properties of friction stir welded AA7075/AA5083 butt joints using neural network and particle swarm algorithm. Mater Des 44:190–198. https://doi.org/10.1016/j.matdes.2012.07.025

114. Sönmez F, Başak H, Baday Ş (2017) Sürtünme kariştirma kaynaği ile birleştirilen alüminyum alaşimlarinin mekanik dayaniminin yapay sinir ağlari ile modellenmesi. In: IDAP 2017 - International Artificial Intelligence and Data Processing Symposium. Institute of Electrical and Electronics Engineers Inc., pp 1–4
115. Dehabadi VM, Ghorbanpour S, Azimi G (2016) Application of artificial neural network to predict Vickers microhardness of AA6061 friction stir welded sheets. J Cent South Univ 23:2146–2155. https://doi.org/10.1007/s11771-016-3271-1
116. Vangalapati M, Balaji K, Gopichand A (2019) ANN modeling and analysis of friction welded AA6061 aluminum alloy. Mater Today Proc 18:3357–3364. https://doi.org/10.1016/j.matpr.2019.07.258
117. Farghaly AA, El-Nikhaily AE, Essa ARS (2019) Prediction of tensile strength of friction stir welded 6061 Al plates. China Weld (English Ed 28:1–6. https://doi.org/10.12073/j.cw.20190617001
118. Lakshminarayanan AK, Balasubramanian V (2009) Comparison of RSM with ANN in predicting tensile strength of friction stir welded AA7039 aluminium alloy joints. Trans Nonferrous Met Soc China (English Ed 19:9–18. https://doi.org/10.1016/S1003-6326(08)60221-6
119. Okuyucu H, Kurt A, Arcaklioglu E (2007) Artificial neural network application to the friction stir welding of aluminum plates. Mater Des 28:78–84. https://doi.org/10.1016/j.matdes.2005.06.003
120. Tansel IN, Demetgul M, Okuyucu H, Yapici A (2010) Optimizations of friction stir welding of aluminum alloy by using genetically optimized neural network. Int J Adv Manuf Technol 48:95–101. https://doi.org/10.1007/s00170-009-2266-6
121. De Filippis LAC, Serio LM, Facchini F, et al (2016) Prediction of the vickers microhardness and ultimate tensile strength of aa5754 h111 friction stir welding butt joints using artificial neural network. Materials (Basel) 9:. https://doi.org/10.3390/ma9110915
122. Muthu Krishnan M, Maniraj J, Deepak R, Anganan K (2018) Prediction of optimum welding parameters for FSW of aluminium alloys AA6063 and A319 using RSM and ANN. Mater Today Proc 5:716–723. https://doi.org/10.1016/j.matpr.2017.11.138

123. Ranjith R, Giridharan PK, Senthil KB (2017) Predicting the tensile strength of friction stir welded dissimilar aluminum alloy using ann. Int J Civ Eng Technol 8:345–353
124. Dewan MW, Huggett DJ, Warren Liao T, et al (2016) Prediction of tensile strength of friction stir weld joints with adaptive neuro-fuzzy inference system (ANFIS) and neural network. Mater Des 92:288–299. https://doi.org/10.1016/j.matdes.2015.12.005
125. Maleki E (2015) Artificial neural networks application for modeling of friction stir welding effects on mechanical properties of 7075-T6 aluminum alloy. IOP Conf Ser Mater Sci Eng 103:. https://doi.org/10.1088/1757-899X/103/1/012034
126. Lumsden JB, Mahoney MW, Rhodes CG, Pollock GA (2003) Corrosion behavior of friction-stir-welded AA7050-T7651. Corrosion 59:212–219. https://doi.org/10.5006/1.3277553
127. Büchler M, Watari T, Smyrl WH (2000) Investigation of the initiation of localized corrosion on aluminum alloys by using fluorescence microscopy. Corros. Sci. 42:1661–1668
128. Peng GS, Chen KH, Fang HC, et al (2010) EIS study on pitting corrosion of 7150 aluminum alloy in sodium chloride and hydrochloric acid solution. Mater Corros 61:783–789. https://doi.org/10.1002/maco.200905413
129. Keddam M, Kuntz C, Takenouti H, et al (1997) Exfoliation corrosion of aluminium alloys examined by electrode impedance. Electrochim Acta 42:87–97. https://doi.org/10.1016/0013-4686(96)00170-3
130. He M, Kang J, Fu R, et al (2009) In-situ investigation on the pitting corrosion behavior of friction stir welded joint of AA2024-T3 aluminium alloy. Corros Sci 52:620–626. https://doi.org/10.1016/j.corsci.2009.10.027
131. Petroyiannis P V., Kamoutsi E, Kermanidis AT, et al (2005) Evidence on the corrosion-induced hydrogen embrittlement of the 2024 aluminium alloy. Fatigue Fract Eng Mater Struct 28:565–574. https://doi.org/10.1111/j.1460-2695.2005.00900.x
132. Buchheit, R. G. Grant, R. P. Hlava, P. F. Zender L (1997) Local Dissolution Phenomena Associated with S Phase (Al2CuMg) Particles in Aluminum Alloy 2024-T3. J Electrochem Soc 144:2621. https://doi.org/10.1149/1.1837874

133. Paidar M, Khodabandeh A, Sarab ML, Taheri M (2015) Effect of welding parameters (plunge depths of shoulder, pin geometry, and tool rotational speed) on the failure mode and stir zone characteristics of friction stir spot welded aluminum 2024-T3 sheets. J Mech Sci Technol 29:4639–4644. https://doi.org/10.1007/s12206-015-1009-x
134. Burleigh TD (1991) Postulated mechanisms for stress corrosion cracking of aluminum alloys. A review of the literature 1980-1989. Corrosion 47:89–98. https://doi.org/10.5006/1.3585235
135. Bocchi S, Cabrini M, D'Urso G, et al (2020) Stress enhanced intergranular corrosion of friction stir welded AA2024-T3. Eng Fail Anal 111:. https://doi.org/10.1016/j.engfailanal.2020.104483
136. Holroyd NJJH, Evans JT, Scamans GM (2015) Pre-exposure embrittlement of an Al-Cu-Mg alloy, AA2024-T351. Corros Rev 33:361–372. https://doi.org/10.1515/corrrev-2015-0037
137. Cabrini M, Lorenzi S, Bocchi S, et al (2017) Evaluation of corrosion behavior of AA2024 T3 welded by means of FSW. In: EUROCORR 2017 - The Annual Congress of the European Federation of Corrosion, 20th International Corrosion Congress and Process Safety Congress 2017. Asociace koroznich inzenyru z.s.-AKI - Czech Association of Corrosion Engineers
138. Bocchi S, D'Urso G, Giardini C, Maccarini G (2019) Effects of cooling conditions on microstructure and mechanical properties of friction stir welded butt joints of different aluminum alloys. Appl Sci 9:. https://doi.org/10.3390/app9235069
139. Zhang W, Frankel GS (2002) Localized Corrosion Growth Kinetics in AA2024 Alloys. J Electrochem Soc 149:B510. https://doi.org/10.1149/1.1513984
140. Jones DA (1996) Localized Surface Plasticity during Stress Corrosion Cracking. Corros 52:356–362. https://doi.org/10.5006/1.3292123
141. Hatamleh O, Singh PM, Garmestani H (2009) Corrosion susceptibility of peened friction stir welded 7075 aluminum alloy joints. Corros Sci 51:135–143. https://doi.org/10.1016/j.corsci.2008.09.031
142. Sutton MA, Yang B, Reynolds AP, Taylor R (2002) Microstructural studies of friction stir welds in 2024-T3 aluminum. Mater Sci Eng A 323:160–166. https://doi.org/10.1016/S0921-5093(01)01358-2

143. Fonda RW, Bingert JF, Colligan KJ (2004) Development of grain structure during friction stir welding. Scr Mater 51:243–248. https://doi.org/10.1016/j.scriptamat.2004.04.017
144. Vijaya Kumar P, Madhusudhan Reddy G, Srinivasa Rao K (2015) Microstructure and pitting corrosion of armor grade AA7075 aluminum alloy friction stir weld nugget zone – Effect of post weld heat treatment and addition of boron carbide. Def Technol 11:166–173. https://doi.org/10.1016/j.dt.2015.01.002
145. Li J, Dang J (2017) A summary of corrosion properties of Al-Rich solid solution and secondary phase particles in al alloys. Metals (Basel). 7:84
146. Queiroz FM, Magnani M, Costa I, de Melo HG (2008) Investigation of the corrosion behaviour of AA 2024-T3 in low concentrated chloride media. Corros Sci 50:2646–2657. https://doi.org/10.1016/j.corsci.2008.06.041
147. Liu X, Frankel GS, Zoofan B, Rokhlin SI (2007) In-situ observation of intergranular stress corrosion cracking in AA2024-T3 under constant load conditions. Corros Sci 49:139–148. https://doi.org/10.1016/j.corsci.2006.05.013
148. Cabrini M, Lorenzi S, Pellegrini S, Pastore T (2015) Environmentally assisted cracking and hydrogen diffusion in traditional and high-strength pipeline steels. Corros Rev 33:529–545. https://doi.org/10.1515/corrrev-2015-0051
149. Georgiou EP, Celis JP, Panagopoulos CN (2017) The effect of cold rolling on the hydrogen susceptibility of 5083 aluminum alloy. Metals (Basel) 7:451. https://doi.org/10.3390/met7110451
150. Kamoutsi H, Haidemenopoulos GN, Bontozoglou V, Pantelakis S (2006) Corrosion-induced hydrogen embrittlement in aluminum alloy 2024. Corros Sci 48:1209–1224. https://doi.org/10.1016/j.corsci.2005.05.015
151. Kumar S, Namboodhiri TKG (2011) Precipitation hardening and hydrogen embrittlement of aluminum alloy AA7020. Bull Mater Sci 34:311–321. https://doi.org/10.1007/s12034-011-0066-8
152. Scully JR, Young GA, Smith SW (2012) Hydrogen embrittlement of aluminum and aluminum-based alloys. In: Gaseous Hydrogen Embrittlement of Materials in Energy Technologies: The Problem, its Characterisation and Effects on Particular Alloy Classes. Woodhead Publishing, pp 707–768
153. Sanchez J, Lee SF, Martin-Rengel MA, et al (2016) Measurement of hydrogen and

embrittlement of high strength steels. Eng Fail Anal 59:467–477. https://doi.org/10.1016/j.engfailanal.2015.11.001

154. Vasco MC, Tserpes K, Pantelakis SG (2018) Numerical simulation of tensile behavior of corroded aluminum alloy 2024 T3 considering the hydrogen embrittlement. Metals (Basel) 8:56. https://doi.org/10.3390/met8010056
155. Cabrini M, Lorenzi S, Marcassoli P, Pastore T (2008) Effetto della diffusione dell'idrogeno sui fenomeni di environmental assisted cracking di acciai per pipeline in condizioni di protezione catodica. Metall Ital 100:15–22
156. Kim YS, Kim SS, Choe BH (2019) The role of hydrogen in hydrogen embrittlement of metals: The case of stainless steel. Metals (Basel) 9:406. https://doi.org/10.3390/met9040406
157. Xiong Z, Zheng W, Liu Y, et al (2019) Hydrogen diffusion mechanism around a crack tip in type 304L austenite stainless steel considering the influence of the volume expansion of strain-induced martensite transformation. Metals (Basel) 9:977. https://doi.org/10.3390/met9090977
158. Ferri M, Trueba M, Trasatti SP, et al (2017) Electrochemical investigation of corrosion and repassivation of structural aluminum alloys under permanent load in bending. Corros Rev 35:225–239. https://doi.org/10.1515/corrrev-2017-0068
159. Gutman EM (1998) Mechanochemistry of materials. Cambridge International Science Publishing, Cambridge
160. Revie RW (1983) Effects of dissolution on plastic deformation and cracking of metals. Prog Surf Sci 14:53–111. https://doi.org/10.1016/0079-6816(83)90014-X
161. Venugopal T, Rao KS, Rao KP (2004) Studies on Friction Stir Welded Aa 7075 Aluminum Alloy. 57:659–663
162. Fooladfar H, Hashemi B, Younesi M (2009) The Effect of the Surface Treating and High-Temperature Aging on the Strength and SCC Susceptibility of 7075 Aluminum Alloy. J Mater Eng Perform 2009 196 19:852–859. https://doi.org/10.1007/S11665-009-9562-Z
163. D'Urso G, Giardini C, Lorenzi S, et al (2017) The influence of process parameters on mechanical properties and corrosion behaviour of friction stir welded aluminum joints. Procedia Eng 207:591–596. https://doi.org/10.1016/J.PROENG.2017.10.1026

164. Mahoney MW, Rhodes CG, Flintoff JG, et al (1998) Properties of friction-stir-welded 7075 T651 aluminum. Metall Mater Trans A 1998 297 29:1955–1964. https://doi.org/10.1007/S11661-998-0021-5
165. Srinivasan PB, Dietzel W, Zettler R, et al (2005) Stress corrosion cracking susceptibility of friction stir welded AA7075-AA6056 dissimilar joint. Mater Sci Eng A 392:292–300. https://doi.org/10.1016/j.msea.2004.09.065
166. Maitra S, English GC, Maitra S, English GC (1982) Environmental factors affecting localized corrosion of 7075-t7351 aluminum alloy plate. MTA 13:161–166. https://doi.org/10.1007/BF02642428
167. Huang TS, Frankel GS (2006) Influence of grain structure on anisotropic localised corrosion kinetics of AA7XXX-T6 alloys. Corros Eng Sci Technol 41:192–199. https://doi.org/10.1179/174327806X120739
168. Muller IL, Galvele JR (1977) Pitting potential of high purity binary aluminium alloys-I. AlCu alloys. Pitting and intergranular corrosion. Corros Sci 17:179–193. https://doi.org/10.1016/0010-938X(77)90044-0
169. Ramgopal T, Gouma PI, Frankel GS (2002) Role of grain-boundary precipitates and solute-depleted zone on the intergranular corrosion of aluminum alloy 7150. Corrosion 58:687–697. https://doi.org/10.5006/1.3287699
170. Goswami R, Lynch S, Holroyd NJH, et al (2013) Evolution of grain boundary precipitates in Al 7075 upon aging and correlation with stress corrosion cracking behavior. In: Metallurgical and Materials Transactions A: Physical Metallurgy and Materials Science. Springer, pp 1268–1278
171. Najjar D, Magnin T, Warner TJ (1997) Influence of critical surface defects and localized competition between anodic dissolution and hydrogen effects during stress corrosion cracking of a 7050 aluminium alloy. Mater Sci Eng A 238:293–302. https://doi.org/10.1016/S0921-5093(97)00369-9
172. Scamans GM, Alani R, Swann PR (1976) Pre-exposure embrittlement and stress corrosion failure in AlZnMg Alloys. Corros Sci 16:443–459. https://doi.org/10.1016/0010-938X(76)90065-2
173. Vasudevan AK, Sadananda K (2010) Role of Slip Mode on Stress Corrosion Cracking Behavior. Metall Mater Trans A 2010 422 42:405–414. https://doi.org/10.1007/S11661-010-0471-4

174. Rajan K, Wallace W, Beddoes JC (1982) Microstructural study of a high-strength stress-corrosion resistant 7075 aluminium alloy. J Mater Sci 17:2817–2824. https://doi.org/10.1007/BF00644656
175. Asahi, T.; Yabusaki, F.; Osamura, K.; Murakami Y (1975) Studies on Microstructure and Stress-Corrosion Cracking Behavior of Al-Zn-Mg Alloys. In: International Conference of Light Metals and Alloys. pp 64–67
176. Talianker M, Cina B (1989) Retrogression and reaging and the role of dislocations in the stress corrosion of 7000-type aluminum alloys. Metall Trans A 1989 2010 20:2087–2092. https://doi.org/10.1007/BF02650294
177. Cho JH, Han SH, Lee CG (2016) Cooling effect on microstructure and mechanical properties during friction stir welding of Al-Mg-Si aluminum alloys. Mater Lett 180:157–161. https://doi.org/10.1016/j.matlet.2016.05.157
178. Zhang Z, Yang X, Zhang J, et al (2011) Effect of welding parameters on microstructure and mechanical properties of friction stir spot welded 5052 aluminum alloy. Mater Des 32:4461–4470. https://doi.org/10.1016/j.matdes.2011.03.058
179. Atik E, Meric C, Karlik B (2004) Determination of hardness of AA 2004 aluminium alloy under ageing conditions by means of artificial neural networks method. Metall 58:448–451
180. Bounds DG, Lloyd PJ, Mathew B, Waddell G (1988) Multi layer perceptron network for the diagnosis of low back pain. Publ by IEEE, pp 481–489
181. Cybenko G (1988) Continuous valued neural networks with two hidden layers are sufficient, Department of computer science. Trfts Univ
182. Cybenko G (1989) Approximation by superpositions of a sigmoidal function. Math Control Signals, Syst 2:303–314. https://doi.org/10.1007/BF02551274
183. Hecht-Nielsen R (1987) Kolmogorov's Mapping Neural Network Existence Theorem. SOS Printing
184. Lippmann RP (1987) An Introduction to Computing with Neural Nets. IEEE ASSP Mag 4:4–22. https://doi.org/10.1109/MASSP.1987.1165576
185. Garcia-Romeu ML, Ceretti E, Fiorentino A, Giardini C (2010) Forming force prediction in two point incremental forming using Backpropagation neural networks in combination with Genetic Algorithms. In: ASME 2010 International

Manufacturing Science and Engineering Conference, MSEC 2010. pp 99–106

186. Maren AJ, Jones D, Franklin S (1990) Configuring and Optimizing the Back-Propagation Network. In: Handbook of Neural Computing Applications. Elsevier, pp 233–250

187. Bocchi S, D'Urso G, Giardini C (2021) The effect of heat generated on mechanical properties of friction stir welded aluminum alloys. Int J Adv Manuf Technol 112:1513–1528. https://doi.org/10.1007/s00170-020-06462-9

188. Zhu XK, Chao YJ (2004) Numerical simulation of transient temperature and residual stresses in friction stir welding of 304L stainless steel. J Mater Process Technol 146:263–272. https://doi.org/10.1016/j.jmatprotec.2003.10.025

189. Arora HS, Singh H, Dhindaw BK (2012) Numerical simulation of temperature distribution using finite difference equations and estimation of the grain size during friction stir processing. Mater Sci Eng A 543:231–242. https://doi.org/10.1016/j.msea.2012.02.081

190. Hagan MT, Demuth HB, Beale MH, De Jesus O (2014) Neural Network Design 2nd Edition (2014)